

# A Model for Continental-Scale Water Erosion and Sediment Transport and Its Application to the Yellow River Basin



Inaugural Dissertation

zur

Erlangung des Doktorgrades

der Mathematisch-Naturwissenschaftlichen Fakultät

der Universität zu Köln

vorgelegt von

**Cong Jiang**

aus Shandong, China

Köln, März 2023

Berichtersteller:

Prof. Dr. Yaping Shao

Prof. Dr. Karl Schneider

Dr. Eric J. R. Parteli

Tag der mündlichen Prüfung: 22.05.2023

## Abstract

Quantifying suspended sediment discharge at large catchment scales has significant implications for various research fields such as water quality, global carbon and nutrient cycle, agriculture sustainability, and landscape evolution. There is growing evidence that climate warming is accelerating the water cycle, leading to changes in precipitation and runoff and increasing the frequency and intensity of extreme weather events, which could lead to intensive erosion and sediment discharge. However, suspended sediment discharge is still rarely represented in regional climate models because it depends not only on the sediment transport capacity based on streamflow characteristics but also on the sediment availability in the upstream basin. This thesis introduces a continental-scale Atmospheric and Hydrological-Sediment Modelling System (AHMS-SED), which overcomes the limitations of previous large-scale water erosion models. Specifically, AHMS-SED includes a complete representation of key hydrological, erosion and sediment transport processes such as runoff and sediment generation, flow and sediment routing, sediment deposition, gully erosion and river irrigation.

In this thesis, we focus on developing and applying AHMS-SED in the Yellow River Basin of China, an arid and semi-arid region known for its wide distribution of loess and the highest soil erosion rate in the world. There are three key issues involving the model development and application: human perturbation (irrigation) of the water cycle, the uncertainty of precipitation forcing on the water discharge and the large-scale water erosion and sediment transport. This thesis addresses all these three issues in the following way.

First, a new irrigation module is integrated into the Atmospheric and Hydrological Modelling System (AHMS). The model is calibrated and validated using in-situ and remote sensing observations. By incorporating the irrigation module into the simulation, a more realistic hydrological response was obtained near the outlet of the Yellow River Basin. Second, an evaluation of six precipitation-reanalysis products is performed based on observed precipitation and model-simulated river discharge by the AHMS for the Yellow River Basin. The hydrological model is driven with each of the precipitation-reanalysis products in two ways, one with the rainfall-runoff parameters recalibrated and the other without. Our analysis contributes to better quantifying the reliability of

hydrological simulations and the improvement of future precipitation-reanalysis products. Third, a regional-scale water erosion and sediment transport model, referred to as AHMS-SED, is developed and applied to predicting continental-scale fluvial transport in the Yellow River Basin. This model couples the AHMS with the CASCade 2-Dimensional SEDiment (CASC2D-SED) and takes into account gully erosion, a process that strongly affects the sediment supply in the Chinese Loess Plateau. The AHMS-SED is then applied to simulate water erosion and sediment processes in the Yellow River Basin for a period of eight years, from 1979 to 1987. Overall, the results demonstrate the good performance of the AHMS-SED and the upland sediment discharge equation based on rainfall erosivity and gully area index. AHMS-SED is also used to predict the evolution of sediment transport in the Yellow River Basin under specific climate change scenarios. The model results indicate that changes in precipitation will have a significant impact on sediment discharge, while increased irrigation will reduce the sediment discharge from the Yellow River.

## **Zusammenfassung**

Die Quantifizierung des Schwebstoffaustrags in großen Einzugsgebieten hat erhebliche Auswirkungen auf verschiedene Forschungsbereiche wie Wasserqualität, globaler Kohlenstoff- und Nährstoffkreislauf, Nachhaltigkeit in der Landwirtschaft und Landschaftsentwicklung. Es gibt immer mehr Belege dafür, dass die Klimaerwärmung den Wasserkreislauf beschleunigt, was zu Veränderungen bei den Niederschlägen und dem Abfluss führt und die Häufigkeit und Intensität extremer Wetterereignisse erhöht, was zu intensiver Erosion und Sedimentaustrag führen könnte. Der Abfluss von Schwebstoffen wird jedoch in regionalen Klimamodellen noch selten dargestellt, da er nicht nur von der Sedimenttransportkapazität auf der Grundlage der Abflusscharakteristiken, sondern auch von der Sedimentverfügbarkeit in den flussaufwärts gelegenen Einzugsgebieten abhängt. In dieser Arbeit wird ein kontinentales Atmospheric and Hydrological-Sediment Modelling System (AHMS-SED) vorgestellt, das die Grenzen bisheriger großmaßstäblicher Wassererosionsmodelle überwindet. AHMS-SED enthält eine vollständige Darstellung der wichtigsten hydrologischen, Erosions- und Sedimenttransportprozesse wie Abfluss- und Sedimentbildung, Abfluss- und Sedimentführung, Sedimentablagerung, Gully-Erosion und Flussbewässerung.

In dieser Arbeit konzentrieren wir uns auf die Entwicklung und Anwendung von AHMS-SED im Einzugsgebiet des Gelben Flusses in China, einer ariden und semi-ariden Region, die für ihre weite Verbreitung von Löß und die höchste Bodenerosionsrate der Welt bekannt ist. Bei der Entwicklung und Anwendung des Modells geht es um drei Schlüsselfragen: die Beeinflussung des Wasserkreislaufs durch den Menschen (Bewässerung), die Ungewissheit über die Auswirkungen des Niederschlags auf den Wasserabfluss und die großräumige Wassererosion und den Sedimenttransport. Die vorliegende Arbeit befasst sich mit all diesen drei Themen auf folgende Weise.

Zunächst wird ein neues Bewässerungsmodul in das Atmospheric and Hydrological Modelling System (AHMS) integriert. Das Modell wird anhand von In-situ- und Fernerkundungsbeobachtungen kalibriert und

validiert. Durch die Einbeziehung des Bewässerungsmoduls in die Simulation wurde eine realistischere hydrologische Reaktion in der Nähe der Mündung des Gelben Flussbeckens erzielt. Zweitens wird eine Bewertung von sechs Niederschlagsanalyseprodukten auf der Grundlage von beobachteten Niederschlägen und modellsimulierten Flussabflüssen durch das AHMS für das Einzugsgebiet des Gelben Flusses vorgenommen. Das hydrologische Modell wird mit jedem der Niederschlags-Analyseprodukte auf zwei Arten betrieben, einmal mit und einmal ohne Rekalibrierung der Niederschlag-Abfluss-Parameter. Unsere Analyse trägt dazu bei, die Zuverlässigkeit der hydrologischen Simulationen besser zu quantifizieren und künftige Niederschlagsanalyseprodukte zu verbessern. Drittens wird ein regionales Wassererosions- und Sedimenttransportmodell (AHMS-SED) entwickelt und zur Vorhersage der kontinentalen fluvialen Transportprozesse im Einzugsgebiet des Gelben Flusses eingesetzt. Dieses Modell verbindet das AHMS mit dem CASCADE 2-Dimensional SEDiment (CASC2D-SED) und berücksichtigt die Erosion durch Gullys, ein Prozess, der die Sedimentversorgung im chinesischen Lößplateau stark beeinflusst. Die AHMS-SED wird dann angewandt, um Wassererosion und Sedimentprozesse im Becken des Gelben Flusses für einen Zeitraum von acht Jahren, von 1979 bis 1987, zu simulieren. Insgesamt zeigen die Ergebnisse die gute Leistungsfähigkeit von AHMS-SED und der Gleichung für den Abfluss von Sedimenten aus dem Hochland, die auf der Eosivität von Niederschlägen und dem Flächenindex von Gullys basiert. AHMS-SED wird auch zur Vorhersage der Entwicklung des Sedimenttransports im Einzugsgebiet des Gelben Flusses unter bestimmten Szenarien des Klimawandels verwendet. Die Modellergebnisse deuten darauf hin, dass sich Änderungen der Niederschläge erheblich auf den Sedimentabfluss auswirken werden und dass eine verstärkte Bewässerung den Sedimentabfluss aus dem Gelben Fluss verringern wird.

# Contents

<b>1 Introduction</b> .....	<b>1</b>
<b>1.1 Background</b> .....	<b>1</b>
<b>1.2 Water Erosion in the Yellow River Basin</b> .....	<b>3</b>
<b>1.3 Motivation</b> .....	<b>5</b>
1.3.1 Study I .....	5
1.3.2 Study II .....	7
1.3.3 Study III.....	8
<b>1.4 Objectives and Outline</b> .....	<b>11</b>
<b>2 Water Erosion and Sediment Transport Modelling</b> .....	<b>14</b>
<b>2.1 Introduction</b> .....	<b>14</b>
<b>2.2 Hydraulic and Sediment Variables</b> .....	<b>14</b>
2.2.1 Hydraulic Variables.....	14
2.2.2 Sediment Variables.....	16
<b>2.3 Shallow Water and Sediment Transport Equations</b> .....	<b>19</b>
<b>2.4 Water Erosion and Sediment Transport Modelling in the Watershed</b> <b>21</b>	
2.4.1 Universal Soil Loss Equation .....	24
2.4.2 Revised Universal Soil Loss Equation .....	25
2.4.3 Modified Universal Soil Loss Equation .....	26
2.4.4 Kilinc and Richardson's equation (1973) .....	26
2.4.5 CASCade Two-dimensional Sediment Model (CASC2D-SED) .....	28
2.4.6 Pelletier's Model (2012).....	31
2.4.7 Sediment Yield Component of Système Hydrologique Européen ...	31
2.4.8 European Soil Erosion Model (EUROSEM).....	33
<b>3 Introduction to the AHMS-SED</b> .....	<b>35</b>
<b>3.1 Introduction</b> .....	<b>36</b>
<b>3.2 Atmospheric and Hydrological-Sediment Modelling System</b> .....	<b>36</b>
<b>3.3 Atmospheric and Hydrological Modelling System</b> .....	<b>37</b>
<b>3.4 Vertical Movement of Soil Moisture in the Land Model</b> .....	<b>38</b>
<b>3.5 2D Single-layer Distributed Groundwater Model</b> .....	<b>39</b>

<b>3.6</b>	<b>Channel Routing Model .....</b>	<b>39</b>
3.6.1	Manning Equation .....	40
3.6.2	Channel Bathymetry and Floodplain .....	41
<b>3.7</b>	<b>Irrigation Model.....</b>	<b>42</b>
<b>3.8</b>	<b>Water Erosion and Sediment Transport Model .....</b>	<b>44</b>
<b>4</b>	<b>A Regional Hydrological Model for Arid and Semi-Arid River Basins with Consideration of Irrigation .....</b>	<b>48</b>
<b>4.1</b>	<b>Introduction.....</b>	<b>49</b>
<b>4.2</b>	<b>Model Input Data.....</b>	<b>49</b>
4.2.1	Topography Data .....	49
4.2.2	Soil and Vegetation Data.....	50
4.2.3	Subsurface Data.....	50
4.2.4	Meteorological Data .....	50
4.2.5	Validation Data.....	50
<b>4.3</b>	<b>Model Setup and Spin-up.....</b>	<b>52</b>
<b>4.4</b>	<b>Model Performance Evaluation Indices.....</b>	<b>53</b>
<b>4.5</b>	<b>Parameter Calibration of Hydrological Model .....</b>	<b>53</b>
<b>4.6</b>	<b>Evaluation and Discussion .....</b>	<b>55</b>
4.6.1	Terrestrial Water Budget .....	55
4.6.2	Evapotranspiration.....	56
4.6.3	Terrestrial Water Storage.....	57
<b>4.7</b>	<b>Irrigation Impact on the Runoff, Evapotranspiration and Streamflow in the Yellow River Basin .....</b>	<b>59</b>
<b>4.8</b>	<b>Predict the Evolution of Streamflow under Specific Climate Change Scenarios .....</b>	<b>65</b>
<b>4.9</b>	<b>Conclusion and Outlook.....</b>	<b>66</b>
<b>5</b>	<b>Evaluation of Precipitation Reanalysis Products for Regional Hydrological Modelling in the Yellow River Basin .....</b>	<b>70</b>
<b>5.1</b>	<b>Introduction.....</b>	<b>71</b>
<b>5.2</b>	<b>Data .....</b>	<b>71</b>
5.2.1	Non-gauge-corrected Reanalysis Precipitation Datasets.....	71
5.2.2	Observed Precipitation Datasets.....	72
5.2.3	Gauge Corrected Reanalysis Precipitation Datasets.....	72

5.2.4	Streamflow Dataset .....	73
<b>5.3</b>	<b>Method .....</b>	<b>75</b>
5.3.1	Hydrological Model Setup .....	75
5.3.2	Evaluation Metrics .....	77
5.3.3	Standard Deviation of Elevation .....	78
<b>5.4</b>	<b>Results .....</b>	<b>78</b>
5.4.1	Performance Evaluation Using Gauge Observation.....	78
5.4.2	Performance Evaluation Using Offline AHMS.....	85
<b>5.5</b>	<b>Discussions .....</b>	<b>89</b>
5.5.1	Why Do the Non-gauge Corrected Reanalysis Datasets Overestimate the Precipitation in the Yellow River Basin?.....	89
5.5.2	Why Do CMFD and WFDE5/(CRU+CRU) Agree the Best with the Precipitation Observations? .....	91
5.5.3	How Do We Constrain Model Uncertainty and Quantify Anthropogenic Influences on Streamflow in This Study?.....	92
<b>5.6</b>	<b>Summary and Conclusions .....</b>	<b>92</b>
<b>5.7</b>	<b>Data Availability Statement.....</b>	<b>94</b>
<b>6</b>	<b>Development and Application of AHMS-SED to the Yellow River Basin with     Consideration of Gully Erosion .....</b>	<b>96</b>
<b>6.1</b>	<b>Introduction.....</b>	<b>97</b>
<b>6.2</b>	<b>Data .....</b>	<b>97</b>
6.2.1	Near Surface Meteorological Data .....	97
6.2.2	Geo-static Data .....	97
6.2.3	Measured River Discharge and Suspended Sediment Concentration .....	98
<b>6.3</b>	<b>Model Configuration and Experimental Design .....</b>	<b>98</b>
6.3.1	Model Configuration .....	98
6.3.2	Hydrological Modelling Parameters .....	99
6.3.3	Water Erosion and Sediment Transport Model Parameters .....	99
6.3.4	Experimental Design .....	100
6.3.5	Model Performance Evaluation Indices .....	101
<b>6.4</b>	<b>Results .....</b>	<b>102</b>
6.4.1	Model Calibration and Validation.....	102
6.4.2	Large Permanent Gully Erosion.....	104

6.4.3	Predicting Upland Sediment Discharge.....	105
6.4.4	Model Prediction for the Evolution of Sediment Yields Under Specific Climate Change Scenarios in the Yellow River Basin.....	107
<b>6.5</b>	<b>Discussions .....</b>	<b>108</b>
6.5.1	Gully Factor vs Slope Factor .....	108
6.5.2	Scaling Issues .....	110
6.5.3	Cropland Erosion.....	111
6.5.4	Sedimentation in Reservoirs.....	112
<b>6.6</b>	<b>Conclusions and Outlook .....</b>	<b>112</b>
6.6.1	Development of a Regional Model for Water Erosion and Sediment Transport .....	113
6.6.2	Insights From the Model Application to Yellow River Basin With Consideration of Gully Erosion.....	113
6.6.3	Outlook.....	115
<b>6.7</b>	<b>Data Availability Statement.....</b>	<b>115</b>
<b>7</b>	<b>Conclusions and Outlook.....</b>	<b>117</b>
7.1	Summary.....	117
7.2	Main Achievements.....	118
7.3	Main Limitations.....	120
7.4	Recommendations for Future Research .....	121
<b>Appendix A</b>	<b>.....</b>	<b>123</b>
<b>A.1</b>	<b>Discretization of the Richards equation .....</b>	<b>123</b>
<b>A.2</b>	<b>Discretization of the Diffusion Wave Equation .....</b>	<b>124</b>
<b>A.3</b>	<b>Discretization of Two-Dimensional Boussinesq Equation .....</b>	<b>126</b>
<b>Appendix B</b> .....		<b>128</b>
<b>B.1</b>	<b>Infiltration and Infiltration-Excess Runoff.....</b>	<b>128</b>
<b>B.2</b>	<b>Interaction Fluxes of River-Groundwater and River-Vadose.....</b>	<b>129</b>
<b>B.3</b>	<b>Terrestrial Water Budget and Changes .....</b>	<b>130</b>
<b>B.4</b>	<b>Major Reservoirs Along the Yellow River .....</b>	<b>130</b>
<b>B.5</b>	<b>Noah-MP Parameterization.....</b>	<b>132</b>
<b>B.6</b>	<b>Sensitivity Analysis .....</b>	<b>132</b>
<b>B.7</b>	<b>Spatial Distribution of the Hydrological Variables .....</b>	<b>137</b>
<b>B.8</b>	<b>Calibration and Sensitivity Analysis of Irrigation Model Parameters</b>	<b>139</b>

<b>Appendix C .....</b>	<b>140</b>
<b>C.1 Required Meteorological Variables for Offline AHMS.....</b>	<b>140</b>
<b>C.2 Irrigation Scheme in AHMS-IRR.....</b>	<b>140</b>
<b>C.3 Evaluation Metrics for Performance.....</b>	<b>141</b>
<b>C.4 Calibration of Rainfall-Runoff Model.....</b>	<b>142</b>
<b>C.5 Performance Evaluation Using Offline Atmospheric and Hydrological Modelling System (AHMS) .....</b>	<b>144</b>
<b>Appendix D .....</b>	<b>146</b>
<b>D.1 Definition of Slope and Interpolation Method.....</b>	<b>146</b>
<b>D.2 Observed and Predicted Sediment Discharge at Five Stations.....</b>	<b>147</b>
<b>Bibliography .....</b>	<b>149</b>
<b>Acknowledgments .....</b>	<b>165</b>
<b>Eidesstattliche Versicherung.....</b>	<b>167</b>
<b>Publications.....</b>	<b>168</b>

# List of Figures

- Figure 1.1:** Location and topography of the Yellow River Basin, including the locations of the five main hydrological stations: Tangnaihe (TNH), Lanzhou (LZ), Toudaoguai (TDG), Longmen (LM) and Huayuankou (HYK). The colours indicate the height above sea level from the digital elevation model (DEM). The dotted area, separating the stations of Longmen at the south and Toudaoguai at the north, corresponds to an area of permanent gully activity and very high-intensity water erosion. Sediment yield modulus within the time span from 1999 to 2019 exceeded  $5000 \text{ tons km}^{-2} \text{ yr}^{-1}$  in this area (<http://www.ncdc.ac.cn>). Subfigure: a typical landscape of permanent gullies in the Chinese Loess Plateau. .... 4
- Figure 1.2:** Observed average annual runoff and sediment yield in the sub-basins of the Yellow River Basin from 1979 to 1987 based on data from gauging stations. The four sub-basins, namely HW - TNH, TNH - LZ, LZ - TDG and TDG - HYK, are identified by the four main hydrological stations along the Yellow River. Annual observed runoff and sediment yield are converted from the daily streamflow and sediment concentration at gauging stations of TNH, LZ, TDG and HYK. Daily measurements of water discharge and suspended sediment concentration for the Yellow River can be obtained upon request from the National Earth System Science Data Center of China (<http://ge.geodata.cn>). .... 5
- Figure 1.3:** Annual gross water use in the Yellow River Basin from 1956 to 2019. For the period from 1956 to 2000, data were obtained from Jia et al. (2006), while for the period 2001-2019, data were collected from the Yellow River Bulletin of Water Resources, published by the Yellow River Conservancy Commission (YRCC) of the Ministry of Water Resources of China (<http://www.yrcc.gov.cn/other/hhgb/>). .... 7
- Figure 1.4:** Schematic diagram of online and offline Atmospheric and Hydrological Modelling System (AHMS) and its extension and application in the studies that comprise this thesis. .... 12
- Figure 2.1:** Schematic of upland and channel sediment transport in CASC2D-SED. .... 30
- Figure 3.1:** A simplified flowchart of AHMS-SED, integrating the Atmospheric and Hydrological Modelling System (AHMS) with a modified water erosion and sediment transport model (CASC2D-SED). .... 37
- Figure 3.2:** Sketch of the hydrologic cycle modelled in AHMS. .... 38
- Figure 3.3:** Simple river-floodplain storage model used in the sub-grid cross-section of the AHMS. The main channel area (blue) corresponds to the parameter  $A_c$  in Eq. (3.4). Furthermore, the equivalent floodplain area (green) is based on  $f_b$ , which is computed using Eq. (3.9). Modified after

Cunge (1980).....	42
<b>Figure 4.1:</b> Monthly terrestrial water storage anomaly (TWSA) with equivalent water height (EWH) over 2002-2022 in the Yellow River Basin calculated from JPL-Mascon (solid blue line), detrend (solid yellow line), and linear trend line (green). The trend is about 0.5 cm per year. ....	52
<b>Figure 4.2:</b> Predicted (dashed line) and observed (solid line) monthly streamflow from 1979 to 1987 at the hydrological stations: Tangnaihe (a), Lanzhou (b), Toudaoguai (c) and Huayuankou (d).....	54
<b>Figure 4.3:</b> (a) Results from the water budget analysis. Displayed are the predicted and observed annual averaged precipitation, evapotranspiration and runoff over 1979-1988 in the Yellow River Basin. Annual observed precipitation is upscaled from daily precipitation data provided by the China Meteorological Administration, and GLEAM is the Global Land Evaporation Amsterdam Model, while the annual observed runoff is converted from daily streamflow at the gauging station (Huayuankou). (b) Predicted and observed annual runoff averaged over 1979-1988 in the five subbasins of the Yellow River. Annual observed runoff is converted from the daily streamflow at gauging stations of Tangnaihe, Lanzhou, Toudaoguai and Huayuankou.....	56
<b>Figure 4.4:</b> Comparison of evapotranspiration simulated by GLEAM and AHMS over 1980-1988 in the Yellow River Basin (a) monthly evapotranspiration (b) annual cycles of monthly evapotranspiration. ...	57
<b>Figure 4.5:</b> Monthly terrestrial water storage change (TWSC) with equivalent water height over 2003-2011 in the Yellow River Basin calculated from GRACE dataset observation: JPL-mascons (solid blue line with circles), the offline AHMS simulation (solid black line; red circle) and the Global Land Data Assimilation System (GLDAS) (dash black line and black rectangle).....	58
<b>Figure 4.6:</b> Comparison of the monthly GRCAE-based TWSC with components of AHMS simulation, including changes in surface water ( $\Delta W_{sf}$ ; green line and circles), soil moisture water ( $\Delta W_{us}$ ; red dash line and triangles) and groundwater ( $\Delta W_{gw}$ ; black dash line and rectangles) over 2003-2011 in the Yellow River Basin. ....	58
<b>Figure 4.7:</b> (a) Monthly and (b) annual averaged cycles of total irrigation amount (green line) in the Yellow River Basin (upper reaches of Huayuankou station) for the period of 1978-1988, including river irrigation (blue line) and groundwater irrigation (orange line). ....	60
<b>Figure 4.8:</b> As in Fig. 4.3, but now considering irrigation in the AHMS simulation. ....	61
<b>Figure 4.9:</b> As in Fig. 4.4, but now considering irrigation in the AHMS simulation (orange line). ....	62

- Figure 4.10:** As in Fig. 4.5 and Fig. 4.6, but now considering irrigation in the AHMS simulation. .... 63
- Figure 4.11:** Comparison of (a) monthly and (b) averaged annual cycles of predicted (dashed lines), which is with (red) and without (blue) consideration of irrigation, and observed (solid line) streamflow at outlet of middle reaches of Yellow River Basin (Huayuankou station) for the period of 1979-1988. .... 64
- Figure 4.12:** Comparison of (a) monthly and (b) averaged annual cycles of predicted (dashed lines), which is under (red) and not under (blue) specific climate change scenarios (Scenario 1, 2, 3 and 4) and observed (solid line) streamflow at outlet of middle reaches of Yellow River Basin (Huayuankou station) for the period of 1979-1987. Subfigure (1) **Scenario 1:** precipitation halves, which means the rate of precipitation is uniformly halved during the study period. Subfigure (2) **Scenario 2:** temperature rises by 2 degrees evenly during the study period. Subfigure (3) **Scenario 3:** precipitation time (or amount) is halved, which means no rainfall on the even days (1979.01.02, 1979.01.04, 1979.01.06...) during the study period. Subfigure (4) **Scenario 4:** doubling the amount of river irrigation during the study period. .... 65
- Figure 5.1:** Annual precipitation in the Yellow River Basin from 1979 to 1989: NCEP (brown dashed line), OBS (solid orange line), GLDAS 2.0 (orange dashed line), ERA5 (green dashed line), WFDE5/CRU (blue dashed line), WFDE5/(CRU+GPCC) (pink dashed line) and CMFD (green dotted line). .... 79
- Figure 5.2:** Density curve (kernel density estimates KDE, which is the estimation of probability density functions of random variables based on kernels as weights) of annual precipitation of the products over the Yellow River Basin from 1979-1989. .... 80
- Figure 5.3:** Spatial distribution of the daily mean precipitation of the seven precipitation products considered in the present study, i.e., (a) OBS, (b) NCEP, (c) ERA5, (d) GLDAS 2.0, (e) WFDE5/CRU, (f) WFDE5/(CRU+GPCC) and (g) CMFD, from 1979 to 1989 over the Yellow River Basin (upland of Huayuankou), along with the Pearson correlation coefficient (PCC) between the reanalysis dataset and OBS for each grid in the basin. .... 81
- Figure 5.4:** Spatial distribution of the 99th percentile precipitation of the seven precipitation products considered in the present study, i.e., (a) OBS, (b) NCEP, (c) ERA5, (d) GLDAS 2.0, (e) WFDE5/CRU, (f) WFDE5/(CRU+GPCC) and (g) CMFD, from 1979 to 1989 over the Yellow River Basin (upland of Huayuankou), along with the root mean square error (RMSE, mm) and the Pearson correlation coefficient (PCC) between the reanalysis dataset and OBS for each grid in the basin. .... 82
- Figure 5.5:** (a) Monthly precipitation of the products over the Yellow River Basin from 1979-1989. (b) The annual cycle of monthly precipitation averaged

over 1979-1989. ....	83
<b>Figure 5.6:</b> Averaged monthly evaluation metrics of the precipitation products over the Yellow River Basin from 1979-1989: (a) RMSE (mm), (b) PCC, (c) MAE (mm), and (d) MAPE (%).....	84
<b>Figure 5.7:</b> Seasonal evaluation metrics of the precipitation products over the Yellow River Basin from 1979-1989: DJF (winter, December to February), MAM (spring, March to May), JJA (summer, June to August), SON (autumn, September to November), (a) RMSE (mm), (b) PCC, (c) MAE(mm), and (d) MAPE (%).....	85
<b>Figure 5.8:</b> Comparison of monthly streamflow simulated by offline AHMS-IRR with gauge-calibrated parameters (Scenario 1). The comparison includes seven different precipitation products against observed monthly streamflow at all four main hydrological stations, i.e., Tangnaihe (a), Lanzhou (b), Toudaoguai (c) and Huayuankou (d). The calibration period ranges from January 1, 1979, to December 31, 1983, while the validation period spans from January 1, 1984, to December 31, 1987. Note that OBS represents the observed streamflow, while OBS_P represents the streamflow simulated using the gauged precipitation.....	86
<b>Figure 5.9:</b> Performance of streamflow simulations forced by seven different precipitation products using the static rainfall-runoff parameters during the validation period (Scenario 1). (a) NSE, (b) mKGE. ....	86
<b>Figure 5.10:</b> Same as in Fig. 5.8 but with product-specific calibrated parameters for each of the seven precipitation products (Scenario 2).....	87
<b>Figure 5.11:</b> Performance of offline AHMS simulations of streamflow forced by seven different precipitation products using the dynamic rainfall-runoff parameters during the validation period (Scenario 2). (a) NSE, (b) mKGE. ....	88
<b>Figure 5.12:</b> Performance of offline AHMS simulations in terms of evapotranspiration forced by seven different precipitation products using the static (Scenario 1 in blue) and dynamic (Scenario 2 in yellow) rainfall-runoff parameters during the validation period. (a) RMSE (mm), (b) NSE.....	88
<b>Figure 5.13:</b> Pearson correlation coefficient (PCC) between (a) the average annual observed precipitation and (b) six reanalysis precipitation datasets with a standard deviation of elevation calculated in each 20-km grid over the Yellow River Basin. (c) The number of grids with a 20 km resolution and standard deviation of elevation over the Yellow River Basin. ....	89
<b>Figure 5.14:</b> Distribution of weather stations of the China Meteorological Administration in the Yellow River Basin (upstream of HYK station). Twenty-two national benchmark climate stations are shared worldwide through the Global Telecommunication System (GTS) (red points), and the other 60 national ordinary stations (green points) are not shared	

through the GTS. .... 91

**Figure 6.1:** The input geo-static data include elevation (a), slope (b), soil type (c), vegetation type (d), soil erodibility (e) and gully area index (f) for the Yellow River Basin. In subplot (f), the red line represents sediment source hotspots in the middle reaches of the Yellow River, the Loess Plateau of China. .... 100

**Figure 6.2:** Comparison of observed and predicted monthly suspended sediment discharge at the five hydrological stations: TNH (a), LZ (b), TDG (c) and HYK (d). HYK corresponds to the midstream outlet. Results of EXP 1 are shown here, and the upland erosion equation is based on USLE rainfall erosivity ( $EI_{30}$ ). Note that the range of the y-axis is not the same for the five subplots. .... 103

**Figure 6.3:** Simulation and corresponding observations of annual mean sediment yield averaged over 1979–1987 in the Yellow River. The simulations with and with the gully factor are EXP1 and EXP 7. .... 105

**Figure 6.4:** Spatial distribution of offline AHMS-SED simulated annual mean sediment transport capacity of overland flow, net eroded and deposited soil in the Yellow River over 1979–1987, subfigure (a) and (b) without the gully factor (EXP 1) while subfigure (c) and (d) with the gully factor (EXP 7). .... 105

**Figure 6.5:** Comparison of (a) monthly and (b) averaged annual cycles of predicted (dashed lines), which are under (red) and not under (blue) specific climate change scenarios (Scenario 1, 2, and 3) and observed (solid line) sediment flux at the outlet of middle reaches of Yellow River Basin (Huayuankou station) for the period of 1979-1987. Subfigure (1) **Scenario 1:** precipitation halves, which means the precipitation rate is uniformly halved during the study period. Subfigure (2) **Scenario 2:** temperature rises by 2 degrees evenly during the study period. Subfigure (3) **Scenario 3:** precipitation time (or amount) is halved, which means no rainfall on the even days (1979.01.02, 1979.01.04, 1979.01.06, ...) during the study period. (4) **Scenario 4:** doubling the amount of river irrigation during the study period. .... 108

**Figure 6.6:** Pearson correlation coefficient (PCC) between slope and gully area index at 20 km resolution in the Yellow River Basin. .... 110

**Figure 6.7:** Same as Fig. 6.3, but mean annual sediment yields in sub-basins are from EXP 1 and EXP 5, with different no-tillage method factors. .... 111

**Figure 6.8:** Annual cycles of observed monthly inflow and outflow sediment flux of the Longyangxia Reservoir (a), Liujiaxia Reservoir (b) and Sanmenxia Reservoir (c), averaged over 1979-1987. .... 112

**Figure B.1:** Annual cycles of measured monthly inflow (Tangnaihe station) and outflow (Guide station) of the Longyangxia reservoir (a), monthly inflow (Xunhua station) and outflow (Lanzhou minus Minhe and

Minxian station) of the Liujiaxia reservoir (b) and monthly inflow (Longmen plus Haxian and Hejin station) and outflow (Sanmenxia station) of the Sanmenxia reservoir (d), averaged over 1979-1988. .... 131

**Figure B.2:** Annual cycles of averaged weekly streamflow for the period of 1979-1988 at six main hydrological stations of the Yellow River, TangnaiHe (a), Lanzhou (b), Toudaoguai (c) and Huayuankou (e), with standard infiltration scheme  $0.5\beta$  (blue dashed line),  $1.0\beta$  (orange dashed line),  $1.5\beta$  (green dashed line) and observed discharge (red solid line with a grey fill), where  $\beta$  is the decay factor of soil saturated hydraulic conductivity..... 134

**Figure B.3:** Annual cycles of averaged weekly streamflow for the period of 1979-1988 at four main stations of Yellow River, Tangnaihe (a), Lanzhou (b), Toudaoguai (c) and Huayuankou (d), with Manning roughness coefficient of river  $n \times 0.5$  (blue),  $n$  (orange),  $n \times 1.5$  (green), observed discharge (red solid line with a grey fill). ..... 134

**Figure B.4:** Annual cycles of averaged weekly streamflow for the period of 1979-1988 at four main stations of the Yellow River, Tangnaihe (a), Lanzhou (b), Toudaoguai (c) and Huayuankou (d), with the depth of river  $B \times 0.5$  (blue),  $B$  (orange),  $B \times 1.5$  (green), observed discharge (red solid line with a grey fill)..... 135

**Figure B.5:** Annual cycles of averaged weekly streamflow for the period of 1979-1988 at four main stations of Yellow River, Tangnaihe (a), Lanzhou (b), Toudaoguai (c) and Huayuankou (d), with the width of the river  $W \times 0.5$  (blue),  $W$  (orange),  $W \times 1.5$  (green), observed discharge (red solid line with a grey fill)..... 135

**Figure B.6:** Annual cycles of averaged weekly streamflow for the period of 1979-1988 at four main stations of the Yellow River, Tangnaihe (a), Lanzhou (b), Toudaoguai (c) and Huayuankou (d), with an exponent of the fraction of riverbed  $\alpha = 0.4$  (blue),  $0.5$  (orange),  $0.8$  (green), observed discharge (red solid line with a grey fill). ..... 136

**Figure B.7:** Annual cycles of averaged weekly streamflow for the period of 1979-1988 at four main stations of the Yellow River, Tangnaihe (a), Lanzhou (b), Toudaoguai (c) and Huayuankou (d), with hydraulic conductance of stream-aquifer interconnection  $C_s = 0.4$  (blue),  $0.5$  (orange),  $0.8$  (green), observed discharge (red solid line with a grey fill)..... 136

**Figure B.8:** Spatial distribution of mean annual (a) precipitation, (b) evapotranspiration, (c) runoff, (d) streamflow, (e) soil moisture, (f) groundwater depth, (g) surface runoff, (h) subsurface runoff, averaged over 1979-1988, at the Yellow River Basin..... 138

**Figure D.1:** Same as Fig. 6.2 but use the runoff in the KR equation (EXP 10)..... 147

**Figure D.2:** Same as Fig. 6.2 but use the overland flow in the KR equation (EXP 17).  
..... 148

## List of Tables

<b>Table 2.1:</b> Rainfall erosivity and sediment transport capacity for overland flow in selected water erosion and sediment transport models. ....	23
<b>Table 2.2:</b> Modified sediment transport equations for overland flow (adopted from Julien & Simons (1985)) .....	27
<b>Table 2.3:</b> Particle mean diameter and settling velocity. ....	30
<b>Table 4.1:</b> Comparison of statistical and simulated areal average annual irrigation in the Yellow River Basin from 1979 to 1987 (mm/yr).....	60
<b>Table 5.1:</b> Overview of seven (3 or 6-) hourly gridded precipitation datasets evaluated in this study. Abbreviations in the data source column are defined as follows: G: gauge; S: satellite; and R: reanalysis. ....	74
<b>Table 5.2:</b> Two scenarios are designed to evaluate different precipitation products using the offline Atmospheric and Hydrological Modelling System integrated IRRigation module (AHMS-IRRIG).....	76
<b>Table 5.3:</b> Annual precipitation statistics for the Yellow River Basin from 1979 to 1989 (unit: mm), associated with the different products considered in this study. ....	80
<b>Table 5.4:</b> Statistics of the monthly precipitation of the products over the Yellow River Basin from 1979 to 1989 (unit: mm).....	83
<b>Table 6.1:</b> Experimental design to evaluate the different sediment transport capacity equations for overland flow.....	101
<b>Table 6.2:</b> Statistical evaluation for the suspended sediment discharge, predicted by the model, based on corresponding observations at five hydrological stations.....	104
<b>Table 6.3:</b> Statistical evaluation of the modelling ensemble average of suspended sediment discharge obtained with the model along with corresponding observations at five hydrological stations. ....	106
<b>Table B.1:</b> Information of four major reservoirs along the mainstream of Yellow River.....	131
<b>Table B.2:</b> Noah-MP parameterization options used in this study.....	132
<b>Table B.3:</b> Experimental design for hydrological parameters sensitivity analysis. ....	133
<b>Table B.4:</b> Experimental design for calibration and validation of irrigation model. ....	139
<b>Table B.5:</b> Comparison of statistical and simulated areal average annual irrigation in the Yellow River Basin, as well as the NSE of monthly streamflow at outlet of YRB (HYK) from 1979 to 1987 (mm yr <sup>-1</sup> ).....	139

<b>Table C.1:</b> List of meteorological variables required to run AHMS in an offline mode. ....	140
<b>Table C.2:</b> Evaluation metrics, range, and perfect agreement value.....	142
<b>Table C.3:</b> Calibrated soil parameters against observed runoff in the sub-basins. .	142
<b>Table C.4:</b> Simulated and observed mean annual area runoff from 1979 to 1987 in the Yellow River Basin including four subbasins, Sub-basins 1 (HW-TNH), Sub-basins 2 (TNH-LZ), Sub-basins 3 (LZ-TDG) and Sub-basins 4 (TDG-HYK). ....	143
<b>Table C.5:</b> Comparison of monthly streamflow simulated with gauge-calibrated parameters using seven different precipitation products and observed streamflow. ....	144
<b>Table C.6:</b> Same as Table C.5, but with recalibrated parameters for each of the six precipitation products (Scenario 2). ....	145
<b>Table C.7:</b> Root-Mean-Square Error (RMSE) and Nash-Sutcliffe Efficiency (NSE) computed between the measured and simulated evapotranspiration produced by the numerical experiments for the period January 1980 to December 1987.....	145

## List of abbreviations

<b>Abbreviation</b>	<b>Definition</b>
ADI	Alternating Direction Implicit method
AHMS	Atmospheric and Hydrological Modeling System
AHMS-IRRIG	Atmospheric and Hydrological Modelling System integrated IRRigation module
AHMS-SED	Atmospheric and Hydrological-Sediment Modeling System
BIAS	Relative Bias
CASC2D-SED	CASCade 2-Dimensional Sediment Model
CMA	China Meteorological Administration
CMFD	China Meteorological Forcing Dataset
CRU	Climatic Research Unit
DEM	Digital Elevation Model
ECMWF	European Center for Medium-Range Weather Forecasts
ERA5	Fifth-generation reanalysis product created by the European Center for Medium-Range Weather Forecasts
EUROSEM	European Soil Erosion Model
GLDAS	Global Land Data Assimilation System
GPCC	Global Precipitation Climatology Centre
GPCP	Global Precipitation Climatology Project
GTS	Global Telecommunications System
GWD-LR	Global Width Database of Large Rivers
HMS	Hydrologic Model System
HYK	Huayuankou
IPCC	Intergovernmental Panel on Climate Change
KDE	Kernel Density Estimates
mKGE	Modified Kling-Gupta Efficiency
KR	Kilinc and Richardson's equation (1973)
LAI	Leaf Area Index
LISEM	Lisem Integrated Spatial Earth Modeller
LM	Longmen
LSM	Land Surface Model

LZ	Lanzhou
MAE	Mean Absolute Error
MAPE	Mean Absolute Percentage Error
MERIT	Multi-Error-Removed Improved-Terrain DEM
MODIS	Moderate Resolution Imaging Spectroradiometer
MUSLE	Modified Universal Soil Loss Equation
NSE	Nash–Sutcliffe model Efficiency coefficient
NCEP/NCAR	National Centers for Environmental Prediction and the National Center for Atmospheric Research
ORCHIDEE	Organising Carbon and Hydrology in Dynamic Ecosystems
PCC	Pearson Correlation Coefficient
PE	Percentage Error
PSL	Physical Sciences Laboratory (NOAA)
RCM	Regional Climate Model
RMSE	Root Mean Square Error
RUSLE	Revised Universal Soil Loss Equation
SBI	Sediment Balance Index
SDE	Standard Deviation of Elevation
SHE	Système Hydrologique Européen
TDG	Toudaoguai
TNH	Tangnaihe
USLE	Universal Soil Loss Equation
WBI	Water Budget Index
WEPP	USDA-Water Erosion Prediction Project
WFDE5	WATCH Forcing Data methodology applied to ERA5 reanalysis data
WPS	WRF Preprocessing System
WRF	Weather Research and Forecasting Model
YRB	Yellow River Basin
YRCC	Yellow River Conservancy Commission

## List of symbols

Symbol	Unit	Definition
<b>Greek</b>		
$\alpha$	-	gully empirical parameter
$\alpha_l$	-	the exponent in the river-floodplain storage model
$\beta_m$	-	momentum correction factor
$\varepsilon$	MJ ha <sup>-1</sup> mm <sup>-1</sup>	rainfall kinetic energy per unit rainfall depth per hectare
$\eta$	-	exponent
$\rho$	kg m <sup>-3</sup>	water density
$\rho_b$	kg m <sup>-3</sup>	soil bulk density
$\rho_s$	kg m <sup>-3</sup>	sediment density
$\rho_m$	kg m <sup>-3</sup>	mixture density of the fluid
$\gamma$	N m <sup>-3</sup>	the specific weight of water
$\gamma_s$	N m <sup>-3</sup>	specific weight of sediment
$\omega$	J m <sup>-2</sup> s <sup>-1</sup>	stream power
$\omega_{cr}$	J m <sup>-2</sup> s <sup>-1</sup>	critical stream power
$\omega_u$	m s <sup>-1</sup>	unit stream power
$\omega_{ucr}$	m s <sup>-1</sup>	critical unit stream power
$\omega_{eff}$	N <sup>1.5</sup> s <sup>-1.5</sup> m <sup>-2.17</sup>	effective stream power
$\omega_{effcr}$	N <sup>1.5</sup> s <sup>-1.5</sup> m <sup>-2.17</sup>	critical value of $\omega_{eff}$
$\tau, \tau_{xx}, \tau_{yx}$	N m <sup>-2</sup>	shear stress on the face of the infinitesimal cubical
$\tau_{zx}$		volume element
$\tau_0$	N m <sup>-2</sup>	bed shear stress
$\tau_{cr}$	N m <sup>-2</sup>	critical shear stress
$\tau^*$	-	Shields number
$\theta$	degree	slope
$\nu$	m <sup>2</sup> s <sup>-1</sup>	kinematic viscosity
$\psi$	m	soil matric potential
$\Delta x$	m	width of the grid cell
$\lambda$	m	slope length

### **Latin**

$a, c$	-	coefficients of the hydraulic geometric equation
$a_1$	-	location coefficient in MUSLE
$A$	$\text{t ha}^{-1} \text{yr}^{-1}$	annual soil loss
$A_c$	$\text{m}^2$	cross-section area of the flow
$b, f$		exponents in the hydraulic geometric equation
$b_1$	-	location coefficient in MUSLE
$c_2$	-	coefficient in Govers (1990)'s transport capacity equation
$C$	-	vegetation cover or crop factor
$C_d$	-	drag coefficient
$C_g, C_u,$	$\text{m}^3 \text{s}^{-1}$	water flux exchange by the river with saturated soil, unsaturated soil and lake
$C_{lake}$		
$C_l$	-	lift coefficient
$C_v$	$\text{m}^3 \text{m}^{-3}$	volumetric sediment concentration
$C_w$	$\text{NN}^{-1}$	sediment concentration by weight
$CL$	%	clay content in percent
$d_1, d_2$	-	exponents
$d_{50}$	m	median grain diameter
$d_s$	m	diameter of sediment particle
$D_f$	$\text{m}^3 \text{m}^{-1} \text{s}^{-1}$	detachment of soil volume by overland flow per unit length of the flow
$D_{fm}$	$\text{kg m}^{-2} \text{s}^{-1}$	detachment of soil mass by overland flow
$D_r$	$\text{m}^3 \text{m}^{-1} \text{s}^{-1}$	detachment of soil volume by raindrops per unit length of the flow
$D_{rm}$	$\text{kg m}^{-2} \text{s}^{-1}$	detachment of soil mass by raindrops
$e_1$	-	scaling parameter
$e_2$	-	exponent
$e_3$	-	exponent
$E$	$\text{MJ ha}^{-1}$	rainfall kinetic energy of the interval $\Delta t$
$f_d$	-	fraction of the soil within each soil texture bin of grain diameter
$f_b$	-	fractional area of riverbed

$f_{no-till}$	-	no-tillage method factor
$f_w$	-	wetted surface fraction
$Fr$	-	Froude number
$F_B$	N	buoyancy force
$F_D$	N	drag force
$F_L$	N	lift force
$F_R$	N	resisting force
$F_W$	N	gravitational acceleration force
$F_{crop}$	-	irrigation fraction
$F_{iloss}$	-	fraction of flood irrigation loss
$F_{veg}$	-	vegetation fraction
$g$	$m\ s^{-2}$	acceleration of gravity
$G_a$	-	gully area index
$G_f$	-	gully factor
$G_s$	-	sediment specific gravity
$h$	m	flow depth
$h_r$	m	river level
$h_g$	m	groundwater level
$\bar{h}$	m	uniform depth of flow
$h_{\Delta t}$	mm	rainfall depth in each time interval $\Delta t$
$i$	-	size fraction
$I_{30}$	$mm\ hr^{-1}$	maximum 30 min rainfall intensity
$I_e$	$m\ s^{-1}$	effective rainfall intensity
$k_r$	$g\ J^{-1}$	soil detachability for rainfall
$k_f$	$g\ J^{-1}$	soil detachability for flow
$K$	$m\ s^{-1}$	soil hydraulic conductivity
$K_{sat}$	$m\ s^{-1}$	soil saturated hydraulic conductivity
$K_{usle}$	$tons\ ha\ hr\ ha^{-1}$ $MJ^{-1}\ mm^{-1}$	soil erodibility index
$L$	-	slope length factor
LAI	-	leaf area index
$M$	-	number of rainfall intervals in one event
$Mr, Md$	$(kg\ m\ s^{-1})^2\ m^{-2}\ s^{-1}$	momentum squared for rain and leaf drip

$n$	$s\ m^{-1/3}$	Manning's roughness coefficient
$N$	-	number of the individual event
$p1, p2$	-	empirical parameters in Pelletier (2012)
$P$	-	soil conservation factor
$P_w$	m	the wetted perimeter of the flow
$P_e$	mm	event precipitation
$P_s$	-	simulation values
$P_o$	-	observation values
$\overline{P}_o$	-	average observation values
$q_u$	$m^2\ s^{-1}$	water discharge per unit width
$q_{cr}$	$m^2\ s^{-1}$	critical water discharge
$q_s$	tons $m^{-1}\ s^{-1}$	sediment discharge per unit width by mass
$q_p$	$m^3\ s^{-1}$	peak flow rate
$Q_{irr}$	$m^3\ s^{-1}$	irrigation water flux
$Q_{irr,sf}$	$m^3\ s^{-1}$	irrigation water flux from surface water
$Q_{irr,gw}$	$m^3\ s^{-1}$	irrigation water flux from groundwater water
$Q_e$	mm	event runoff
$Q_R$	-	event runoff coefficient ( $Q_e/P_e$ )
$Q_v$	$m^3$	volume of runoff
$r_i$	mm $hr^{-1}$	rainfall intensity
$R$	MJ mm $ha^{-1}\ hr^{-1}$ $yr^{-1}$	rainfall-runoff erosivity index
Re	-	Reynolds number
$R_{ev}$	MJ mm $ha^{-1}\ hr^{-1}$	erosivity index of an individual event ( $i$ ),
$R_h$	m	hydraulic radius
$R_k$	mm $yr^{-1}$	mean monthly rainfall
$R_{sf}$	$m\ s^{-1}$	surface runoff rate
$R_O$	-	Rouse number
$R_O\ \#$	-	Rouse number used in Pelletier (2012)
$S_{30m}$	-	surface slope at 30 m resolution
$S_{20km}$	-	surface slope at 20 km resolution
$S$	-	slope steepness factor
$S_0$	-	surface or bed slope

$S_f$	-	fraction slope
$SM$	m	integrated soil moisture
$SM_{ref}$	m	integrated field capacity and wilting point in the
$SM_{wlt}$		root area
$SMA$	-	soil moisture availability
$SY$	tons	sediment yield
$T_c$	$m^3 m^{-3}$	sediment transport capacity for overland flow
$T_{c,rill}$	$m^3 m^{-3}$	sediment transport capacity for rill
$T_{c,interill}$	$m^3 m^{-3}$	sediment transport capacity for inter rill
$u^*$	$m s^{-1}$	fraction velocity
$v_x, v_y, v_z$	$m s^{-1}$	flow velocity in $x, y$ and $z$ direction
$v_s$	$m s^{-1}$	sediment fall velocity
$V$	$m s^{-1}$	average velocity of the flow cross-section
$w$	m	flow width



# 1 Introduction

## 1.1 Background

Erosion and sedimentation are natural terrestrial processes that have been active from geological time to the present day, shaping the landscape of the world today (Julien, 2010). Further, soil erosion is a major resource and environmental problem today, as it damages agricultural soils and sustainability by reducing soil fertility and field productivity (Mao et al., 2010). Soil erosion by water is the main cause of soil erosion on a global scale, although wind erosion is more severe in many arid regions (Lal, 2017; Shao, 2008). Water erosion and sediment transport processes also play an important role in the global nutrient and carbon cycle by detaching nutrients and carbon from the terrestrial carbon and nutrient pools and transporting them into rivers and oceans (Lal, 2003; Ludwig & Probst, 1996). Moreover, sediment degrades the quality of freshwater because not only is it a major pollutant, but the aggregation of sediment catalyzes, carries and stores other forms of pollutants (Oschwald, 1972). Furthermore, sedimentation in streams or reservoirs can reduce water storage capacity and reduce the role of reservoirs in flood control, water supply, irrigation, and power generation, or even lead to their abandonment (Dutta, 2016).

The response of the water cycle and the associated energy, transported carbon, nutrients and sediments to climate change constitutes a topic of great interest to the scientific community and has significant implications for society (Chahine, 1992; Schlesinger & Bernhardt, 2020). A growing body of evidence (Allen & Ingram, 2002; Folland et al., 2002; Genfo et al., 1991; Huntington, 2006; Loaiciga et al., 1996; Trenberth, 1999) suggests that climate warming will accelerate the water cycle, leading to changes in precipitation and runoff, and will increase the frequency and intensity of extreme hydrological events, which could lead to intensive erosion and sediment discharge. During such events, very heavy rain leads to flooding and severe water erosion, such as landslides and mudslides in natural hazards, posing a very high risk to life and property, such as the floods in western Germany in 2021 (Watts, 2021).

Water erosion and sediment transport not only play an important role in human

production and livelihoods but are also, in turn, heavily influenced by human activities within the basin (Walling, 1999). Specifically, in the sediment source areas (upland), water erosion processes are often accelerated through land management activities (Wicks, 1988), including ploughing and tillage in agriculture, deforestation, road construction, mining, and urbanization, and decelerated by vegetation restoration. In the sediment transfer area (river) and sink areas (reservoir), man-induced changes to the hydraulic characteristics of the river, the river sand mining, check dams and the reservoirs have drastically altered (decrease by sedimentation) the sediment load in the river (Wang et al., 2016).

As the study basin of this thesis, the Yellow River Basin of China (See Section 1.2), is mostly arid and semi-arid, the response of the water cycle to human perturbation and the water erosion and sediment transport specific to arid and semi-arid regions are described below.

The IPCC report (Pörtner et al., 2022) highlights that ecosystems and freshwater in drylands are susceptible to changes in precipitation, and they are at high risk of climate change due to water scarcity and poor resilience. Human alterations to the water cycle can be extreme (Vorosmarty & Sahagian, 2000). Specifically, human activities, such as irrigation and regulation of reservoirs in drylands, strongly interfere with the water cycle. For example, freshwater consumption in the rivers and lakes (irrigation and domestic use) can reduce runoff and increase evaporation; flood control dams can reduce the peak flow; reservoirs can alter the seasonal variation of flow and increase the evaporation from the water bodies; land use change from reforestation or afforestation (deforestation) will lead to increased (decreased) evaporation and decreased (increased) runoff in the watershed. In the drylands, the combined impacts of climate change and strong human interference on the water cycle make it difficult to differentiate their respective contributions to changes in hydrological variables (Wang et al., 2015).

On the other hand, water erosion in drylands is severe, mostly due to the sparse vegetation, heterogeneous rainfall, and intensive human farming (Langbein & Schumm, 1958). According to Langbein & Schumm (1958), based on records from 170 gauging stations and reservoirs in the USA, the sediment yield in the watershed reaches the maximum when the mean annual precipitation is around 254 mm to 356 mm. This is caused, on the one hand, by aridity leading to a lack of runoff. On the

other hand, increased rainfall leads to increased vegetation density, which means increased surface soil cover and protection. Therefore, it has also been suggested that future increases in precipitation under climate change may not always increase water erosion in the world but will depend on the climate before the change (Langbein & Schumm, 1958). A typical example of the special and intense water erosion of the arid and semi-arid Chinese Loess Plateau in the Yellow River Basin is presented in detail below.

## 1.2 Water Erosion in the Yellow River Basin

Interestingly, our planet's most severe soil erosion area is located on the arid and semi-arid Chinese Loess Plateau. As shown in Fig. 1.1, the Chinese Loess Plateau, located in the middle reaches of the Yellow River, covers an area of 640,000 km<sup>2</sup> in northwest China. This plateau is well known for large-scale loess cover and for its high soil erosion rates (approximately 1.6 Gt yr<sup>-1</sup> on average over 1950-1980, according to Qian & Dai (1980)). Over 60% of land in the Loess Plateau is undergoing severe soil erosion, with an average soil yield of 2000-2500 tons km<sup>-2</sup> yr<sup>-1</sup> and about 0.01-2 cm of topsoil being washed away every year (Shi & Shao, 2000). According to Hessel et al. (2003) and Zheng & Wang (2014), the world's highest soil erosion rate is the result of several factors, including high soil erodibility, sparse vegetation, large permanent gullies, concentrated and high-intensity rainfall, as well as intensive long-term human activity. Further, over the past 60 years, the sediment load of the Yellow River has decreased by approximately 90% (Yu et al., 2013) due to the reductions in water discharge and sediment concentration. These changes can be attributed to regional climatic changes and human interventions such as soil conservation on the Loess Plateau, increased water consumption, and several dams along the Yellow River (Wang et al., 2016; Yu et al., 2013).

In addition, investigating water erosion and sediment yield on the Loess Plateau requires knowledge of the Yellow River Basin in which it is located. The Yellow River is the second-longest river in China (5464 km), and the Yellow River Basin (795,000 km<sup>2</sup>) is the largest river basin in north China. The Yellow River flows across the Qinghai-Tibet Plateau, Inner Mongolia Plateau, Chinese Loess Plateau and Huanghuaihai Plain. The annual mean air temperature in the Yellow River Basin ranges from -4° to 2°, and the annual mean precipitation is approximately 450 mm (Yellow River Water Bulletin), which is unevenly distributed. Moreover, the basin is

characterized by a plateau and temperate climate and is strongly affected by the East Asian monsoon.

As seen in Fig. 1.2, the mean annual runoff in sub-basin 3 is negative, which can be attributed to the river water used for irrigation in this region. Therefore, it is known that river water used for irrigation is an important component of the water balance, particularly in the semi-arid areas of the Yellow River Basin. Moreover, the sediment discharge of the Yellow River significantly increases as it flows through the Loess Plateau. As seen in Fig. 1.2, the upper-stream area of TDG supplies only 10% of the sediment load to the Yellow River. In comparison, nearly 90% of the sediment load comes from the middle-stream area (TDG - HYK), where the main geological characteristic is the wind-deposited Loess Plateau. Therefore, the main focus of this study is the representation of human perturbation (irrigation) of the water cycle and severe water erosion in this important part of the Yellow River Basin, as detailed below.

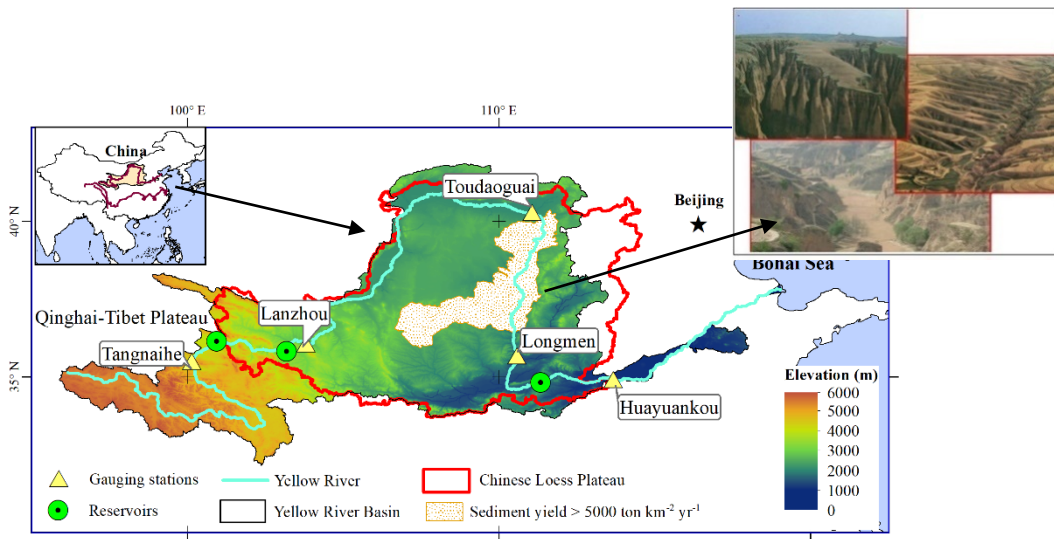


**Figure 1.1:** Location and topography of the Yellow River Basin, including the locations of the five main hydrological stations: Tangnaihe (TNH), Lanzhou (LZ), Toudaoguai (TDG), Longmen (LM) and Huayuankou (HYK). The colours indicate the height above sea level from the digital elevation model (DEM). The dotted area, separating the stations of Longmen at the south and Toudaoguai at the north, corresponds to an area of permanent gully activity and very high-intensity water erosion. Sediment yield modulus within the time span from 1999 to 2019 exceeded 5000 tons  $\text{km}^{-2} \text{yr}^{-1}$  in this area (<http://www.ncdc.ac.cn>). Subfigure: a typical landscape of permanent gullies in the Chinese Loess Plateau.

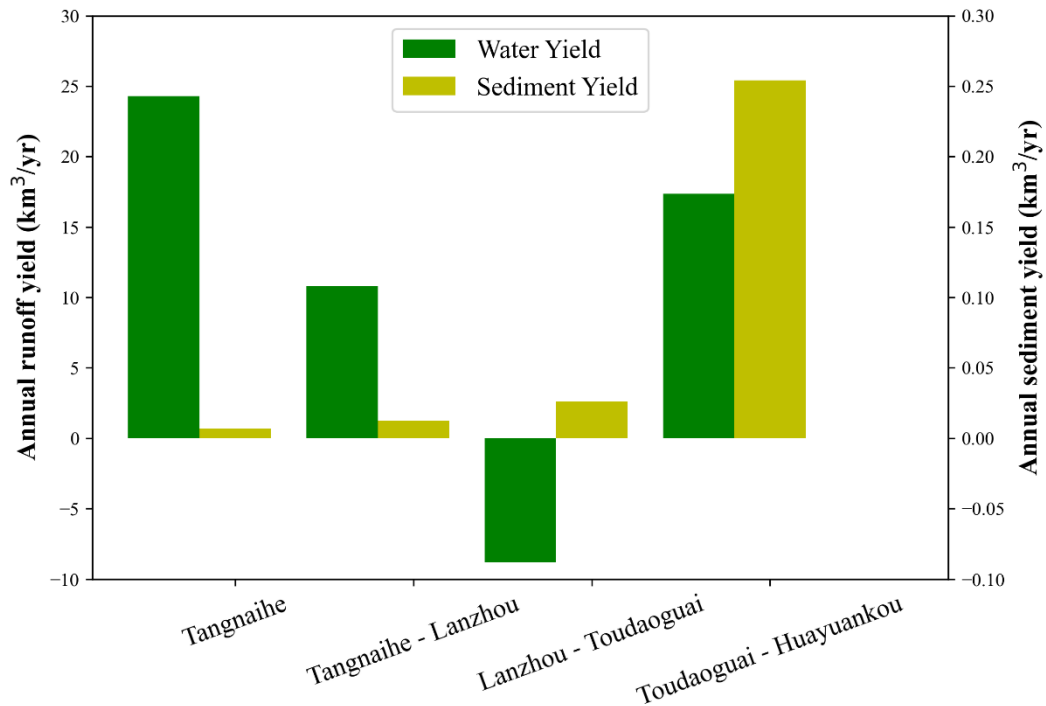


**Figure 1.2:** Observed average annual runoff and sediment yield in the sub-basins of the Yellow River Basin from 1979 to 1987 based on data from gauging stations. The four sub-basins, namely HW - TNH, TNH - LZ, LZ - TDG and TDG - HYK, are identified by the four main hydrological stations along the Yellow River. Annual observed runoff and sediment yield are converted from the daily streamflow and sediment concentration at gauging stations of TNH, LZ, TDG and HYK. Daily measurements of water discharge and suspended sediment concentration for the Yellow River can be obtained upon request from the National Earth System Science Data Center of China (<http://gre.geodata.cn>).

### 1.3 Motivation

Three key issues related to developing and applying the Atmospheric and Hydrological-Sediment Modeling System (AHMS-SED) in the Yellow River Basin are shown below.

Study I: human perturbation (irrigation) of the water cycle

Study II: the uncertainty of precipitation forcing on the water discharge

Study III: large-scale water erosion and sediment transport

In the following, the aims of the three studies are motivated.

#### 1.3.1 Study I

Atmospheric and hydrological models have been developed substantially in recent years, as they provide a powerful tool for the prediction and assessment of regional

meteorological and hydrological processes and for investigating the dynamic feedback between the atmosphere and hydrosphere (Gochis et al., 2015; Maxwell et al., 2011; Shrestha et al., 2014; Wagner et al., 2016). Such models have found diverse applications in studies on basin-scale hydrological responses to climate change and anthropogenic activities (Maxwell et al., 2007; Wilby et al., 1994).

However, hydrological simulation in arid and semi-arid regions remains a formidable task because the reliable representations of the often low and heterogeneous rainfall, intermittent river flow and impacts of human activities are particularly challenging (Pilgrim et al., 1988; Rafiei-Sardooi et al., 2022). Thus, we focus here on the development of a hydrological model for arid and semi-arid regions.

Specifically, the Yellow River Basin is selected as the research area owing to its unique hydrological characteristics and important position in China. The average water resources in the Yellow River Basin account for only 2% of the total water resources in China, but the water from this basin feeds 12% of the Chinese population. However, water shortage constitutes a serious problem given the increasing water demand in the area, with continuing population growth and urban development. In 1997, the downstream 704 km from the estuary dried up for more than 226 days (Cong et al., 2009). The large irrigation districts in the Yellow River Basin are mainly located in arid and semi-arid areas, and irrigation has accounted, for instance, for more than 80% (60%) of the gross human water use in the period from 1956 to 2010 (2001-2019) and rapidly increasing with time (see Fig. 1.3). For instance, the Hetao region takes about 5 billion m<sup>3</sup> of water every year from the Yellow River.

Most previous studies about hydrological processes in the Yellow River Basin neglected explicit consideration of river water use in large-scale irrigation districts (e.g. Cong et al. (2009), Yuan et al. (2016)). Jia et al. (2006) introduced a water use module in the distributed hydrological model to assess the water resources in the Yellow River Basin by taking the census irrigation data as input. In the latter study, irrigation water requirements in the model were estimated using statistical methods and data, not physically based modelling. Yin et al. (2021) extended the global land surface model ORCHIDEE (ORganizing Carbon and Hydrology in Dynamic EcosystEms) by including a model for irrigation, crop and offline dam operation. Their model assumes that streams supply water to the crops within the grid cells they

flow across only, neglecting water transfer over long distances. Given the commonly used channels in the irrigation districts of arid and semi-arid regions, this neglect may lead to an underestimation of actual river irrigation volumes and affect the accuracy of hydrological simulations over large, irrigated districts (Yin et al., 2021).

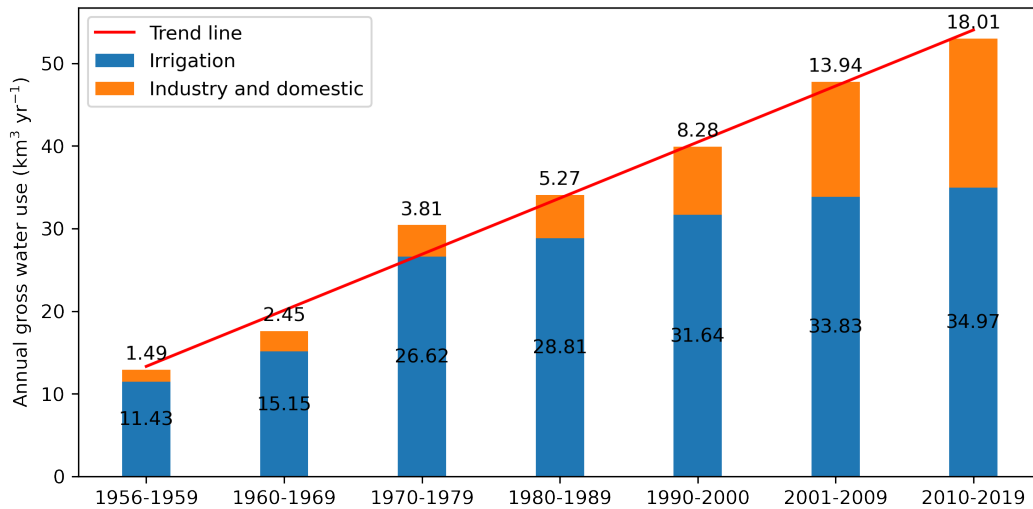


**Figure 1.3:** Annual gross water use in the Yellow River Basin from 1956 to 2019. For the period from 1956 to 2000, data were obtained from Jia et al. (2006), while for the period 2001-2019, data were collected from the Yellow River Bulletin of Water Resources, published by the Yellow River Conservancy Commission (YRCC) of the Ministry of Water Resources of China (<http://www.yrcc.gov.cn/other/hhgb/>).

### 1.3.2 Study II

Precipitation is an important meteorological variable that is usually measured using rain gauges, ground-based weather radars, satellite sensors, etc. For continental-scale estimates, precipitation reanalysis is generated by the assimilation of observations into weather prediction models or climate models, and precipitation reanalysis products have been widely used for hydrological modelling (Michaelides et al., 2009). Several such products have been developed with different objectives, temporal ranges, data sources and resolutions, as summarized in Table 5.1. Precipitation is one of the most important forcing variables for hydrological modelling. Thus, it is crucial to evaluate how the hydrological model responds to different precipitation products to gain insight into model uncertainty and characterize the different biases in precipitation reanalysis. Moreover, although rainfall measurements are assimilated in the reanalysis, different data sources and assimilation systems lead to different accuracies, which are difficult to assess. Therefore, hydrological modellers are often confronted with the question of how

their hydrological simulations depend on the choice of precipitation datasets and which dataset performs the best for a given region and time (Bitew et al., 2012).

Numerous studies have evaluated precipitation datasets to understand their respective advantages and limitations (Beck et al., 2019, 2020; Maggioni et al., 2016). Some studies (Dinku et al., 2008; Gao & Liu, 2013; Hersbach et al., 2020; Hirpa et al., 2010) used statistical methods and rain gauge observations for the evaluation, while others (Bitew et al., 2012; Qi et al., 2016; Stisen & Sandholt, 2010; Tang et al., 2016) employed hydrological modelling to compare the simulated streamflow or soil moisture with the corresponding observations. Although hydrological models offer the possibility of using observed water discharge to evaluate precipitation products, previous studies have focused primarily on wet headwater areas and small mountainous basins when using hydrological models (Bitew et al., 2012; Tang et al., 2016; Wang et al., 2023). This is because quantifying the streamflow in large watersheds remains challenging, especially in arid and semiarid areas (Pilgrim et al., 1988; Vorosmarty & Sahagian, 2000).

Therefore, this study aims to evaluate precipitation products in large-scale, arid and semiarid basins using a sub-continental scale hydrological model considering the significant impacts of human activities on the water cycle. Specifically, we evaluate precipitation reanalysis datasets for the Yellow River Basin in China using the offline Atmospheric and Hydrological Modelling System (AHMS-IRR), which integrates with an irrigation module (Jiang et al., 2022). The Yellow River Basin offers a compelling case study for assessing the accuracy of these precipitation datasets for its diverse range of climates and geomorphic features. Our evaluation includes widely used near-surface precipitation reanalysis datasets, including NCEP/NCAR, ERA5, GLDAS 2.0, WFDE5/CRU, WFDE5/(CRU+GPCC), and CMFD. We directly compare these datasets with rain gauge observations and indirectly assess their impact on the hydrological response of the basin using streamflow observations.

### **1.3.3 Study III**

The quantitative understanding of the dynamics of soil erosion and sediment transport and the concatenated spatial and temporal distribution of suspended sediment discharge is of considerable importance for various research fields such as

agriculture (Montgomery, 2007; Syvitski et al., 2005), hydraulic and sedimentation engineering (Rijn, 1986; Vanoni, 2006), hydrology (Fagundes et al., 2021; Gao et al., 2013), ecology (Newbold et al., 2015; Oost et al., 2007), and geomorphology (Dietrich et al., 2003; Tucker & Hancock, 2010). However, suspended sediment load at a given cross-section of a river depends not only on the stream transport capacity but also on the sediment availability in the upstream watershed (Einstein, 1964; Julien, 2010). Water-induced soil erosion in a watershed is influenced by multiple environmental factors, including climate (rainfall and runoff), soil (erodibility), topography (slope), ground cover (vegetation and rock), and human influences (tillage and soil conservation practices). For example, these influences are encoded within the widely applied Universal Soil Loss Equation (USLE) (Wischmeier & Smith, 1978) and its revised version, RUSLE (Renard et al., 2017). However, despite intensive research conducted over the last few decades (Morgan et al., 1998; Pelletier, 2012; Wicks & Bathurst, 1996), estimating large-scale suspended sediment load in watersheds poses a challenging task due to the complexity of the watershed environment and the insufficient quantitative understanding of large-scale water erosion and transport processes.

The limitations of current modelling and the key scientific questions associated with them are described in detail below.

Despite these efforts, predicting regional water erosion and suspended sediment discharge still constitutes an active matter of research (de Vente et al., 2013). Very few studies have considered suspended sediment discharge in regional climate models (RCMs). Most process-based models developed earlier are only applicable to processes at small spatial (field or small watershed,  $<100 \text{ km}^2$ ) and temporal (event) scales and therefore have uncertain applicability to regional-scale simulations. Empirical models, such as USLE and RUSLE, do not address the intricate aspects of sediment transport and deposition processes, nor do they provide comprehensive coverage of sediment supply resulting from gully and channel erosion. Such models are also inadequate for applications to large areas where gully or channel erosion prevails and sediment transport capacity is limited.

One further limitation is that sediment transport equations for overland flow are derived from flume experiments conducted under limited hydraulic conditions. It has been shown that sediment transport equations developed from fluvial bed load

equations perform poorly in representing overland flow processes (Ali et al., 2013; Hessel & Jetten, 2007). Attempts have also been made (Fagundes et al., 2021; Mao et al., 2010; Stewart et al., 2017; Tan et al., 2017) to test the validity of such models for region-scale simulations. However, some current regional sediment discharge simulations (Fagundes et al., 2021; Stewart et al., 2017; Tan et al., 2017) overlook the detachment–transport coupling approach, which is crucial to describe regional-scale processes adequately. The sediment yield models with and without the transport process are mixed (Fagundes et al., 2021; Stewart et al., 2017; Tan et al., 2017), which do not allow for a complete assessment of the existing sediment yield equations (Fagundes et al., 2021).

One of the most significant drawbacks of the existing models is that gully erosion and its effects on sediment flux are neglected. Gully erosion plays a vital role in large-scale sediment yield, as pointed out in various studies (de Vente & Poesen, 2005; Poesen et al., 2003; Poesen et al., 1996). It represents a major process for fluvial sediment supply on the Loess Plateau of the Yellow River Basin, the study area of this research (see Section 1.2). The representation of gully erosion in the framework of large-scale sediment transport modelling constitutes a challenging task owing to the poor understanding of concentrated flow and stochastic gravity erosion on high-gradient hillslopes and the lack of data for the characterization of gully distribution (e.g., gully density) and morphology (e.g., width, depth, and volume). Such information is indispensable to upscale from existing sediment transport models - which apply to the scale of flume experiments and small watersheds, to regional scale. Therefore, a new approach to quantify the sediment supply from gully erosion is required for improved modelling of continental-scale hydrological erosion processes.

The motivation of this work is thus to develop a soil erosion and sediment transport model that is applicable to regional-scale hydrological transport processes, which incorporates the sediment supply by gully erosion, a major hydrological process on the Loess Plateau (Osterkamp & Toy, 1997). The present study addresses the following key science questions:

- I. How to model upland sediment detachment and transport capacity in a large-scale hydrological model? Which erosivity predictors based on rainfall, runoff or overland flow perform best?

- II. How can a large-scale model incorporate gully erosion and the concatenated sediment supply?
- III. What scale effects, such as decaying precipitation and slope with decreasing spatial and temporal resolution, need to be considered when building the large-scale erosion and sediment transport model?

#### 1.4 Objectives and Outline

This thesis was carried out within the framework of the Atmospheric and Hydrological Modelling System (AHMS) project (Jiang et al., 2020, 2022; Xia, 2019) of the University of Cologne, in association with the Heisenberg Programme "Multiscale Simulation of Earth Surface Processes" at the University of Duisburg-Essen (project number: 434377576) and SFB 1211 "Earth - Evolution at the Dry Limit" (project number: 268236062) jointly, support by German Research Foundation (DFG). This joint project aims to improve the understanding of the hydrological, erosion and sediment transport processes and to investigate the response of the hydrological cycle and sediment yield to climate change and anthropogenic impacts.

Several features of the Yellow River Basin particularly need to be addressed.

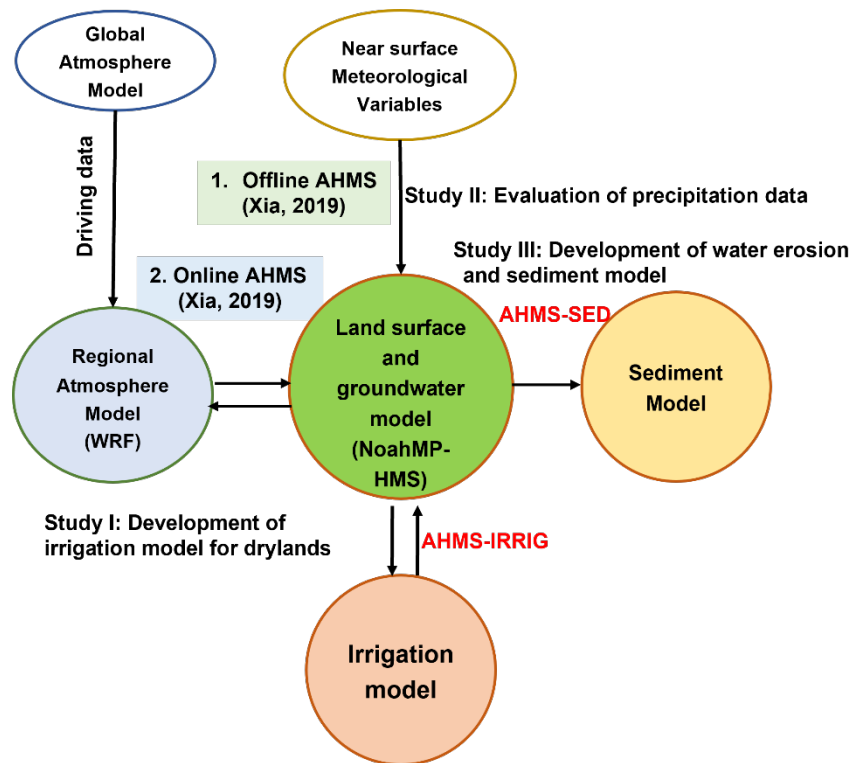
- human perturbation (intensive irrigation) of the water cycle in the arid and semi-arid areas
- complex topography ranging from the mountainous Tibetan Plateau to the arid and semi-arid Chinese Loess Plateau
- large permanent gullies in the Chinese Loess Plateau and the huge sediment load in the Yellow River

Figure 1.4 depicts the contribution of this thesis to the development of AHMS, including model development, application and evaluation, and evaluation of forcing precipitation data, comprising this thesis (Study I-III). As shown, AHMS can either be run online, i.e., coupled with the full WRF model for atmospheric dynamics, or offline – which is the situation adopted in the present study – by using prescribed near-surface atmospheric forcing variables.

The main objectives of this thesis are:

- a. development of a regional hydrological model for the arid and semi-arid regions

- with consideration of irrigation (AHMS-IRRIG)
- b. calibration and evaluation of offline AHMS-IRRIG using in-situ and remote sensing observations in the Yellow River Basin
- c. evaluation of precipitation-reanalysis products based on offline AHMS-IRRIG and observed water discharge
- d. development of a regional model for water erosion and sediment transport with consideration of gully erosion and its sediment supplements (AHMS-SED)
- e. application and evaluation of offline AHMS-SED in the Yellow River Basin



**Figure 1.4:** Schematic diagram of online and offline Atmospheric and Hydrological Modelling System (AHMS) and its extension and application in the studies that comprise this thesis.

The structure of this thesis is described below. Chapter 2 presents the relevant theories and models of water erosion and sediment transport. Chapter 3 describes the AHMS-SED and associated components of irrigation, water erosion and sediment transport models. Chapter 4 describes the development and application of a regional hydrological model for the arid and semi-arid river basin with consideration of irrigation. Precipitation reanalysis products are evaluated using gauge observations and hydrological modelling in Chapter 5. Chapter 6 introduces the development of the continental-scale water erosion and sediment transport model AHMS-SED and their application to the Yellow River Basin. Last but not least, a summary and

conclusion drawn from the simulation results of this project are presented in Chapter 7.

## 2 Water Erosion and Sediment Transport Modelling

### 2.1 Introduction

Erosion and sediment transport processes are driven by hydrological processes in the watershed and by stream hydraulics. At a particle scale, a sediment particle undergoes several stages, including detachment, transport and deposition. Before reaching the ocean, these processes go through several cycles. These processes depend on the physical properties and interactions between fluids and particles. Therefore, this chapter provides an overview of the hydraulic and sediment variables associated with the overland and channel flow (Section 2.2), as well as shallow water and sediment transport equations (Section 2.3) and water erosion and sediment transport modelling (Section 2.4).

### 2.2 Hydraulic and Sediment Variables

This section focuses on the hydraulic and sediment variables that are well-parameterized in existing sediment detachment functions and sediment transport capacity equations.

#### 2.2.1 Hydraulic Variables

The movement of water over the land is known as overland flow, which can occur either as diffuse sheet flow (laminar or mixed laminar flow) or as concentrated flow (turbulent flow) in rills and gullies (Ward & Robinson, 1975). On the other hand, open channel flow refers to the movement of liquid within a conduit with a free surface (Akan, 2006). Hydraulic variables such as shear stress, fraction velocity, stream power, unit stream flow, effective stream power, and Shield's number, etc., are among the most commonly used predictors in soil detachment functions and sediment transport capacity equations for overland and channel flow. These predictors and the associated basic hydraulic variables are described and explained below.

The hydraulic radius ( $R_h$ ) of the rectangular channel is given by

$$R_h = \frac{A_c}{P_w} = \frac{wh}{w+2h} \quad (2.1)$$

where  $A_c$  is the cross-sectional area of the flow ( $\text{m}^2$ ),  $P_w$  is the wetted perimeter of the flow (m),  $w$  is the flow width (m), and  $h$  is the flow depth (m). For the wide and shallow river or overland flow, if  $w \gg h$ , then  $R_h \approx h$ .

The Manning equation is frequently employed to estimate the average velocity of a river flow cross-section ( $V$  in  $\text{m s}^{-1}$ ), which is given by

$$V = n^{-1} R_h^{2/3} S_f^{1/2} \quad (2.2)$$

where  $n$  is Manning's roughness coefficient ( $\text{s m}^{-1/3}$ ), and  $S_f$  is the friction slope (-). It is worth noting that (Chow et al., 1988) pointed out that the Manning equation is only applicable to turbulent flows.

In the case of steady overland flow and the wide and shallow river, the water discharge per unit width ( $\text{m}^2 \text{s}^{-1}$ ) can be expressed as:

$$q_u = V \cdot h \quad (2.3)$$

Two important dimensionless numbers used to describe shallow water flow are the Reynolds number (Re) and the Froude number (Fr). The Reynolds number is the ratio of inertial forces to viscous forces in a flowing fluid and can be used to identify the flow patterns, such as laminar, turbulent or laminar-turbulent transitional flow. The Froude number is the ratio of inertial force to gravitational force and is used to predict whether the flow is sub-critical flow ( $\text{Fr} < 1$ ), super-critical flow ( $\text{Fr} > 1$ ) or critical flow ( $\text{Fr} \approx 1$ ). The expressions for the Reynolds and Froude numbers read:

$$\text{Re} = \frac{4 \cdot V \cdot R_h}{\nu} \quad (2.4)$$

$$\text{Fr} = \frac{V}{\sqrt{g \cdot \bar{h}}} \quad (2.5)$$

where  $\nu$  is the kinematic viscosity ( $\text{m}^2 \text{s}^{-1}$ ),  $g$  is the gravitational acceleration ( $\text{m s}^{-2}$ ) and  $\bar{h}$  is the uniform depth of flow (m), which is equal to the cross-sectional area  $A_c$  divided by free-surface width  $w$ .

The bed shear stress, denoted as  $\tau_0$ , represents the force per unit area ( $\text{N m}^{-2}$ ) that water flow exerts on the soil. It is given by

$$\tau_0 = \rho g R_h S_f \quad (2.6)$$

where  $\rho$  is the water density ( $\text{kg m}^{-3}$ ).

Friction velocity, also known as shear velocity  $u_*$  ( $\text{m s}^{-1}$ ), represents the gradient of stream velocity in boundary layer flow and is defined as

$$u_* = \sqrt{\frac{\tau_0}{\rho}} \quad (2.7)$$

The concept of stream power was introduced by Bagnold (1966) based on the assumption that the rate of sediment transport is proportional to the rate of potential energy consumption per unit bed area. Bagnold's research demonstrated that a stream's capacity for sediment transport is determined by its available power rather than its available energy (Yang, 1973). Stream power  $\omega$  ( $\text{J m}^{-2} \text{s}^{-1}$ ) is defined as

$$\omega = V \cdot \tau_0 \quad (2.8)$$

According to Yang (1972), sediment transport rates are associated with the potential energy expenditure rate per unit weight of water. The unit stream power  $\omega_u$  ( $\text{m s}^{-1}$ ) can be defined as the product of flow velocity and slope gradient, as given as

$$\omega_u = V \cdot S_0 \quad (2.9)$$

where  $S_0$  is the bed slope (-).

Moreover, effective stream power is an empirical relationship based on the concept of shear stress (Bagnold, 1980). This concept was primarily employed by Govers (1990) and Everaert (1991) to establish empirical relationships for predicting sediment transport rates. The effective stream power  $\omega_{\text{eff}}$  ( $\text{N}^{1.5} \text{s}^{-1.5} \text{m}^{-2.17}$ ) is given as

$$\omega_{\text{eff}} = \frac{(V \cdot \tau_0)^{1.5}}{h^{2/3}} \quad (2.10)$$

### 2.2.2 Sediment Variables

Furthermore, the relevant sediment variables included in this thesis are described below. The specific gravity ( $G_s$ ) is defined as

$$G_s = \frac{\gamma_s}{\gamma} = \frac{\rho_s}{\rho} \quad (2.11)$$

where  $\gamma_s$  is the specific weight of the sediment particle ( $\text{N m}^{-3}$ ),  $\gamma$  is the specific weight of the water ( $\text{N m}^{-3}$ ), and  $\rho_s$  is the sediment density ( $\text{kg m}^{-3}$ ).

The volumetric sediment concentration  $C_v$  (-) and sediment concentration by weight  $C_w$  (-) of the suspension are given by

$$C_v = \frac{V_s}{V_t} = \frac{V_s}{V_s + V_w} \quad (2.12)$$

$$C_w = \frac{W_s}{W_t} = \frac{W_s}{W_s + W_w} \quad (2.13)$$

where  $V_s$  is the volume of the solid ( $\text{m}^3$ ),  $V_w$  is the volume of the water ( $\text{m}^3$ ),  $V_t$  is the total volume ( $\text{m}^3$ ),  $W_s$  is the weight of the solid (N),  $W_w$  is the weight of the water (N), and  $W_t$  is the total weight (N).

The particle Reynolds number  $Re_*$  characterizes the nature of the surrounding flow and the fall velocity of the particle,

$$Re_* = \frac{u_* d_s}{\nu} \quad (2.14)$$

where  $d_s$  is the particle diameter (m).

The settling velocity is obtained from the balance between gravity and drag forces,

$$(\gamma_s - \gamma) \frac{\pi d_s^3}{6} = C_d \frac{\pi d_s^2}{4} \frac{\rho v_s^2}{2} \quad (2.15)$$

where  $C_d$  is the drag coefficient (-), which is usually a function of the particle Reynolds number ( $Re_*$ ), and  $v_s$  is the sediment fall velocity ( $\text{m s}^{-1}$ ).

For sufficiently small particle Reynolds numbers, the flow around spherical particles is laminar, and the resistance of the flow around the particles can be calculated with the analytical model by Stokes (1851). However, for large particle Reynolds numbers, the flow around the sphere becomes turbulent, making it difficult to obtain an analytical solution for the drag coefficient. Therefore, in the regime of high particle Reynolds numbers, empirical models have been developed based on experimental evaluations. According to Stokes (1851) and Engelund & Hansen (1967), the drag coefficient and the corresponding settling velocity can be calculated by the following equations, respectively.

$$Re_* \leq 0.5$$

$$C_d = \frac{24}{Re_*} \quad (2.16)$$

$$v_s = \frac{1}{18} \frac{\gamma_s - \gamma}{\gamma} \frac{g d_s^2}{\nu} \quad (2.17)$$

$$Re_* > 0.5$$

$$C_d = \frac{24}{Re_*} + 1.5 \quad (2.18)$$

$$v_s = \frac{8\nu}{d_s} \left\{ \left[ 1 + 0.0139 d_s^3 \frac{(G_s - 1)g}{\nu^2} \right]^{0.5} - 1 \right\} \quad (2.19)$$

where  $\nu$  is the kinematic viscosity ( $m^2 s^{-1}$ ).

The sediment transport takes place when the horizontal hydrodynamic force exceeds the vertical resisting force. The ratio between these two forces represents the threshold condition for the initiation of sediment transport in a fluid flow (Shields, 1936). The value of the Shields number, denoted here  $\tau_*$ , can be calculated using the equation:

$$\tau_* = \frac{\text{hydrodynamic forces}}{\text{resisting forces}} = \frac{F_L + F_D - F_R}{F_W - F_B} \quad (2.20)$$

where  $F_L$  is the lift force and is proportional to  $C_l \rho_m u^2 d_s^2$  and  $\tau_0 d_s^2$ ,  $u$  is the flow velocity, and  $C_l$  is the lift coefficient (-),  $F_D$  is the drag force and is proportional to  $C_d \rho_m u^2 d_s^2$  and  $\tau_0 d_s^2$ ,  $F_R$  is the resisting force,  $F_W$  is the particle gravitational acceleration force and is proportional to  $\gamma_s d_s^3$ , and  $F_B$  is the buoyancy force and is proportional to  $\gamma d_s^3$ . By neglecting the lift force, Eq. (2.20) can be rewritten as follows:

$$\tau_* = \frac{\tau_0 d_s^2}{\gamma_s d_s^3 - \gamma d_s^3} = \frac{\tau_0}{(\gamma_s - \gamma) d_s} = \frac{\rho u_*^2}{(\gamma_s - \gamma) d_s} \quad (2.21)$$

The ratio of the sediment fall velocity ( $v_s$ ) to the upwards velocity of the grain, which is the product of the von Kármán constant ( $\kappa$ , typically 0.4) and the shear velocity ( $u_*$ ), as shown by Eq. (2.22), is known as the Rouse number ( $R_o$ ). This number is used to characterize the concentration profile of suspended sediment and analyze sediment transported in a flowing fluid.

$$R_o = \frac{v_s}{\kappa u_*} \quad (2.22)$$

### 2.3 Shallow Water and Sediment Transport Equations

This section presents commonly used shallow water and sediment transport equations. The shallow water equations, also known as the Saint-Venant equations, consist of continuity and momentum equations that describe the behaviour of shallow water. The derivation and explanation of these equations are provided below.

The continuity equation asserts that the total mass of a fluid within a closed system remains constant with time. In differential form, the continuity equation (Julien, 2010) reads:

$$\frac{\partial \rho_m}{\partial t} + \frac{\partial \rho_m v_x}{\partial x} + \frac{\partial \rho_m v_y}{\partial y} + \frac{\partial \rho_m v_z}{\partial z} = 0 \quad (2.23)$$

where  $\rho_m$  is the mixture density of the fluid ( $\text{kg m}^{-3}$ ),  $t$  denotes the time (s), and  $v_x$ ,  $v_y$  and  $v_z$  refer to the flow velocities ( $\text{m s}^{-1}$ ) in the  $x$ ,  $y$  and  $z$  directions, respectively.

The momentum equation is derived from the hydrodynamic forces balance. The differential form of the momentum equation (Julien, 2010) in the  $x$ -component is given below.

$$\frac{\partial v_x}{\partial t} + v_x \frac{\partial v_x}{\partial x} + v_y \frac{\partial v_x}{\partial y} + v_z \frac{\partial v_x}{\partial z} = g_x - \frac{1}{\rho_m} \frac{\partial p}{\partial x} + \frac{1}{\rho_m} \left( \frac{\partial \tau_{xx}}{\partial x} + \frac{\partial \tau_{yx}}{\partial y} + \frac{\partial \tau_{zx}}{\partial z} \right) \quad (2.24)$$

where  $p$  is the pressure ( $\text{N m}^{-2}$ ),  $g_x = g \sin \theta$  is the horizontal (downstream) component of the gravitational acceleration ( $\text{m s}^{-2}$ ), with  $\theta$  denoting the angle between the riverbed plain and the horizontal, and  $\tau$  is the shear stress ( $\text{N m}^{-2}$ ). The stress components  $\tau_{xx}$ ,  $\tau_{yx}$ , and  $\tau_{zx}$  denote the applied stress components in the  $x$  direction,  $\tau_{xx}$  being the stress on the  $x$ -face of the infinitesimal cubical volume element and  $\tau_{yx}$  and  $\tau_{zx}$  representing the stresses on  $y$ - and  $z$ -faces, respectively.

In order to apply these equations to slow and unsteady flow in a one-dimensional open channel, the above equations are multiplied by the differential area,  $dA$ , and then integrated over the control area, which corresponds to the cross-sectional area  $A_c$ . Thus, the integral form of the continuity equation can be written as

$$\int_{A_c} \frac{\partial \rho_m}{\partial t} dA_c + \int_{A_c} \frac{\partial v_x}{\partial x} + \frac{\partial v_y}{\partial y} + \frac{\partial v_z}{\partial z} dA_c = 0 \quad (2.25)$$

Given the  $v_y$  and  $v_z$  are zero in one-dimensional flow, and assuming (i) constant

density with depth and (ii) averaging out the turbulent component in the  $v_y$  and  $v_z$ , the above equation can be simplified as follows:

$$\frac{\partial h}{\partial t} + \frac{\partial(hV)}{\partial x} = 0 \quad (2.26)$$

where  $h$  is the depth of flow (m), and  $V$  is the cross-sectional averaged velocity ( $\text{m s}^{-1}$ ).

The momentum correction factor  $\beta_m$  is defined as follows:

$$\beta_m = \frac{1}{A_c V_x^2} \int_{A_c} v_x^2 dA_c \quad (2.27)$$

The momentum equation in nonconservation form for a one-dimensional open channel is given below under several assumptions. Firstly, in the one-dimensional flow,  $v_y = v_z = \tau_{xx} = 0$ . Additionally, the Saint-Venant equation neglects lateral inflow, wind shear, and eddy losses. It assumes that the bed shear stress ( $\tau_0$ ) is equal to the bank shear stress ( $\tau_s$ ), that the wind shear ( $\tau_w$ ) (a component of  $\tau_{zx}$ ) is zero, that channel inclination is a small ( $\sin\theta \approx S_0$ ), and that  $\beta_m$  is equal to 1.

$$\underbrace{\frac{\partial V}{\partial t}}_{\text{Local acceleration term}} + \underbrace{g \frac{\partial h}{\partial x}}_{\text{Pressure force term}} + \underbrace{V \frac{\partial V}{\partial x}}_{\text{Convective acceleration term}} = \underbrace{g S_0}_{\text{Gravity force term}} - \underbrace{g S_f}_{\text{Friction force term}} \quad (2.28)$$

The dependencies of the terms in the above equation are explained below.

- Local acceleration term: the changes of momentum due to changes in velocity along the channel
- Pressure force term: proportional to the change in the water depth
- Convective acceleration term: the changes in momentum
- Gravity force term: proportional to the bed slope
- Friction force term: proportional to the fraction slope

In nature, the flood waves of different rivers might have their own different characteristics. Thus, the relatively small terms can be ignored in order to simplify the calculation and use the simplified Saint-Venant dynamical equation. Specifically, the completed form of the Saint-Venant dynamical equation is called the dynamic wave approximation, as follows:

$$\frac{1}{g} \frac{\partial V}{\partial t} + \frac{\partial h}{\partial x} + \frac{1}{g} V \frac{\partial V}{\partial x} = S_0 - S_f \quad (2.29)$$

According to Bates et al. (2010), the convective term is neglected in the local inertial form approximation,

$$\frac{1}{g} \frac{\partial V}{\partial t} + \frac{\partial h}{\partial x} = S_0 - S_f \quad (2.30)$$

While the gravity and friction force terms are neglected in the gravity wave approximation,

$$\frac{1}{g} \frac{\partial V}{\partial t} + \frac{\partial h}{\partial x} + \frac{1}{g} V \frac{\partial V}{\partial x} = 0 \quad (2.31)$$

Moreover, the local and convective acceleration terms are neglected in the diffuse wave approximation,

$$\frac{\partial h}{\partial x} = S_0 - S_f \quad (2.32)$$

which leads to the kinematic wave approximation by further neglecting the pressure terms,

$$S_0 - S_f = 0 \quad (2.33)$$

If the transport medium is replaced by sediment, a similar equation can be obtained. The differential form of the sediment continuity equation is given by

$$\frac{\partial C_v}{\partial t} + \frac{\partial(C_v v_x)}{\partial x} + \frac{\partial(C_v v_y)}{\partial y} + \frac{\partial(C_v v_z)}{\partial z} = 0 \quad (2.34)$$

Given the  $v_y$  and  $v_z$  are zero in one-dimensional flow, and assuming (i) constant flow density with depth and (ii) averaging out the turbulent component in the  $v_y$  and  $v_z$ , the integrated form of the sediment continuity equation for a one-dimensional open channel is given by

$$\frac{\partial(hC_v)}{\partial t} + \frac{\partial(hVC_v)}{\partial x} = 0 \quad (2.35)$$

## 2.4 Water Erosion and Sediment Transport Modelling in the Watershed

There are a number of soil water erosion and sediment transport models for

watershed and fluvial systems, which vary in complexity, process description, data requirements, and spatial and temporal scales (de Vente et al., 2013; de Vente & Poesen, 2005; Hajjigholizadeh et al., 2018; Harmon et al., 2001; Merritt et al., 2003). But in essence, there are three main types of erosion models: empirical, process-based, and conceptual models (Table 2.1).

Empirical models, such as USLE and RUSLE, are the most widely used for long-term and large-scale predicting of soil loss from sheet and rill erosion. These models are based on the empirical relations developed from observations over more than 10,000 plot-years of rainfall and soil loss data on a hillslope.

Several process-based water erosion models have been developed to estimate suspended sediment load. These models include, for instance, WEPP (Laflen et al., 1991), EUROSEM (Morgan et al., 1998), LISEM (De Roo et al., 1996), SHESED (Wicks & Bathurst, 1996), SHETRAN (Ewen et al., 2000) and CASC2D-SED (Rojas et al., 2003). In these models, sediment detachment due to rainfall is calculated based on the rainfall kinetic energy (SHESED and WEPP). The detachment effect of runoff in the watershed is modelled by means of excess shear stress (SHESED and WEPP) or detachment–transport coupling approach, for example, by employing effective sediment transport capacity theory (WEPP, EUROSEM, LISEM and CASC2D-SED). Furthermore, the sediment transport capacity of overland and stream flow are based on theories of shear stress (DuBoys, 1879; Govers, 1992; Yalin, 1963), stream power (Bagnold, 1966, 1980; Engelund & Hansen, 1967), unit stream power (Yang, 1972) and unit effective stream power (Bagnold, 1980; Govers, 1990). These equations are derived either from experimental data collected in laboratory flumes or from bedload transport models for fluvial systems. By using dimensional analysis and experimental data obtained from laboratory flumes (Julien & Simons, 1985; Kilinc, 1972; Kirkby, 1971), the various sediment transport capacity equations for overland flow can be unified to a general relationship as the power function of surface slope ( $S_0$ ), unit water discharge ( $q$ ) and excess shear stress ( $1-\tau_{cr}/\tau_0$ ), as shown in Table 2.2.

**Table 2.1:** Rainfall erosivity and sediment transport capacity for overland flow in selected water erosion and sediment transport models.

Model	Spatial and temporal scale	Type	Process	Rainfall, runoff and overland flow erosivity		Reference
				Method and Equation		
USLE	Hillslope/Event-based	Empirical	Erosion	Rainfall kinetic energy	$R_{ev} = EI_{30}$	Wischmeier & Smith (1978)
MUSLE (SWAT-MUSLE)	Hillslope/Event-based (Watershed/Continuous)			Runoff kinetic energy	$R_{ev} = a_1(Q_v q_p)^{b_1}$	Arnold et al. (1998); Neitsch et al. (2011)
USLE-M	Hillslope/Event-based			Rainfall kinetic energy	$R_{ev} = Q_R EI_{30}$	Kinnell & Risse (1998)
USLE-MM				$R_{ev} = (Q_R EI_{30})^{d_1}$	Bagarello et al. (2008)	
CASC2D- SED	Watershed/Continuous	Process-oriented	Erosion, transport, and deposition	Unit flow discharge (Kilinc & Richardson, 1973)	$T_c \sim S_0^{e_2} q_u^{e_3}$	Rojas et al. (2003)
WEPP	Watershed/Continuous			Rainfall and runoff intensity; excess shear stress theory (Yalin, 1963)	$T_{c,interill} \sim r_i R_{sf}$ $T_{c,rill} \sim \tau_0^{0.5} (\tau_0 - \tau_{cr})$	Lafren et al. (1991)
EUROSEM	Watershed/Single event			Excess unit stream power and excess effective stream power theories (Bagnold, 1980; Everaert, 1991; Yang, 1972)	$T_{c,interill} \sim (\omega_{eff} - \omega_{effcr})^\eta$ $T_{c,rill} \sim (\omega_u - \omega_{ucr})^{d_2}$	Morgan et al. (1998)
LISEM				De Roo et al. (1996)		
SHETRAN	Watershed/Continuous			Rainfall momentum squared and excess shear stress theory	$D_r \sim M_r$ $D_f \sim \left(\frac{\tau_0}{\tau_{cr}} - 1\right)$	Ewen et al. (2000)
SHESED				Wicks & Bathurst (1996)		

\*These variables are described above and in the list of symbols.

### 2.4.1 Universal Soil Loss Equation

The Universal Soil Loss Equation (USLE) (Wischmeier & Smith, 1978) was initially designed to predict long-term annual average soil loss associated with inter-rill and rill erosion. This is achieved by using empirical relationships that consider a broad range of environmental factors, including climate, soil, topography and land use and management practices. The original version of this equation reads

$$A = R \cdot K_{\text{usle}} \cdot L \cdot S \cdot C \cdot P \quad (2.36)$$

where  $A$  is the annual soil loss per unit area per year based on the original USLE ( $\text{tons ha}^{-1} \text{yr}^{-1}$ ),  $R$  is the rainfall-runoff erosivity index ( $\text{MJ mm ha}^{-1} \text{hr}^{-1} \text{yr}^{-1}$ ),  $K_{\text{usle}}$  is the soil erodibility index ( $\text{tons ha hr ha}^{-1} \text{MJ}^{-1} \text{mm}^{-1}$ ),  $L$  is the slope length factor (-),  $S$  is the slope steepness factor (-),  $C$  is the vegetation cover or called crop factor (-), and  $P$  is the practice factor (-). For consistency with the sources, we use "tons" and "ha" in the text below, which are abbreviations for the metric tonnes and hectares, non-SI units equal to 1000 kg and 10,000 m<sup>2</sup>, respectively.

The erosivity index  $R$  is calculated as the cumulative effect of the contribution of individual events, as given below.

$$R = \sum_{i=1}^N (R_{ev})_i \quad (2.37)$$

$$R_{ev} = EI_{30} \quad (2.38)$$

$$E = \sum_{\Delta t=1}^M \varepsilon h_{\Delta t} \quad (2.39)$$

where  $R_{ev}$  is the erosivity index ( $\text{MJ mm ha}^{-1} \text{hr}^{-1}$ ) of an individual event ( $i$ ),  $N$  is the number of individual events per year,  $E$  is the rainfall kinetic energy of the interval  $\Delta t$  ( $\text{MJ ha}^{-1}$ ),  $I_{30}$  is the maximum 30 min rainfall intensity ( $\text{mm hr}^{-1}$ ),  $M$  is the number of rainfall intervals in one event,  $\varepsilon$  is the rainfall kinetic energy per unit rainfall depth per hectare ( $\text{MJ ha}^{-1} \text{mm}^{-1}$ ), and  $h_{\Delta t}$  is the rainfall depth in each time interval  $\Delta t$  (mm). As shown by Equation (2.37), the erosivity index of an individual event is the product of the kinetic energy of the raindrops ( $E$ ) and the 30-minute maximum rainfall ( $I_{30}$ ). Therefore, USLE explicitly quantifies the effect of raindrop impact to detach sediment particles and implicitly the amount and rate of runoff associated

with rainfall. Kinnell (2005) highlights that raindrop-impact flow is the main factor in rill and sheet erosion. The influence of raindrop impact on the sediment transport mechanism is significant and overlooked by the current process-based models.

According to Wischmeier & Smith (1978), the unit kinetic energy is calculated as

$$\begin{cases} \varepsilon_{\text{usle}} = 0.119 + 0.0873 \log_{10}(r_i) & r_i \leq 76 \text{ mm h}^{-1} \\ \varepsilon_{\text{usle}} = 0.283 & r_i > 76 \text{ mm h}^{-1} \end{cases} \quad (2.40)$$

where  $r_i$  is the rainfall intensity ( $\text{mm hr}^{-1}$ ).

Moreover, the soil erodibility index measures the resistance of surface soil to detachment by water. In the original USLE, it is given by

$$K_{\text{usle}} = 2.77 \times 10^{-7} \times (12 - P_{OM}) P_M^{1.14} + 4.3 \times 10^{-3} \times (S_t - 2) + 3.3 \times 10^{-3} \times (S_p - 3) \quad (2.41)$$

$$P_M = \alpha_{ss} (100 - \gamma_{sc}) \quad (2.42)$$

where  $P_{OM}$  is the soil organic matter content (%),  $S_t$  is the index related to soil texture,  $S_t=1$  is for very fine granular,  $S_t=4$  is for massive compacted,  $S_p$  is the index related to the soil permeability class, ranging from 1 to 6,  $\alpha_{ss}$  is the percentage of silt divided by sand, and  $\gamma_{sc}$  is the percentage of silt divided by clay.

The slope length factor in the original USLE is given by

$$L = \left( \frac{\lambda}{22.13} \right)^m \quad \text{where} \quad \begin{cases} m = 0.5 & \theta > 9 \\ m = 0.4 & 3 > \theta \geq 9 \\ m = 0.3 & 3 \geq \theta \geq 1 \\ m = 0.2 & \theta < 1 \end{cases} \quad (2.43)$$

where  $\lambda$  is the slope length (m),  $m$  is the exponent, and  $\theta$  is the slope (in degrees).

The slope steepness factor in the original USLE is given by

$$S = 6.613 \cdot (0.43 + 0.30S_0 + 0.043S_0^2) \quad (2.44)$$

where  $S_0$  is the slope gradient in percent.

In addition, crop and practice factors ( $C$  and  $P$ ) depend on specific vegetation growth stages and individual support practices such as tillage planning, terrace farming systems and stable waterways, which are not addressed here.

## 2.4.2 Revised Universal Soil Loss Equation

Renard et al. (2017) revised the USLE model to create the Revised Universal Soil Loss Equation (RUSLE) model by incorporating newer research and technology that emerged after (Wischmeier & Smith (1978)). The RUSLE model features improvements to the  $R$ ,  $K_{usle}$ , and  $S$  factors. Here, the  $\epsilon_{rusle}$  and  $S$  factors used in RUSLE are described below.

RUSLE uses the exponential equation proposed by Brown & Foster (1987) to calculate the unit kinetic energy as follows:

$$\epsilon_{rusle} = 0.29(1 - 0.72e^{-0.05i}) \quad (2.45)$$

McCool et al. (1987) revised the slope steepness factor. Liu et al. (1994) discovered that  $S$  underestimated soil loss on steep slopes and proposed a new factor applicable to slopes greater than  $10^\circ$ . The equations of these two studies are combined as follows:

$$S = \begin{cases} 10.80 \sin(\theta) + 0.03 & \theta \leq 5^\circ \\ 16.80 \sin(\theta) - 0.50 & 5^\circ < \theta < 10^\circ \\ 21.91 \sin(\theta) - 0.96 & \theta \geq 10^\circ \end{cases} \quad (2.46)$$

### 2.4.3 Modified Universal Soil Loss Equation

The USLE and RUSLE have a limitation in that they do not take into account runoff in an explicit manner. To address this issue, Williams (1975) developed the Modified Universal Soil Loss Equation (MUSLE), in which the rainfall-energy factor used in the USLE is replaced by a runoff energy factor:

$$SY = a_1 (Q_r \cdot q_p)^{b_1} \cdot K_{usle} \cdot L \cdot S \cdot C \cdot P \quad (2.47)$$

where  $SY$  is the sediment yield (tons) for the entire watershed on a storm basis,  $Q_r$  is the runoff volume ( $m^3$ ), and  $q_p$  is the peak runoff rate in a storm ( $m^3 s^{-1}$ ). For areas where the equation was developed, the coefficients  $a_1$  and  $b_1$  are 11.8 and 0.5, respectively.

### 2.4.4 Kilinc and Richardson's equation (1973)

Kilinc (1972) and Kilinc & Richardson (1973) studied sheet and rill erosion using flume experiments and derived an equation (Kilinc and Richardson's equation, KR) for predicting sediment discharge in uniform flow over the bare sandy soil. They

found that unit sediment discharge, denoted as  $q_s$  (tons  $m^{-1} s^{-1}$ ), increases with the square of water discharge and with the  $5/3$  power of the slope, i.e.,

$$q_s \sim S_0^{5/3} \cdot q_u^2 \quad (2.48)$$

where  $S_0$  is the soil slope ( $m m^{-1}$ ), and  $q_u$  is the unit flow discharge ( $m^2 s^{-1}$ ).

Julien & Simons (1984) derived a general relationship between unit sediment discharge, slope and water discharge through dimensional analysis. Their equation, which builds on the work of Kilinc & Richardson (1973), is as follows:

$$q_s \sim S_0^{e_2} \cdot q_u^{e_3} \cdot \left(1 - \frac{\tau_{cr}}{\tau_0}\right)^{e_4} \quad (2.49)$$

where  $e_2$ ,  $e_3$  and  $e_4$  are exponents. The coefficient  $e_2$  ranges from 1.2 to 1.9, and  $e_3$  ranges from 1.4 to 2.4.  $\tau_{cr}$  is critical bed shear stress for the initiation of soil particle motion ( $N m^{-2}$ ). When  $\tau_{cr}$  remains small compared with  $\tau_0$ , the last term of Eq. (2.49) can be neglected.

Furthermore, Julien (2010) modified the KR equation to account for non-uniform flows by considering soil type, vegetation and practice factors, which are parameters encoded in USLE. The equation, according to Julien (2010), is as follows:

$$q_s = 23210 \cdot S_0^{5/3} \cdot q_u^2 \cdot K_{usle} \cdot C \cdot P \quad (2.50)$$

**Table 2.2:** Modified sediment transport equations for overland flow (adopted from Julien & Simons (1985))

Investigator	Equation	Laminar flow			Turbulent flow		
		$e_2$	$e_3$	$e_4$	$e_2$	$e_3$	$e_4$
Meyer-Peter and Muller, 1948	$q_s \sim (\tau - \tau_{cr})^{1.5}$ *	1	0.5	1.5	1.05	0.9	1.5
Bagnold, 1986	$q_s \sim \tau_0^{0.5} (\tau - \tau_{cr})$	1	0.5	1	1.05	0.9	1
Yalin 1963 ( $\tau \gg \tau_{cr}$ )	$q_s \sim \tau^{0.5} (\tau - \tau_{cr})$	1	0.5	1	1.05	0.9	1
WES, 1935	$q_s \sim (\tau - \tau_{cr})^{1.5}$	1	0.5	1.5	1.05	0.9	1.5
Chang et al. 1965	$q_s \sim \tau V$	1	1	0	1	1	0
Du Boys, 1979	$q_s \sim \tau_0 (\tau - \tau_{cr})$	1.33	0.66	1	1.4	1.2	1
Barekyan, 1962	$q_s \sim S q_u V$	1.33	1.67	0	1.3	1.4	0
Schoklitsch, 1934	$q_s \sim S^{1.5} (q_u - q_{ucr})$	1.5	1	-	1.5	1	-
Shields, 1936	$q_s \sim S q (\tau - \tau_{cr})$	1.67	1.33	1	1.7	1.6	1
Engelund-Hansen, 1967	$q_s \sim \tau^{1.5} V^2$	1.67	1.83	0	1.65	1.7	0
Yalin 1977 ( $\tau \approx \tau_c$ )	$q_s \sim \tau^{2.0} (\tau - \tau_{cr})$	1.67	0.83	2	1.75	1.5	2

\* These variables are described above and in the list of symbols.

### 2.4.5 CASCade Two-dimensional Sediment Model (CASC2D-SED)

The original iteration of the CASCade 2 Dimensional SEDiment (CASC2D-SED) model was founded upon a two-dimensional overland flow routing algorithm developed by Professor P.Y. Julien at Colorado State University (Julien et al., 1995). Later, CASC2D was reformulated to add continuous simulation capabilities and additional hydrologic components such as interception, infiltration, evapotranspiration and diffusive-wave channel routing model, etc. (Billy Edmond Johnson, 1997) incorporated the upland erosion and channel sediment transport module to CASC2D, called CASC2D-SED, based on previous work by Mustafa Yilmaz Kilinc (1972) and Kilinc & Richardson (1973). Rojas (2002) enhanced sediment transport algorithms in CASC2D-SED over Johnson et al. (2000) by improving the simulation of transition between supply-limited and capacity-limited transport, allowing transport by advection of suspended material even with negligible capacity and improving sedimentation simulation in backwater areas.

The model has the following characteristics:

- (1) The transport capacity of overland flow (caused by the sheet and rill erosion) is estimated by the modified Kilinc-Richardson equation (Eq. 2.50) depending on water flow erosivity (water discharge), topography (slope), soil erodibility ( $K_{usle}$  factor), vegetation ( $C$  factor) and land use practice ( $P$  factor).
- (2) The transport capacity of channel flow is estimated with the Engelund and Hansen equation (1967) (Eq. 2.51) based on hydraulic parameters (hydraulic radius, flow velocity and friction slope) and particle characteristics (specific gravity and particle diameter).
- (3) Once it is in suspension, the sediment is transported through advection even under transport capacity limited conditions.
- (4) The particle sizes are divided into three size fractions: sand, silt and clay (see Table 2.3). The median of the corresponding particle size distribution ( $d_{50}$ ) is used for each fraction to characterise the particle sizes associated with the sand, silt and clay fractions. The settling time of particles is then calculated according to the constant settling velocity based on the sediment type and water depth (Eq. 2.19).

### **a) Sediment Transport Approximation**

Once eroded from the soil, a soil particle is entrained into the water flow and transported downstream in the watershed. At any downstream cross-section, sediment flux is controlled mainly by two factors: sediment availability and stream transport capacity. The finer material (clay) is easily carried by the water flow, so its transport is limited mainly by the sediment supply in the watershed. By contrast, the coarse material (sand) is associated with higher resistance to flow. Transport of this coarse material is, therefore, limited mainly by the transport capacity of the flow. Furthermore, fine material is transported primarily in suspension as wash load, while the transport of the coarse material occurs mainly as (near-surface) bed load. Therefore, the total sediment load consists of the wash load of fine particles and the bed load of coarse grains. The wash load can be estimated by measurements and predicted using the upland sediment yield equation. The bed-material load can be estimated by the flow condition using the sediment transport equations.

The processes of upland soil erosion, as well as upland and channel sediment transport, can be summarized through the following steps 1-4 (see also Fig. 2.1).

Step 1: The transport capacity of the water flow is calculated using the modified Kilinc and Richardson's equation (1973) (Eq. 2.50) for overland flow and Engelund and Hansen's equation (1967) (Eq. 2.51) for channel flow.

Step 2: The transport capacity of the water flow is used to estimate the transport rate of the suspended sediment for the various particle size fractions considered.

Step 3: Deposited sediment is entrained into suspension transport based on the excess transport capacity, i.e., the total transport capacity minus the amount of suspended sediment.

Step 4: If the amount of suspended and deposited sediment is exceeded by the total sediment transport capacity, then bed soil erosion in the upland occurs. The percentage of soil eroded is proportional to the percentage of the corresponding size fraction of the parent material. However, channel erosion is not considered.

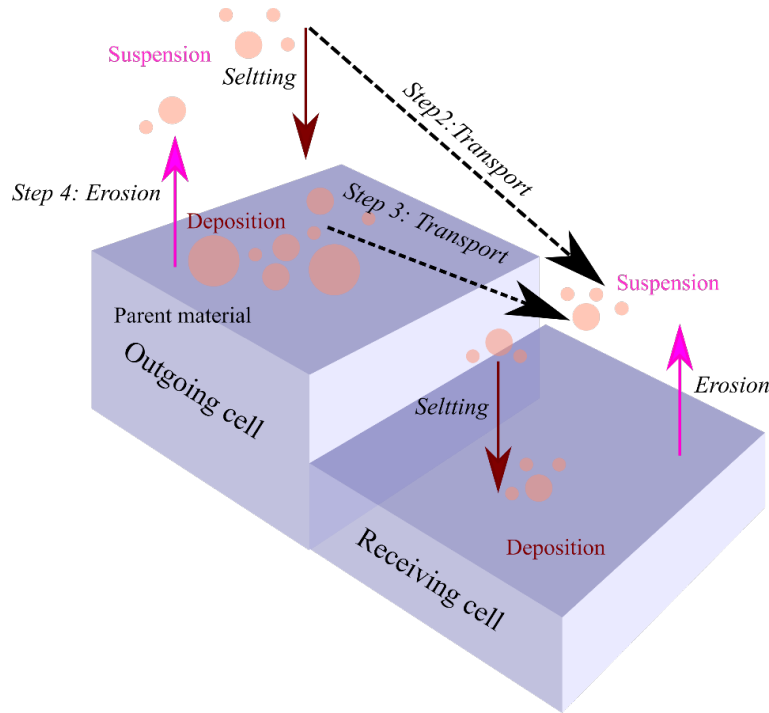


**Figure 2.1:** Schematic of upland and channel sediment transport in CASC2D-SED.

### b) The sediment transport capacity of rivers

The equation of Engelund & Hansen (1967) employs Bagnold's stream power model and the similarity principle to estimate the sediment concentration by weight, called transport capacity in the river. The equation reads,

$$C_{w,i} = 0.05 \left( \frac{G_s}{G_s - 1} \right) \frac{VS_f}{\sqrt{(G_s - 1)gd_{s,i}}} \sqrt{\frac{R_h S_f}{(G_s - 1)d_{s,i}}} \quad (2.51)$$

where  $C_{w,i}$  is the sediment concentration of flow by weight for the size fraction  $i$  (-), and  $d_{s,i}$  is the size diameter (m) of fraction  $i$ .

### c) Suspended sediment settling velocity

The median of the corresponding particle size distribution ( $d_{50}$ ) is used here for every corresponding fraction to characterize the particle sizes associated with the sand, silt and clay fractions. Moreover, the settling velocity ( $v_s$ ) is estimated based on the sediment settling velocity equation (Eq. 2.19).

**Table 2.3:** Particle mean diameter and settling velocity.

Size fraction ( $i$ )	$d_{50}$ (mm)	$v_s$ (m s <sup>-1</sup> )
Sand	0.35	0.036
Silt	0.016	2.20E-04
Clay	0.001	8.60E-07

### 2.4.6 Pelletier's Model (2012)

Pelletier (2012) developed a globally applicable spatially distributed model that predicts long-term suspended sediment discharge and drainage basin delivery ratio for pre-dam conditions. This model comprises a soil detachment rate equation for each local grid and a sediment routing model. The soil detachment rate equation is given by

$$D_{\text{Pelletier}}(x, y, d) = p_1 \cdot \rho_b \cdot f_d \cdot S_0^{5/4} \cdot \sum_{k=1..12} R_k \cdot e^{-L_k} \quad (2.52)$$

where  $D_{\text{Pelletier}}(x, y, d)$  is the detachment rate ( $\text{kg m}^{-2} \text{ yr}^{-1}$ ) calculated at every location  $(x, y)$  and for each grain diameter  $d$ ;  $p_1$  is an empirical parameter (-), which is calibrated to the measured global sediment discharge data;  $\rho_b$  is the bulk density of the soil ( $\text{kg m}^{-3}$ ), assumed to be  $1500 \text{ kg m}^{-3}$ ;  $f_d$  is the fraction of the soil within each soil texture bin of grain diameter  $d$  (-);  $R_k$  is the mean monthly rainfall ( $\text{m yr}^{-1}$ ), which is indexed by  $k$  and varies from January to December, and  $L_k$  is the mean monthly leaf area index (-).

Pelletier (2012) employed the Rouse numbers in the sediment routing model to determine whether a sediment of a specific size is transported to the next pixel downstream in the fluvial system. The Rouse number used in Pelletier (2012) differs from the original Rouse number, i.e.,

$$R_{O\#} = p_2 \frac{v_s}{S_0^{1/2}} \quad (2.53)$$

where  $R_{O\#}$  is the Rouse numbers used in Pelletier (2012), and  $p_2$  is an empirical parameter ( $\text{s m}^{-1}$ ), which must be calibrated using the sediment yield data from global rivers. The model assumes that the shear velocity is solely dependent on the slope and does not account for the effect of flow depth variations on the shear velocity.

### 2.4.7 Sediment Yield Component of Système Hydrologique Européen

Wicks & Bathurst (1996) integrated a process-based, spatially distributed erosion and sediment yield component into the watershed-scale Système Hydrologique Européen (SHE) hydrological modelling system (Bathurst & Cooley, 1996). The component,

known as SHESED, simulates water erosion, which is caused by the impact of the raindrop, leaf drip and overland sheet flow (without rill), as well as sediment transport on hillslopes. For channels, the SHESED simulates bed material erosion and downstream sediment transport. The soil net detachment rate is determined based on the momentum squared of rainfall and excess shear stress of overland flow,

$$D_{rm} = k_r F_w (1 - C_g) \left( (1 - C_c) M_r + M_d \right) \quad (2.54)$$

$$D_{fm} = \begin{cases} k_f (1 - C_r) \left( \frac{\tau_0}{\tau_{cr}} - 1 \right) & \tau \geq \tau_{cr} \\ 0 & \tau < \tau_{cr} \end{cases} \quad (2.55)$$

where  $D_{rm}$  is the soil mass detachment rate by the raindrop ( $\text{kg m}^{-2} \text{s}^{-1}$ ),  $D_{fm}$  is the soil mass detachment rate by overland flow ( $\text{kg m}^{-2} \text{s}^{-1}$ ),  $k_r$  and  $k_f$  are soil erodibility coefficient by the raindrop and overland flow ( $\text{J}^{-1}$ ),  $C_g$  is the proportion of soil protected by ground cover,  $C_r$  is the proportion of ground protected by canopy cover,  $M_r$  is the momentum squared of rain ( $(\text{kg m s}^{-1})^2 \text{m}^{-2} \text{s}^{-2}$ ),  $M_d$  is the momentum squared of leaf drip ( $(\text{kg m s}^{-1})^2 \text{m}^{-2} \text{s}^{-2}$ ),  $\tau_{cr}$  is critical shear stress for initiation of soil particle motion ( $\text{N m}^{-2}$ ) from the Shields curve extended by (Mantz, 1977).

Hillslope sediment routing of SHESED is based on the two-dimensional partial differential equation for the conservation of sediment mass, reads

$$\frac{\partial(h \cdot C_v)}{\partial t} + (1 - \lambda) \frac{\partial z}{\partial t} + \frac{\partial q_{s,x}}{\partial x} + \frac{\partial q_{s,y}}{\partial y} = 0 \quad (2.56)$$

where  $\lambda$  is the soil surface porosity (-),  $z$  is soil surface elevation (m), and  $q_{s,x}$  and  $q_{s,y}$  are the sediment transport rates per unit width in the  $x$  and  $y$  directions ( $\text{m}^3 \text{s}^{-1} \text{m}^{-1}$ ), respectively.

Similarly, channel sediment routing of SHESED is based on the one-dimensional partial differential equation for the conservation of sediment mass, which reads

$$\frac{\partial(A_c C_v)}{\partial t} + (1 - \lambda) w \frac{\partial z}{\partial t} + \frac{\partial(A_c C_v V_{\text{sed}})}{\partial x} = \frac{\partial}{\partial x} \left( A_c \varepsilon \frac{\partial C_v}{\partial x} \right) + q_{s,o} \quad (2.57)$$

where  $\lambda$  is the bed porosity (-),  $w$  is the active bed width for which there is sediment transport (m),  $z$  is the channel bed elevation (m),  $V_{\text{sed}}$  is the longitudinal sediment velocity ( $\text{m s}^{-1}$ ),  $\varepsilon$  is the longitudinal dispersion coefficient ( $\text{m}^2 \text{s}^{-1}$ ), and  $q_{s,o}$  is the

overland flow sediment input to the channel per unit length of flow ( $\text{m}^3 \text{s}^{-1} \text{m}^{-1}$ ).

#### 2.4.8 European Soil Erosion Model (EUROSEM)

The European Soil Erosion Model (EUROSEM) is a dynamic and distributed model for simulating water erosion, sediment transport and deposition processes in the field and small catchment scales in a single storm (Morgan et al., 1998). In EUROSEM, soil detachment by rainfall is based on the kinetic energy of the rain. The soil detachment rate by rainfall for time step ( $\Delta t$  in s) is calculated by

$$D_r = \frac{k_r}{\rho_s} \cdot KE \cdot e^{-bh} \quad (2.58)$$

where  $D_r$  is the soil detachment by raindrop impact per unit length of flow ( $\text{m}^3 \text{m}^{-1} \text{s}^{-1}$ ),  $k_r$  is soil erodibility coefficient by raindrop impact ( $\text{kg J}^{-1}$ ),  $KE$  is the total kinetic energy of the rain ( $\text{J m}^{-2}$ ),  $b$  is an exponent,  $h$  is the depth of the surface water layer (mm).

The total kinetic energy of rain  $KE$  includes the kinetic energy of direct rainfall  $KE_{DT}$  ( $\text{J m}^{-2} \text{mm}^{-1}$ ) and leaf drainage  $KE_{LD}$  ( $\text{J m}^{-2} \text{mm}^{-1}$ ) from the vegetation top. It is given as:

$$KE = (KE_{DT} \cdot Q_{DT} + KE_{LD} \cdot Q_{LD}) \cdot \Delta t \quad (2.59)$$

where  $Q_{DT}$  is the direct throughfall intensity ( $\text{mm hr}^{-1}$ ), and  $Q_{LD}$  is the leaf drainage intensity ( $\text{mm hr}^{-1}$ ).

While the kinetic energy of direct rainfall  $KE_{DT}$  is calculated by Marshall & Palmer (1948) as follows

$$KE_{DT} = 8.95 + 8.44 \log_{10}(r_i) \quad (2.60)$$

where  $r_i$  is the rainfall intensity ( $\text{mm hr}^{-1}$ ).

While the kinetic energy of leaf drainage  $KE_{LD}$  is obtained using Brandt (1990):

$$KE_{LD} = 15.8 \sqrt{h_{veg}} - 5.87 \quad (2.61)$$

where  $h_{veg}$  is the effective height of the plant canopy (m).

The soil detachment rate by runoff is modelled in terms of a generalized erosion-deposition theory proposed by Smith et al. (1995). This theory assumes that the

transport capacity of the runoff ( $T_c$ ) reflects a balance between the two continuous counteracting processes of erosion and deposition. Accordingly, the soil net detachment rate by the flow per unit length of flow ( $\text{m}^3 \text{m}^{-1} \text{s}^{-1}$ ),  $D_f$ , reads

$$D_f = k_f w v_s (T_c - C_v) \quad (2.62)$$

where  $k_f$  is a flow detachment efficiency coefficient (-),  $v_s$  is the settling velocity of particles ( $\text{m s}^{-1}$ ),  $w$  is the width of the channel, and  $T_c$  is the flow transport capacity ( $\text{m}^3 \text{m}^{-3}$ ).

The rill transport capacity equation by Govers (1990) simulates the total sediment load in overland and channel flows and reads

$$T_c = c_2 (\omega - \omega_{cr})^{d_2} \quad (2.63)$$

where  $\omega$  and  $\omega_{cr}$  are the unit stream power ( $\text{m s}^{-1}$ ) and critical unit stream power ( $\omega_{cr} = 4 \text{ mm s}^{-1}$ ), respectively, while  $c_2$  and  $d_2$  are experimentally determined coefficients depending on particle size (-), defined as

$$c_2 = \frac{(d_{50} + 5)^{-0.6}}{0.32} \quad (2.64)$$

$$d_2 = \frac{(d_{50} + 5)^{0.25}}{300} \quad (2.65)$$

The sediment routing model in EUROSEM uses a one-dimensional partial differential equation for the conservation of sediment mass to route sediment over the land surface, which is expressed as follows:

$$\frac{\partial(A_c C_v)}{\partial t} + \frac{\partial(Q C_v)}{\partial x} - e(x, t) = q_s(x, t) \quad (2.66)$$

where  $q_s$  is the external input or extraction of sediment per unit length of flow ( $\text{m}^3 \text{s}^{-1} \text{m}^{-1}$ ), and  $e(x, t)$  is the net detachment rate or rate of erosion of the bed per unit length of flow ( $\text{m}^3 \text{m}^{-1} \text{s}^{-1}$ ). The equation for  $e(x, t)$  reads

$$e(x, t) = D_r + D_f \quad (2.67)$$

### 3 Introduction to the AHMS-SED

Part of this chapter was published as a section of the publication “A regional hydrological model for arid and semi-arid river basins with consideration of irrigation” in the November 2022 issue of *Environmental Modelling & Software* (Impact Factor: 5.471), Volume 157 and can be accessed from this DOI link: <https://doi.org/10.1016/j.envsoft.2022.105531>.

**Cong Jiang<sup>a,\*</sup>, Eric J. R. Parteli<sup>b</sup>, Qian Xia<sup>c</sup>, Xin Yin<sup>a</sup> and Yaping Shao<sup>a</sup>**

<sup>a</sup>*Institute for Geophysics and Meteorology, University of Cologne, Pohligstr. 3, Cologne, 50969, North Rhine-Westphalia, Germany*

<sup>b</sup>*Faculty of Physics, University of Duisburg-Essen, Duisburg, Lotharstr. 1, 47057, North Rhine-Westphalia, Germany*

<sup>c</sup>*School of Water Resources and Hydropower Engineering, Wuhan University, Bayi road. 299, 430072, Hubei Province, China*

#### Authors contributions to this publication

**Cong Jiang:** Formal analysis, Methodology, Software, Validation, Writing-Original Draft, Writing - Review & Editing.

**Eric J.R. Parteli:** Conceptualization, Supervision, Funding acquisition, Writing-Review & Editing.

**Qian Xia:** Software.

**Xin Yin:** Investigation, Visualization.

**Yaping Shao:** Conceptualization, Supervision, Funding acquisition, Writing-Review & Editing, Resources.

#### Reference

Jiang, C., Parteli, E. J., Xia, Q., Yin, X., & Shao, Y. (2022). A regional hydrological model for arid and semi-arid river basins with consideration of irrigation. *Environmental Modelling & Software*, 157, 105531. doi: [10.1016/j.envsoft.2022.105531](https://doi.org/10.1016/j.envsoft.2022.105531).

### **3.1 Introduction**

The previous chapter provided an overview of the hydraulic and sediment variables and the most widely used soil erosion and sediment transport models. This chapter presents the Atmospheric and Hydrological-Sediment Modelling System (AHMS-SED) in Section 3.2, the Atmospheric and Hydrological Modelling System (AHMS) in Section 3.3, and highlights the irrigation model (Section 3.7) and the water erosion and sediment transport model (Section 3.8) developed in this thesis, along with various other related components. These components consist of the surface soil model (Section 3.4), the groundwater model (Section 3.5) and the channel routing model (Section 3.6).

### **3.2 Atmospheric and Hydrological-Sediment Modelling System**

The Atmospheric and Hydrological-Sediment Modelling System (AHMS-SED) is developed by incorporating a water erosion and sediment transport module into AHMS (Jiang et al., 2022; Xia, 2019). Specifically, the water erosion and sediment transport model of CASC2D-SED (Rojas et al., 2003) is modified and incorporated into the AHMS. This modelling system accounts for irrigation and has been shown to accurately reproduce the observations on a broad range of hydrological processes at Yellow River Basin – including water budget, evapotranspiration, terrestrial water storage changes, and streamflow in this basin (Jiang et al., 2022). The coupled AHMS-SED provides the capability to estimate the watershed-scale or continental-scale sediment discharge while considering gully erosion. Figure 3.1 shows the flowchart of the water erosion and sediment transport module coupled within the large-scale hydrological model.

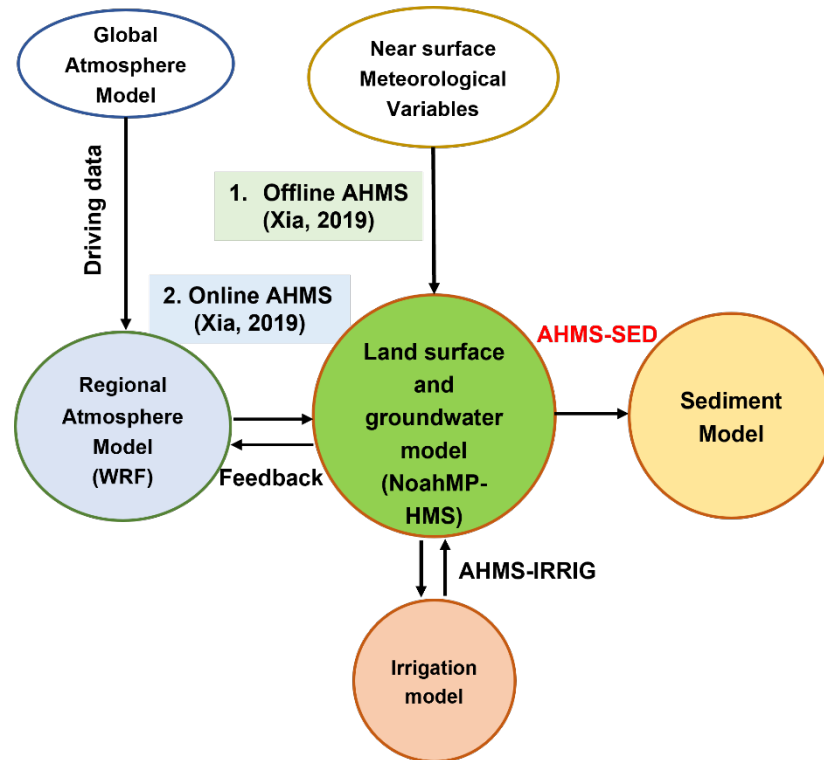


**Figure 3.1:** A simplified flowchart of AHMS-SED, integrating the Atmospheric and Hydrological Modelling System (AHMS) with a modified water erosion and sediment transport model (CASC2D-SED).

### 3.3 Atmospheric and Hydrological Modelling System

As shown in Fig. 3.1, the Atmospheric and Hydrological Modelling System (AHMS) is a fully coupled atmospheric and hydrological modelling system (Xia, 2019). Specifically, AHMS couples the Weather Research and Forecasting (WRF) modelling system (Skamarock & Klemp, 2008) with the physically-based distributed regional Hydrological Model System HMS (Yu et al., 2006) through the Noah-Multiparameterization Land Surface Model (Noah-MP) (Chen & Dudhia, 2001; Niu et al., 2011). Furthermore, the module in WRF-Hydro (Gochis et al., 2015) is employed for downscaling and upscaling variables between the grids of the land surface model and hydrological model.

AHMS can either be run online, i.e., coupled with the full WRF model for atmospheric dynamics, or offline – which is the situation adopted in the present study – by using prescribed near-surface atmospheric forcing variables. A schematic diagram identifying the main components of the online and offline AHMS simulations is displayed in Fig. 3.1. As shown in this figure, while the online AHMS can be employed to study the dynamic feedback between the atmosphere, surface and

subsurface, the offline AHMS can be used to effectively calibrate and validate hydrological models. The difference between online and offline is whether the land surface model is combined with the weather forecast model WRF.

Figure 3.2 displays a schematic diagram of the hydrological cycle represented in AHMS, which also includes the irrigation processes. The development and application of the irrigation module will be introduced in Section 3.7 and Chapter 4, respectively.

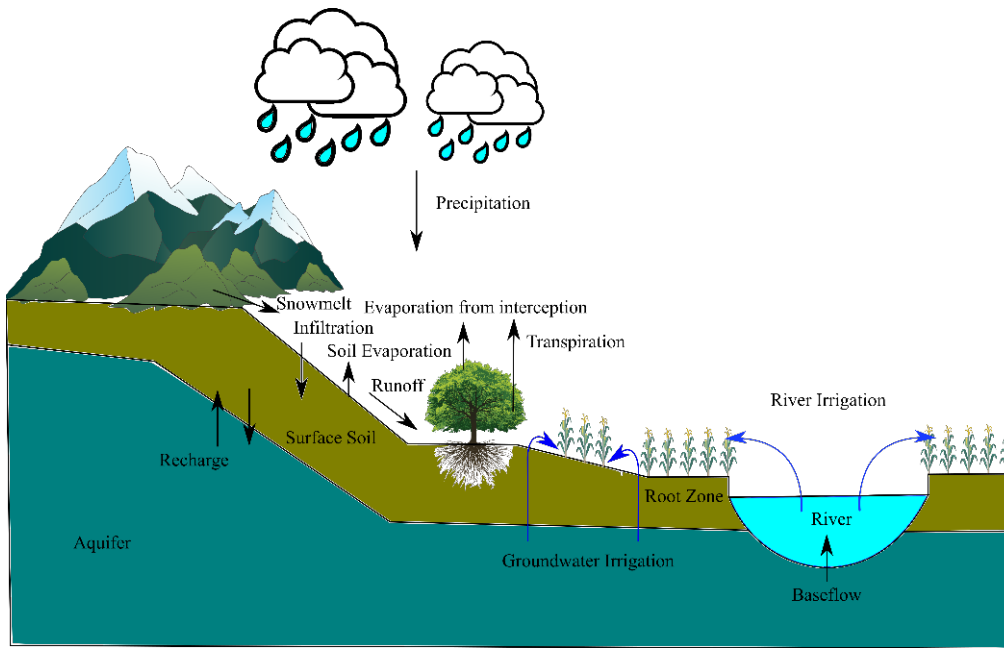


**Figure 3.2:** Sketch of the hydrologic cycle modelled in AHMS.

### 3.4 Vertical Movement of Soil Moisture in the Land Model

The movement of soil water in the vertical direction is described by the Richards equation (Pachepsky et al., 2003; Richards, 1931):

$$\frac{\partial \theta}{\partial t} = \frac{\partial}{\partial z} \left[ K \frac{\partial (\Psi + z)}{\partial z} \right] - S(z, t) \quad (3.1)$$

where  $\theta$  is the volumetric soil water content (-),  $t$  is time (s),  $z$  is the height above the data in the soil column (positive upward) (m),  $K$  is the hydraulic conductivity ( $\text{m s}^{-1}$ ),  $\Psi$  is the soil matric potential (m), and  $S(z, t)$  is the soil moisture sink term (e.g., transpiration losses in the root zone). To solve Eq. (3.1), the following top boundary condition is considered

$$Q_{\text{wat}} = P_t + M - E_g - R_{\text{sf}} + Q_{\text{irr}} \quad (3.2)$$

where  $Q_{\text{wat}}$  denotes the water input on the soil surface,  $P_t$  is the throughfall precipitation,  $M$  is the snow melt,  $E_g$  is the ground evaporation,  $R_{\text{sf}}$  is the surface runoff and  $Q_{\text{irr}}$  is the actual irrigated water, including river irrigation and groundwater irrigation, which in the present study is added to the soil surface. Furthermore, it is assumed that the irrigation water is spread evenly and horizontally over the ground, while the actual irrigation input value on the soil surface is calculated from Eq. 3.12 (see Section 3.7).

### 3.5 2D Single-layer Distributed Groundwater Model

The dynamics of the horizontal movement of groundwater are described by the following partial differential Boussinesq equation for unconfined conditions,

$$S_p \frac{\partial h_g}{\partial t} = \frac{\partial}{\partial x} \left( T_g \frac{\partial h_g}{\partial x} \right) + \frac{\partial}{\partial y} \left( T_g \frac{\partial h_g}{\partial y} \right) - Q_{\text{net}}(x, y, t) \quad (3.3)$$

where  $T_g$  is the aquifer transmissivity ( $\text{m}^2 \text{s}^{-1}$ ),  $S_p$  is the storage coefficient (porosity) ( $\text{m}^3 \text{m}^{-3}$ ),  $Q_{\text{net}}$  ( $\text{m} \text{s}^{-1}$ ) denotes the net contribution of sink and source terms, including the interaction flux between groundwater and unsaturated soil, the exchange of water between rivers and groundwater, and the extraction of groundwater from wells ( $Q_{\text{irr\_gw}}$ ).

### 3.6 Channel Routing Model

River and lake levels are represented by the prognostic variable  $h_r$  (m), which represents the thickness of surface water averaged over the grid cell. By combining the continuity of mass in the cell with the momentum equation for transport between cells, the rate of change of  $h_r$  can be written as

$$\begin{aligned} A \frac{\partial h_r}{\partial t} = & \frac{\partial}{\partial x} \left( A_c \frac{1}{n} R_h^{2/3} \frac{\partial h_r}{\partial x} \left| \frac{\partial h_r}{\partial x} \right|^{-1/2} \right) + \frac{\partial}{\partial y} \left( A_c \frac{1}{n} R_h^{2/3} \frac{\partial h_r}{\partial y} \left| \frac{\partial h_r}{\partial y} \right|^{-1/2} \right) \\ & + R_{\text{sf}} - f_w (C_g + C_u) - C_{\text{lake}} - Q_{\text{irr\_sf}}(x, y, t) \end{aligned} \quad (3.4)$$

where  $A$  is the river bed area of water in the river or lake ( $\text{m}^2$ ),  $A_c$  is the cross-sectional area of water in the river or lake at cell boundaries ( $\text{m}^2$ ),  $n$  is Manning's

roughness coefficient ( $s\ m^{-1/3}$ ), and  $R_h$  is the hydraulic radius (m), which is equivalent to  $wh_r/(2h_r + w)$  for an open channel flow through a rectangular cross-section, with  $w$  and  $d$  denoting the width and depth of the river (m). Furthermore,  $x$  and  $y$  denote the horizontal directions, and the water flow term between neighbouring grid cells is computed by considering all eight directions on the plane, including the diagonals. Specifically, for every grid cell in the square lattice constituting the simulation domain, Eq. (3.4) is solved by considering both nearest neighbouring cells in  $x$  and  $y$  directions, as well as in the diagonals (omitted from Eq. (3.4) for clarity). In addition,  $R_{sf}$  is the surface runoff ( $m^3s^{-1}$ ), which encodes the infiltration-excess runoff ( $R_{ins}$ ) and the saturation-excess runoff ( $R_{sat}$ ), while  $f_w$  is the wetted surface fraction, which is set to 1 for lakes and to  $f_b$  for running rivers, with  $f_b$  denoting the fractional area of the river bed (computed following the method described next; see Eq. (3.9) in Section 3.6.2). Moreover,  $C_g$ ,  $C_u$  and  $C_{lake}$  denote the values of water flux exchanged by the river with saturated soil, unsaturated soil and lake, respectively ( $m^3\ s^{-1}$ ), while  $Q_{irr\_sf}$  is equal to the irrigated water from surface water, which has been added to the model in this study ( $m^3\ s^{-1}$ ). Water supply from the streams to the crops is modelled based on irrigation water demand predicted by the dynamic irrigation scheme in Noah-MP and constrained by the amount of available water in the stream (see Section 3.7 Eq. (3.13)). Specifically, water is supplied to the crops located within the grid cells the streams flow across, as well as to the crops located in adjacent (off-stream) grid cells. The flow process is modelled here by means of the proximity grid search method, which considers the nearest neighbouring cells in  $x$  and  $y$  directions, as well as in the diagonals.

### 3.6.1 Manning Equation

The Manning equation is used to estimate the average velocity  $V$  ( $m\ s^{-1}$ ) of the river flow cross-section,

$$V = n^{-1}R_h^{2/3}S_f^{1/2} \quad (3.5)$$

where  $S_f$  is the friction slope (-). To model  $V$ , the diffusive wave equation (Eq. 2.32) is applied, neglecting the local and convective acceleration terms and assuming that  $S_f = S_{ws}$ , where  $S_{ws}$  is the water surface slope (-). Here, following (Chow, 1968; De

Paiva et al., 2013; Yamazaki et al., 2011), it is assumed that the Manning roughness coefficient is constant throughout the Yellow River Basin.

### 3.6.2 Channel Bathymetry and Floodplain

It is assumed that the hydraulic geometric shape of the channel follows the power-law function of the bank full discharge  $Q_{BF}$  (Leopold & Maddock, 1953), i.e.,

$$w = aQ_B^b \quad (3.6)$$

$$d = cQ_{BF}^f \quad (3.7)$$

where  $Q_{BF}$  ( $\text{m}^3 \text{s}^{-1}$ ) is estimated by multiplying the upstream area by the uniform local river input (assuming that the local river input is 0.5 mm/day based on the average of historical data) for each cell (Yu et al., 2006), while the coefficients  $a$  and  $c$  and the exponents  $b$  and  $f$  must be determined from observations. According to Parker (1979), the scale factors ( $a$  and  $c$ ) vary over different locations, while the values of the exponents  $b$  ( $\sim 0.5$ ) and  $f$  ( $0.3 \sim 0.4$ ) exhibit a remarkable degree of consistency. Here, it is assumed that exponents  $b = 0.5$  and  $f = 0.3$ , which are values roughly consistent with the observations of Leopold & Maddock (1953), who estimated the values of these exponents for river basins. Furthermore, we estimate  $a = 5.0$  through measurements of the river width from Google Earth satellite imagery, and we assume  $c = 0.6$  in consistency with observations of shallow river cross sections throughout the Yellow River Basin. Indeed, the Yellow River has a wide and shallow cross-section in the Hetao and North China Plains, as indicated in the China River Sediment Bulletin 2000 for the Yangtze River and the Yellow River. Additionally, its lower reaches are shallow due to the flat terrain in the area and the substantial sediment deposition within the channel. Since the river routing model needs to define the width  $w$  and depth  $d$  of the channel in each grid, it is assumed that the minimum values of depth and width are 2 m and 10 m, respectively. The width and depth of the river are defined as follows

$$\begin{cases} w = \max[5.0 \cdot Q_{BF}^{0.5}, 10.0] \\ d = \max[0.6 \cdot Q_{BF}^{0.3}, 2.0] \end{cases} \quad (3.8)$$

As shown in Fig. 3.3, flood inundation is simulated using the storage model in Cunge et al. (1980) and De Paiva et al. (2013), i.e., assuming that (1) the flow velocity

parallel to the river direction vanishes on the floodplain, (2) the floodplain acts only as storage areas, and (3) the water level of the floodplain equals the water level of the main channel. The fractional area of the riverbed  $f_b$  is then estimated as

$$f_b = \left(\frac{w}{\Delta_x}\right)^{\alpha_1} \quad (3.9)$$

where  $w$  is the width of the channel (m) and  $\Delta_x$  is the grid size (m). The default value of  $\alpha_1$  is 0.5, which is related to the river's meandering and floodplain geometry.

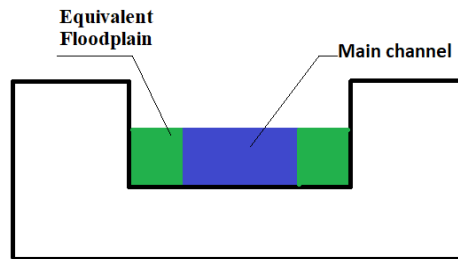


**Figure 3.3:** Simple river-floodplain storage model used in the sub-grid cross-section of the AHMS. The main channel area (blue) corresponds to the parameter  $A_c$  in Eq. (3.4). Furthermore, the equivalent floodplain area (green) is based on  $f_b$ , which is computed using Eq. (3.9). Modified after Cunge (1980).

### 3.7 Irrigation Model

This study aims to develop an irrigation model applicable to arid and semi-arid regions, different from the previous study by Xia et al. (2022) that combined the land surface hydrological model with the Global Crop Water Model (GCWM) to study hydrological processes in water-rich areas of China. To this end, AHMS is extended to incorporate and modify a dynamic irrigation scheme (Xu et al., 2019) in Noah-MP, allowing us to quantify the dynamic irrigation water requirements of dryland crops based on the soil moisture deficit method (Ozdogan et al., 2010). Furthermore, the water uptake applicable to irrigation districts located in arid and semi-arid regions is incorporated into the channel routing model and groundwater model of HMS. Specifically, a channel routing model has been developed that considers long-distance water supply processes in irrigation areas characteristic of arid and semi-arid regions, such as those in the Yellow River Basin.

The soil moisture deficit method in Noah-MP is employed to calculate the irrigation water requirements, i.e., when, where and how much to irrigate (Ozdogan et al., 2010;

Xu et al., 2019). The equations for the integrated soil moisture availability (SMA) in root zones and irrigation water requirements (IWR) read:

$$SMA = \frac{SM - SM_{wlt}}{SM_{ref} - SM_{wlt}} \quad (3.10)$$

$$IWR = (SM_{ref} - SM) \cdot F_{veg} \cdot F_{crop} \cdot (1.0 + F_{iloss}) \quad (3.11)$$

where  $SM$  is the integrated soil moisture (m), and  $SM_{ref}$  and  $SM_{wlt}$  denote the integrated field capacity and wilting point in the root zones (m), respectively,  $F_{veg}$  is the vegetation fraction (-), taken from the MODIS-based climatological dataset for the period from 2001 to 2012 (Broxton et al., 2014), and  $F_{crop}$  denotes the associated 500-m MODIS-based irrigation fraction (Ozdogan & Gutman, 2008).  $F_{iloss}$  is the fraction of flood irrigation loss, which is set as 0.1 in this study.

The following irrigation conditions, based on irrigation fraction, rainfall, leaf area index, and soil water availability, are considered. Xu et al. (2019) reviewed the progress made in the control and optimization of various irrigation models and found that the following irrigation conditions apply to a broad range of scales, from the field scale to the continental scale.

- (1) Cropland fraction: the irrigation fraction is larger than the irrigation fraction threshold (IRR\_FRAC), which is set to 0.25.
- (2) Dry soil: soil moisture availability is less than the irrigation trigger criterion (IRR\_MAD), which is set to 0.5.
- (3) Weather: rainfall is less than the threshold rainfall rate (IR\_RAIN), which is set to 1 mm/hr.
- (4) Crop growing season: the leaf area index is larger than the threshold leaf area index (IRR\_LAI), which is set to 0.6.

The actual total irrigation water amount  $Q_{irr}$  is associated with both surface water and groundwater. However, this actual amount is limited by the availability of surface water in rivers and lakes. The following model applies,

$$Q_{irr} = Q_{irr,sf} + Q_{irr,gw} \quad (3.12)$$

$$Q_{irr,sf} = \min(I_{max} \cdot A_g \cdot F_{irr,sw}, W_{sf,avail}) \quad (3.13)$$

$$Q_{\text{irr,gw}} = I_{\text{max}} \cdot A_g \cdot F_{\text{irr,gw}} \quad (3.14)$$

$$\text{IWRR}(t) = \max\left(\text{IWRR}(t - \Delta t) - \frac{Q_{\text{irr}} \cdot \Delta t}{A_g}, 0\right) \quad (3.15)$$

where  $Q_{\text{irr,sf}}$  and  $Q_{\text{irr,gw}}$  denote the actual amounts of irrigation water from surface water (see Section 3.6, Eq. (3.4) in) and groundwater (see Section 3.5, Eq. (3.3) ) ( $\text{m}^3 \text{s}^{-1}$ ), respectively, while  $F_{\text{irr,sw}}$  and  $F_{\text{irr,gw}}$  are the corresponding area fractions of surface water (river) and groundwater irrigation, based on the ‘‘Global Map of Irrigation Areas’’ (Siebert et al., 2005).  $I_{\text{max}}$  is the infiltration capacity ( $\text{m s}^{-1}$ ), which is considered in the irrigation scheme in the present study (see Section B.1 of Appendix B), while  $A_g$  refers to the grid area ( $\text{m}^2$ ). Moreover,  $W_{\text{sf,avail}}$  denotes the available surface water in the river or lake according to the channel routing model ( $\text{m}^3 \text{s}$ ). Furthermore, we assume that groundwater is sufficient to meet irrigation demand.  $\text{IWRR}(t)$  and  $\text{IWRR}(t - \Delta t)$  are the remaining irrigation water requirements at  $t$  and  $t - \Delta t$  time step (m), respectively and  $\Delta t$  is the time step.

### 3.8 Water Erosion and Sediment Transport Model

A summary of the CASC2D-SED is described in Section 2.4.5, and a full description of the original version can be found in Rojas et al. (2003). This section presents the updated sediment transport capacity model for overland flow used in this study. The sediment transport capacity equation for overland flow is based on the Universal Soil Loss Equation (USLE, USLE-M and USLE-MM) and Kilinc and Richardson's equation (KR). Specifically, the USLE-type erosivity factor and the modified KR equations are based on rainfall, runoff and unit-width water discharge.

#### a) Modified Kilinc and Richardson's equation

Kilinc and Richardson's equation (Kilinc & Richardson, 1973) and the modified KR equation by Julien (2010) are described in Section 2.4.4. In this thesis, the KR equation, including the modification of Julien (2010), is further improved to incorporate concentrated flow in the gullies. As discussed in the previous section, this extension is essential for the accurate modelling of sediment transport capacity at the regional scale. Specifically, the sediment discharge  $q_s$  is assumed to be proportional to the gully area factor  $G_f$  (see Eq. (3.24)), by taking into account

concentrated flow and additional parameters related to sediment supply due to gullies and gravity erosion. The equation for  $q_s$ , the unit sediment discharge ( $\text{tons m}^{-1} \text{s}^{-1}$ ), reads

$$q_s = e_{1,kr} \cdot S_0^{5/3} \cdot q_u^2 \cdot K_{usle} \cdot C \cdot P \cdot G_f \quad (3.16)$$

where  $q_s$  is the unit sediment discharge based on the KR equation, including the modification introduced in the present study ( $\text{tons m}^{-1} \text{s}^{-1}$ ),  $e_{1,kr}$  is a dimensionless free parameter, which needs to be calibrated with the help of sediment discharge data;  $G_f$  is the gully area factor (-).

The sub-grid hydraulic model in AHMS efficiently simulates the large-scale water surface elevation, wave velocity and inundation extent. In this study, the overland flow is incorporated here by computing the unit discharge ( $q_u$ ) of overland flow both from the surface runoff rate ( $R_{sf}$ ) and using the Manning equation. For one-dimensional overland flow, the unit flow discharge is equal to the runoff rate multiplied by the runoff length on the slope, while in the Manning equation, the slope of the energy line is equal to the slope of the soil surface (kinematic wave approximation). It is given by

$$q_u = \begin{cases} R_{sf} \Delta x \\ \frac{1}{n} R_h^{5/3} S_0^{1/2} \end{cases} \quad (3.17)$$

where  $R_{sf}$  is the surface runoff rate ( $\text{m s}^{-1}$ ),  $\Delta x$  is the width of grid cells applied in the simulations (m),  $n$  is the Manning roughness coefficient, which is selected according to the type of ground cover, and  $R_h$  is the hydraulic depth (m).

### **b) Extension to the Universal Soil Loss Equation (USLE) to incorporate gully erosion**

As described in Chapter 2, Section 2.4.1, the original version of the Universal Soil Loss Equation (USLE) (Wischmeier & Smith, 1978) has been developed to predict long-term soil erosion based on different environmental factors. To calculate the sediment discharge in the upland areas of the Yellow River Basin, the USLE is extended to incorporate additional parameters associated with the sediment supply from gullies and gravity erosion. Specifically, the equation for  $q_s$ , the unit sediment

discharge (tons m<sup>-1</sup> s<sup>-1</sup>), reads

$$q_s = e_{1, \text{usle}} \cdot 10^4 \cdot \frac{\Delta x}{\Delta t} \cdot R_{\Delta t} \cdot S \cdot K_{\text{usle}} \cdot C \cdot P \cdot G_f \quad (3.18)$$

where  $q_s$  is the sediment discharge per unit width based on the USLE with the modification introduced in the present study,  $e_1$  is a dimensionless free parameter, which needs to be calibrated with the help of sediment discharge data, and  $R_{\Delta t}$  is the erosivity index (MJ mm ha<sup>-1</sup> hr<sup>-1</sup>) for a time step  $\Delta t$  (s).

### c) $K_{\text{usle}}$ , $S$ , $C$ , $P$ and $G_f$ factors

In the original USLE, the soil erodibility factor ( $K_{\text{usle}}$ ) encodes information about the inherent resistance of sediment on the soil to water erosion, which is related to soil texture, organic matter and permeability. Many studies have found that soil erodibility is mainly associated with clay content. Zhang et al. (2004) developed and validated, thus, the following soil erodibility equation related to clay content using experimental field data from the Chinese Loess Plateau.

$$K_{\text{usle}} = 0.031 - 0.0013 \cdot CL \quad (3.19)$$

where  $CL$  is the clay content in percent (%).

The length and slope factors ( $L$  and  $S$ , respectively) represent the geomorphological controls in the original USLE. Since it is difficult to represent the slope length factor  $L$  in a continental-scale domain, Pelletier (2012) suggests using  $S$  as the only geomorphological control parameter and employing a model that is not based on  $L$ . We follow Pelletier (2012) and use the following equation for  $S$ .

$$S = 20S_0^{5/4} \quad (3.20)$$

The crop factor is calculated based on the vegetation greenness and cropland fraction  $F_{\text{veg}}$  and  $F_{\text{crop}}$ , respectively, and corresponds to the tillage method factor. To represent and quantify soil conservation practices on a large scale, we assume a practice factor  $P$  value of 1.0. Summarizing,

$$F_{\text{veg}} = 1 - e^{-0.52 \cdot LAI} \quad (3.21)$$

$$C = f_{\text{no-till}}(1 - F_{\text{veg}}) + f_{\text{till}}F_{\text{veg}}F_{\text{crop}} \quad (3.22)$$

where  $F_{\text{crop}}$  is the cropland fraction obtained from 500 m MODIS-based irrigation fraction (Ozdogan & Gutman, 2008). Moreover,  $LAI$  is the leaf area index (-) obtained from lookup tables on land use types and the calendar month, and  $f_{\text{till}}$  is the tillage method factor, which accounts for agricultural soil erosion due to ploughing and tillage. For the cropland, we assumed to  $f_{\text{till}} = 1.0$ . Furthermore,  $f_{\text{no-till}}$  is the no-tillage method factor for nature land, which is less than 1.0 and will be calibrated with the help of measurements of measured sediment discharge. (Wilkinson & McElroy, 2007) indicated that soil erosion on cultivated land is four times greater than on natural land on a continental scale. Thus, the default value of  $f_{\text{no-till}}$  is assumed as 0.25.

In this thesis, a novel gully area index  $G_a$  (-) to predict the gully area fraction (gully areas in grid / grid areas) on regional scales is proposed. We assume that the gully area index describing the extent of ground fragmentation can be estimated from the rate with which the slope decreases as the resolution of DEM decreases. Here, the gully area index  $G_a$  is defined as the quotient ratio of  $S_{30\text{m}}$  and  $S_{20\text{km}}$ , i.e., the average slopes derived from the 30 m high-resolution DEM and the average slopes derived from the 20 km resolution DEM, respectively. Please note that the definition of slope and the interpolation method using raster data is detailed in Section D.1 of the appendix.

$$G_a = \frac{S_{30\text{m}}}{S_{20\text{km}}} \quad (3.23)$$

The gully area factor  $G_f$  is therefore defined as the exponential equation of the gully area index.

$$G_f = \exp(\alpha(G_a - 1)) \quad (3.24)$$

where  $G_a \geq 1.0$  and  $\alpha$  is an empirical dimensionless parameter, which must be calibrated with observed sediment discharge data from rivers.

## 4 A Regional Hydrological Model for Arid and Semi-Arid River Basins with Consideration of Irrigation

This work was published in the November 2022 issue of *Environmental Modelling & Software* (Impact Factor: 5.471), Volume 157. The formal publications on ScienceDirect can be accessed from this DOI link: <https://doi.org/10.1016/j.envsoft.2022.105531>, and the copyright belongs to Elsevier Ltd.

**Cong Jiang<sup>a,\*</sup>, Eric J. R. Parteli<sup>b</sup>, Qian Xia<sup>c</sup>, Xin Yin<sup>a</sup> and Yaping Shao<sup>a</sup>**

<sup>a</sup>*Institute for Geophysics and Meteorology, University of Cologne, Pohligstr. 3, Cologne, 50969, North Rhine-Westphalia, Germany*

<sup>b</sup>*Faculty of Physics, University of Duisburg-Essen, Duisburg, Lotharstr. 1, 47057, North Rhine-Westphalia, Germany*

<sup>c</sup>*School of Water Resources and Hydropower Engineering, Wuhan University, Bayi road. 299, 430072, Hubei Province, China*

### Authors contributions to this publication

**Cong Jiang:** Formal analysis, Methodology, Software, Validation, Writing-Original Draft, Writing - Review & Editing.

**Eric J.R. Parteli:** Conceptualization, Supervision, Funding acquisition, Writing-Review & Editing.

**Qian Xia:** Software.

**Xin Yin:** Investigation, Visualization.

**Yaping Shao:** Conceptualization, Supervision, Funding acquisition, Writing-Review & Editing, Resources.

### Reference

Jiang, C., Parteli, E. J., Xia, Q., Yin, X., & Shao, Y. (2022). A regional hydrological model for arid and semi-arid river basins with consideration of irrigation. *Environmental Modelling & Software*, 157, 105531. doi: [10.1016/j.envsoft.2022.105531](https://doi.org/10.1016/j.envsoft.2022.105531).

## 4.1 Introduction

The main purpose of this section is to develop a hydrological model for long-term, large-scale hydrological processes in arid and semi-arid basins, focusing on the Yellow River Basin. Our model development builds on the offline mode of the coupled Atmospheric and Hydrological Modelling System (AHMS) developed at the University of Cologne (Jiang et al., 2020; Xia, 2019). An example of the AHMS applications to wet hydrological basins can be found in Xia et al. (2022). The use of river water and groundwater for irrigation in the Yellow River Basin is expected to profoundly impact the regional hydrological processes. We thus extend the AHMS to include river water and groundwater use processes to better simulate the streamflow and assess the water resources in the Yellow River Basin. To this end, the land surface, channel routing and groundwater models of AHMS are extended to account for river water and groundwater use in irrigation and to include a scheme for estimating irrigated water requirement as proposed by Xu et al. (2019). These new developments lead to improved AHMS simulations by reducing the errors associated with the underestimation of evaporation and the overestimation of runoff in the Yellow River Basin. We also show that the modelling of streamflow in the arid and semi-arid regions of the Yellow River Basin also improves upon the consideration of irrigation.

## 4.2 Model Input Data

A Lambert conformal projection with standard parallel 38.3° N centred at 109.0° E is used to process input data at a resolution of 20 km for the Yellow River Basin.

### 4.2.1 Topography Data

The high-resolution geographic digital elevation data set Multi-Error-Removed Improved-Terrain DEM (MERIT) with a 3-sec resolution (Yamazaki et al., 2019) is used and upscaled to 20-km resolution by using an AHMS pre-processing program (Yu et al., 2006). In the upscaling process, the lower values are weighted more strongly to derive a consistent river network. The AHMS pre-processing program is combined with the method of Leopold & Maddock (1953) and the hydrology toolset in ArcGIS to obtain the related hydrological data, i.e., river depth and width, water surface elevation, upstream area, and sub-basin area. Furthermore, the depth and width of the river channel are estimated from the empirical channel discharge-depth-

width relationship (see Section 3.6.2) based on the theory of hydraulic geometry (Leopold & Maddock, 1953).

#### **4.2.2 Soil and Vegetation Data**

The study utilizes the United States Department of Agriculture (USDA) 16-class soil classification system (Davis & Bennett, 1927; Soil Survey Division Staff, 1993) for categorizing soils. The State Soil Geographic Database Food and Agriculture Organization (STATSGO/FAO) (FAO, 1991) soil dataset provides the soil type map. Furthermore, soil type map and USGS 24-category vegetation (land use) datasets are aggregated from 5 arc min resolution to model grid in the Yellow River Basin using the WRF Preprocessing System (WPS), as depicted in Section 6, Figs. 6.1c and 6.1d.

#### **4.2.3 Subsurface Data**

The initial groundwater head is derived from the simulations using the global groundwater model (de Graaf et al., 2015). By using the China 1:4,000,000 Geology Dataset, the hydrogeologic parameters, including aquifer thickness, porosity and hydraulic conductivity of the aquifer, are obtained correspondingly for each lithologic type with a lookup method (Yang et al., 2010).

#### **4.2.4 Meteorological Data**

The forcing data applied in our simulations are obtained from the China Meteorological Forcing Dataset (CMFD) (He et al., 2020). These data include precipitation, near-surface air temperature, near-surface specific humidity, surface pressure, near-surface wind, surface downwelling shortwave and longwave radiation. CMFD is a high spatial-temporal resolution gridded near-surface meteorological dataset, which is specially designed for studies of land surface processes in China. This dataset was generated by combining remote sensing products, reanalysis datasets and in-situ observations from weather stations. Precipitation fields in CMFD were produced based on the assimilation of 753 weather stations from the China Meteorological Administration (CMA) and gridded background data, including TRMM and GLDAS-NOAH.

#### **4.2.5 Validation Data**

To calibrate and validate AHMS and the new irrigation model introduced here, we consider the observed daily water discharge dataset, publicly available from the

National Earth System Science Data Center of China (<http://loess.geodata.cn>), and the estimated annual averages of surface water withdrawals for the period 1979-1988. The area associated with the referred dataset comprises the four main gauging stations TN (a), LZ (b), TDG (c) and HYK (d) of Yellow River Basin.

Specifically, due to the lack of data on direct statistical surface withdrawals from 1979 to 1987, we have estimated the corresponding annual averages of surface water withdrawals at the four gauging stations mentioned above based on information available for five years from the Yellow River Bulletin of Water Resources (1999~2003) and Jia et al. (2006). According to the Yellow River Bulletin of Water Resources, in the period from 1999 to 2003, the percentage of whole basin average surface water withdrawals was 0.6%, 9.12%, 45.38% and 17.18% at the four main gauging stations, respectively. Moreover, Jia et al. (2006) reported a value of approximately 24 km<sup>3</sup>/yr for the average annual surface water withdrawals from 1980 to 1989. Therefore, the surface water use in the upper reaches of the TNH is negligible – the corresponding values are 2.34, 10.91 and 4.13 km<sup>3</sup>/yr from 1979 to 1989 for the remaining three subbasins, respectively. Similarly, we have estimated the corresponding annual averages of surface water and groundwater withdrawals for irrigation from 1979 to 1989 in the area upstream of the HYK station mentioned above, which are 14.93 and 6.05 km<sup>3</sup>/yr, respectively, for the period 1979 to 1989.

To validate our model prediction for evapotranspiration, we employ the Global Land Evaporation Amsterdam Model (GLEAM) v3.5 dataset (Martens et al., 2017), which has been acquired from satellite observations. Moreover, here we consider Gravity Recovery and Climate Experiment (GRACE) terrestrial water storage (TWS) data to evaluate modelled TWS on a regional scale. To this end, we have downloaded the latest GRACE products from the JPL-RL06M Mascon solutions (thereafter JPL-Mascon) (Wiese et al., 2018), provided by the Jet Propulsion Laboratory (JPL) at the 0.5-degree resolution and native resolution of JPL-RL06M of 3 degrees. JPL-Mascon has been pre-processed as follows. It is, firstly, masked by the land grid, and subsequently rescaled by using the scaling factors obtained by comparing the TWS of JPL-Mascon with the CLM4-based TWS provided by the GRACE website. Thereafter, the dataset is interpolated to a 0.25-degree grid (approximately 30 km on the equator).

Figure 4.1 shows that the TWS in the Yellow River Basin (upstream of HYK) is

declining, with a linear trend of approximately 0.5 cm/yr from 2002 to 2022. Previous studies (Feng et al., 2013) have attributed this phenomenon to groundwater over-exploitation in north China. However, our current model does not account for the process of land use change (e.g., afforestation or reforestation) and improvement of groundwater irrigation systems on farmland that led to the groundwater over-exploitation in the Yellow River Basin. Therefore, to apply the TWS dataset for the validation of our model, here we perform a detrend analysis to remove the associated multi-year trend from the JPL-Mascon, thereby obtaining the orange curve in Fig. 4.1.

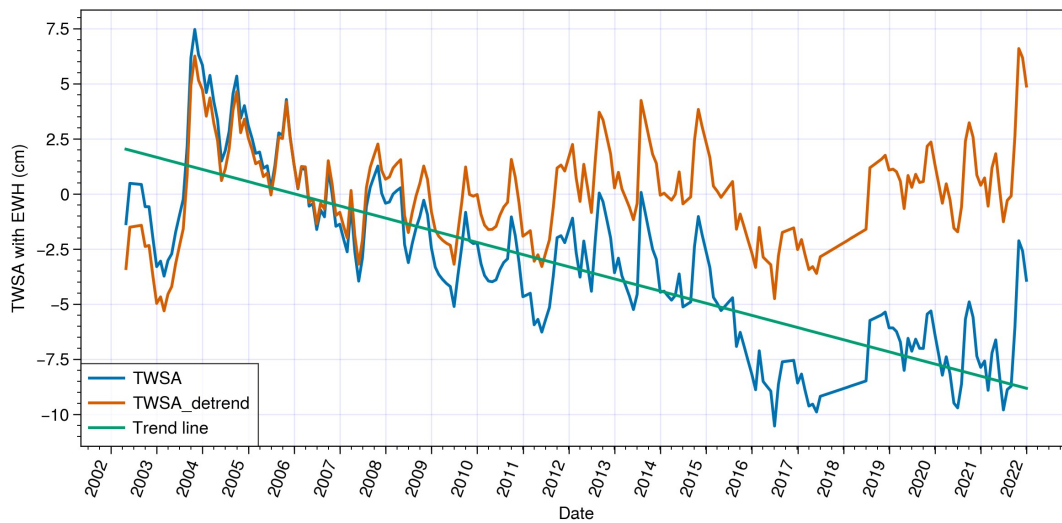


**Figure 4.1:** Monthly terrestrial water storage anomaly (TWSA) with equivalent water height (EWH) over 2002-2022 in the Yellow River Basin calculated from JPL-Mascon (solid blue line), detrend (solid yellow line), and linear trend line (green). The trend is about 0.5 cm per year.

### 4.3 Model Setup and Spin-up

Human interventions in the Yellow River Basin, including irrigation and dam construction, experienced substantial intensification during the last decades, with uncertain impacts on the evolution of the natural streamflow in the basin. Here, we focus on streamflow simulations from 1979 to 1988, for which both observed streamflow and meteorological data are available. To this end, model spin-up was conducted, firstly, over several decades to reach dynamic equilibrium, while the vegetation type and soil texture were assumed unchanged for the entire simulation period. The spatial and temporal resolutions of the land surface and hydrological models are 20 km and 60 minutes, respectively. Moreover, a summary of the physical and control parameterization schemes used in Noah-MP is listed in Table B.2 in Section B.5 of the Supplementary Material.

#### 4.4 Model Performance Evaluation Indices

The agreement between the predicted and observed values of a given variable can be quantified using the percentage error (PE) and the square of the correlation coefficient according to Bravais-Pearson ( $r^2$ )

$$\text{PE} = \frac{P - O}{O} \times 100\% \quad (3.1)$$

$$r^2 = \left( \frac{\sum_{i=1}^N (O^i - \bar{O})(P^i - \bar{P})}{\sqrt{\sum_{i=1}^N (O^i - \bar{O})^2} \sqrt{\sum_{i=1}^N (P^i - \bar{P})^2}} \right)^2 \quad (3.2)$$

where  $O$  and  $P$  denote observed and predicted values,  $N$  is the total number of observations, which are identified by the index  $i$  in the summation operator, and the upper horizontal bar indicates averaging over all data points in the time series. Furthermore, to quantify the agreement between predicted and observed streamflow, we employ the Nash–Sutcliffe model efficiency coefficient (NSE), defined through

$$\text{NSE} = 1 - \frac{\sum_{i=1}^N (Q_s^i - Q_0^i)^2}{\sum_{i=1}^N (Q_0^i - \bar{Q}_0)^2} \quad (3.3)$$

where  $Q_s$  and  $Q_0$  are the predicted and observed values of the streamflow, respectively, and  $\bar{Q}_0$  denotes the average of the observed values. NSE ranges from minus infinity (poor fit) to 1.0 (perfect fit). In general, model prediction is considered to be satisfactory if  $\text{NSE} > 0.5$  (Moriassi et al., 2007).

#### 4.5 Parameter Calibration of Hydrological Model

The calibration of the hydrological model parameters often constitutes a laborious task due to a large number of parameters and a range of uncertainties. The sensitivity analysis presented in Section B.6 in the Supplementary Material and (Cuntz et al., 2016) indicates that the output fluxes, evapotranspiration, and runoff predicted from Noah-MP are sensitive to parameters related to both soil and vegetation characteristics. However, to calibrate average runoff in the land surface model for further studies, here we select the soil parameters (saturated hydraulic conductivity) that directly affect runoff generation and soil water budget. Moreover, the saturated

hydraulic conductance of the riverbed ( $C_s$ ) is calibrated against the observed baseflow.

However, according to Fig. 1.3, the amount of artificial water withdrawals, including irrigation and domestic water, is very large and cannot be neglected in the computation of the regional water budget. Therefore, to calibrate the hydrological parameters, here we consider surface withdrawals (see Section 3.2.4) by comparing simulated total runoff with the sum of surface withdrawals and observed runoff. Four subbasins were selected to calibrate soil saturated hydraulic conductivity according to the climate, landscape conditions and human activity impact. The selected subbasins are the upstream areas of the Tangnaihai (TNH), Lanzhou (LZ), Toudaoguai (TDG) and Huayuankou (HYK) gauges (see Fig. 1.1).

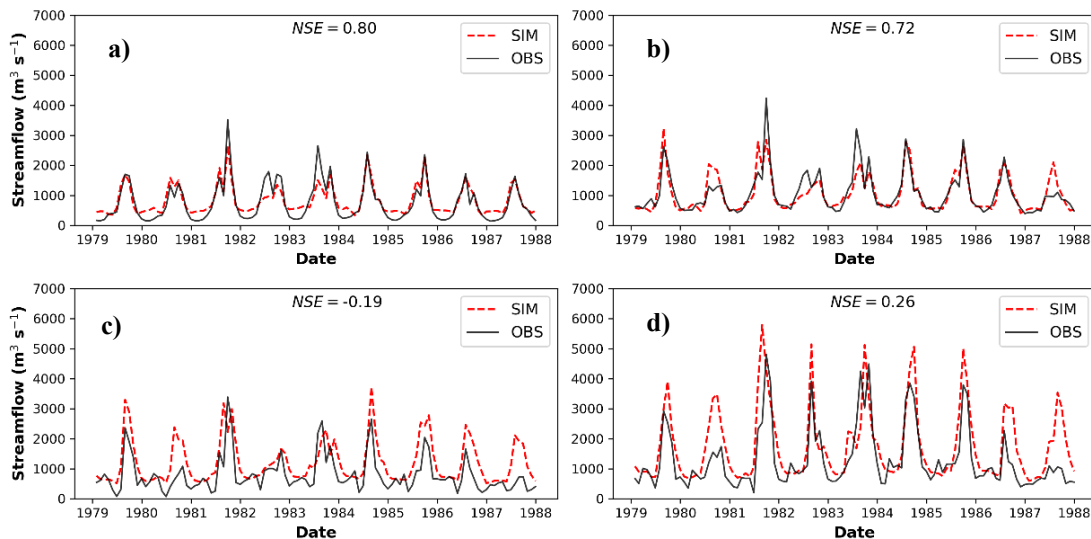


**Figure 4.2:** Predicted (dashed line) and observed (solid line) monthly streamflow from 1979 to 1987 at the hydrological stations: Tangnaihe (a), Lanzhou (b), Toudaoguai (c) and Huayuankou (d).

The calibrated hydrographs and the corresponding statistics are presented in Fig. 4.2. In this figure, the monthly streamflow series predicted with our simulations are compared with the observations at the four gauging stations from 1979 to 1988. The hydrograph is greatly improved by the calibration procedure, and a reasonable agreement is found between these observations and the simulation results for upper stream stations (Tangnaihe and Lanzhou). Notably, the agreement is better at the upstream stations than at other stations in the midstream arid region. We thus conclude that the model must be improved to incorporate human activities in the midstream region, including the effect of river irrigation, which is the subject of

Section 5.

## 4.6 Evaluation and Discussion

The performance of the offline AHMS is evaluated in this section by means of terrestrial water budget analysis and by comparing the predicted and observed mean annual runoff and monthly streamflow, evapotranspiration and terrestrial water storage anomaly in the Yellow River Basin. Moreover, Section B.7 in the Supplementary Material further describes the spatial distribution of eight hydrological variables, including precipitation, evapotranspiration, runoff, streamflow, soil moisture, groundwater depth, surface runoff and subsurface runoff averaged annually from 1979 to 1988.

### 4.6.1 Terrestrial Water Budget

Water budget analysis offers a means to verify and evaluate hydrological models (De Paiva et al., 2013; Maurer et al., 2001). The corresponding mean annual terrestrial water budget for the Yellow River Basin is presented in Fig. 4.3a. As we can see from this figure, predicted and observed averaged annual precipitation values agree upon a percentage error (PE) of -2%, which gives us confidence that the input precipitation data from CMFD reanalysis products are reliable for the purpose of the present study. The deviation of the model water budget amounts to about 3% for precipitation, while the changes in total terrestrial water storage are about 3% of the precipitation. Furthermore, from the results obtained for the average annual evapotranspiration (PE is -5%) and runoff (PE is 35%), we conclude that the AHMS underestimates the evapotranspiration and overestimates the runoff if river irrigation is neglected.

Based on these findings, we further conclude that irrigation constitutes an essential component of the water balance in the Yellow River Basin and must be incorporated into the AHMS model to improve the hydrological simulations. In Fig. 4.3b, the mean annual runoff over 1979-1988, as predicted from our simulations, is compared with the corresponding observation at four gauging stations over the same period, from 1979 to 1988. The APE values of runoff in the subbasins of TNH, TNH-LZ, LZ-TDG and TDG-HYK are 3%, 4%, -124% and 23%, respectively. Therefore, Figure 4.3b shows that the PE of the mean annual runoff is significant at the LZ-TDG subbasin. As mentioned before, the main source of this bias can be attributed to

the river water used for irrigation in this region. Therefore, river water used for irrigation is an important component of the water balance, particularly in the semi-arid areas of the Yellow River Basin. Section 5 discusses the incorporation of river water taken for irrigation into AHMS simulations.

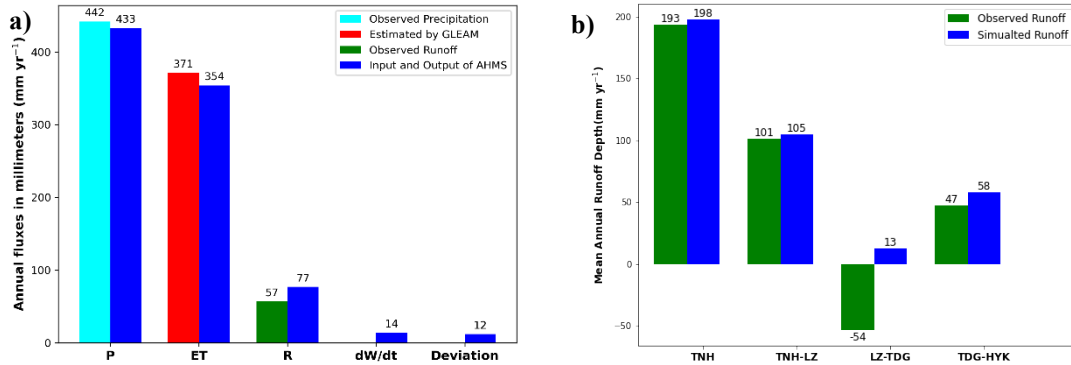


**Figure 4.3:** (a) Results from the water budget analysis. Displayed are the predicted and observed annual averaged precipitation, evapotranspiration and runoff over 1979-1988 in the Yellow River Basin. Annual observed precipitation is upscaled from daily precipitation data provided by the China Meteorological Administration, and GLEAM is the Global Land Evaporation Amsterdam Model, while the annual observed runoff is converted from daily streamflow at the gauging station (Huayuankou). (b) Predicted and observed annual runoff averaged over 1979-1988 in the five subbasins of the Yellow River. Annual observed runoff is converted from the daily streamflow at gauging stations of Tangnaihe, Lanzhou, Toudaoguai and Huayuankou.

#### 4.6.2 Evapotranspiration

Figure 4.4 displays monthly evapotranspiration at the Yellow River Basin estimated from the GLEAM, along with the corresponding prediction from the AHMS, for the period from 1980 to 1988. As shown in Fig. 4.4, the AHMS prediction agrees well with the GLEAM estimate, with the square of the correlation coefficient  $r^2 = 0.98$ , thus further corroborating the capability of our AHMS simulations to quantitatively describe long-term hydrological processes at the Yellow River Basin.

However, the AHMS slightly underestimates evapotranspiration, especially in the winter, notwithstanding the good agreement between the AHMS and GLEAM estimates with regard to the evaporation peaks. In particular, the evapotranspiration in January predicted using AHMS is clearly lower than the corresponding GLEAM estimate. Two factors could explain this underestimation. First, since groundwater provides the main source of water for evaporation during dry seasons, this underestimation of evapotranspiration could be associated with underestimated groundwater recharge in winter. Second, it has been noted in previous studies

(Groisman & Legates, 1994; Yeh & Famiglietti, 2008) that measured precipitation from rain gauges has a systematic negative bias because of the local wind effect around rain gauges. This negative bias is greater in winter since snowflakes are more prone to wind deflections than raindrops. This underestimation of evapotranspiration may be thus caused by negative bias in the precipitation dataset, especially in winter.

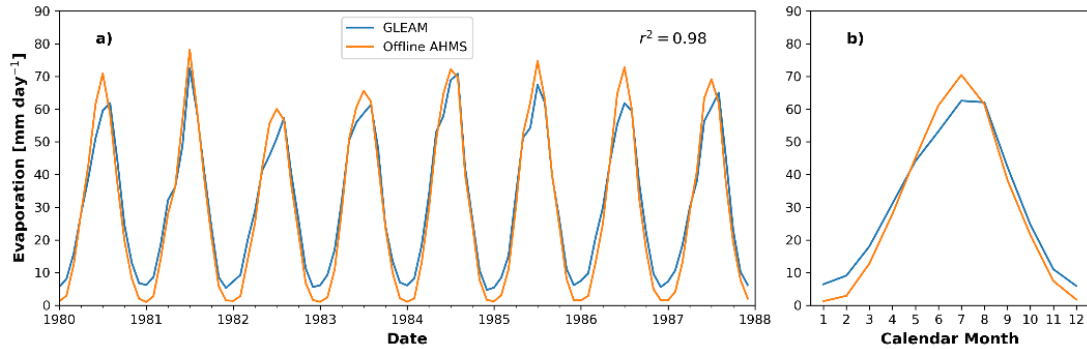


**Figure 4.4:** Comparison of evapotranspiration simulated by GLEAM and AHMS over 1980-1988 in the Yellow River Basin (a) monthly evapotranspiration (b) annual cycles of monthly evapotranspiration.

### 4.6.3 Terrestrial Water Storage

In Fig. 4.5, terrestrial water storage change (TWSC) predicted in numerical simulations using AHMS and GLDAS is compared with the corresponding GRACE-based observation results. As can be now seen from Fig. 4.5, we find a good quantitative agreement ( $r^2 = 0.55$ ) between the corresponding AHMS simulation predictions and their observation counterparts from the GRACE datasets. Moreover, the agreement of our AHMS simulation predictions compares reasonably well with corresponding predictions from the Global Land Data Assimilation System (GLDAS) results ( $r^2 = 0.56$ ) too, as can be seen from Fig. 4.5. Therefore, AHMS represents the long-term, large-scale water cycle in the Yellow River basin with a good quantitative agreement with observations.

Furthermore, as shown in Fig. 4.5, our results indicate that terrestrial water storage changes (TWSC) in 2003-2004 have been much larger than in other years. This finding is consistent with the flooding that occurred in the middle and lower reaches of the Yellow River basin (Weihe River sub-basin) in August 2003. According to the 2003 Yellow River Water Resources Bulletin, the areal precipitation (555.6mm) of 2003 in the Yellow River Basin was 28.6% higher than the average areal precipitation (432mm) over the years (1956~2000). We thus attribute the higher TWS in the period from 2003 to 2004 (see Fig. 4.5) to the 2003 floods and the

concatenated increase in infiltration and groundwater recharge. Our interpretation is in line with the association between precipitation and terrestrial water storage (Chen et al., 2010).

It should be noted that while the TWSC in AHMS simulations is obtained by explicitly considering soil moisture, groundwater, and surface water of rivers and lakes, GLDAS (LSM-Noah) makes no explicit consideration of rivers and lakes in the simulations. This difference could explain the larger amplitude of the TWSC predicted using AHMS compared to the corresponding GLDAS prediction. Therefore, we compare in Fig. 4.6 the GRACE-based monthly TWSC with the AHMS prediction TWSC of the surface water ( $\Delta W_{sf}$ ), soil moisture water ( $\Delta W_{us}$ ), and groundwater ( $\Delta W_{gw}$ ). Figure 4.6 indicates that changes in surface water, soil moisture and groundwater are associated with TWSC fluctuations of nearly the same magnitude.

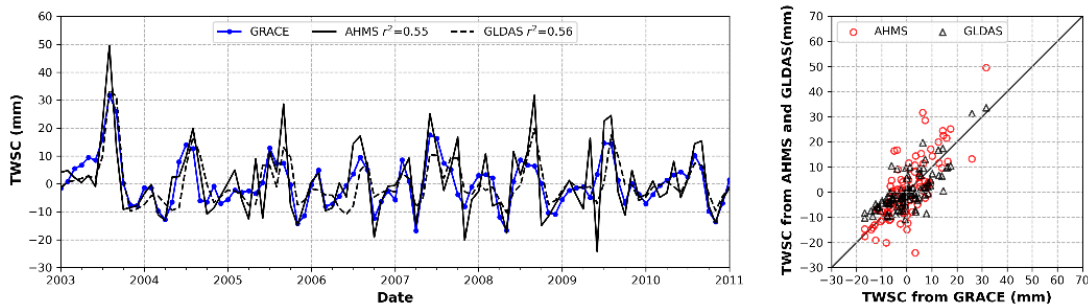


**Figure 4.5:** Monthly terrestrial water storage change (TWSC) with equivalent water height over 2003-2011 in the Yellow River Basin calculated from GRACE dataset observation: JPL-mascons (solid blue line with circles), the offline AHMS simulation (solid black line; red circle) and the Global Land Data Assimilation System (GLDAS) (dash black line and black rectangle).

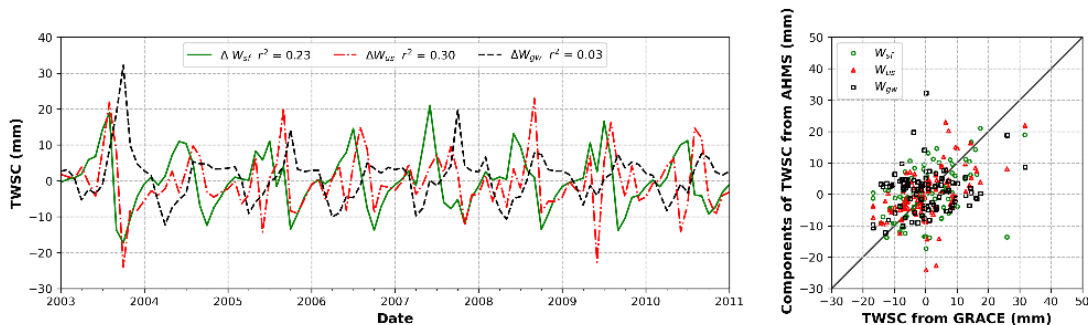


**Figure 4.6:** Comparison of the monthly GRACE-based TWSC with components of AHMS simulation, including changes in surface water ( $\Delta W_{sf}$ ; green line and circles), soil moisture water ( $\Delta W_{us}$ ; red dash line and triangles) and groundwater ( $\Delta W_{gw}$ ; black dash line and rectangles) over 2003-2011 in the Yellow River Basin.

It is interesting to note that surface water storage change, including in rivers and lakes, has been largely ignored in previous studies. For example, Cai et al. (2014) found, by applying the Noah-MP model for the Mississippi Basin, that soil moisture dominates the TWS anomalies, while groundwater constitutes the second component for this basin. However, consideration of surface water storage is indispensable for hydrological simulations of arid and semi-arid regions, such as the Yellow River Basin. Since the average annual precipitation in the Yellow River Basin is only about 450 mm, the upper reaches provide the main water resources for the arid and semi-arid middle and lower reaches, i.e., terrestrial water storage in rivers plays a fundamental role in the Yellow River Basin and must be considered in the simulations.

We note that the TWSC should further depend on river width and depth, and on the area of the floodplains, so the caveat must be added that some uncertainty exists about the values of these parameters, as discussed in the previous sections. Furthermore, the original AHMS models natural terrestrial water cycles, i.e., it does not consider the interference of human activities, such as reservoir storage and agricultural irrigation. The present work applies a coupled hydrological model of groundwater, soil moisture and channel routing model, thus making it possible to explicitly describe the contribution of each component to hydrological processes in the Yellow River Basin.

#### **4.7 Irrigation Impact on the Runoff, Evapotranspiration and Streamflow in the Yellow River Basin**

Irrigation water is an important component of the water balance in arid and semi-arid areas and strongly affects streamflow in the Yellow River Basin. As can be seen from Fig. 4.3b, the Lanzhou-Tangnaihe (LZ-TDG) subbasin is a net water consumption region. However, the current operational version of the AHMS does not account for the effect of water taken from the Yellow River for irrigation. We thus attribute the discrepancy between the predicted and observed average annual runoff at the LZ-TDG station (see Fig. 4.3b; the predicted average annual runoff is positive while the observed one is negative) to the lack of a representation of irrigation water in the model.

Here, we extend the land surface, channel routing and groundwater models of AHMS

to include the effect of water taken from the Yellow River for irrigation ( $Q_{\text{irr}}$  in Eq. (3.2),  $Q_{\text{irr\_gw}}$  in Eq. (3.3) and  $Q_{\text{irr\_sf}}$  in Eq. (3.4)). To this end, we combine the land surface model Noah-MP in the AHMS with a dynamic irrigation scheme (Xu et al., 2019) to quantify the dynamic water requirements for irrigation, which is based on soil moisture deficit. Furthermore, the actual river irrigation is further constrained by the amount of available water, as well as by the fraction of river water within the total irrigation based on the statistics of irrigation facilities (see Section 3.7). As described in Section 3.7, five parameters related to the irrigation model are considered. The calibration and sensitivity analysis of these parameters are shown in Section B.8 of the Supplementary Material. In the following paragraphs, we discuss the results obtained from AHMS using the calibrated parameter values in our irrigation model.

**Table 4.1:** Comparison of statistical and simulated areal average annual irrigation in the Yellow River Basin from 1979 to 1987 (mm/yr)

Period	River irrigation			Groundwater irrigation			Total irrigation		
	Statistics	Simulation	PE (%)	Statistics	Simulation	PE (%)	Statistics	Simulation	PE (%)
1979~1987	20.5	14.9	-27.3	8.3	11.2	35.0	28.8	26.1	9.4

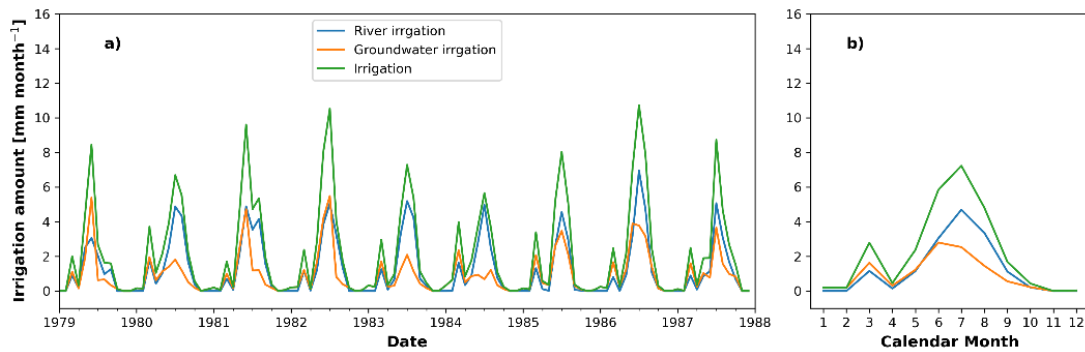


**Figure 4.7:** (a) Monthly and (b) annual averaged cycles of total irrigation amount (green line) in the Yellow River Basin (upper reaches of Huayuankou station) for the period of 1978-1988, including river irrigation (blue line) and groundwater irrigation (orange line).

To validate and evaluate the irrigation model, we compare the simulated areal average annual irrigation amount with regional statistics (see Section 4.2.4) from 1979 to 1988. As shown in Table 4.1, the model simulates the total areal average annual irrigation well, but the model underestimates river irrigation and overestimates groundwater irrigation. Moreover, we perform the sensitivity analysis of the irrigation amount, including river irrigation and groundwater irrigation and the

average monthly streamflow at the outlet of the Yellow River Basin (HYK) to the irrigation parameters (see Table B.4 in Section B.8 of the Supplementary Material). We find that the model greatly underestimates the amount of river irrigation in the Yellow River Basin if the long-distance transfer of water from the river to the irrigation area is not considered (see Table B.5 in Section B.8 of the Supplementary Material). Furthermore, Figure 4.7 represents the monthly and annual averaged cycles of actual irrigation amount, including river irrigation and groundwater irrigation in the Yellow River Basin. The temporal distribution of irrigation water consumption indicates that the maximum water consumption rate occurs in June, while during the winter, the basin relies heavily on groundwater irrigation.

Figure 4.8a displays the annual averaged precipitation, evapotranspiration and runoff for the period 1979-1988, obtained from the simulation under consideration of irrigation in the Yellow River Basin, along with the corresponding observations. Compared to the results displayed in Fig. 4.3 (no irrigation), the percentage error (PE) of evapotranspiration and runoff changed from -5% to -2% and from 35% to 9%, respectively. Moreover, the annual average runoff obtained from the model with irrigation is compared against the observed value in Fig. 4.8b. As can be seen by comparing Fig. 4.8b with Fig. 4.3b (no irrigation), the incorporation of irrigation substantially improved the model predictions. In particular, in Fig. 4.8b, the negative average annual runoff at the LZ-TDG subbasin is accurately reproduced by the model as a result of considering irrigation.

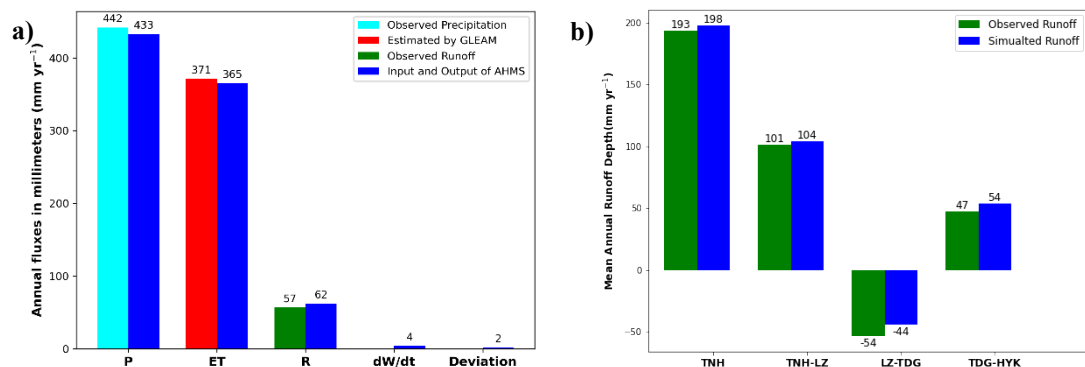


**Figure 4.8:** As in Fig. 4.3, but now considering irrigation in the AHMS simulation.

Furthermore, we compare the GLEAM estimate for evapotranspiration in the Yellow River Basin in the period of 1980-1988 with the corresponding predictions from the AHMS simulation, obtained under consideration of taking water from the river for irrigation. The results for the Yellow River Basin are shown in Fig. 4.9. Since

microwave observations of surface soil moisture are assimilated into the GLEAM soil profile to correct for forcing errors in GLEAM (Martens et al., 2016), the evapotranspiration estimated by GLEAM should be able to reflect the effects of irrigation. However, the incorporation of irrigation into the model does not improve the agreement between GLEAM estimates and AHMS predictions of evapotranspiration – the coefficient of determination ( $r^2$ ) decreased slightly from 0.98 to 0.97 upon including irrigation. This behavior can be understood by noting that the original AHMS simulation without irrigation already overestimates evapotranspiration in the summer (see Section 4.2). We find that this overestimation is slightly enhanced by considering irrigation, as indicated by the respective square of the correlation coefficient. Our findings clearly show, thus, that evapotranspiration is overestimated by AHMS in the summer and underestimated in the winter, and that this behaviour is not caused by our irrigation model. Therefore, future research should focus on elucidating this behaviour to improve the overall accuracy of AHMS, and its applicability to the arid and semi-arid regions of the Yellow River Basin.

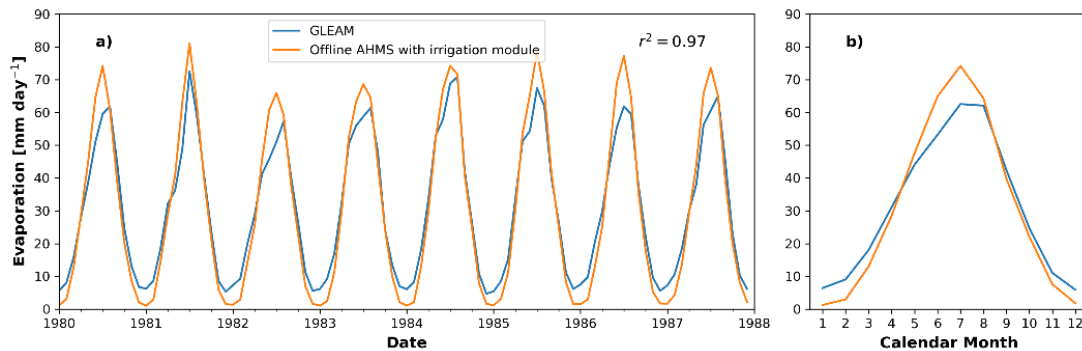


**Figure 4.9:** As in Fig. 4.4, but now considering irrigation in the AHMS simulation (orange line).

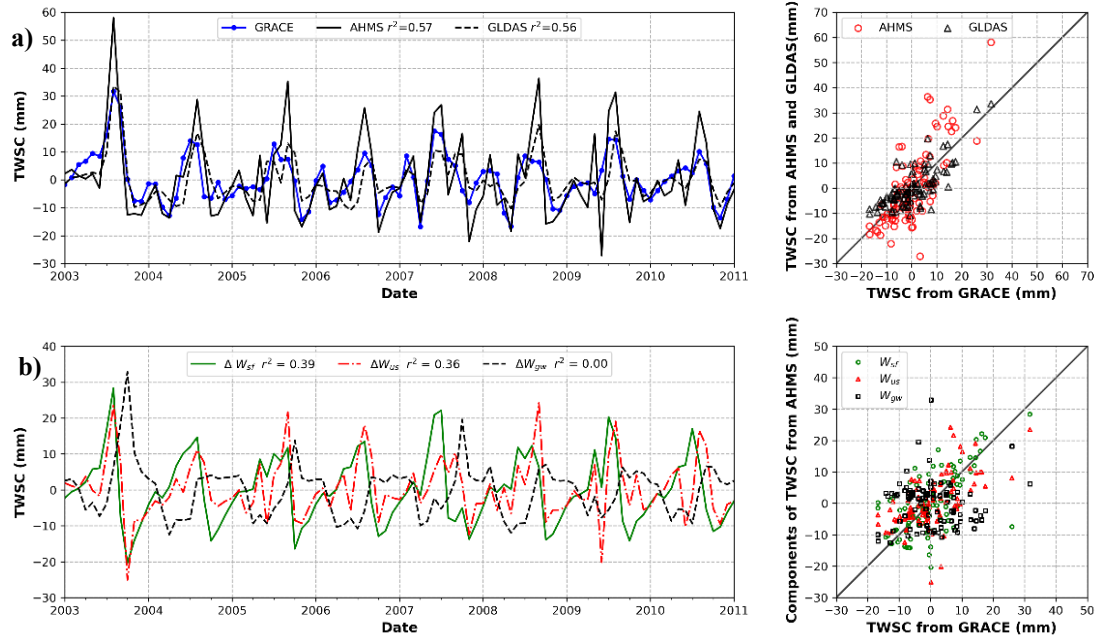


**Figure 4.10:** As in Fig. 4.5 and Fig. 4.6, but now considering irrigation in the AHMS simulation.

Next, we investigate the effect of irrigation on the changes in terrestrial water storage change (TWSC). Figure 4.10a and Figure 4.10b compare TWSC computed from the GRACE-based monthly observations with the prediction from the AHMS simulation, considering the different model components affected by water taken from rivers and groundwater for irrigation. We find that the agreement of TWSC between AHMS simulations and GRACE observations improved when irrigation was taken into account, with the respective  $r^2$  values changing from 0.55 (without irrigation) to 0.57 (with irrigation). In particular, the consistency between the GRACE-based TWSC and the surface water changes ( $\Delta W_{sf}$ ) improved significantly due to the inclusion of irrigation, with the associated  $r^2$  increasing from 0.23 to 0.39. Moreover, the difference between the GRACE-based TWSC and the soil moisture water changes ( $\Delta W_{us}$ ) was reduced moderately, with the associated  $r^2$  increasing from 0.30 to 0.36. However, there are no significant improvements in the comparison between the GRACE-based TWSC and groundwater changes ( $\Delta W_{gw}$ ).

Figure 4.11 compares our model predictions with observations of the monthly (Fig. 4.11a) and averaged monthly (Fig. 4.11b) streamflow at the outlet of the middle reaches of the Yellow River Basin (Huayuankou station) for 1979-1988. In Figs. 4.11a and 4.11b, the comparison is made both with and without water taken from the river for irrigation in the large irrigation districts – including the Hetao Plateau and

Ningxia agriculture area. The results displayed in Figs. 4.11a and 4.11b show that AHMS predictions of streamflow agree more closely with observation data when irrigation is considered in the simulation.

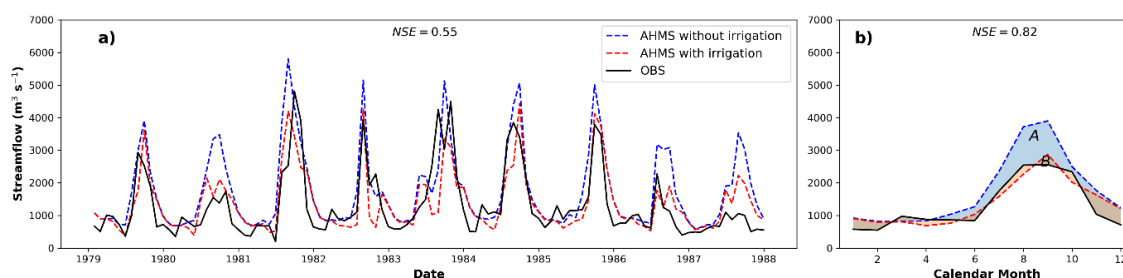


**Figure 4.11:** Comparison of (a) monthly and (b) averaged annual cycles of predicted (dashed lines), which is with (red) and without (blue) consideration of irrigation, and observed (solid line) streamflow at outlet of middle reaches of Yellow River Basin (Huayuankou station) for the period of 1979-1988.

Consideration of irrigation has led to a reduction in the systematic errors associated with the streamflow simulations. As can be seen in Fig. 4.11b, the integration error has been reduced from zone to zone in the Yellow River Basin. More precisely, the Nash-Sutcliffe model efficiency (NSE) changed from 0.26 (without irrigation) to 0.55 (with irrigation) for the monthly streamflow changes, and from 0.27 (without irrigation) to 0.82 with irrigation) for the mean monthly streamflow changes. Model performance improves significantly (see area A in Fig. 4.11b) with consideration of irrigation. However, various sources for the remaining error associated with the area in Fig. 4.11 should be elucidated in future work. To address the remaining error in streamflow (see area B in Fig. 4.11b), the influence of industrial and domestic water use, as well as dam regulations, should also be included in future modelling to improve the model of water use in AHMS.

Our model has provided insights into the relevance of irrigation for hydrological processes throughout the Yellow River Basin. As can be seen from Figs. 4.2 and 4.3a, a good agreement between predicted and observed runoff and streamflow in the basin's upstream region (Tangnaihe and Lanzhou stations) could be obtained in simulations without irrigation after calibration of the soil hydraulic conductivity. However, the mere calibration of this parameter could not yield a satisfactory comparison between corresponding observations and model results in the midstream area (Huayuankou station). Good quantitative agreement, including the midstream area, could only be found after the incorporation of our irrigation module – see Figures 4.8b and 4.11. Therefore, our model results clearly show that irrigation plays

a major role in hydrological processes in the midstream area of the Yellow River Basin (Huayuankou station), which is characterized by an arid and semi-arid climate. Our irrigation module should be thus considered in future regional hydrological modelling of arid and semi-arid hydrological basins.

#### 4.8 Predict the Evolution of Streamflow under Specific Climate Change Scenarios

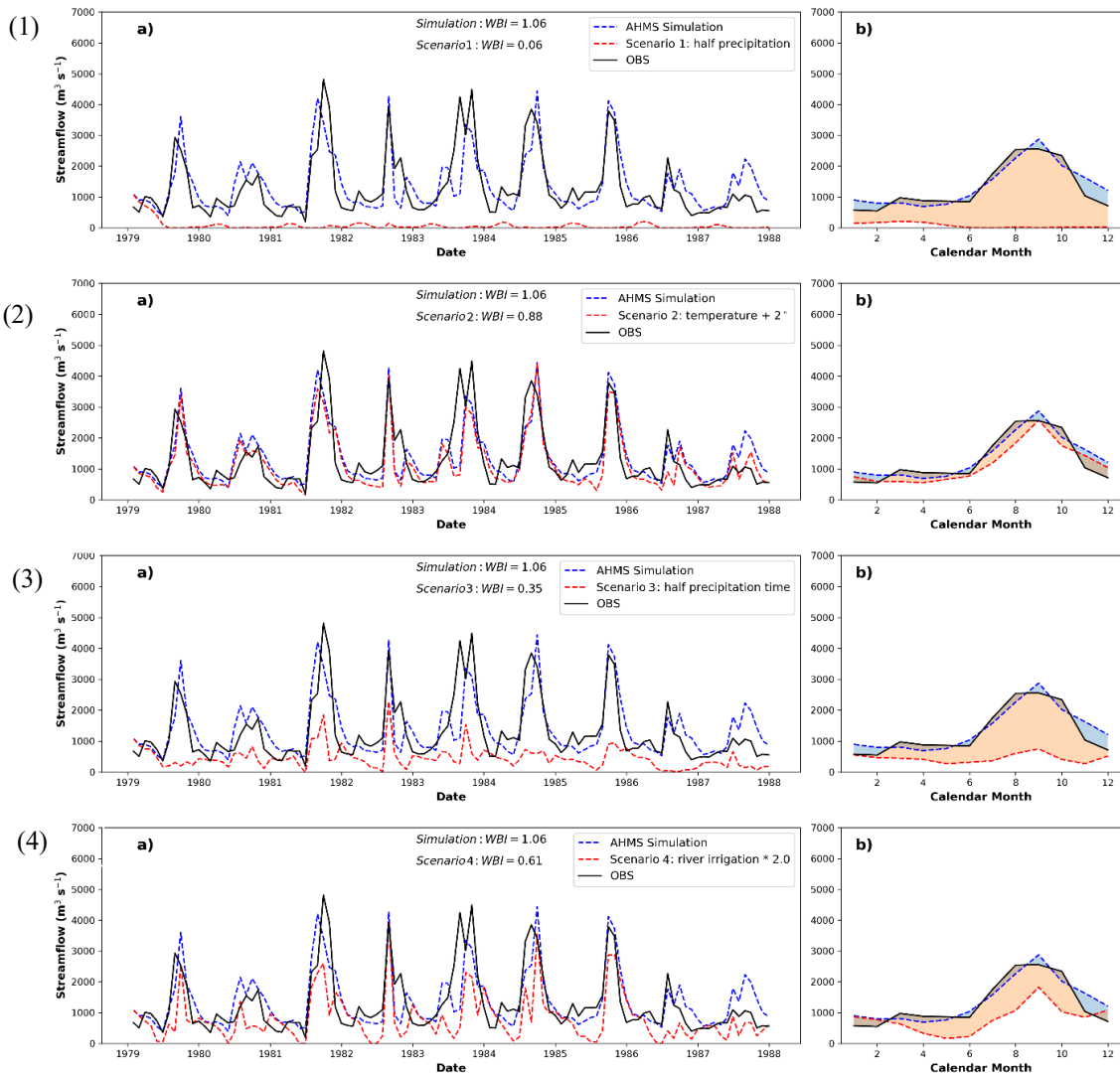


**Figure 4.12:** Comparison of (a) monthly and (b) averaged annual cycles of predicted (dashed lines), which is under (red) and not under (blue) specific climate change scenarios (Scenario 1, 2, 3 and 4) and observed (solid line) streamflow at outlet of middle reaches of Yellow River Basin (Huayuankou station) for the period of 1979-1987. Subfigure (1) **Scenario 1:** precipitation halves, which means the rate of precipitation is uniformly halved during the study period. Subfigure (2) **Scenario 2:** temperature rises by 2 degrees evenly during the study period. Subfigure (3) **Scenario 3:** precipitation time (or amount) is halved, which means no rainfall on the even days (1979.01.02, 1979.01.04, 1979.01.06...) during the study period. Subfigure (4) **Scenario 4:** doubling the amount of river irrigation during the study period.

As mentioned in Section 1.1., the response of the water cycle to climate change is of great interest to the scientific community and has major implications for society (Chahine, 1992; Schlesinger & Bernhardt, 2020). However, predicting the evolution of climate change-driven decadal discharge water on a regional scale is challenging due to the wide range of atmospheric, hydrological and anthropogenic variables involved.

Here, we predict the evolution of water discharge using the AHMS-IRRIG model and historical meteorology data under specific climate change scenarios in the Yellow River Basin. Figure 4.12 compares predicted, i.e., under real historical meteorological data and specific climate change scenarios, with observed monthly and monthly average streamflow. The simulations of streamflow are divided into two cases. Specifically, one case is offline AHMS driven by historical meteorological data. The others are the model driven by modified historical meteorological data, which is based on certain climate change scenarios. We find that climate change Scenario 1, which is the uniform halving of rainfall, has the greatest impact on water discharge of the Yellow River Basin at the outlet (Huayuankou station) with the WBI of 0.06 and 0.35, as seen in Fig. 4.12 (1) and (3). This indicates that water discharge is most sensitive to changes in precipitation, especially changes in precipitation rate, followed by a doubling amount of irrigation in the basin and a doubling of temperature. As shown in Fig. 4.12 (2), the increase in temperature, resulting in an increase in evaporation, tends to have a slight impact on water discharge. As shown in Fig. 4.12 (4), the increase in irrigation tends to have a moderate impact on water discharge, particularly by exacerbating the scarcity of spring river water.

#### **4.9 Conclusion and Outlook**

In the present work, a regional model for long-term, large-scale hydrological processes under consideration of irrigation in the arid and semi-arid regions (AHMS-IRRIG) has been presented. The model (AHMS-IRRIG) combines the land surface model, the flow routing model and the groundwater model of the Atmospheric and Hydrological Modelling System (AHMS) with a modified irrigation scheme (Xu et al., 2019) to quantify the dynamic irrigation amount in arid and semi-arid basins. Specifically, this study developed a dynamic irrigation model based on the soil moisture deficit method and constrained by water availability for the arid and semi-arid regions. Moreover, the channel routing model and groundwater model of the

AHMS have been modified here to incorporate the water uptake applicable to the long-distance water supply to irrigation districts in an arid and semi-arid basin. Furthermore, the actual amount of irrigation is therefore constrained by the water availability estimated with the flow routing, as well as the irrigation fractions of surface water and groundwater based on the “Global Map of Irrigation Areas”. AHMS-IRRIG has been then applied to hydrological simulations of the Yellow River Basin for the period 1979-2011 to assess the impact of irrigation on the land surface processes in the basin’s arid and semi-arid areas.

To this end, AHMS has been first calibrated and evaluated for the Yellow River Basin by means of a parameter sensitivity analysis and a terrestrial water budget analysis and through a comparison of model predictions for the mean annual runoff, monthly streamflow, evapotranspiration and terrestrial water storage anomaly with corresponding observation data, both from in-situ and remote sensing datasets. Furthermore, to account for water consumption in the Yellow River, the land surface, channel routing, and groundwater models have been extended to account for water taken from the river for irrigation. The irrigation water demand calculated by the dynamic irrigation scheme in Noah-MP was added to the sink term and further constrained by water availability in the flow routing and groundwater model, and then actual irrigation water is distributed evenly and horizontally over the ground in the land surface model.

By incorporating the irrigation module into the simulation, a more realistic hydrologic response near the outlet of the Yellow River Basin could be obtained. Moreover, a quantitative agreement was found between the predicted discharge at the upstream gauging stations, namely, Tangnaihe and Lanzhou, and the corresponding observation data. A reasonable agreement between model TWSC and observations from GRACE was also found. Monthly evapotranspiration estimated by GLEAM and the one modelled by AHMS were found to agree well with each other, with the square of correlation coefficient ( $r^2$ ) of about 0.98. Our results thus demonstrate the capability of AHMS of reproducing long-term hydrological processes in the Yellow River Basin, provided water taken from irrigation is considered in the simulation.

Therefore, the main novelties of our model development and application can be summarized as follows:

- 1) The development of an irrigation model that considers the long-distance water transfer off-stream from the river to irrigation districts – is fully neglected by previous irrigation models. With our model, the actual irrigation amount is explicitly computed using the soil moisture deficit method and constrained by the water availability estimated with the flow routing, as well as the irrigation fractions of surface water and groundwater based on the “Global Map of Irrigation Areas”;
- 2) The development of a regional hydrological model that is applicable to arid and semi-arid regions, through the incorporation of irrigation sink and source terms into the channel routing and groundwater models;
- 3) The incorporation of the advanced Earth gravity satellite (GRACE) dataset for the verification of our hydrological model and the assessment of irrigation impacts on hydrological processes in the arid and semi-arid environments of the Yellow River Basin.

Therefore, the future application of our model has the potential to substantially improve the quantitative assessment of the irrigation impacts on hydrological processes in arid and semi-arid areas, by incorporating our irrigation module into the regional AHMS simulation. Furthermore, our model shall provide a helpful tool in the study of feedback effects between irrigation, rainfall and temperature in arid and semi-arid regions, by means of (online) numerical simulations coupled with the Weather Research Forecasting (WRF) modelling system. Moreover, the hydrological model extended here to incorporate our irrigation module shall also find application in the study of irrigation effects on local environmental processes under consideration of changes in climate and land use type.

However, the current version of AHMS needs to be improved in different ways to more accurately represent hydrological processes in the semi-arid and arid areas of the Yellow River Basin. In the present study, only soil parameters were calibrated from the land surface model. The incorporation of vegetation parameters into the calibration of the numerical simulations would constitute one important model extension in future work. Additional measurement data of river and floodplain geometry for the channel routing model of the AHMS would also improve the prediction of flood timing and peak. Furthermore, the incorporation of various

anthropogenic influences, such as damming or change in land use, and the inclusion of the dynamic land use change (e.g. reforestation or afforestation) and damming processes into AHMS constitutes an open modelling task, which will be important to improve the quantitative assessment of the hydrological processes in future work.

Overall, the extension of AHMS presented here led to a more reliable model for predicting runoff and streamflow in arid and semi-arid regions, such as the Yellow River Basin. The progress achieved in the present work shall pave the way toward a wider model application of AHMS at the regional scale over the Yellow River Basin and other hydrological systems in future work, including a broader range of climatic and environmental conditions, and anthropogenic influences.

## 5 Evaluation of Precipitation Reanalysis Products for Regional Hydrological Modelling in the Yellow River Basin

This chapter is the manuscript being prepared for submission.

**Cong Jiang<sup>a</sup>, Eric J. R. Parteli<sup>b</sup>, Qian Xia<sup>c</sup> and Yaping Shao<sup>a\*</sup>**

<sup>a</sup>*Institute for Geophysics and Meteorology, University of Cologne, Pohligstr. 3, Cologne, 50969, North Rhine-Westphalia, Germany*

<sup>b</sup>*Faculty of Physics, University of Duisburg-Essen, Duisburg, Lotharstr. 1, 47057, North Rhine-Westphalia, Germany*

<sup>c</sup>*School of Water Resources and Hydropower Engineering, Wuhan University, Bayi road. 299, 430072, Hubei Province, China*

### **Authors contributions to this publication**

**Cong Jiang:** Formal analysis, Methodology, Software, Validation, Writing - Original Draft, Writing - Review & Editing.

**Eric J.R. Parteli:** Conceptualization, Supervision, Funding acquisition, Writing - Review & Editing.

**Qian Xia:** Software, Writing - Review & Editing.

**Yaping Shao:** Conceptualization, Supervision, Funding acquisition, Writing – Review & Editing, Resources.

### **Reference**

**Jiang, C.,** Parteli, E. J., Xia, Q. & Shao, Y. Evaluation of Precipitation Reanalysis Products for Regional Hydrological Modelling in the Yellow River Basin

## **5.1 Introduction**

The most widely used and more recent versions of near-surface precipitation reanalysis datasets, including NCEP/NCAR, ERA5, GLDAS 2.0, WFDE5/CRU, WFDE5/(CRU+GPCC) and CMFD, are evaluated here by directly comparing them with the rain gauge observations and indirectly the model simulated streamflow obtained using these rainfall products with streamflow observations. We investigate how the hydrological model responds to different precipitation products to gain insight into its sensitivity to precipitation inputs and potential biases in precipitation reanalysis in a large basin context.

## **5.2 Data**

Table 5.1 presents the six precipitation reanalysis products and the gridded rain gauge datasets included in this study. These datasets were classified into three types: the first was based exclusively on gauge data, the second on reanalysis data that are not bias-corrected by gauge data, and the third on the assimilation of reanalysis data and gauge data. Among these, we consider one first-type (OBS), two second-type (NCEP/NCAR and ERA5) and four third-type (WFDE5/CRU, WFDE5/(CRU+GPCC), GLDAS 2.0 and CMFD) datasets.

### **5.2.1 Non-gauge-corrected Reanalysis Precipitation Datasets**

NCEP/NCAR (National Centers for Environmental Prediction and the National Center for Atmospheric Research) Reanalysis is a global dataset of atmospheric variables to support the needs of the climate research communities (Kalnay et al., 1996). A frozen state-of-the-art global data assimilation system and a complete database were used in the NCEP/NCAR Reanalysis project.

ERA5 is the fifth-generation reanalysis product created by the European Center for Medium-Range Weather Forecasts (ECMWF) for global weather and climate from 1979 to near real-time (Hersbach et al., 2020). This reanalysis is carried out with the 4D-Var data assimilation and model forecasts in CY41R2 of the Integrated Forecast System (IFS). ERA5 hourly data on a single level is used in the present work. ERA5 has the following main advantages compared to other reanalysis datasets: higher spatial and temporal resolutions, advanced modelling and data assimilation systems (4D-Var), and a more considerable amount of integrated historical observations and

parameters.

### **5.2.2 Observed Precipitation Datasets**

An observed hourly gridded precipitation dataset across China was developed by Yang et al. (2010) based on the observed daily precipitation data provided by the China Meteorological Administration (CMA). Hereby, the daily rain gauge data from 833 weather stations across China from 1951 to 2006 were gridded using the method described in Milly & Dunne (2002) and Xia (2008), which considered the topographic effects on rainfall. Furthermore, the daily gridded precipitation was downscaled to hourly by using a random statistical function that is the same over a calendar month (Waichler & Wigmosta, 2003).

### **5.2.3 Gauge Corrected Reanalysis Precipitation Datasets**

WATCH Forcing Data methodology applied to ERA5 (WFDE5) is derived from ERA5 with the methodology used to derive the widely employed water, energy and climate change (WATCH) forcing data. It is often used as a meteorological forcing dataset for land surface and hydrological models (Cucchi et al., 2020). The referenced reanalysis consists of a bias-corrected reconstruction of near-surface meteorological variables based on ERA5 (Hersbach et al., 2020).

Precipitation fields in the WFDE5 have been adjusted using monthly-scale bias corrections based on Climatic Research Unit (CRU) and Global Precipitation Climatology Centre (GPCC) data. Two different precipitation datasets (WATCH/CRU and WATCH/(CRU+GPCC)) come from WFDE5. One was corrected using the CRU TS dataset, and the other was corrected using both the CRU TS and the GPCC observational datasets.

The China Meteorological Forcing Dataset (CMFD) is a high spatio-temporal resolution gridded near-surface meteorological dataset that was developed for studies on land surface processes (He et al., 2020). This dataset combines remote sensing and reanalysis datasets with in-situ observations from weather stations. Precipitation fields in the CMFD are produced based on the assimilation of 753 weather stations from the CMA and gridded background data (base reanalysis) GLDAS NOAH10SUBP 3H for the research period of this work, i.e., from 1979 to 1989.

The goal of the Global Land Data Assimilation System (GLDAS) is to integrate

satellite and ground-based observational data products using advanced land surface modelling and data assimilation techniques to generate optimal fields of land surface states and fluxes (Rodell et al., 2004). GLDAS 2.0 is one of the two components of the GLDAS Version 2 (GLDAS-2) dataset, which was produced by GLDAS. Moreover, GLDAS 2.0 was derived from the global meteorological forcing dataset from Princeton University (Sheffield et al., 2006). Specifically, precipitation in GLDAS 2.0 was constructed by combining global observation-based datasets from the Global Precipitation Climatology Project (GPCP) daily product, the Tropical Rainfall Measuring Mission (TRMM, in operation from 1997 to 2015) 3-hourly real-time dataset and the National Centers for Environmental Prediction–National Center for Atmospheric Research (NCEP/NCAR) reanalysis.

#### **5.2.4 Streamflow Dataset**

To calibrate and validate streamflow, observed daily streamflow ( $\text{m}^3 \text{s}^{-1}$ ) for the period 1979-1987 was acquired from the National Science & Technology Infrastructure of China (<http://gre.geodata.cn>), including the four main gauging stations in the basin, i.e., Tangnaihe (a), Lanzhou (b), Toudaoguai (c) and Huayuankou (d).

**Table 5.1:** Overview of seven (3 or 6-) hourly gridded precipitation datasets evaluated in this study. Abbreviations in the data source column are defined as follows: G: gauge; S: satellite; and R: reanalysis.

Filename	Description	Data source	R data	G data	Spatial resolution	Temporal resolution	Temporal coverage	Reference
OBS	Gridded rain gauge data from CMA	G	None	CMA		Hourly	1979-2003	Yang et al. (2010)
NCEP/NCAR	National Centers for Environmental Prediction and National Centers for Atmospheric Research	R	NCEP/NCAR	None	2.5°	6-Hourly	1979-2021	Kalnay et al. (1996)
ERA5	The fifth generation ECMWF reanalysis for the global climate and weather	R	ERA5	None	0.25°	Hourly	1959-present	Hersbach et al. (2020)
GLDAS 2.0	Global Land Data Assimilation System	G, S, R	NCEP/NCAR	GPCP and TRMM	0.5°	3-hourly	1979-2015	Sheffield et al. (2006)
WFDE5/ CRU	WATCH Forcing Data methodology applied to ERA5	G, R	ERA5	CRU TS	0.5°	Hourly	1979-2019	Cucchi et al. (2020)
WFDE5/ (CRU+GPCC)				CRU TS and GPCC				
CMFD	The China Meteorological Forcing Dataset	G, S, R	GLDAS	CMA	0.1°	3-hourly	1979-2018	He et al. (2020)

## 5.3 Method

### 5.3.1 Hydrological Model Setup

The AHMS-IRR model was configured for the Yellow River Basin with a temporal resolution of one hour and a spatial resolution of 20 km (Jiang et al., 2022). The key input static parameters, including vegetation type and soil texture data, are aggregated from the 30 arc-second data of the hybrid State Soil Geographic Database Food and Agriculture Organization (STATSGO/FAO) soil texture dataset and the USGS 24-category vegetation (land use) datasets. The performance of AHMS-IRR was rigorously assessed through a comprehensive evaluation, incorporating a combination of ground-based (in situ) and remote-sensing data sources. This evaluation encompassed various factors, including observed streamflow, terrestrial water storage data derived from the Gravity Recovery and Climate Experiment (GRACE), and assimilated evaporation data provided by the Global Land Evaporation Amsterdam Model (GLEAM). Much better agreements between predicted and observed streamflow in the middle reaches of the Yellow River Basin can be obtained if AHMS is run with the irrigation module.

Based on sensitivity analysis conducted by Jiang et al. (2022), the most crucial parameters for calibrating the model against observations were identified as soil saturated hydraulic conductivity in the rainfall-runoff model, Manning's roughness coefficient in the flow routing model, and irrigation-triggered soil moisture availability and leaf area index in the irrigation model. In order to effectively achieve our objective of evaluating various precipitation products using hydrological modelling in this study, we focused our calibration efforts solely on the rainfall-runoff model parameter known as soil saturated hydraulic conductivity. We incorporated calibrated values of Manning's roughness coefficient, irrigation-induced soil water availability, and leaf area index from the study of Jiang et al. (2022).

Furthermore, following the approach of Bitew et al., (2012) and Tang et al. (2016), we designed two scenarios to distinguish between uncertainties related to rainfall datasets and those related to numerical simulations. For Scenario 1, the rain-runoff model parameters were calibrated using gauged precipitation and remained constant for the other precipitation products. For Scenario 2, the rain-runoff model parameters were recalibrated for each precipitation product.

Table 5.2 lists the two hydrological settings used for model calibration or validation. In Scenario 1, the offline AHMS-IRRIG is calibrated for gauged precipitation from 1 Jan 1979 to 31 Dec 1983. The model is then validated using the same parameters (Para 1) for each of the six (non-)gauge-corrected precipitation reanalysis products described above from 1 Jan 1984 to 31 Dec 1987.

In Scenario 2, the offline AHMS-IRRIG was recalibrated for every precipitation product, and the set of parameters was named accordingly (Para 1 to Para 7). For scenarios 1 and 2, the performance of six (non-) gauge-corrected precipitation reanalysis products was assessed by comparing simulated and observed streamflow from major hydrological stations during the validation period. Moreover, it should be noted that the other required near-surface atmospheric forcing variables (as shown in Table C.1), except for precipitation, were the same for each setup and were derived from ERA5 in Scenarios 1 and 2.

**Table 5.2:** Two scenarios are designed to evaluate different precipitation products using the offline Atmospheric and Hydrological Modelling System integrated IRRigation module (AHMS-IRRIG).

Scenario	Setup	Calibration or Validation	Period	Precipitation Dataset	Parameter Set
I	1	Calibration	1 Jan 1979-31 Dec 1983 (the same as below)	OBS	Para 1
	1-7	Validation	1 Jan 1984-31 Dec 1987 (the same as below)	All datasets	
II	1	Calibration	-	OBS	Para 1
		Validation	-		
	8	Calibration	-	CMFD	Para 2
		Validation	-		
	9	Calibration	-	GLDAS 2.0	Para 3
		Validation	-		
	10	Calibration	-	WFDE5/CRU	Para 4
		Validation	-		
	11	Calibration	-	WFDE5/(CRU+GPCC)	Para 5
		Validation	-		
	12	Calibration	-	NCEP/NCAR	Para 6
		Validation	-		
	13	Calibration	-	ERA5	Para 7
		Validation	-		

Furthermore, Table C.3 in Appendix C shows the calibrated parameters (soil saturated hydraulic conductivity) of the rainfall-runoff model in the four subbasins, including Headwater-Tangnaihe, Tangnaihe-Lanzhou, Lanzhou-Toudaoguai and Toudaoguai-Huayuankou. Specifically, we calibrated the rainfall-runoff model against the mean annual observed runoff in the calibration period (from 1979 to 1983). Moreover, Table C.4 in Appendix C presents the simulated and observed mean annual area runoff from 1979 to 1987, including the calibration and validation periods in the Yellow River Basin. The parameters in the rainfall-runoff model were calibrated here to keep the BIAS (see next section) of runoff for each reanalysis product as small as possible.

### 5.3.2 Evaluation Metrics

The agreement between the model-predicted and observed values was quantified by employing the following performance metrics: the Nash–Sutcliffe model efficiency coefficient (NSE) (Nash & Sutcliffe, 1970), the root-mean-square error (RMSE), the Pearson correlation coefficient (PCC), the mean absolute error (MAE), the mean absolute percentage error (MAPE), the relative bias (BIAS) and the modified Kling-Gupta efficiency (mKGE) (Gupta et al., 2009; Kling et al., 2012). These performance metrics are defined as follows, and the value ranges and perfect agreement corresponding values are summarized in Table B.2 in the Supplement.

$$\text{NSE} = 1.0 - \frac{\sum_{i=1}^N (P_s^i - P_o^i)^2}{\sum_{i=1}^N (P_o^i - \bar{P}_o)^2} \quad (5.1)$$

$$\text{RMSE} = \sqrt{\frac{1}{N} \sum_{i=1}^N (P_s^i - P_o^i)^2} \quad (5.2)$$

$$\text{PCC} = \frac{\sum_{i=1}^N (P_o^i - \bar{P}_o)(P_s^i - \bar{P}_s)}{\sqrt{\sum_{i=1}^N (P_s^i - \bar{P}_s)^2 (P_o^i - \bar{P}_o)^2}} \quad (5.3)$$

$$\text{MAE} = \frac{1}{N} \sum_{i=1}^N |P_o^i - P_s^i| \quad (5.4)$$

$$\text{MAPE} = \frac{1}{N} \sum_{i=1}^N \left| \frac{P_o^i - P_s^i}{P_o^i} \right| \times 100\% \quad (5.5)$$

$$\text{BIAS} = \frac{\sum_{i=1}^N (P_o^i - P_s^i)}{\sum_{i=1}^N P_o^i} \times 100\% \quad (5.6)$$

$$\text{mKGE} = 1 - \sqrt{(\text{PCC} - 1)^2 + (\beta - 1)^2 + (\gamma - 1)^2}$$

$$\beta = \text{bias ratio} = \frac{\mu_s}{\mu_o} \quad (5.7)$$

$$\gamma = \text{variability ratio} = \frac{\sigma_s / \mu_s}{\sigma_o / \mu_o}$$

where  $P_s$  and  $P_o$  are the simulated and observed values of the  $P$  variable, respectively, and  $\bar{P}_o$  is the mean value of  $P_o$ . Moreover,  $\mu_s$  and  $\mu_o$  represent the averages of the predicted and observed values, respectively, while  $\sigma_s$  and  $\sigma_o$  correspond to the standard deviations of the predicted and observed values, respectively.

### 5.3.3 Standard Deviation of Elevation

The standard deviation of elevation is used to depict the complexity of the terrain and is defined as follows

$$\text{SDE} = \sqrt{\frac{\sum_{i=1}^N (x_i - \mu)^2}{N}} \quad (5.8)$$

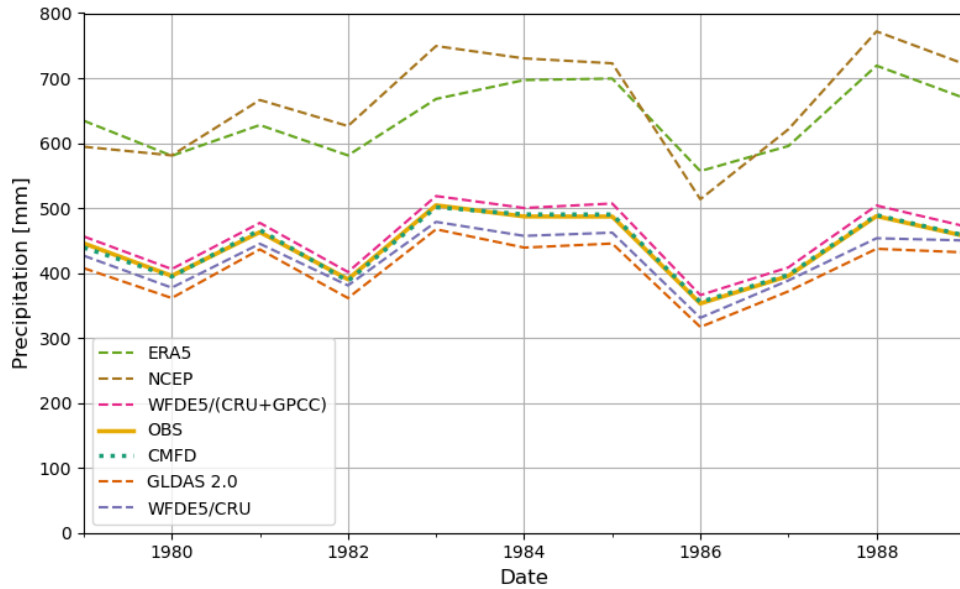
where SDE is the standard deviation of elevation of the larger grid, which is at a 20 km resolution in this study,  $x_i$  is the elevation of the  $i$ th sub-grid at a 1 km resolution in the cell,  $N$  is the number of sub-grids at a 1 km resolution in the larger cell, and  $\mu$  is the average elevation of the cell. In this study, a moving window of  $20 \times 20$  was used to calculate the standard deviation of elevations. Values close to zero indicate no variation (i.e., flat areas), while high standard deviations indicate areas with complex and steep terrain.

## 5.4 Results

### 5.4.1 Performance Evaluation Using Gauge Observation

In this section, the performance of six reanalysis precipitation products, namely NCEP/NCAR, GLDAS 2.0, ERA5, WFDE5/CRU, WFDE5/(CRU+GPCC) and CMFD, were assessed on annual, seasonal and monthly scales by comparison with

the gauge precipitation (OBS). The daily scale was used as the base time scale.



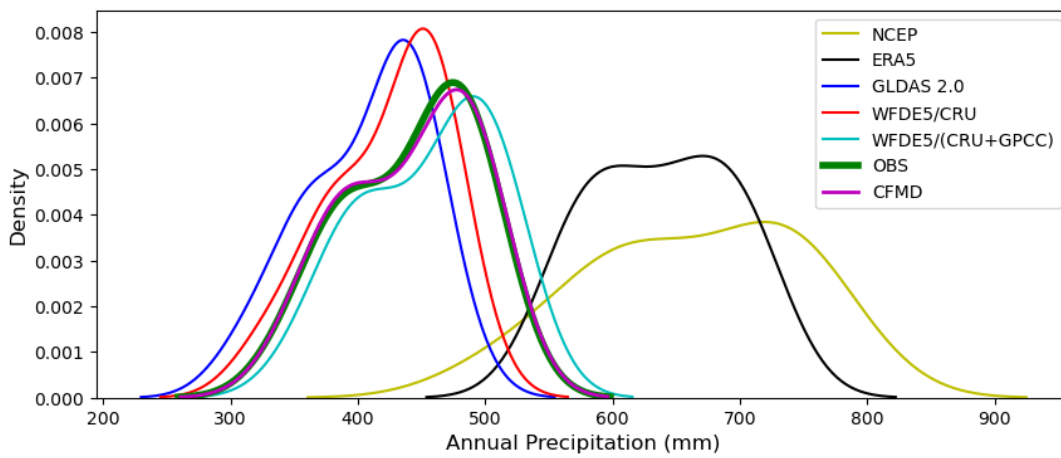
**Figure 5.1:** Annual precipitation in the Yellow River Basin from 1979 to 1989: NCEP (brown dashed line), OBS (solid orange line), GLDAS 2.0 (orange dashed line), ERA5 (green dashed line), WFDE5/CRU (blue dashed line), WFDE5/(CRU+GPCC) (pink dashed line) and CMFD (green dotted line).

Fig. 5.1 displays the average yearly precipitation of each product along with the observed annual precipitation. As shown, the non-gauge-corrected reanalysis precipitation datasets (NCEP and ERA5) significantly overestimated precipitation by 50% and 45%, respectively. Furthermore, the CMFD dataset results were almost identical to the observed precipitation on an annual scale.

Moreover, Table 5.3 lists the annual precipitation statistics of seven products from 1979 to 1989. As shown, NCER/NCAR yielded the highest average annual precipitation (664mm), had the widest range in the annual mean precipitation (514-772 mm), and was associated with the largest deviation (82.3 mm) over the Yellow River Basin. To compare, WFDE5/CRU had the narrowest range in the annual mean precipitation (331-479 mm) as well as the smallest associated deviation (46.3 mm). As shown in Fig. 5.2, the annual precipitation density from the CMFD dataset yielded the best agreement with the gauge data (OBS), followed by the WFDE5/(CRU+GPCC). Moreover, WFDE5/CRU and GLDAS 2.0 yielded an overall low precipitation level with a peak of approximately 450 mm. Furthermore, the non-gauge corrected datasets NCEP/NCAR and ERA5 significantly overestimated the precipitation levels in the study period.

**Table 5.3:** Annual precipitation statistics for the Yellow River Basin from 1979 to 1989 (unit: mm), associated with the different products considered in this study.

Index	Minimum	Median	Mean	Maximum	Standard Deviation
OBS	353	457	442	504	50.6
NCEP/NCAR	514	666	664	772	<b>82.3</b>
ERA5	557	635	639	719	55.4
GLDAS 2.0	317	432	407	467	47.0
WFDE5/CRU	331	445	423	479	<b>46.3</b>
WFDE5/(CRU+GPCC)	366	472	456	518	52.2
CMFD	355	457	443	501	51.0



**Figure 5.2:** Density curve (kernel density estimates KDE, which is the estimation of probability density functions of random variables based on kernels as weights) of annual precipitation of the products over the Yellow River Basin from 1979-1989.

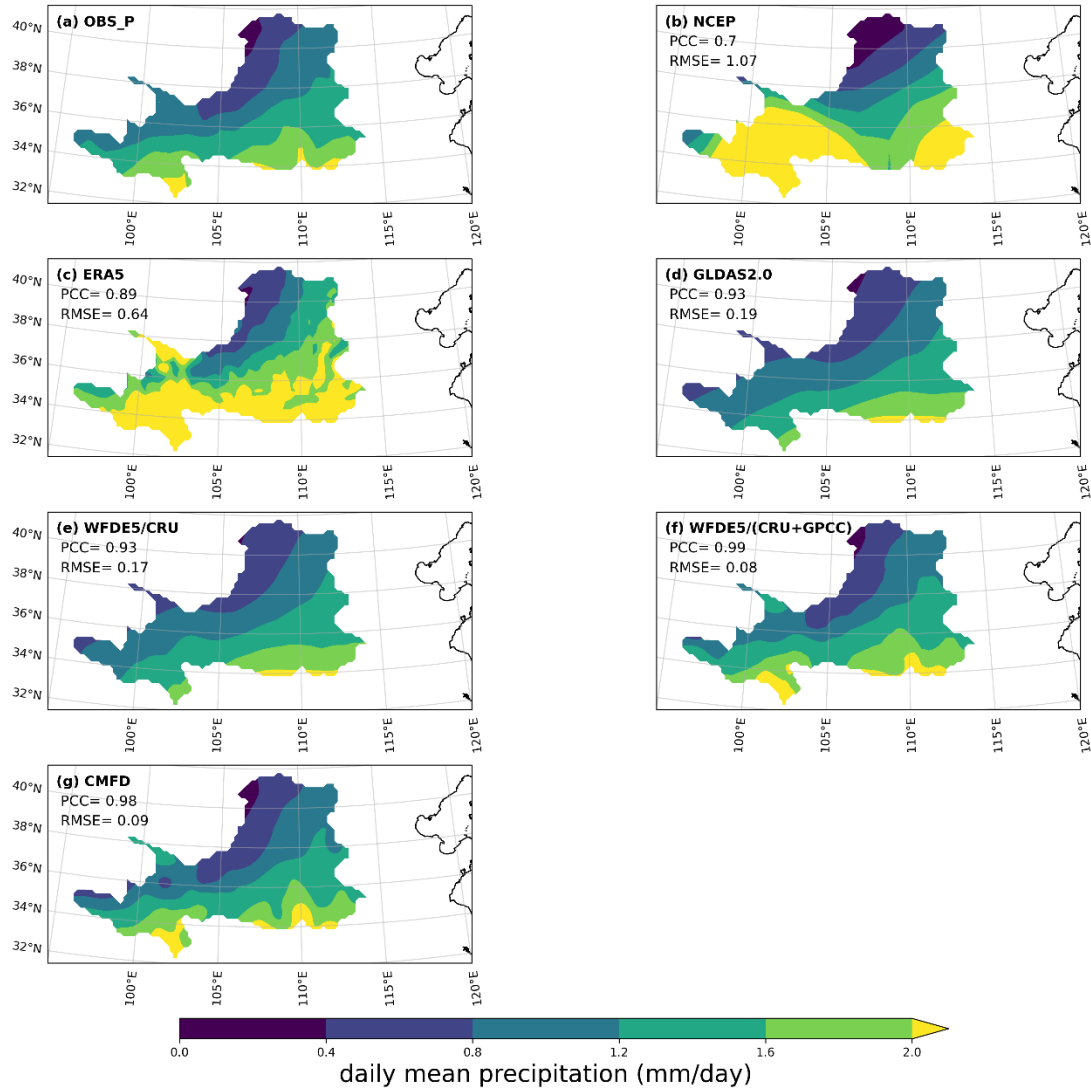


**Figure 5.3:** Spatial distribution of the daily mean precipitation of the seven precipitation products considered in the present study, i.e., (a) OBS, (b) NCEP, (c) ERA5, (d) GLDAS 2.0, (e) WFDE5/CRU, (f) WFDE5/(CRU+GPCC) and (g) CMFD, from 1979 to 1989 over the Yellow River Basin (upland of Huayuankou), along with the Pearson correlation coefficient (PCC) between the reanalysis dataset and OBS for each grid in the basin.

Fig. 5.3 displays the spatial distributions of the precipitation from all products and the Pearson correlation coefficients (PCCs) for the six reanalysis products in the Yellow River Basin (upland of Huayuankou) from 1979 to 1989. This figure shows that the average annual precipitation gradually increased from northwest to southeast. The areas with the highest annual precipitation were located in the southern Yellow River Basin, including the upper reaches of this basin, the Weihe Basin, and the Sanmenxia to Huayuankou area (see Fig. 1.1). In contrast, the lowest annual precipitation occurs at Ningxia and the Hetao Plateau in the northwest of the basin. According to the PCC, precipitation data from WFDE5/(CRU+GPCC) (PCC=0.99)

and CMFD (PCC=0.98) were the most consistent with OBS. GLDAS 2.0 and WFDE5/CRU slightly underestimate precipitation in the upper reaches of the river, while the non-gauges-corrected precipitation products (NCEP/NCAR and ERA5) significantly overestimated precipitation, especially in the mountainous area of the basin). For further details and interpretations, please refer to the discussion in Section 5.5.1.

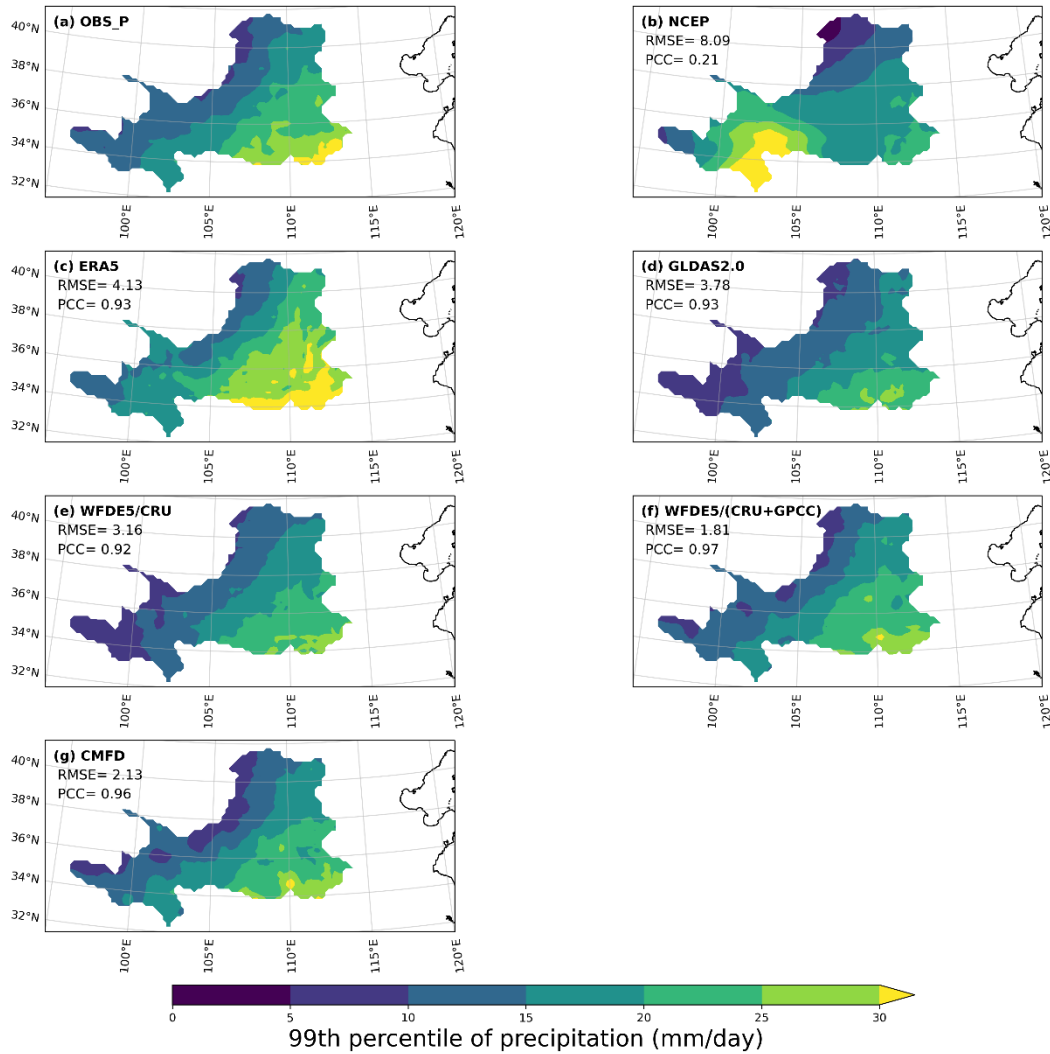


**Figure 5.4:** Spatial distribution of the 99th percentile precipitation of the seven precipitation products considered in the present study, i.e., (a) OBS, (b) NCEP, (c) ERA5, (d) GLDAS 2.0, (e) WFDE5/CRU, (f) WFDE5/(CRU+GPCC) and (g) CMFD, from 1979 to 1989 over the Yellow River Basin (upland of Huayankou), along with the root mean square error (RMSE, mm) and the Pearson correlation coefficient (PCC) between the reanalysis dataset and OBS for each grid in the basin.

To evaluate extreme precipitation, we calculated the 99th percentile of the daily precipitation for each precipitation dataset. The results are presented in Fig. 5.4. Based on the RMSE and PCC values calculated over the research area, the spatial

distribution of extreme precipitation (i.e., 99th percentile precipitation) predicted from WFDE5/(CRU+GPCC) (PCC=0.97 and RMSE=1.81) and CMFD (PCC=0.96 and RMSE=2.13) exhibited the best agreement with the observations (OBS). Remarkably, although NCEP and ERA5 exhibited similar annual precipitation, their spatial patterns of extreme precipitation showed significant differences, as indicated by the RMSE values of 8.09 and 4.13 and the PCC values of 0.21 and 0.93 for NCEP and ERA5, respectively.

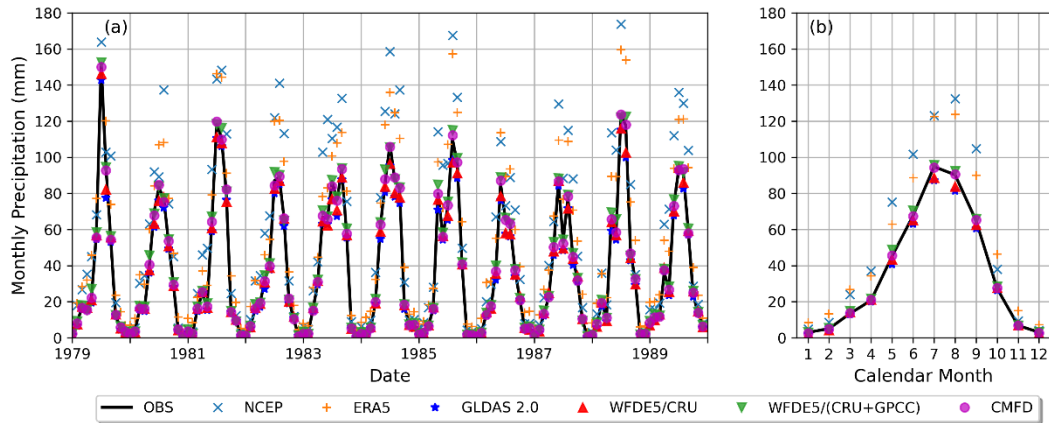


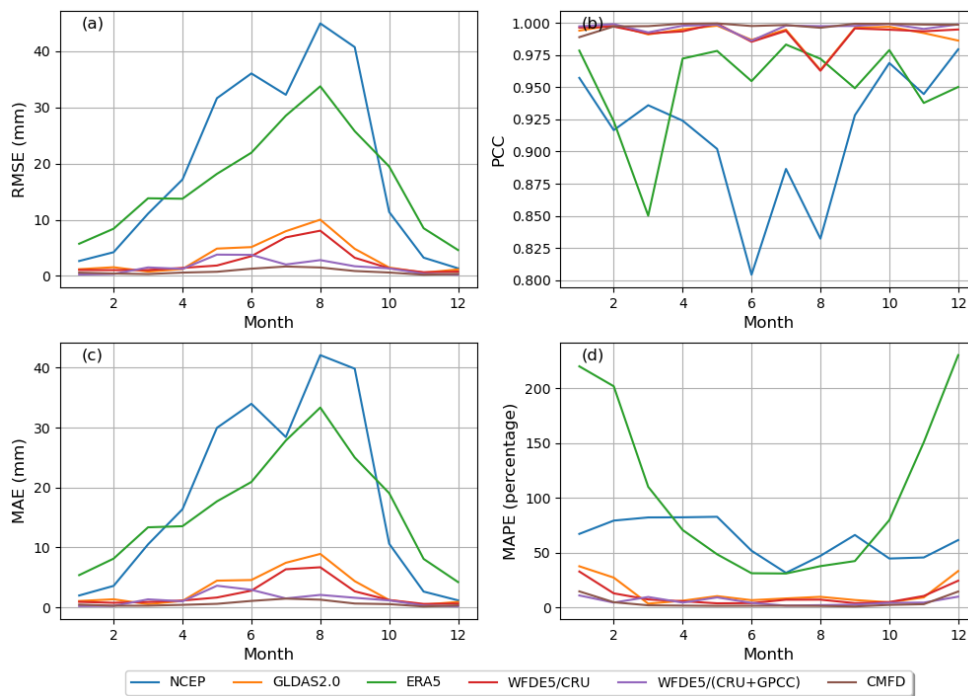
**Figure 5.5:** (a) Monthly precipitation of the products over the Yellow River Basin from 1979-1989. (b) The annual cycle of monthly precipitation averaged over 1979-1989.

**Table 5.4:** Statistics of the monthly precipitation of the products over the Yellow River Basin from 1979 to 1989 (unit: mm).

Index	PCC	RMSE	MAE	MAPE
NCEP/NCAR	0.976	25.18	18.43	61.8
ERA5	0.993	19.11	16.39	104.44
GLDAS	0.998	4.53	3.02	13.64
WFDE5/CRU	0.997	0.99	2.18	10.4
WFDE5/(CRU+GPCC)	0.999	2.02	1.34	5.68
CMFD	1.000	0.88	0.61	4.20

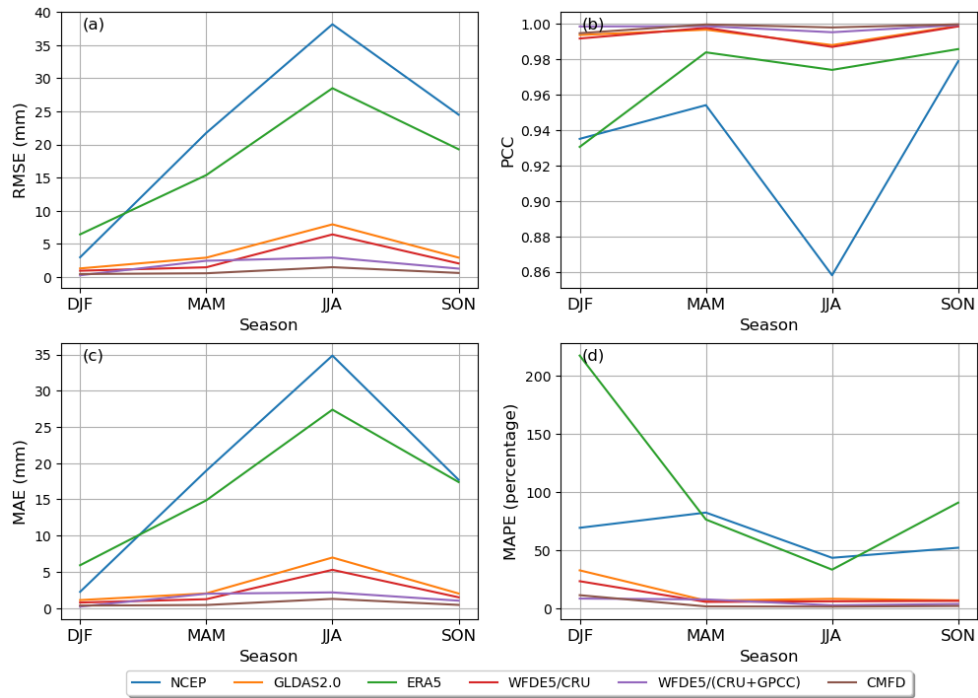
Fig. 5.5 shows the monthly precipitation of the products in the Yellow River Basin from 1979-1989 and the average annual cycle of monthly precipitation for this period. As shown in Fig. 5.5, NCEP/NCAR and ERA5 overestimated precipitation in all months, while all other products did not differ much in terms of monthly precipitation. Table 5.4 lists monthly precipitation statistics of the six reanalysis precipitation datasets. These monthly statistics showed that CMFD yielded the highest correlation coefficient. Similarly, CMFD attained the lowest MAE, MAPE and RMSE.

Fig. 5.6 shows the average monthly evaluation metrics of the precipitation products in the Yellow River Basin from 1979 to 1989. As seen, Fig. 5.6 indicates that CMFD had the lowest RMSE, MAE and MAPE, while NCEP/NCAR performed the worst. Compared to other months, all data showed the most considerable error in August. On the contrary, Figure 5.6d shows that the percentage error in precipitation for these products was significantly higher in December, January and February.



**Figure 5.6:** Averaged monthly evaluation metrics of the precipitation products over the Yellow River Basin from 1979-1989: (a) RMSE (mm), (b) PCC, (c) MAE (mm), and (d) MAPE (%).

Similarly, Fig. 5.7 shows that CMFD (NCEP/NCAR) produced the lowest (largest) RMSE, MAE and MAPE for seasonal precipitation, while all products led to an overestimation of this precipitation in the summer. Fig. 5.7d shows that the percentage error in precipitation for these products increased significantly in the winter, especially for NCEP/NCAR and ERA5. This finding is consistent with Beck et al. (2017) and Jiang et al. (2021), as it occurs because the atmospheric model produces spurious drizzle and tends to overestimate low rainfall due to deficiencies in the rainfall generation parameterization scheme. For further insights and interpretations, please refer to Section 5.5.1.



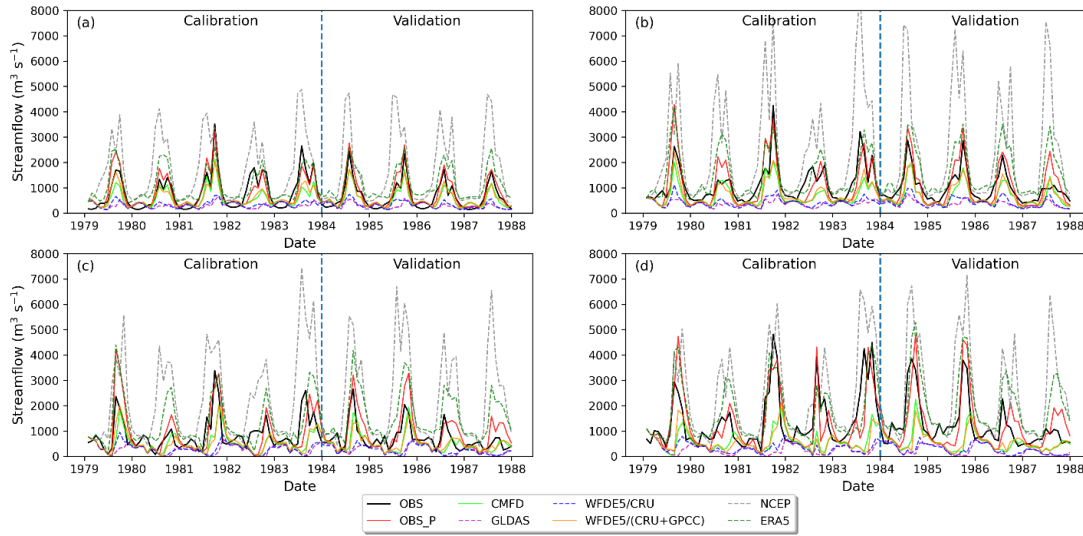
**Figure 5.7:** Seasonal evaluation metrics of the precipitation products over the Yellow River Basin from 1979-1989: DJF (winter, December to February), MAM (spring, March to May), JJA (summer, June to August), SON (autumn, September to November), (a) RMSE (mm), (b) PCC, (c) MAE(mm), and (d) MAPE (%).

#### 5.4.2 Performance Evaluation Using Offline AHMS

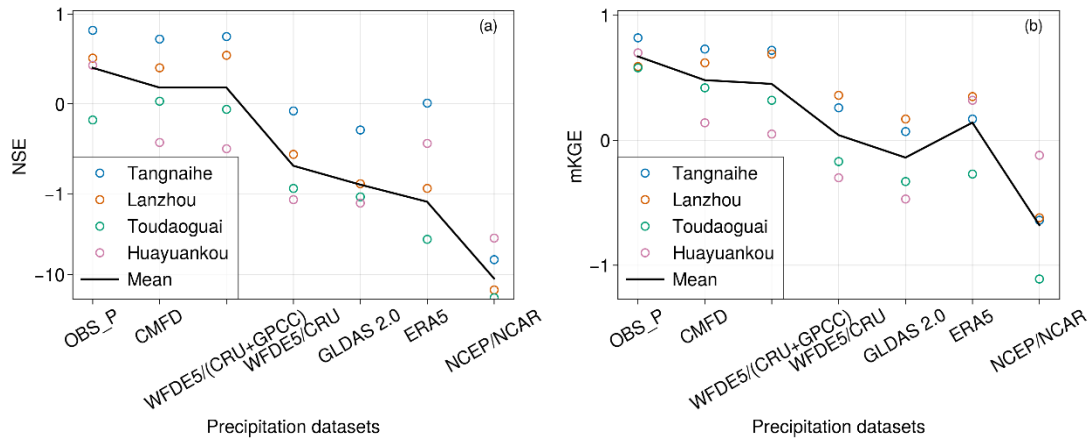
In this section, we evaluated the performance of the six reanalysis precipitation data products by comparing the offline AHMS-IRRIG simulated monthly streamflow with the corresponding observations. Fig. 5.8 compares simulated monthly streamflow with gauge-calibrated parameters and observed monthly streamflow in both the calibration and the validation periods at all four main hydrological stations (Tangnaihe, Lanzhou, Toudaoguai and Huayuankou).

As seen, the monthly streamflow was significantly overestimated when using NCEP and ERA5 products and slightly underestimated when using gauge-corrected reanalysis precipitation products. The associated values of the Nash–Sutcliffe model efficiency coefficient (NSE) and the modified Kling-Gupta efficiency (mKGE) in both the calibration and the validation periods are displayed in Fig. 5.9 and Table C.5 in the Supplementary Material. As shown in Fig. 5.9, the model performed much better upstream than in the middle stream area. In particular, the highest values of NSE (0.82) and mKGE (0.82) were observed at the Tangnaihai station in the validation period (from 1984 to 1987). Moreover, WFDE5/(CRU+GPCC) and CMFD outperformed the other products during the validation period, with the

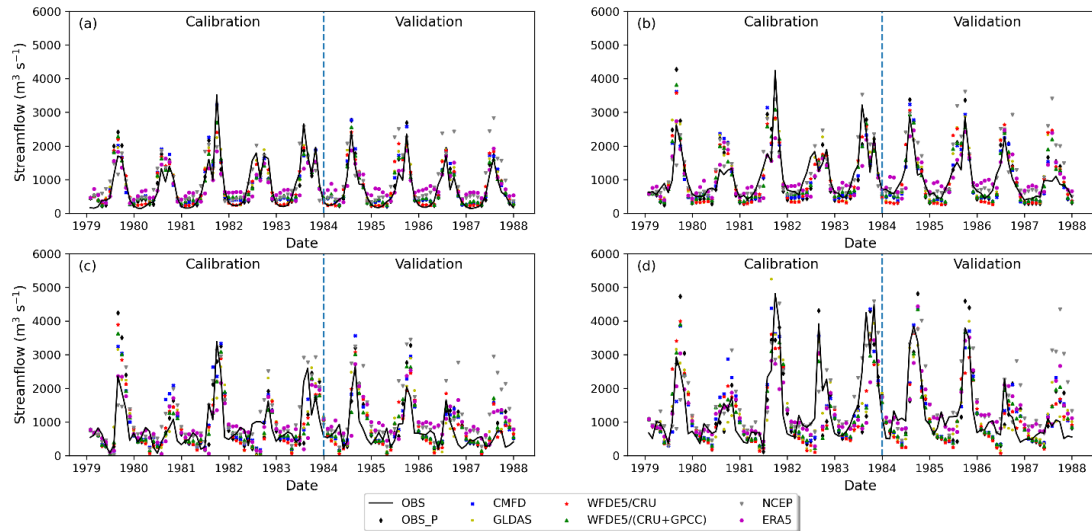
highest mean NSE and mKGE values of the four stations, consistent with our statistical comparison discussed in the previous text.



**Figure 5.8:** Comparison of monthly streamflow simulated by offline AHMS-IRR with gauge-calibrated parameters (Scenario 1). The comparison includes seven different precipitation products against observed monthly streamflow at all four main hydrological stations, i.e., Tangnaihe (a), Lanzhou (b), Toudaoguai (c) and Huayuankou (d). The calibration period ranges from January 1, 1979, to December 31, 1983, while the validation period spans from January 1, 1984, to December 31, 1987. Note that OBS represents the observed streamflow, while OBS\_P represents the streamflow simulated using the gauged precipitation.

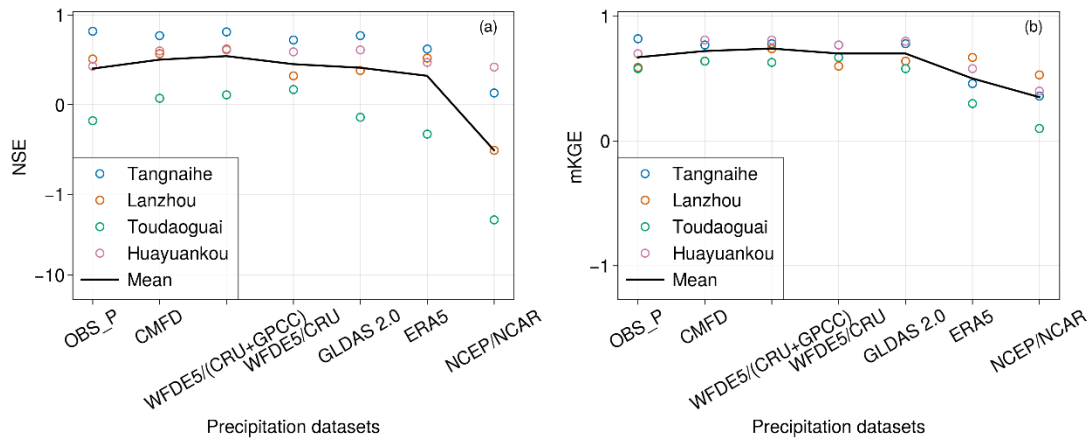


**Figure 5.9:** Performance of streamflow simulations forced by seven different precipitation products using the static rainfall-runoff parameters during the validation period (Scenario 1). (a) NSE, (b) mKGE.

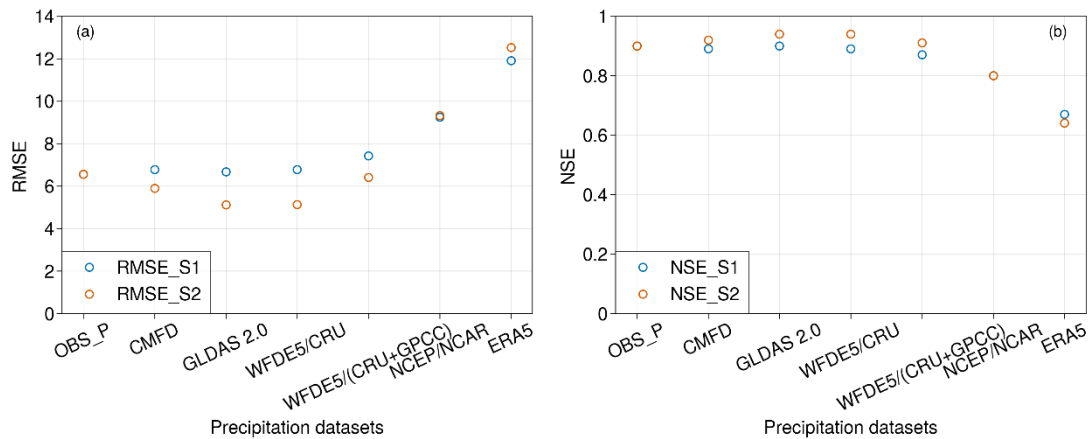


**Figure 5.10:** Same as in Fig. 5.8 but with product-specific calibrated parameters for each of the seven precipitation products (Scenario 2).

Fig. 5.10 compares simulated and observed monthly streamflow, where the simulated values were obtained from the hydrological model run with recalibrated parameters. Furthermore, Fig. 5.11 and Table C.6 in the Supplement show the model performance (NSE and mKGE) associated with the different precipitation products in Scenario 2. The recalibration of the rainfall-runoff model substantially improved the model performance for all precipitation products compared to the results of Scenario 1 (Fig. 5.9). The improvement in model performance was particularly notable for models using gauge-corrected reanalysis precipitation datasets. For the validation period considered in the present work, the gauge-corrected reanalysis precipitation datasets, including WFDE5/(CRU+GPCC) and CMFD, demonstrated slightly better performance than other gauge-corrected products. However, non-gauge-corrected reanalysis precipitation datasets such as NCEP and ERA5 exhibited poorer performance than gauge-corrected datasets. Overall, the performance of all gauge-corrected reanalysis precipitation dataset products was similar.



**Figure 5.11:** Performance of offline AHMS simulations of streamflow forced by seven different precipitation products using the dynamic rainfall-runoff parameters during the validation period (Scenario 2). (a) NSE, (b) mKGE.



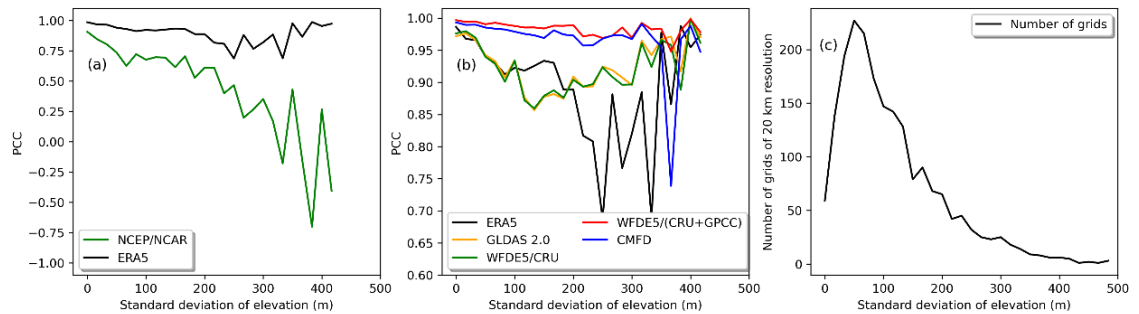
**Figure 5.12:** Performance of offline AHMS simulations in terms of evapotranspiration forced by seven different precipitation products using the static (Scenario 1 in blue) and dynamic (Scenario 2 in yellow) rainfall-runoff parameters during the validation period. (a) RMSE (mm), (b) NSE.

Fig. 5.12 displays the performance of the offline AHMS (RMSE and NSE) in predicting evapotranspiration by comparing it with the GLEAM results (Martens et al., 2017). The analysis is associated with the different precipitation products used in Scenarios 1 and 2. The results suggest that simulations driven by the non-gauge-corrected precipitation products significantly overestimated evapotranspiration. Moreover, the recalibration of the rainfall-runoff model led to an increase in runoff and an improvement in the evapotranspiration simulation for the gauge-corrected precipitation products, whereas it did not produce similar effects for the non-gauge-corrected precipitation products. Therefore, both Figs. 5.11 and 5.12 reveal that when the precipitation bias exceeded a specific threshold (e.g., ERA5 and NCEP/NCAR with  $\text{BIAS} \geq 45\%$ ), the calibration of the hydrological model was no longer valid in terms of improving the model's performance.

## 5.5 Discussions

### 5.5.1 Why Do the Non-gauge Corrected Reanalysis Datasets Overestimate the Precipitation in the Yellow River Basin?

Many previous studies concluded that the reanalysis dataset overestimates the observed precipitation in areas of complex terrain, which is consistent with the present study (see Fig. 5.1). Amjad et al. (2020) and Izadi et al. (2021) found that ERA5 consistently overestimated the observed precipitation over the mountainous areas of Turkey and Iran, while Jiang et al. (2022) reported that ERA5 tended to overestimate light precipitation events, especially in the mountainous area.



**Figure 5.13:** Pearson correlation coefficient (PCC) between (a) the average annual observed precipitation and (b) six reanalysis precipitation datasets with a standard deviation of elevation calculated in each 20-km grid over the Yellow River Basin. (c) The number of grids with a 20 km resolution and standard deviation of elevation over the Yellow River Basin.

There are two possible reasons for the overestimation of precipitation in areas with complex terrain. On the one hand, this overestimation may be due to the scarcity of weather stations in areas of complex terrain, where the limited observations do not capture precipitation patterns in sufficient detail (Jiao et al., 2021). On the other hand, the precipitation simulations in complex terrain areas are not accurate because the resolution of the precipitation simulation is relatively coarse in areas of complex terrain. Specifically, as discussed in previous work (Amjad et al., 2020; Izadi et al., 2021), the mechanisms of humidity injection and turbulence through land surface-atmosphere interactions in complex terrain areas are poorly understood. Furthermore, the lack of snow removal processes in the ERA5 simulation could lead to excessive snowfall and precipitation in the Tibetan Plateau region, according to Orsolini et al. (2019). These findings are consistent with the fact that the percentage errors of non-gauged-corrected precipitation products (ERA5 and NCEP/NCAR) were much larger in winter than in summer (see Figs. 5.6 and 5.7).

To analyse the effect of the complex topography of the Yellow River Basin on the quality of the reanalysis precipitation data, Pearson correlation coefficients (PCCs) were calculated between precipitation observations and individual reanalysis precipitation using the standard deviation of elevation and mean annual precipitation over the Yellow River Basin. According to Eq. 5.8, the standard deviation of elevation was calculated at a 20 km resolution and was based on a digital estimation model at a 1 km resolution (USGS 1K). As shown in Fig. 5.13a, the Pearson correlation coefficient between the average annual observed precipitation and NCEP/NCAR reanalysis precipitation decreased rapidly with the standard deviation of elevation, while ERA5 precipitation maintained a highly stable correlation with the observed data. This behaviour was most likely due to the higher resolution of ERA5 ( $2.5^\circ$  of NCEP and  $0.25^\circ$  of ERA5) and the advanced 4d-Var data assimilation system of ERA5. Surprisingly, as the standard deviation of elevation increased ( $>230$  m), the Pearson correlation coefficient for ERA5 also slightly increased and fluctuated, which was also observed in the gauge-corrected reanalysis precipitation datasets (see Fig. 5.13b). As shown in Fig. 5.13c, this behaviour may be explained by the fact that grids with higher standard deviation elevations are scarce. Furthermore, Fig. 5.13b shows that the gauge-corrected reanalysis precipitation data maintained a stable correlation with the observed data as the standard deviation of elevation changed compared with the non-gauge-corrected reanalysis precipitation datasets. Specifically, WFDE5/(CRU+GPCC) and CMFD performed better than GLDAS 2.0 and WFDE5/CRU.

Considering the influence of complex terrain on precipitation simulations, the simulation grid for future climate modelling should be refined in areas of complex terrain to reach a pre-defined threshold of the standard deviation of elevation (Bacon et al., 2000; Dietachmayer, 1992). This refinement process improves the simulation of precipitation in areas with complex terrain without wasting computing capacity (Skamarock & Klemp, 2008).

### 5.5.2 Why Do CMFD and WFDE5/(CRU+CRU) Agree the Best with the Precipitation Observations?

The difference in the performances of gauge-corrected and uncorrected reanalysis precipitation datasets is related to the algorithms used and the number of assimilated rain gauges. Furthermore, during the study period (1979~1989), only some weather stations from CMA were shared globally through the Global Telecommunications System (GTS). Fig. 5.14 shows the distribution of a total of 82 CMA weather stations in the Yellow River Basin, including 22 national benchmark climate stations shared worldwide through the GTS and the other 60 national ordinary stations not shared via GTS. This is an important reason why the gauge corrected reanalysis precipitation datasets (WFDE5/CRU and GLDAS 2.0) underestimated the annual precipitation compared with gauge observations and explained why CMFD and WFDE5/(CRU+GPCC) agreed the best with the precipitation observations.

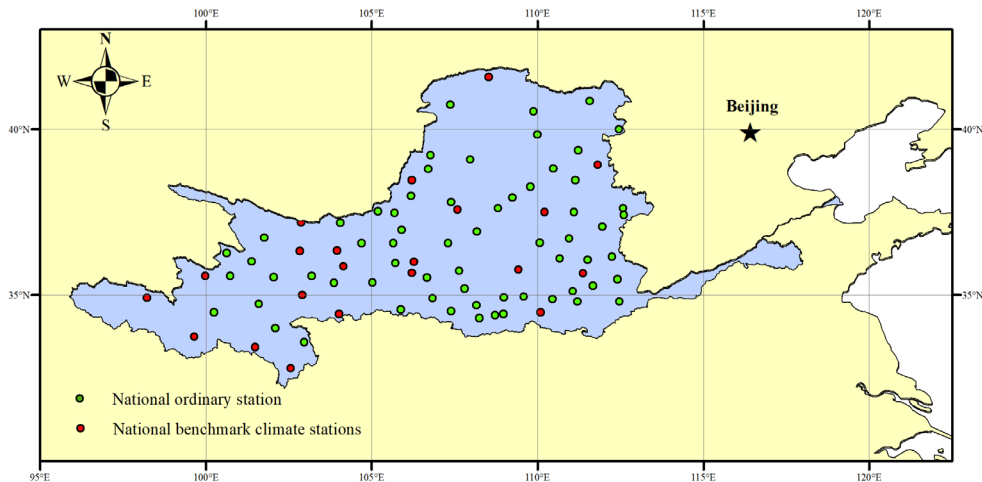


**Figure 5.14:** Distribution of weather stations of the China Meteorological Administration in the Yellow River Basin (upstream of HYK station). Twenty-two national benchmark climate stations are shared worldwide through the Global Telecommunication System (GTS) (red points), and the other 60 national ordinary stations (green points) are not shared through the GTS.

Specifically, CMFD and WFDE5/(CRU+GPCC) employed a more significant number of stations than WFDE5/CRU and GLDAS 2.0. According to He et al. (2020) and Yu et al. (2020), the CMFD uses approximately 753 stations across China, including 82 stations over the Yellow River Basin, while WFDE5/(CRU+GPCC) essentially assimilates the same stations. In contrast, only approximately 300 stations across China and 22 stations over the Yellow River Basin, shared by the Global Telecommunications System (GTS), have been incorporated to derive the

WFDE5/CRU and GLDAS 2.0 datasets. In this study, we found that WFDE5/CRU slightly underestimated the observed annual precipitation, which was consistent with the observations of Shi et al. (2017). These authors also concluded that the CRU TS dataset underestimated precipitation over the three-river headwaters region of China.

### **5.5.3 How Do We Constrain Model Uncertainty and Quantify Anthropogenic Influences on Streamflow in This Study?**

In this study, we employed an offline AHMS-IRRIG and measured water discharge to assess (non-) gauge-corrected precipitation reanalysis. Although the use of offline AHMS-IRRIG and measured water discharge provides us with an additional dimension for assessing precipitation, it is associated with additional uncertainties related to the parameters of the rainfall-runoff model and the flow routing model. Therefore, to reduce model uncertainty as much as possible, we recalibrated the rainfall-runoff model separately with each meteorological forcing data in the present study. In addition, we used two evaluation metrics to evaluate model performance, i.e., the Nash-Sutcliffe model efficiency coefficient (NSE) and the modified Kling-Gupta efficiency (mKGE) (Gupta et al., 2009; Kling et al., 2012). Hereby, we focused on the agreements between the observed and simulated streamflow peak and correlation, bias and variability.

Furthermore, anthropogenic factors such as irrigation play an important role in hydrological processes and profoundly impact the water balance in arid and semi-arid basins such as the Yellow River Basin. To quantify anthropogenic influences, we used the recently introduced and extended offline AHMS-IRRIG that applies to arid and semi-arid regions by explicitly considering the effects of irrigation on hydrological processes (Jiang et al., 2022). The extended offline AHMS-IRRIG integrates a new irrigation module, which computes the dynamic irrigation demand into the modified land surface, flow routing and groundwater models. This new extended offline AHMS-IRRIG explicitly represents anthropogenic processes, such as irrigation, which significantly impact the water balance in the arid and semi-arid areas of the Yellow River Basin.

## **5.6 Summary and Conclusions**

In this study, the performance of six precipitation reanalysis products widely used within the hydrology community was evaluated against gridded gauge precipitation

and observed streamflow using offline AHMS-IRR with consideration of irrigation and focused on the Yellow River Basin as a case study. Specifically, the six precipitation products were evaluated, including two non-gauge-corrected reanalysis products (NCEP/NCAR and ERA5) and four gauge-corrected reanalysis products (GLDAS 2.0, WFDE5/CRU, WFDE5/(CRU+GPCC) and CMFD). We compared the performance of various products based on annual, seasonal and monthly precipitation observation statistics. Furthermore, we compared streamflow observations at the four main hydrological stations along the Yellow River with corresponding predictions using the recently introduced regional hydrological model (Jiang et al., 2022). Hereby, each precipitation dataset constituted the forcing meteorological field for the offline AHMS-IRR simulation, considering two model setups with static and dynamic parameters of the rainfall-runoff model.

The main findings of our study can be summarized as follows:

- 1) According to the comparison of the magnitude and distribution of the annual, seasonal, and monthly mean precipitation with the observed data, the CMFD had the best agreement with the measured data, followed by WFDE5/(CRU+GPCC). The hydrological comparison of the six reanalysis precipitation products considered in our analysis also showed better model performance using gauge-corrected reanalysis precipitation datasets than non-gauge-corrected datasets. Furthermore, the simulated streamflow driven by CMFD and WFDE5/(CRU+GPCC) matched the observed streamflow the best based on the NSE and mKGE evaluation metrics. This is because the CMFD and WFDE5/(CRU+GPCC) combine more rain gauges (273% more stations) than the other precipitation products (WFDE5/CRU and GLDAS 2.0) in the Yellow River Basin and have very high spatial resolutions of  $0.1^\circ$  and  $0.5^\circ$ , respectively.
- 2) Non-gauge-corrected reanalysis precipitation datasets (NCEP/NCAR and ERA5) significantly overestimated precipitation by 50% and 45% on an annual mean scale in the Yellow River Basin. In terms of spatial distribution, the non-gauge-corrected reanalysis precipitation datasets overestimated precipitation, especially in complex terrain-mountain areas. Possible reasons for the overestimation of precipitation in mountainous areas include limited precipitation observations in the mountain areas, deficiencies in rainfall generation parameterization scheme, a poor understanding of the mechanisms of humidity injection and turbulence through land surface-

atmosphere interactions and difficulties in representing snow removal processes. Furthermore, ERA5 performed much better than NCEP/NCAR, especially over the complex terrain of the Yellow River Basin, due to the much higher resolution of ERA5 and the advanced data assimilation system (4D-var).

3) The hydrological response in the Yellow River Basin is significantly influenced by the selection of the precipitation reanalysis dataset, and the proper calibration of the rainfall-runoff model can effectively compensate for deficiencies in available precipitation data. However, when precipitation bias exceeded a specific threshold (e.g., BIAS > 45% for NCEP/NCAR), the calibration of the hydrological model became invalid for improving the model performance.

To accurately model the hydrology of the Yellow River Basin, it is recommended to consider using CMFD or WFDE5/(CUR+GPCC) as near-surface meteorological variables. To improve the quality of reanalysis products in mountainous areas where stations are scarce, it is necessary to incorporate not only rain gauges shared by the Global Telecommunications System (GTS) but also national ordinary climate stations shared by the China Meteorological Administration (CMA). Additionally, precipitation simulations in mountainous regions can be improved through a better understanding and parameterization of land surface-atmosphere interactions and higher-resolution simulations. It is important to carefully calibrate the hydrological model to reduce dependence on the quality of precipitation input, which has significant impacts on the components of the water balance. This allows the model to provide more reliable predictions and assessments of water-related processes and phenomena. Therefore, the evaluation of these products not only contributes to future development and uncertainty analysis for hydrological modelling applications in the Yellow River Basin but also has the potential to significantly enhance Earth system simulations and climate modelling across various lengths and time scales.

## 5.7 Data Availability Statement

NCEP/NCAR is available through the NOAA Physical Sciences Laboratory (PSL) <https://psl.noaa.gov/data/gridded/data.ncep.reanalysis.html>. ERA5, WFDE5/CRU and WFDE5/(CRU+GPCC) are available through the Climate Data Store, <https://cds.climate.copernicus.eu/>. CMFD is available through the China National Tibetan Plateau/Third Pole Environment Data Center,

<https://data.tpdc.ac.cn/en/data/8028b944-daaa-4511-8769-965612652c49/>. GLDAS 2.0 is available through the NASA Goddard Earth Sciences (GES) Data and Information Services Center (DISC), <https://disc.gsfc.nasa.gov/>. Daily water discharge of Yellow River at four hydrological stations, including Tangnaihe, Lanzhou, Toudaoguai, and Huayuankou, are available on request from the National Geographic Resource Science SubCenter, the National Earth System Science Data Center, and the National Science & Technology Infrastructure of China (<http://gre.geodata.cn>). Statistical irrigation data in the Yellow River Basin during the study period can be obtained from Jia et al. (2006) and be downscaled to annual data (Jiang et al., 2022) according to the Yellow River Bulletin of Water Resources from 2000 to 2009, published by the Yellow River Conservancy Commission (YRCC) of the Ministry of Water Resources of China (<http://www.yrcc.gov.cn/other/hhgb/>). Simulation data of AHMS-IRRIG in the Yellow River Basin will be made available on request.

## 6 Development and Application of AHMS-SED to the Yellow River Basin with Consideration of Gully Erosion

This chapter is part of the manuscript being prepared for submission.

**Cong Jiang**<sup>a, \*</sup>, **Eric J. R. Parteli**<sup>b</sup> and **Yaping Shao**<sup>a</sup>

<sup>a</sup>*Institute for Geophysics and Meteorology, University of Cologne, Pohligstr. 3, Cologne, 50969, North Rhine-Westphalia, Germany*

<sup>b</sup>*Faculty of Physics, University of Duisburg-Essen, Duisburg, Lotharstr. 1, 47057, North Rhine-Westphalia, Germany*

### Authors contributions to this publication

**Cong Jiang:** Formal analysis, Methodology, Software, Validation, Writing-Original Draft, Writing - Review & Editing.

**Eric J.R. Parteli:** Conceptualization, Supervision, Funding acquisition, Writing-Review & Editing.

**Yaping Shao:** Conceptualization, Supervision, Funding acquisition, Writing-Review & Editing, Resources.

### Reference

Jiang, C., Parteli, E. J. & Shao, Y. A model for continental-scale water erosion and sediment transport and its application to the Yellow River Basin

## 6.1 Introduction

This Chapter addresses the main task of this thesis by developing and applying a water erosion and sediment transport model in the Yellow River Basin. As mentioned in section 1.3.3, this study is motivated by the need to develop an advanced soil erosion and sediment transport model that can be applied to regional-scale hydrological processes, with a particular focus on addressing the critical issue of gully erosion, which holds considerable relevance in the context of the Chinese Loess Plateau (Osterkamp & Toy, 1997). The present study addresses the following key science questions:

- I. How to model upland sediment detachment and transport capacity in a large-scale hydrological model? Which erosivity predictors based on rainfall, runoff or overland flow perform best?
- II. How can a large-scale model incorporate gully erosion and the concatenated sediment supply?
- III. What scale effects, such as decaying precipitation and slope with decreasing spatial and temporal resolution, need to be considered when building the large-scale erosion and sediment transport model?

## 6.2 Data

### 6.2.1 Near Surface Meteorological Data

The high spatial-temporal resolution gridded China Meteorological Forcing Dataset (CMFD) (He et al., 2020) is adopted as the near-surface meteorological input dataset driving the land surface model. The associated variables include precipitation, near-surface air temperature, near-surface specific humidity, surface pressure, near-surface wind, surface downwelling shortwave and longwave radiation.

### 6.2.2 Geo-static Data

The digital elevation model, including the information about hydrological systems in the study area, is used as the input variable for the flow and sediment routing model. Specifically, the high-resolution geographic digital elevation data set Multi-Error-Removed Improved-Terrain DEM (MERIT) with a 3sec resolution (Yamazaki et al., 2019) is used and upscaled to the model resolution by using an HMS pre-processing

program (Yu et al., 2006). The slope is calculated based on 30 m resolution DEM SRTM (Farr et al., 2007) and then interpolated to 20 km resolution using the four-point bilinear interpolation method and the WRF Preprocessing System (WPS). USGS soil type and USGS vegetation type maps are interpolated to the model resolution with the help of WPS.

The soil erodibility factor  $K_{usle}$  is calculated using Eq. 3.19, while the gully area index is obtained using Eq. 3.23. Also, the clay content is obtained from a 30 arc-seconds resolution soil particle-size distribution dataset for regional land and climate modelling by Shangguan et al. (2012). Furthermore, a basic boundary map of rich sediment areas in the middle reaches of the Yellow River Basin, i.e., the area with sediment transport modulus greater than  $5000 \text{ tons km}^{-2} \text{ yr}^{-1}$  and extensive distribution of permanent gullies.

### **6.2.3 Measured River Discharge and Suspended Sediment Concentration**

In order to calibrate and validate the model predictions for the water and sediment discharge, we employ the daily measured water discharge ( $\text{m}^3 \text{ s}^{-1}$ ) and suspended sediment concentration ( $\text{kg m}^{-3}$ ) for the period 1979-1987 from the National Earth System Science Data Centre, China, including the five major stations along Yellow River, namely Tangnaihe (a), Lanzhou (b), Toudaoguai (c), Longmen (d) and Huayuankou (e). The method for measuring the concentration of suspended sediment at river locations involves collecting instantaneous bucket samples to determine the river water volume-averaged concentration.

## **6.3 Model Configuration and Experimental Design**

### **6.3.1 Model Configuration**

The offline AHMS-SED is set up for modelling hydrological and sediment transport processes in the Yellow River Basin, as described in the following paragraphs.

The spatial and temporal resolutions of the offline AHMS-SED are 20 km and 60 min, respectively. Here, we focus on streamflow simulations around the 1980s, i.e., the early years preceding the construction of the dams, since our model currently does not consider the role of dams and reservoirs in regulating river flow and suspended sediment. Furthermore, to reach the equilibrium conditions of the model, several decades of climatological spin-up are performed under constant geo-static

data and applied cyclic forcing (in the 1980s) before the numerical experiments are performed. As seen in Fig. 6.1, the geo-static variables are re-gridded into the modelled domain in the Yellow River Basin and the gully area index distribution is closely related to the rich sediment areas and permanent gullies (Fig. 6.1f). The parameters of the model are selected from the land surface, river routing, groundwater model, water erosion and sediment transport models.

### 6.3.2 Hydrological Modelling Parameters

Based on the offline AHMS-IRRIG sensitivity analysis, the sensitive hydrological parameters selected in this study include the soil saturated hydraulic conductivity, channel width and depth, hydraulic conductance of riverbed, riverbed fraction and Manning's roughness coefficients, irrigation-triggered soil water availability and triggered leaf area (Jiang et al., 2022). Jiang et al. (2022) calibrated and validated the regional hydrological model of the Yellow River Basin with consideration of irrigation by comparing observed and predicted water discharge, evapotranspiration and terrestrial water storage change using in situ, satellite and assimilated data. A summary of the physical and control parameterization schemes used in the land surface model (Noah-MP) is listed in Table B.2 in Appendix B.

### 6.3.3 Water Erosion and Sediment Transport Model Parameters

Three parameters within the erosion and sediment transport module of AHMS-SED are selected for the parameter sensitivity analysis. These three parameters are the empirical parameter in the gully factor equation ( $\alpha$ ), the scaling parameter in the overland flow transport capacity equation ( $e_1$ ) and the no-tillage parameter in the crop factor equation ( $f_{\text{no-till}}$ ).

We calibrate the offline AHMS-SED against the observed average sediment yields at the HYK station from 1 Jan 1979 to 31 Dec 1983. Therefore, the offline AHMS-SED is validated by comparing the observations and predictions of monthly sediment fluxes at five hydrological stations from 1 Jan 1984 to 31 Dec 1987.

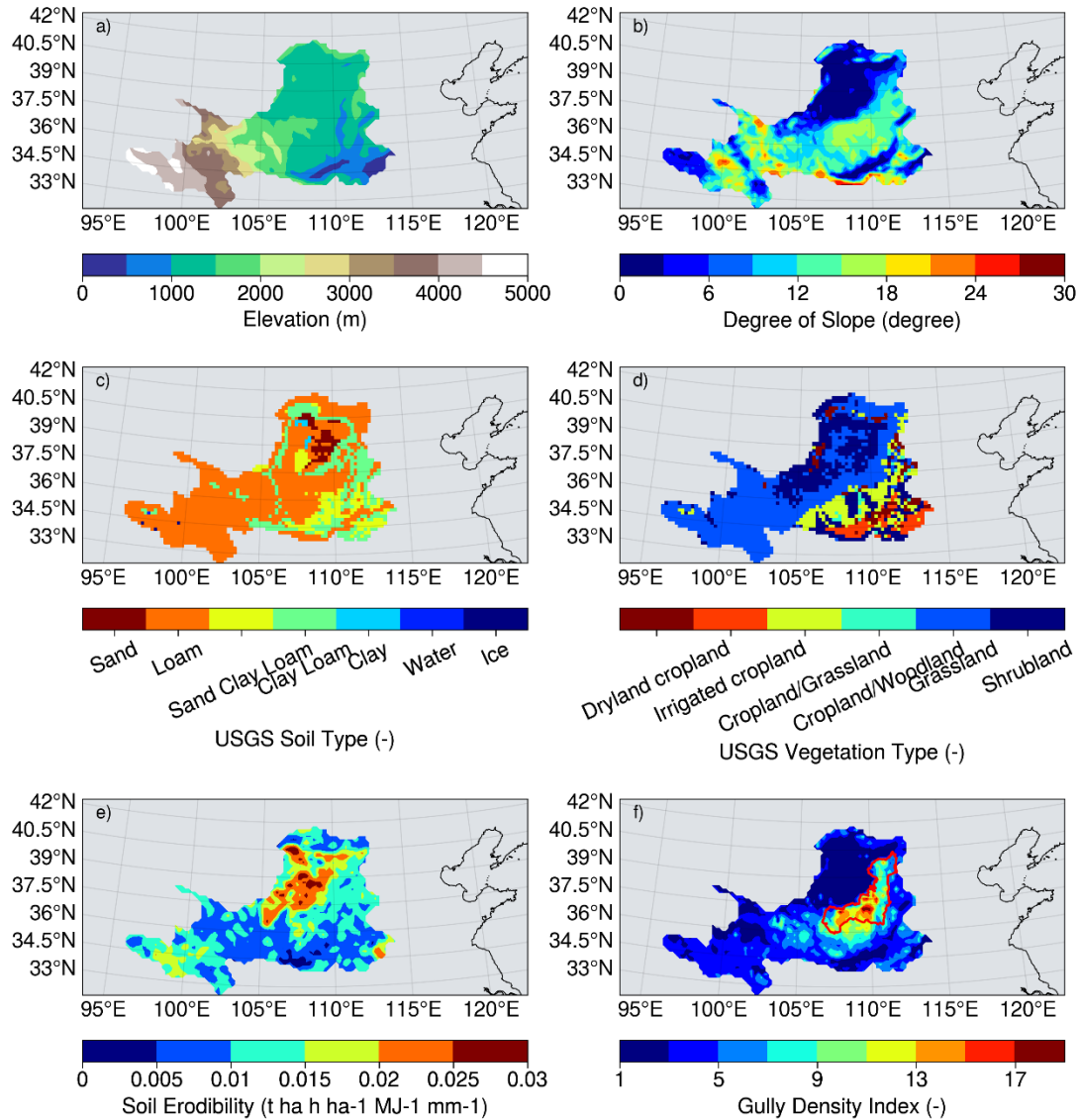


**Figure 6.1:** The input geo-static data include elevation (a), slope (b), soil type (c), vegetation type (d), soil erodibility (e) and gully area index (f) for the Yellow River Basin. In subplot (f), the red line represents sediment source hotspots in the middle reaches of the Yellow River, the Loess Plateau of China.

### 6.3.4 Experimental Design

As shown in Table 6.1, 23 numerical experiments and associated parameters are designed to calibrate and validate AHMS-SED. For each experiment, the simulation periods are from 1 Jan 1979 to 31 Dec 1983 for calibration and 1 Jan 1984 to 31 Dec 1987 for validation. Numerical experiments are categorized into Ensembles I, II and III to examine the different sediment transport equations based on rainfall, runoff and overland flow, respectively, as predictors of erosivity for upland erosion. A parameter sensitivity study is then performed for different ensembles to elucidate the significance of gully and crop factors on the model predictions. Moreover, EXPs 1-3

are conducted to evaluate the models of transport capacity for overland flows using the different rainfall-based revisions of USLE erosivity (USLE, USLE-M and USLE-MM). In particular, all the experiments use the same relevant sediment modules, including the sediment routing module and the equations for sediment transport capacity and deposition velocity.

**Table 6.1:** Experimental design to evaluate the different sediment transport capacity equations for overland flow

	Experiments	Description	Rainfall or runoff factor	Slope term	Scaling $e_1$	Gully factor $\alpha$	$f_{no-til}$	$K_{usle}$ , and $P$
<b>I</b>	EXP 1	USLE	$EI_{30}$	$20S^{1.25}$	38	0.3	0.25	Eq. (3.19) and 1.0
	EXP 2	USLE-M	$Q_R EI_{30}$		77			
	EXP 3	USLE-MM	$(Q_R EI_{30})^{1.55}$		24			
<b>I</b>	EXP 4	USLE Rainfall	$EI_{30}$		129	0.2	0.1	
	EXP 5				65	0.3	0.1	
	EXP 6				27	0.4	0.1	
	EXP 7				230	0.0	0.25	
	EXP 8				81	0.2	0.25	
	EXP 9				15	0.4	0.25	
<b>II</b>	EXP 10	KR-1 Runoff	$q^{2.0}$	$S^{1.66}$	2.4e4	0.3	0.25	
	EXP 11				1.3e5	0.0	0.25	
	EXP 12				4.7e4	0.2	0.25	
	EXP 13				9.8e3	0.4	0.25	
	EXP 14				7.8e4	0.2	0.1	
	EXP 15				4.1e4	0.3	0.1	
	EXP 16				1.8e4	0.4	0.1	
<b>III</b>	EXP 17	KR-2 Flow	$q^{2.0}$		7.2e6	0.3	0.25	
	EXP 18				3.1e7	0.0	0.25	
	EXP 19				1.3e7	0.2	0.25	
	EXP 20				3.6e6	0.4	0.25	
	EXP 21				1.9e7	0.2	0.1	
	EXP 22				1.1e7	0.3	0.1	
	EXP 23			5.8e6	0.4	0.1		

### 6.3.5 Model Performance Evaluation Indices

The model performance is evaluated by using the following metrics: the Nash–

Sutcliffe model efficiency coefficient (NSE) (Nash & Sutcliffe, 1970), Pearson correlation coefficient (PCC), sediment balance index (SBI) and modified Kling-Gupta efficiency (mKGE). These performance metrics are defined as follows.

$$\text{NSE} = 1.0 - \frac{\sum_{i=1}^N (P_s^i - P_o^i)^2}{\sum_{i=1}^N (P_o^i - \bar{P}_o)^2} \quad (6.1)$$

$$\text{PCC} = \frac{\sum_{i=1}^N (P_o^i - \bar{P}_o)(P_s^i - \bar{P}_s)}{\sqrt{\sum_{i=1}^N (P_s^i - \bar{P}_s)^2 (P_o^i - \bar{P}_o)^2}} \quad (6.2)$$

$$\text{SBI} = \frac{\sum_{i=1}^N P_s^i}{\sum_{i=1}^N P_o^i} \quad (6.3)$$

$$\text{mKGE} = 1 - \sqrt{(\text{PCC} - 1)^2 + (\beta - 1)^2 + (\gamma - 1)^2}$$

$$\beta = \text{bias ratio} = \frac{\mu_s}{\mu_o} \quad (6.4)$$

$$\gamma = \text{variability ratio} = \frac{\sigma_s / \mu_s}{\sigma_o / \mu_o}$$

where  $P_s$  and  $P_o$  are the simulated and observed values of the  $P$  variable, respectively, and  $\bar{P}_o$  is the mean value of  $P_o$ ,  $\mu_s$  and  $\mu_o$  denote the mean of the predicted and observed values, respectively, while  $\sigma_s$  and  $\sigma_o$  denote the corresponding standard deviations.

## 6.4 Results

### 6.4.1 Model Calibration and Validation

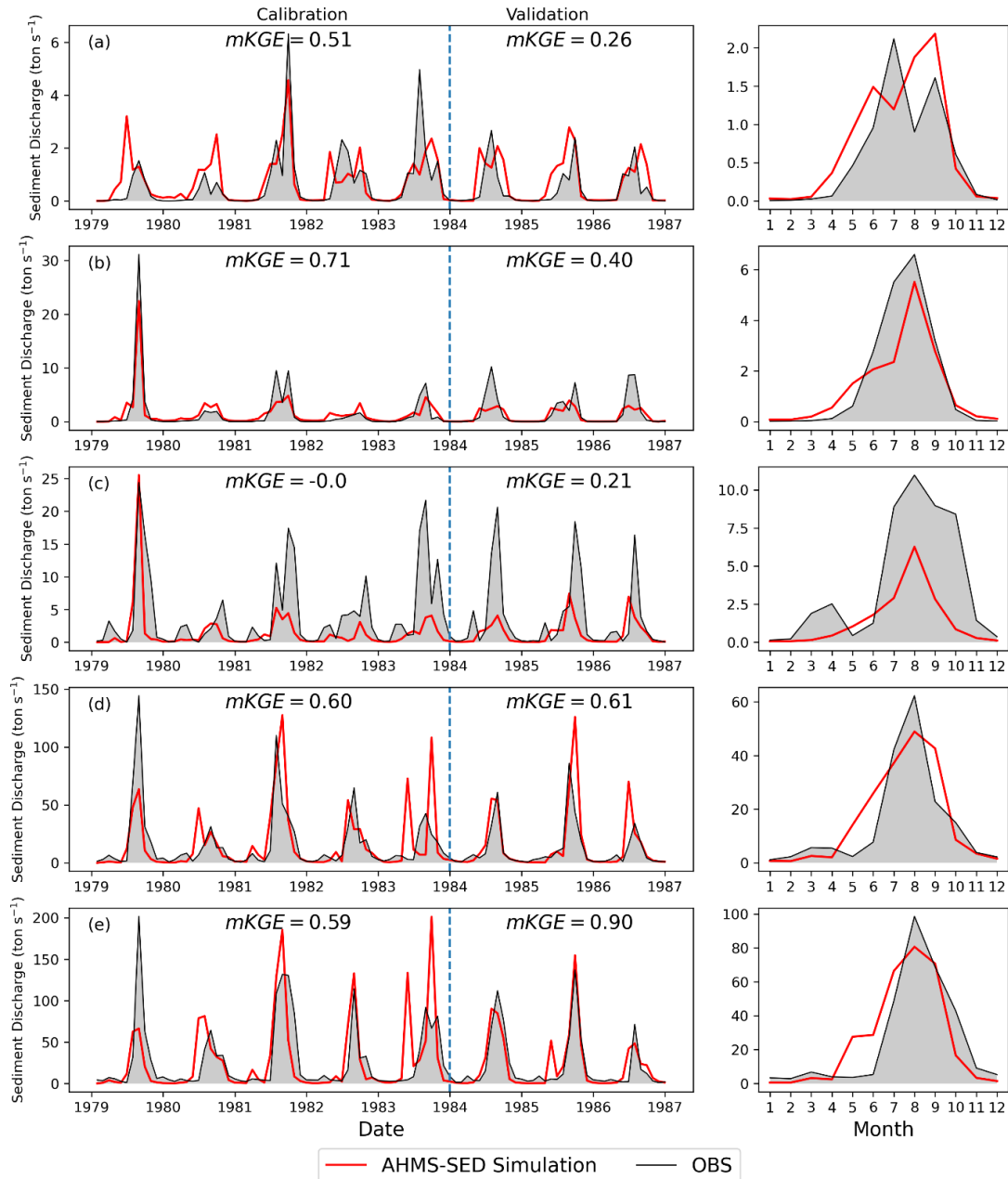


**Figure 6.2:** Comparison of observed and predicted monthly suspended sediment discharge at the five hydrological stations: TNH (a), LZ (b), TDG (c) and HYK (d). HYK corresponds to the midstream outlet. Results of EXP 1 are shown here, and the upland erosion equation is based on USLE rainfall erosivity ( $EI_{30}$ ). Note that the range of the y-axis is not the same for the five subplots.

As shown in Fig. 6.2 and Table 6.2, the observed and predicted sediment fluxes for all stations during the calibration and validation periods are quantitatively consistent, including fluctuations and averages, except for the underestimation of sediment fluxes at the TDG station. In particular, excellent agreement between the predictions and observations ( $mKGE = 0.90$ ) is obtained at the outlet of the middle reaches in the Yellow River Basin (HYK station). Consistent with the observations in Fig. 6.2, the simulated sediment fluxes at TNH, LZ and TDG are relatively small compared with

their counterparts at LM and HYK, with a maximum peak of approximately 20 t/s.

**Table 6.2:** Statistical evaluation for the suspended sediment discharge, predicted by the model, based on corresponding observations at five hydrological stations.

	Calibration period (1979–1983)					Validation period (1984–1986)				
	Mean obs (Mt a <sup>-1</sup> )	Mean sim (Mt a <sup>-1</sup> )	NSE	mKGE	SBI	Mean obs (Mt a <sup>-1</sup> )	Mean sim (Mt a <sup>-1</sup> )	NSE	mKGE	SBI
TNH	20.6	23.5	0.35	0.51	1.14	14.0	20.4	- 0.15	0.26	1.57
LZ	49.9	47.7	0.83	0.71	0.96	53.8	31.3	0.35	0.42	0.63
TDG	127.3	46.0	0.16	-0.00	0.36	109.0	38.0	0.08	0.21	0.38
LM	514.1	517.8	0.17	0.60	1.01	368.1	477.5	0.08	0.61	1.27
HYK	868.5	865.7	0.11	0.59	1.00	666.0	681.7	0.81	0.90	1.04

#### 6.4.2 Large Permanent Gully Erosion

TDG-LM sub-basin is characterized by large permanent gully activity and severe concatenated erosion processes, which provide the Yellow River with large amounts of sediment. Therefore, in order to validate the gully area factor, it is necessary to consider the long-term averaged sediment yield predicted by the model for the different sub-basins: HW-TNH, TNH-LZ, LZ-TDG and TDG-HYK.

As seen in Fig. 6.3, in the absence of the gully factor, the model underestimates the sediment yields in Sub-basin 4 (TDG-LM) and overestimates the sediment yields in gully-free sub-basins 1 and 2. According to our model results, Sub-basin 3 is an area of net deposition. Therefore, crop-induced erosion may have been underestimated in this area. We will further discuss this matter later in Section 6.4.3. As can be seen in Fig. 6.4, the predicted sediment transport capacity of overland flow and net eroded and deposited soils agree well with the observed large permanent gully area. Furthermore, we find that the model overestimates sediment yield in areas without gullies, particularly in steep areas (see Fig. 6.4b).

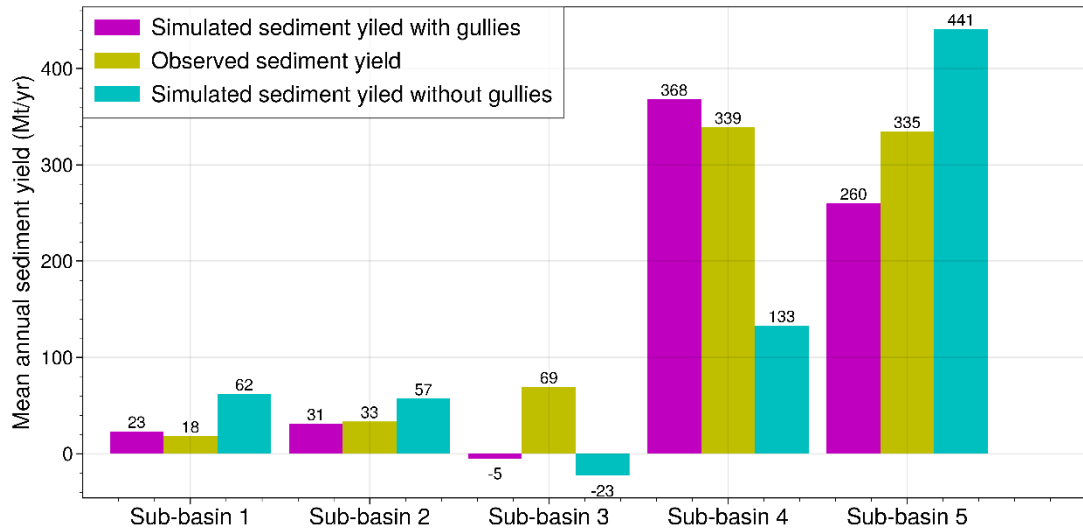


**Figure 6.3:** Simulation and corresponding observations of annual mean sediment yield averaged over 1979–1987 in the Yellow River. The simulations with and with the gully factor are EXP1 and EXP 7.

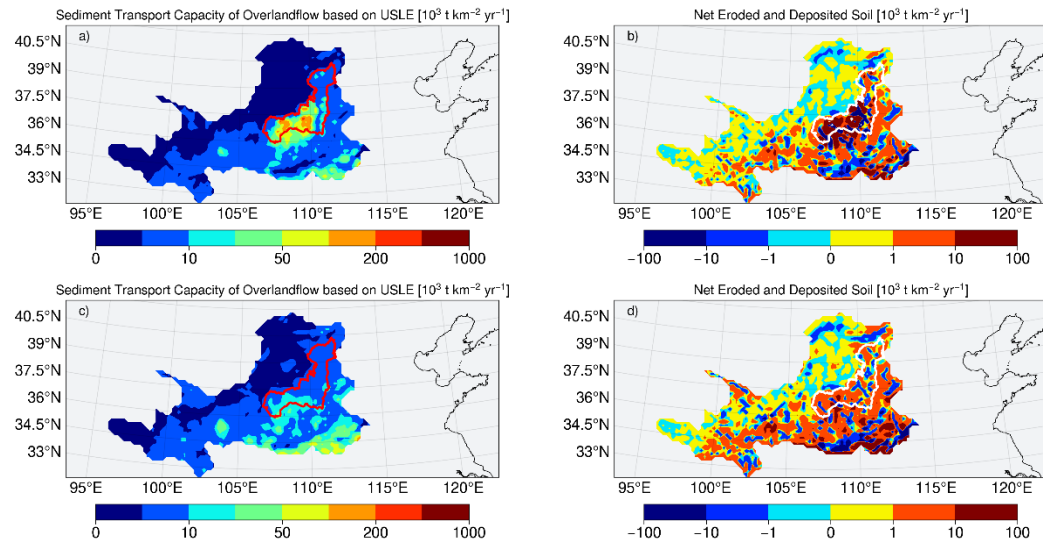


**Figure 6.4:** Spatial distribution of offline AHMS-SED simulated annual mean sediment transport capacity of overland flow, net eroded and deposited soil in the Yellow River over 1979–1987, subfigure (a) and (b) without the gully factor (EXP 1) while subfigure (c) and (d) with the gully factor (EXP 7).

### 6.4.3 Predicting Upland Sediment Discharge

Table 6.3 displays the ensemble modelling results for the suspended sediment discharge, considering the three ensembles I, II and III defined in Section 6.3.4, along with corresponding observations at five hydrological stations. The model performance evaluation indicators at the HYK stations show the best agreement and stability between simulated and corresponding observed data using USLE rainfall erosivity ( $EI_{30}$ ). This best agreement can be understood by noting that rainfall is still the most accurate variable inside large-scale watersheds, while runoff can be

predicted more accurately than overland flow.

Furthermore, as seen in Table 6.3 and Fig. D.1 in Appendix D as an example, we find that the model-predicted sediment yields based on the KR-runoff equation are overestimated in humid mountainous areas (at TNH and LZ), where subsurface runoff plays an important role in total runoff. Indeed, in the land surface model (Noah-MP), surface and subsurface runoff are not accurately distinguished in mountainous areas. As shown in Fig. D.2 in Appendix D, the overland flow-based KR equation function performs poorly in the simulation, particularly in extreme flood events. Overall, we find that consideration of the gully factor and USLE rainfall erosivity ( $EI_{30}$ ) over a time span of nearly one decade yields stable and accurate watershed sediment yields at the LM station (Table 6.3).

**Table 6.3:** Statistical evaluation of the modelling ensemble average of suspended sediment discharge obtained with the model along with corresponding observations at five hydrological stations.

Stations	Ensemble	Calibration period (1979–1983)					Validation period (1984–1986)				
		Mean obs (Mt a <sup>-1</sup> )	Mean sim (Mt a <sup>-1</sup> )	Mean NSE	Mean SBI	Mean mKGE	Mean obs (Mt a <sup>-1</sup> )	Mean sim (Mt a <sup>-1</sup> )	Mean NSE	Mean SBI	Mean mKGE
TNH	I		20.43	0.22	0.99	0.38		19.11	-0.29	1.37	0.23
	II	20.6	68.19	-5.90	3.31	-1.45	14.0	62.77	13.94	4.48	-2.57
	III		30.35	-2.48	1.47	-0.12		24.66	-2.96	1.76	-0.24
LZ	I		45.91	0.78	0.92	0.63		32.37	0.30	0.60	0.37
	II	49.9	119.18	-0.24	2.39	-0.47	53.8	96.21	3.26	1.79	-0.10
	III		201.01	50.39	4.03	-2.19		47.43	0.02	0.88	0.20
TDG	I		44.13	0.10	0.35	-0.10		39.42	0.06	0.36	0.19
	II	127.3	98.23	-0.01	0.77	0.33	109.0	79.21	0.22	0.73	0.32
	III		194.34	35.80	1.53	-2.28		35.79	-0.06	0.33	0.04
LM	I		482.40	0.16	0.94	0.56		435.59	-0.03	1.18	0.59
	II	514.1	450.69	-0.06	0.88	0.51	368.1	211.66	0.30	0.58	0.62
	III		446.41	-0.09	0.87	0.10		144.79	0.13	0.39	0.25
HYK	I		868.50	0.12	1.00	0.59		684.87	0.74	1.03	0.85
	II	868.5	861.26	-0.02	0.99	0.54	666.0	578.31	0.54	0.87	0.68
	III		869.95	-0.01	1.00	0.50		511.71	14.10	0.77	-0.05

#### **6.4.4 Model Prediction for the Evolution of Sediment Yields Under Specific Climate Change Scenarios in the Yellow River Basin**

The response of the water cycle and the transport of carbon, nutrients and sediments to climate change constitutes a topic of great interest to the scientific community and has significant implications for society (Chahine, 1992; Schlesinger & Bernhardt, 2020). These transformations in the water cycle and the concatenated changes in hydrological processes could lead to substantial enhancement of erosion and sediment discharge at the regional scale.

However, predicting climate-change-driven decadal evolution of sediment transport rates at the regional scale is challenging, owing to the broad range of atmospheric, hydrological, anthropogenic and geomorphological variables involved. Indeed, our coupled hydrological-atmospheric simulations incorporate both the effect of irrigation on hydrological processes (Jiang et al., 2022) and a comprehensive module for soil erosion processes at the continental scale. Therefore, given the good performance of our model in the validation tests discussed in Section 6.4.1, we conclude that our simulations provide meaningful estimates of the transport processes in the Yellow River Basin under plausible climate change scenarios.

Here, we predict the evolution of sediment discharge using the AHMS-SED model and historical meteorology data under specific climate change scenarios in the Yellow River Basin. We focused on predicting changes in sediment discharge using historical meteorological data in the 1980s because the model is well calibrated and validated during this period. The IPCC Scenario SSP2, "Middle of the road", with the temperature increase of 2 degrees by 2050, is considered here. As seen in Fig. 6.5, the results of experiments show that reducing precipitation intensity will significantly reduce sediment discharge of the Yellow River Basin. While a two-degree temperature increase only slightly reduces the sediment discharge. Increasing irrigation will also increase sediment deposition and decrease sediment discharge from the Yellow River.

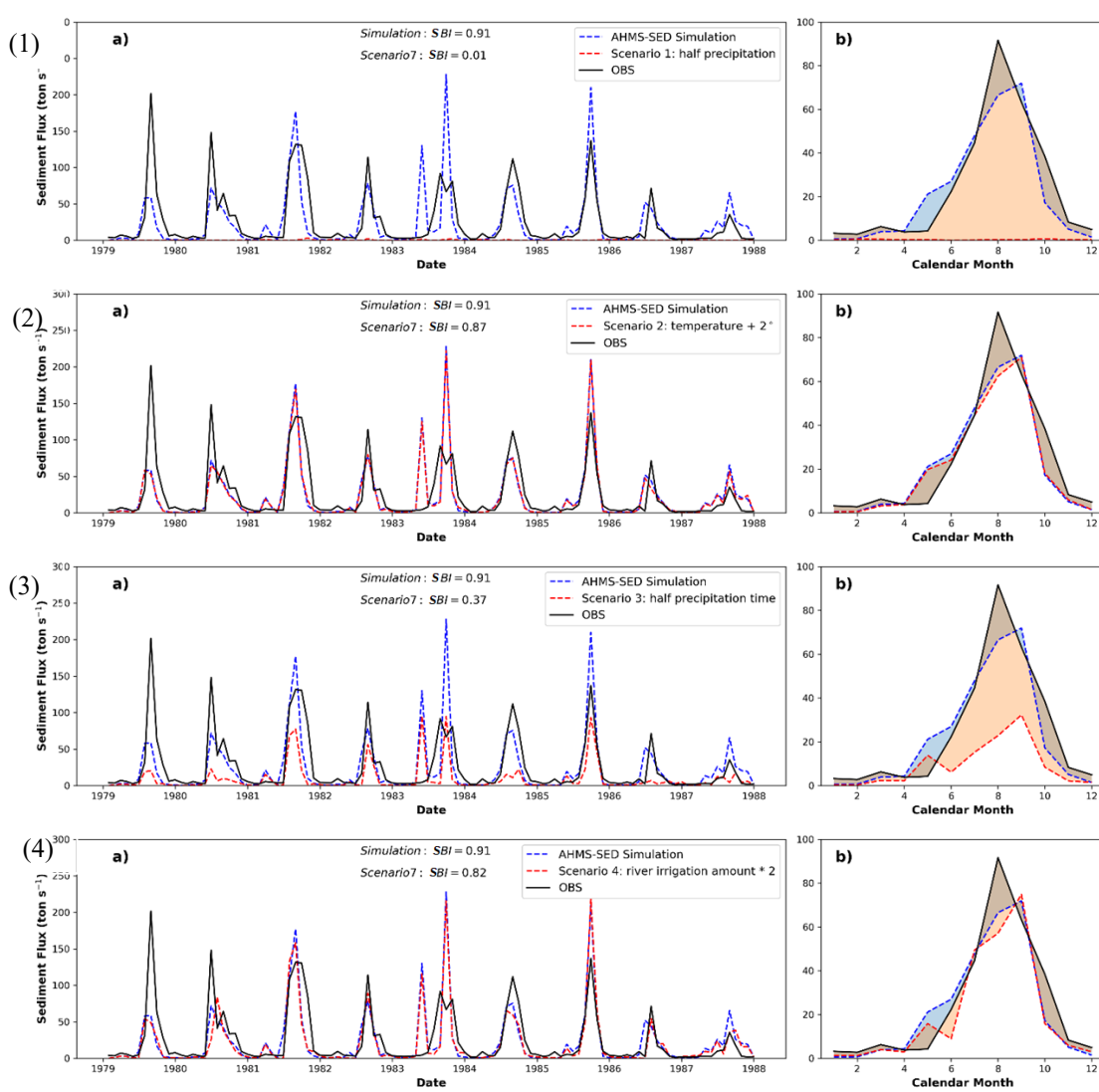


**Figure 6.5:** Comparison of (a) monthly and (b) averaged annual cycles of predicted (dashed lines), which are under (red) and not under (blue) specific climate change scenarios (Scenario 1, 2, and 3) and observed (solid line) sediment flux at the outlet of middle reaches of Yellow River Basin (Huayuankou station) for the period of 1979-1987. Subfigure (1) **Scenario 1:** precipitation halves, which means the precipitation rate is uniformly halved during the study period. Subfigure (2) **Scenario 2:** temperature rises by 2 degrees evenly during the study period. Subfigure (3) **Scenario 3:** precipitation time (or amount) is halved, which means no rainfall on the even days (1979.01.02, 1979.01.04, 1979.01.06, ...) during the study period. (4) **Scenario 4:** doubling the amount of river irrigation during the study period.

## 6.5 Discussions

### 6.5.1 Gully Factor vs. Slope Factor

The slope factor  $S$  (Eq. 3.20), as defined by Pelletier (2012), encodes information about sheet erosion and rill erosion but neglects the contribution from gully erosion to sediment sources in the upland. However, sediment input from gully erosion plays a major role in sediment load and transport in various hydrological basins (de Vente

& Poesen, 2005; Poesen et al., 2003; Poesen et al., 1996) and must be, thus, incorporated into the relationship between slope and upland sediment flux (Pelletier, 2012; Roering et al., 1999).

While previous attempts to incorporate gully erosion effects focused on a small (laboratory) scale, in the present study, we consider the contribution of gully erosion on a continental scale by introducing the gully area index as a parameter in the model (see Eq. 3.23). As indicated by the PCC in Fig. 6.6, there is a strong negative linear relationship between the slope factor ( $S$ ) and the gully area index ( $G_a$ ), especially for large values of the slope. This behavior can be understood by noting that gully erosion is not only related to the slope but also to climate and geological characteristics, the thickness of the topsoil and the proportion of rocks on the surface. Indeed, steep mountainous areas such as the Tibetan Plateau are characterized by little sediment yields compared to the Chinese Loess Plateau of the Yellow River Basin. The variable of the slope is, therefore, not a direct indicator of the intensity of gully erosion. By contrast, the gully area index represents the degree of surface fragmentation, i.e., gully density, and is, thus, a better indicator of gully erosion intensity.

We note that previous studies suffer from a lack of sound formulas and datasets on the density of large-scale gullies to characterize gully erosion. The gully area index introduced in the present study represents a novel descriptor of gully erosion and its contribution to sediment sources in hydrological and sediment transport process modelling at the continental scale. We propose that this gully area index is, indeed, the adequate parameter for regional hydrological and sediment transport modelling, as the slope factor, used in state-of-the-art models, suffers from the deficiencies discussed in the previous paragraph and is applicable to small (laboratory) scale hydrological systems only. In the future, application and evaluation of the gully area index to other watersheds, including different environments, landforms and climate forms., will be necessary to improve the development of regional water erosion and sediment modelling.

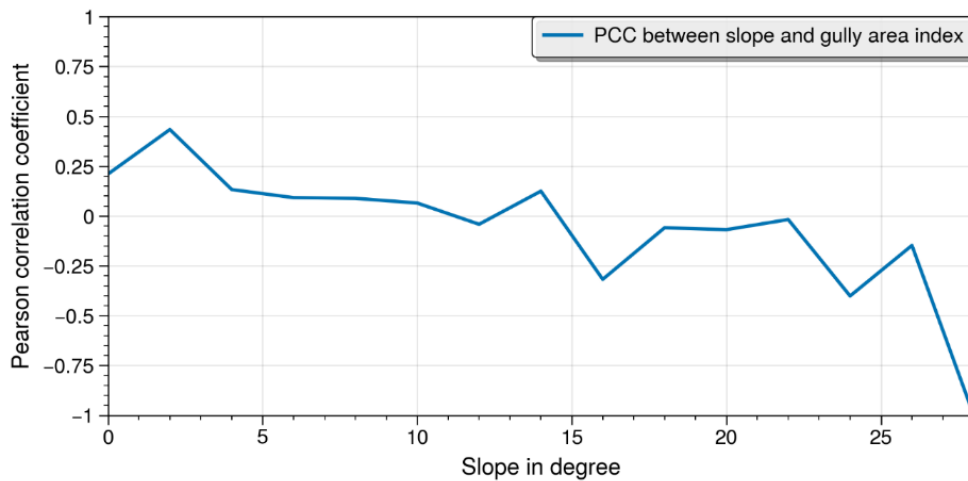


**Figure 6.6:** Pearson correlation coefficient (PCC) between slope and gully area index at 20 km resolution in the Yellow River Basin.

### 6.5.2 Scaling Issues

Scaling issues arise in any study that attempts to model hydrological behavior and related water erosion and sediment transport processes without resolving equations on every minor hillslope valley unit in the watershed (Yu et al., 2006). As Yu et al. (2006), the present investigation also deals with two different scaling issues related to large-scale water erosion and sediment transport modelling: (1) Downscaling climate forcing timescales from long time step (daily) to short duration (hourly) (2) Resolve upland sediment yield at a large-scale using grid cell sizes of one kilometer to several tens kilometers.

Regarding the first scaling issue, some researchers noted that the mean values of precipitation, when averaged over a large scale and long duration, may be substantially smaller than point precipitation. Therefore, following Yin et al. (2007), we derive the 30 mins maximum rainfall rate ( $I_{30}$ ) at a given hydrology grid cell by multiplying the LSM timestep averaged rainfall rate by a linear scaling-dependent parameter that increases with the LSM timestep. We choose the 30 mins time window since the timestep of the climate-forcing dataset is often larger than a half hour. We note that our models could be considered in future work, for instance, by incorporating a random variable that represents the stochastic properties of point precipitation.

Regarding the second scaling issue, the 20 km grid cell size applied in the present work is too coarse to resolve individual gullies and hillslopes, although it proved effective in simulating the hydrological and sediment transport process considered in

the calibration and validation tests (see Section 6.3.4). However, it is still an open question which grid scale should be used for predicting water erosion and sediment transport processes (Pelletier, 2012; Wood et al., 1988). Parameters associated with topography variables, such as slope, usually become rapidly small when grid resolution decreases. Moreover, a grid cell size of several kilometres may not resolve most of the spatial heterogeneities in rainfall, runoff and overland flow. In the present study, we introduced a linear scaling parameter for the decay of slope, rainfall, runoff or overland flow with decreased grid resolution. Overall, of the scaling parameter,  $e_1$  encodes information about rainfall or runoff and slope.

However, this explicitly scaling-dependent parameter increases as the grid resolution decreases. Therefore, in the future, similar to precipitation, it will be necessary to consider random variations at the sub-grid level to represent stochastic properties of runoff, overland flow or shear stress on the ground.

### 6.5.3 Cropland Erosion

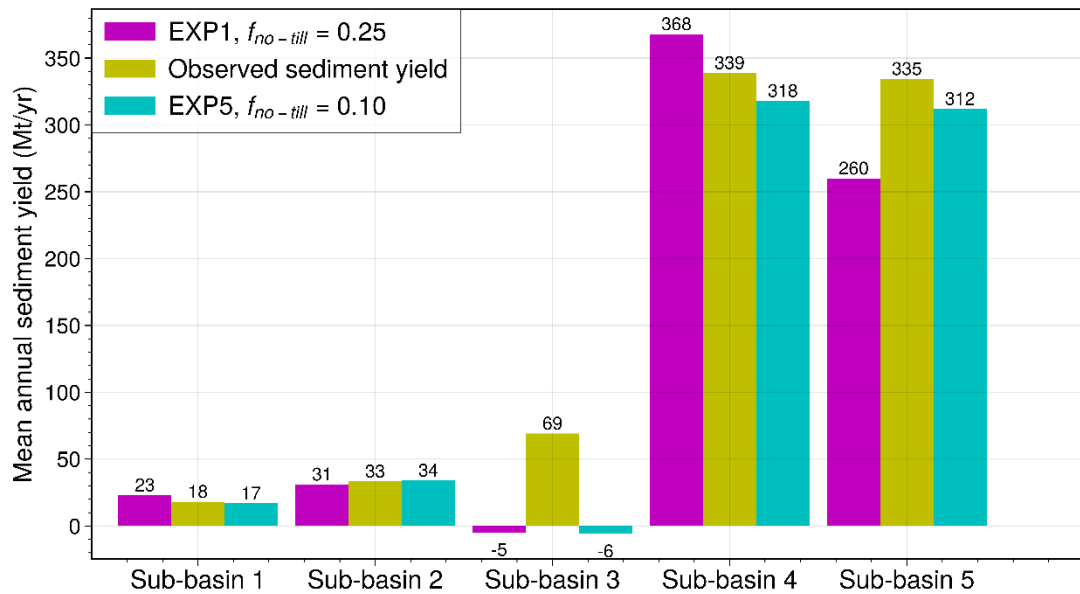


**Figure 6.7:** Same as Fig. 6.3, but mean annual sediment yields in sub-basins are from EXP 1 and EXP 5, with different no-tillage method factors.

According to both the irrigation fraction map (Ozdogan & Gutman, 2008) and the Global Map of Irrigation Areas" (Siebert et al., 2005), irrigation is most intensive in the Sub-basins 3 and 5. Indeed, as shown in Fig. 6.7, EXP 5 indicates that a relatively higher amount of cropland erosion in Sub-basin 5 will yield an improved agreement between predicted and observed sediment yield, compared to EXP 1 (see Fig. 6.2). As seen, changing the no-tillage factor causes no significant change in cropland

erosion for sub-basin 3. We attribute this behavior to the underestimation of sediment transport capacity and the flow velocity in the river in this area. Future research should use additional streamflow observations to evaluate river flow velocity, depth, and corresponding sediment transport capacity.

#### 6.5.4 Sedimentation in Reservoirs

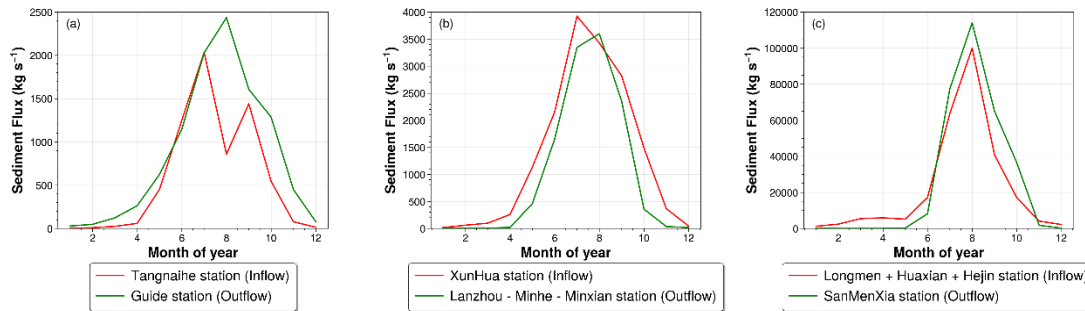


**Figure 6.8:** Annual cycles of observed monthly inflow and outflow sediment flux of the Longyangxia Reservoir (a), Liujiaxia Reservoir (b) and Sanmenxia Reservoir (c), averaged over 1979-1987.

Increasing anthropogenic activities in the Yellow River Basin, such as dams and reservoirs, usually significantly impact the dynamics of suspended sediment load through sedimentation. Here, the potential sedimentation by the reservoir is examined by comparing the sediment fluxes at the reservoir's upstream and downstream gauge stations. Figures 6.8a and 11c show that the outflow sediment flux at the Longyangxia and Sanmenxia Reservoirs is larger than the inflow sediment flux at the same reservoirs. Therefore, we conclude that sediment flux at these reservoirs did not change substantially from 1979 to 1987. However, as shown in Fig. 6.8b, the outflow sediment flux is lower than the inflow of Liujiaxia Reservoir. Therefore, we propose that sediment flux at the Liujiaxia Reservoir changed over time due to sedimentation in the reservoir. It would be interesting to extend the AHMS-SED sediment transport model in future work to incorporate the effects of sedimentation in the reservoirs.

## 6.6 Conclusions and Outlook

The present study has been motivated by the need for a water erosion and sediment transport model that is applicable to the watershed scale or continental scale. Despite the progress achieved in the last few decades in the field of regional hydrological modelling, previous models for sediment transport processes were designed for and tested against observations at the laboratory scale and neglected environmental

factors that are essential to represent regional-scale processes. In particular, one of the most important factors missing in previous models is the input of sediment to rivers due to gully erosion and gravity erosion.

### **6.6.1 Development of a Regional Model for Water Erosion and Sediment Transport**

Therefore, here we presented a model for water erosion and sediment transport that overcomes the deficiencies of previous models, highlighted in the paragraph above, and is, thus, applicable to the regional scale. Our regional model, AHMS-SED, combines the coupled Atmospheric and Hydrological Modeling System, AHMS (Xia, 2019) – which has been recently extended to include the effect of irrigation in the hydrological simulations (Jiang et al., 2022) – with the water erosion and sediment transport model CASC2D-SED (Rojas et al., 2003). Furthermore, our model incorporates a novel module, introduced in the present work, to represent gully erosion and the concatenated effects on sediment sources by means of the gully area index, defined as the local fraction of gully-covered area in the simulation domain. This index quantifies, thus, the extent of potential permanent gully erosion and its effect on sediment supply at the regional scale.

We have then applied our model to simulate regional sediment transport processes in the Yellow River Basin, China, building on previous hydrological simulations within the time span from 1979 to 1986 (Jiang et al., 2022). We have chosen the Yellow River Basin as the study area for the case application, given that gully erosion plays a major role in the sediment budget in the Chinese Loess Plateau. Using our model, we evaluated the applicability of the various sediment transport equations available in the literature to describe upland processes based on rainfall (USLE- $EI_{30}$ ), runoff (KR equation) and overland flow (KR equation). Furthermore, we predicted the evolution of sediment transport in the Yellow River Basin under consideration of specific climate change scenarios, including temperature, irrigation, precipitation volume and rate changes.

### **6.6.2 Insights From the Model Application to Yellow River Basin With Consideration of Gully Erosion**

The main findings from our model application to the Yellow River Basin are summarised as follows.

1. The monthly suspended sediment fluxes predicted by AHMS-SED at the five major hydrological stations along the Yellow River are in reasonably good agreement with observations, including fluctuation and mean (SBI and mKGE). The best agreement was found for LM and HYK stations, where suspended sediment fluxes are larger than at other stations due to gully erosion in the Chinese Loess Plateau.

2. The introduced gully area index and the corresponding sediment transport capacity for overland flow correlate with observed sediment source hotspots in the Chinese Loess Plateau. A comparison of the predicted and observed long-time averaged sediment yield in the sub-basin of TDG-LM indicates that the model with gully erosion performs well and could capture the profound impact of gully erosion on the sediment budget in this area accurately. However, the model tends to significantly overestimate sediment yield in steep regions and could not reproduce the spatial distribution of soil erosion without considering gully erosion.

3. The rainfall erosivity (USLE- $EI_{30}$ ) is the best predictor for large-scale water erosion and sediment transport model. The runoff-based KR equation performs well for the arid and semi-arid areas in the YRB where the excess-infiltration runoff is dominant. However, the runoff-based KR equation tends to overestimate overland flow transport capacity in humid mountainous areas, where subsurface runoff plays an important role. Sediment discharge tends to be overestimated by the overland flow-based KR equation, particularly in extreme flood events.

4. Surprisingly, the transport capacity equation based on USLE-M ( $Q_cEI_{30}$ ) and USLE-MM ( $Q_cEI_{30}$ )<sup>1.55</sup> does not perform much better than the USLE-based equation, even with consideration of the runoff coefficient and nonlinear relations between  $EI_{30}$  and soil erosion. USLE-MM erosivity based transport capacity also tends to overestimate sediment discharge, especially in extreme flood events.

5. Our predictions for sediment fluxes in the Yellow River Basin under consideration of specific climate change scenarios reveal that sediment yield in this basin is particularly sensitive to the changes in precipitation rates, and increasing irrigation will increase the deposition in streams and decrease the sediment yields. In the decades ahead, climate-change-driven alterations in precipitation rates shall have a more important impact on sediment transport processes in the Yellow River Basin

compared to changes in precipitation volume or temperature.

### **6.6.3 Outlook**

There is a broad outlook for future studies building on the present work. Future work should focus on a scale-adaptive parameterization of water erosion to resolve scale-dependent variables without the need for employing scale-related parameters. One further line for model improvement involves applying a random distribution to explicitly represent the stochastic nature of the spatial and temporal distributions of precipitation, runoff and overland flow. Moreover, a sedimentation model should be developed and incorporated into the sediment transport model to account for the effect of sedimentation in reservoirs.

We note that the overestimation of sediment discharge using the KR and USLE-MM equations suggests that future work should also focus on parameter calibration and sensitivity analysis, to better constrain the value of the exponent of water discharge or USLE rainfall erosivity ( $EI_{30}$ ). Moreover, in future studies, model predictions for flow rates in the Yellow River and the concatenated sediment transport capacity should be calibrated and validated with the help of additional data on streamflow observations, including flow velocity and depth. Such studies could help to improve, for instance, the predictions of sediment discharge in the LZ-TDG sub-basin.

The present study demonstrates that our regional model, AHMS-SED, can be applied for regional simulations of continental-scale soil erosion and sediment transport in areas where gully erosion profoundly influences water erosion and sediment yield. As shown here, AHMS-SED is a comprehensive regional model that incorporates a broad range of geological, climatic and environmental factors. Therefore, the future application of AHMS-SED in regional climate modelling has the potential to substantially improve predictions of suspended sediment flux and sediment yield, both at watershed and continental scales.

## **6.7 Data Availability Statement**

The high spatial-temporal resolution gridded China Meteorological Forcing Dataset (CMFD) is available through the China National Tibetan Plateau/Third Pole Environment Data Center, <https://data.tpdc.ac.cn/en/data/8028b944-daaa-4511-8769-965612652c49/>. Multi-Error-Removed Improved-Terrain DEM (MERIT) with a 3sec

resolution is accessible from the MERIT Hydro webpage, [http://hydro.iis.u-tokyo.ac.jp/~yamada/MERIT\\_DEM/](http://hydro.iis.u-tokyo.ac.jp/~yamada/MERIT_DEM/). SRTM is available through the Jet Propulsion Laboratory, <https://www2.jpl.nasa.gov/srtm/>. Daily measured water discharge and suspended sediment concentration of the Yellow River at five hydrological stations, including Tangnaihe, Lanzhou, Toudaoguai, Huayuankou and Huayuankou, are obtainable on request from the National Earth System Science Data Center of China (<http://gre.geodata.cn>). The 30 arc-seconds resolution soil particle-size distribution dataset for regional land and climate modelling in China is accessible from the Land-Atmosphere Interaction Research Group of the Sun Yat-sen University, China (<http://globalchange.bnu.edu.cn/research/soil>). The boundary map of rich sediment areas in the middle Yellow River Basin is available in the National Cryosphere Desert Data Center of China (<http://www.ncdc.ac.cn/portal/metadata/f266f81b-3d5b-43ab-8fd5-c2389e6b90cb>). The results of AHMS-SED simulations in the Yellow River Basin will be made available upon request.

## 7 Conclusions and Outlook

### 7.1 Summary

A continental-scale Atmospheric and Hydrological-Sediment Modelling System (AHMS-SED) has been developed and applied to the Yellow River Basin in China. As mentioned in Chapter 1, this study focuses on three key scientific questions: anthropogenic interference with the hydrological cycle (Study I, Chapter 4), uncertainty in precipitation data and model response (Study II, Chapter 5) and the regional water erosion and sediment transport (Study III, Chapter 6).

In Study I, a regional model (AHMS-IRRIG) for long-term, large-scale hydrological processes under the consideration of irrigation in arid and semi-arid regions has been developed and applied to the Yellow River Basin. AHMS-IRRIG combines the land surface model, flow routing model and groundwater model of the Atmospheric and Hydrological Modelling System (AHMS) with a modified irrigation scheme (Xu et al., 2019) to quantify the dynamic irrigation amount in arid and semi-arid basins. The channel routing model and groundwater model of the AHMS have been modified to incorporate the water uptake connected to the long-distance water supply of irrigation districts in arid and semi-arid basins. The actual amount of irrigation is, therefore, constrained by the water availability estimated with the flow routing and the irrigation fractions of surface water and groundwater based on the “Global Map of Irrigation Areas”. By incorporating the irrigation module into the simulation, a more realistic hydrological response was obtained near the outlet of the Yellow River Basin compared to previous studies (Jia et al., 2006; Yin et al., 2021). The model results thus demonstrate the ability of AHMS to reproduce long-term hydrological processes in the Yellow River Basin, provided that water taken for irrigation is included in the simulation.

In Study II, an evaluation of six precipitation-reanalysis products has been performed using the offline AHMS to understand model uncertainties and characterize the different biases in precipitation forcing data. The six precipitation products are evaluated, including two non-gauge-corrected reanalysis products (NCEP/NCAR and ERA5) and four gauge-corrected reanalysis products (GLDAS 2.0, WFDE5/CRU,

WFDE5/(CRU+GPCC) and CMFD). The hydrological model is then driven with each of the precipitation-reanalysis products in two ways, one with the rainfall-runoff parameters recalibrated and the other without. The model predictions for the streamflow are then compared with the corresponding observations. We also assess these products by comparing the annual, seasonal and monthly precipitations with the gauge data. This analysis will help to better quantify the reliability of hydrological simulations and improve future precipitation reanalysis products.

The objective of Study III is to develop a water erosion and sediment transport model suitable for the watershed or continental scale, while previous models for sediment transport processes were designed for and tested against observations at the laboratory scale and overlooked environmental factors crucial for regional-scale processes. In particular, one of the most important factors missing in previous models is the input of sediment to rivers due to gully erosion and gravity erosion. To address this limitation, a regional-scale water erosion and sediment transport model, called AHMS-SED, is developed by integrating the AHMS with the modified version of CASCade 2-Dimensional SEDiment (CASC2D-SED) to take into account gully erosion, which profoundly affects the sediment supply in the Chinese Loess Plateau. In order to quantify the extent of potential permanent gully erosion and its effect on sediment supply at the regional scale, AHMS-SED incorporates a novel module by means of the gully area index, defined as the local fraction of gully-covered area in the simulation domain. Furthermore, the applicability of various sediment transport equations available in the literature to describe upland processes based on rainfall (USLE-EI30), runoff (KR equation), and overland flow (KR equation) is evaluated. It also predicts the evolution of sediment transport in the Yellow River Basin under specific climate change scenarios, including changes in temperature, irrigation, precipitation volume and rate.

## **7.2 Main Achievements**

### **Study I:**

- (1) This regional hydrological model AHMS-IRRIG, with consideration of irrigation, is calibrated and validated in the Yellow River Basin of China by comparing observed and predicted water discharge, evapotranspiration and terrestrial water storage change using in situ, satellite and assimilated data.

- (2) The development of an irrigation model that considers the long-distance water transfer off-stream from the river to irrigation districts – is fully neglected by previous irrigation models. With AHMS-IRRIG, the actual irrigation amount is explicitly computed using the soil moisture deficit method and constrained by the water availability estimated with the flow routing, as well as the irrigation fractions of surface water and groundwater based on the “Global Map of Irrigation Areas”.
- (3) The development of a regional hydrological model that is applicable to arid and semi-arid regions, through the incorporation of irrigation sink and source terms into the channel routing and groundwater models.
- (4) The advanced Earth gravity satellite data set provided by the GRACE satellites is incorporated and used to verify the hydrological model and assess the impact of irrigation on hydrological processes in the arid and semi-arid environments of the Yellow River Basin.

#### **Study II:**

- (1) The hydrological comparison of the six reanalysis precipitation products considered in our analysis shows better model performance using gauge-corrected reanalysis precipitation datasets than non-gauge-corrected datasets. The non-gauge-corrected products are found to have significantly overestimated precipitation, especially in mountainous regions.
- (2) The results of the hydrological simulations depend heavily on the choice of precipitation reanalysis dataset in the Yellow River Basin, but the calibration of the rainfall-runoff model can greatly reduce this dependence.
- (3) It is found that among the six precipitation-reanalysis products, CMFD and WFDE5/(CRU+GPCC) are the most accurate for the relevant study area and period.

#### **Study III:**

- (1) The regional model, AHMS-SED, has been developed by combining the coupled Atmospheric and Hydrological Modeling System, AHMS (Xia, 2019) – which has been recently extended to include the effect of irrigation in the hydrological simulations (Jiang et al., 2022) – and revised the water erosion and

sediment transport model CASC2D-SED (Rojas et al., 2003).

- (2) The monthly suspended sediment fluxes predicted by AHMS-SED at the five major hydrological stations along the Yellow River are in reasonably good agreement with observations, including fluctuation and mean (SBI and mKGE).
- (3) The gully area index introduced here and the corresponding sediment transport capacity for overland flow correlate with observed sediment source hotspots in the Chinese Loess Plateau.
- (4) A comparison of the predicted and observed long-time averaged sediment yield in the sub-basin of TDG-LM indicates that the model incorporating the proposed gully area index performs well and could capture the profound impact of gully erosion on the sediment budget in this area accurately.
- (5) The rainfall erosivity (USLE- $EI_{30}$ ) is the best predictor for large-scale water erosion and sediment transport model. The runoff-based KR equation performs well for the arid and semi-arid areas in the YRB where the excess-infiltration runoff is dominant. The runoff-based KR equation tends to overestimate overland flow transport capacity in humid mountainous areas, where subsurface runoff plays an important role. Sediment discharge tends to be overestimated by the overland flow-based KR equation, particularly in extreme flood events.
- (6) Our predictions for sediment fluxes in the Yellow River Basin under consideration of specific climate change scenarios reveal that sediment yield in this basin is particularly sensitive to the changes in precipitation rates, and increasing irrigation will increase the deposition in streams and decrease the sediment yields in the Yellow River Basin.

### 7.3 Main Limitations

Despite the achievements highlighted in Section 7.2, there are limitations in the model and the studies. The limitations can mainly be attributed to time and resource constraints, as well as to the complexity of the underlying problem. This is explained below from several perspectives, including model development, calibration and application.

- (1) The water erosion model employs a linear scaling parameter which cannot represent the sub-grid processes. In addition, the influence of soil moisture or

groundwater table on water erosion is not explicitly taken into account.

- (2) Various other anthropogenic influences on the water cycle, water erosion and sediment transport, such as reservoirs, damming or dynamic land use change (e.g., reforestation or afforestation), were not considered in this study.
- (3) The channel routing model is limited by the use of a single set of empirical hydraulic geometry equations to represent the river depth and width. This approach may not produce accurate river bathymetry for the full length of the Yellow River.
- (4) The finer resolution of the simulation (1-10 km) was not tested in the Yellow River Basin as the current channel routing model of AHMS does not support parallel computation. The current 20 km grid cells may be too coarse to resolve the hydrological, water erosion and sediment transport processes on many slopes and valleys in the landscape.
- (5) Another limitation of calibrating a hydrological model is the use of a single optimization target variable, namely streamflow discharge. To improve the overall performance of the hydrological model, a joint calibration target that includes the river's water level, soil moisture, and evapotranspiration within the watershed could be employed.

#### **7.4 Recommendations for Future Research**

A broad outlook for future studies building on the present work is as follows.

- (1) Future work should focus on a scale-adaptive parameterization of water erosion to resolve scale-dependent variables without the need for employing scale-related parameters. An additional method for enhancing the model consists of applying a random distribution to explicitly represent the stochastic characteristics of the spatial and temporal distributions of precipitation, runoff and overland flow.
- (2) The incorporation of various anthropogenic influences, such as damming or change in land use, and the inclusion of the dynamic land use change (e.g., reforestation or afforestation) and damming processes into AHMS constitutes an open modelling task, which will be important to improve the quantitative assessment of the hydrological processes in future work. Moreover, a sedimentation model should be developed and incorporated into the sediment

transport model to account for the effect of sedimentation in reservoirs.

- (3) Additional in-situ and satellite measurements of river and floodplain geometry for the channel routing model of the AHMS would also improve the prediction of flood timing and peak.
- (4) In future studies, model predictions for flow rates in the Yellow River and the concatenated sediment transport capacity should be calibrated and validated with the help of additional data on streamflow observations, including flow velocity and depth. Such studies could help to improve, for instance, the predictions of sediment discharge in the LZ-TDG sub-basin.
- (5) Future research could employ (online) numerical simulations combined with the Weather Research Forecasting modelling system (WRF) to investigate the impact of irrigation on local environmental processes and extreme events like floods, while considering variations in climate and land use types in arid and semi-arid regions.
- (6) The inclusion of vegetation parameters and several optimization target variables, such as river water level and soil moisture and evapotranspiration within the watershed, into the calibration of the numerical simulations will be an important extension of the model in future work.
- (7) Future work should also focus on parameter calibration and sensitivity analysis for the upland sediment discharge equation to better constrain the exponent of water discharge and USLE rainfall erosivity ( $EI_{30}$ ).
- (8) In the future, the application and evaluation of the gully area index to other catchments, including different environments, landforms and climates, will be necessary to improve the development of regional water erosion and sediment modelling.

## Appendix A

### A.1 Discretization of the Richards equation

Hydraulic diffusivity ( $D$ , in units of  $\text{m}^2 \text{s}^{-1}$ ) is defined as

$$D(\theta) = K(\theta) \frac{\partial \Psi}{\partial \theta} \quad (\text{A.1})$$

By substituting the redefinition of hydraulic diffusivity into Eq. (3.1), the diffusivity form of the one-dimensional Richards equation is given by

$$\frac{\partial \theta}{\partial t} = \frac{\partial}{\partial z} \left[ D(\theta) \frac{\partial \theta}{\partial z} + K(\theta) \right] - S(z, t) \quad (\text{A.2})$$

The difference method for the Richards equation uses an implicit time scheme and a centred difference scheme for spatial discretization, as given below

$$\frac{\theta_i^{t+1} - \theta_i^t}{\Delta t} = \frac{q_{i+1/2}^{t+1} - q_{i-1/2}^{t+1}}{\Delta z} - S_i^t \quad (\text{A.3})$$

By substitution and transformation, the above equation is formulated as a tri-diagonal equation as follows

$$A_i \Delta \theta_{i-1}^{t+1} + (1 + B_i) \Delta \theta_i^{t+1} + C_i \Delta \theta_{i+1}^{t+1} = rhs_i \quad (\text{A.4})$$

where the matrix coefficients ( $A_i$ ,  $B_i$  and  $C_i$ ) for the tri-diagonal matrix are given below

$$B_i = -A_i - C_i \quad (\text{A.5})$$

If  $i = 1$ , then,

$$\begin{cases} A_i = 0 \\ C_i = -\frac{D_i}{(-z_i)(-z_{i+1}/2)} \end{cases} \quad (\text{A.6})$$

If  $2 < i < n$ , then

$$C_i = \frac{D_i}{0.5(z_{i-1} - z_{i+1})(z_{i-1} - z_i)} \quad (\text{A.7})$$

If  $i = 2$ , then

$$A_i = \frac{D_{i-1}}{0.5(-z_{i-1})(z_{i-1} - z_i)} \quad (\text{A.8})$$

If  $i \neq 2$ , then

$$A_i = \frac{D_{i-1}}{0.5(z_{i-2} - z_i)(z_{i-1} - z_i)} \quad (\text{A.9})$$

If  $i = n$ , then

$$\begin{cases} A_i = \frac{D_{i-1}}{0.5(-z_{i-2} - z_i)(z_{i-1} - z_i)} \\ C_i = 0 \end{cases} \quad (\text{A.10})$$

$$rhs_i = \frac{q_i^t - q_{i-1}^t}{\Delta z} - S_i^t \quad (\text{A.11})$$

If  $i = 1$ , then

$$rhs_i \Delta z = D_i \frac{\theta_i - \theta_{i+1}}{0.5(-z_{i+1})} + K_i - I_{sfc} + ET_i + E_{sfc} \quad (\text{A.12})$$

If  $1 < i < n$ , then

$$rhs_i \Delta z = D_i \frac{\theta_i - \theta_{i+1}}{0.5(z_{i-1} - z_{i+1})} + K_i - D_{i-1} \frac{\theta_{i-1} - \theta_i}{0.5(z_{i-2} - z_i)} - K_{i-1} + ET_i \quad (\text{A.13})$$

If  $i = n$ , then

$$rhs_i \Delta z = -D_{i-1} \frac{\theta_{i-1} - \theta_i}{0.5(z_i - z_{i-2})} - K_{i-1} + ET_i + Q_{drain} \quad (\text{A.14})$$

where  $i$  is the soil layer index,  $n$  is the last layer,  $z$  is the elevation at the bottom of the soil layer (m),  $q_i^t$  is water flux, which is positive in the outward direction,  $I_{sfc}$  is the infiltration rate at the surface,  $ET$  is the transpiration rate,  $E_{sfc}$  is the soil surface evaporation rate,  $K$  is the hydraulic conductivity ( $\text{m s}^{-1}$ ), and  $Q_{drain}$  is the soil bottom drainage flux.

## A.2 Discretization of the Diffusion Wave Equation

The finite difference method implicitly solves the diffusion wave equation in the

channel routing model (Eq. 3.4) with the time-implicit Newton-Raphson term for slopes. The slope term is given by

$$\left[ \left( \frac{dh}{dl} \right)^{t+1} \right]^{-0.5} = \left| \left( \frac{dh}{dl} \right)^t \right|^{-0.5} \cdot \overline{\left( \frac{dh}{dl} \right)} \quad (\text{A.16})$$

It is assumed that there is a linear relationship between head change and time, given as follows.

$$\begin{aligned} \overline{\left( \frac{dh}{dl} \right)} &= \frac{1}{2} \left[ \left( \frac{dh}{dl} \right)^t + \left( \frac{dh}{dl} \right)^{t+1} \right] \\ &= \frac{1}{2} \left( \frac{h_k^t - h_{i,j}^t}{\Delta l} + \frac{h_k^{t+1} - h_{i,j}^{t+1}}{\Delta l} \right) \\ &= \frac{h_k^t - h_{i,j}^t}{\Delta l} + \frac{(h_k^{t+1} - h_k^t) - (h_{i,j}^{t+1} - h_{i,j}^t)}{2\Delta l} \end{aligned} \quad (\text{A.17})$$

As shown in Eq. (3.4), in the AHMS channel routing model, each grid  $(i, j)$  has eight flow directions for inflows and outflows as follows.

$$A_{i,j} \frac{h_{i,j}^{t+1} - h_{i,j}^t}{\Delta t} = \sum_{k=1}^4 Q_{i,j}^{k,t+1} - \sum_{k=5}^8 Q_{i,j}^{k,t+1} + S_{i,j} \quad (\text{A.15})$$

By substitution and transformation, Eq. (3.4) is formulated as:

$$\begin{aligned} A_{i,j} \frac{h_{i,j}^{t+1} - h_{i,j}^t}{\Delta t} &= \\ &\sum_{k=1}^4 \left[ A_{cr} \frac{1}{n} R_h^{2/3} \left( \frac{h_k^t - h_{i,j}^t}{\Delta l} \right)^{-1/2} \frac{h_k^t - h_{i,j}^t}{\Delta l} + \frac{1}{2} A_{cr} \frac{1}{n} R_h^{2/3} \left( \frac{h_k^t - h_{i,j}^t}{\Delta l} \right)^{-1/2} \frac{(h_k^{t+1} - h_k^t) - (h_{i,j}^{t+1} - h_{i,j}^t)}{\Delta l} \right] \\ &+ \sum_{k=5}^8 \left[ A_{cr} \frac{1}{n} R_h^{2/3} \left( \frac{h_k^t - h_{i,j}^t}{\Delta l} \right)^{-1/2} \frac{h_{i,j}^t - h_k^t}{\Delta l} + \frac{1}{2} A_{cr} \frac{m}{n} R_h^{2/3} \left( \frac{h_{i,j}^t - h_k^t}{\Delta l} \right)^{-1/2} \frac{(h_k^{t+1} - h_k^t) - (h_{i,j}^{t+1} - h_{i,j}^t)}{\Delta l} \right] \\ &+ R_{sf} + f_w (C_g + C_u) - C_l - Q_{irr\_sf} \end{aligned} \quad (\text{A.18})$$

The equation above is reformulated through substitution and transformation as follows:

$$\begin{aligned}
h_{i,j}^{t+1} - h_{i,j}^t = & \\
& zdt * \sum_{k=1}^4 [ZF(h_k^t - h_{i,j}^t)] + \frac{1}{2} zdt \sum_{k=1}^4 [ZF(h_k^{t+1} - h_k^t)] - \frac{1}{2} zdt \sum_{k=1}^4 [ZF(h_{i,j}^{t+1} - h_{i,j}^t)] \\
& + zdt * \sum_{k=5}^8 [ZF(h_{i,j}^t - h_k^t)] + \frac{1}{2} zdt \sum_{k=5}^8 [ZF * (h_{i,j}^{t+1} - h_{i,j}^t)] - \frac{1}{2} zdt \sum_{k=5}^8 [ZF(h_k^{t+1} - h_k^t)] \\
& + R_{sf} + f_w * (C_g + C_u) - C_l - Q_{irr\_sf}
\end{aligned} \tag{A.19}$$

where the constant terms are

$$ZF = \begin{cases} A_{cr} \frac{1}{n} R^{2/3} \left( \frac{h_k^t - h_{i,j}^t}{\Delta l} \right)^{-\frac{1}{2}} \frac{1}{\Delta l} & \text{if } \left( \frac{h_k^t - h_{i,j}^t}{\Delta l} > 10^{-8} \right) \\ A_{cr} \frac{1}{n} R^{2/3} (10^{-8})^{-\frac{1}{2}} \frac{1}{\Delta l} & \text{if } \left( \frac{h_k^t - h_{i,j}^t}{\Delta l} \leq 10^{-8} \right) \end{cases} \tag{A.20}$$

$$zdt = \frac{\Delta t}{A_{i,j}} \tag{A.21}$$

After solving Eq. (A.19),  $h_{i,j}^{t+1} - h_{i,j}^t$  is obtained and the water level and inundation are updated accordingly.

### A.3 Discretization of Two-Dimensional Boussinesq Equation

The alternating direction implicit (ADI) method is used here to discretize the Boussinesq equation as follows:

Step 1: Explicit difference in direction  $x$  and implicit difference in direction  $y$ .

$$\begin{aligned}
S_{si,j} \frac{h_{i,j}^{t+1} - h_{\phi i,j}^t}{\Delta t} = & \frac{1}{\Delta x} \left( T_{xi,j}^t \frac{h_{i+1,j}^t - h_{i,j}^{t+1}}{\Delta x} - T_{xi-1,j}^t \frac{h_{i,j}^{t+1} - h_{i-1,j}^t}{\Delta x} \right) \\
& + \frac{1}{\Delta y} \left( T_{yi,j}^t \frac{h_{i,j+1}^{t+1} - h_{i,j}^{t+1}}{\Delta y} - T_{yi,j-1}^t \frac{h_{i,j}^{t+1} - h_{i,j-1}^{t+1}}{\Delta y} \right)
\end{aligned} \tag{A.22}$$

where  $h_{\phi i,j}$  is the calculated head at node  $(i, j)$  at the end of the previous time increment  $\Delta t$ . The above equation is simplified to a tridiagonal equation of the form:

$$AA_i * h_{i,j-1}^{t+1} + BB_i * h_{i,j}^{t+1} + CC_i * h_{i,j+1}^{t+1} = DD_i \tag{A.23}$$

where the matrix coefficients and right-hand side terms are

$$\begin{cases} AA_i = -T_{yi,j-1}^t \\ BB_i = T_{xi,j}^t + T_{xi-1,j}^t + T_{yi,j}^t + T_{yi,j-1}^t + \frac{S_{si,j}\Delta x^2}{\Delta t} \\ CC_i = -T_{yi,j}^t \\ DD_i = T_{xi-1,j}^t h_{i-1,j}^t + \left( \frac{S_{si,j}\Delta x^2}{\Delta t} \right) h_{\phi i,j}^t + T_{xi,j}^t h_{i+1,j}^t \end{cases} \quad (\text{A.24})$$

Step 2: Explicit difference in direction  $y$  and implicit difference in direction  $x$ .

$$\begin{aligned} S_{si,j} \frac{h_{i,j}^{t+1} - h_{\phi i,j}^t}{\Delta t} &= \frac{1}{\Delta x} \left( T_{xi,j}^t \frac{h_{i+1,j}^{t+1} - h_{i,j}^{t+1}}{\Delta x} - T_{xi-1,j}^t \frac{h_{i,j}^{t+1} - h_{i-1,j}^{t+1}}{\Delta x} \right) \\ &+ \frac{1}{\Delta y} \left( T_{yi,j}^t \frac{h_{i,j+1}^t - h_{i,j}^{t+1}}{\Delta y} - T_{yi,j-1}^t \frac{h_{i,j}^{t+1} - h_{i,j-1}^t}{\Delta y} \right) \end{aligned} \quad (\text{A.25})$$

The above equation is simplified to a tridiagonal equation of the form as

$$AA_i * h_{i-1,j}^{t+1} + BB_i * h_{i,j}^{t+1} + CC_i * h_{i+1,j}^{t+1} = DD_i \quad (\text{A.26})$$

where the matrix coefficients and right-hand side terms are

$$\begin{cases} AA_i = -T_{xi-1,j}^t \\ BB_i = T_{xi,j}^t + T_{xi-1,j}^t + T_{yi,j}^t + T_{yi,j-1}^t + \frac{S_{si,j}\Delta x^2}{\Delta t} \\ CC_i = -T_{xi,j}^t \\ DD_i = T_{yi,j-1}^t h_{i,j-1}^t + \left( \frac{S_{si,j}\Delta x^2}{\Delta t} \right) h_{\phi i,j}^t + T_{yi,j}^t h_{i,j+1}^t \end{cases} \quad (\text{A.27})$$

After solving the set equations in Eq. (A.24) and Eq. (A.27), the groundwater head is updated to be  $h_{i,j}^{t+1}$ .

## Appendix B

### Supplemental Material for *A Regional Hydrological Model for Arid and Semi-Arid River Basins with Consideration of Irrigation*

Cong Jiang<sup>a</sup>, Eric J. R. Parteli<sup>b</sup>, Qian Xia<sup>c</sup>, Xin Yin<sup>a</sup> and Yaping Shao<sup>a</sup>

<sup>a</sup>*Institute for Geophysics and Meteorology, University of Cologne, Pohligstr. 3, Cologne, 50969, North Rhine-Westphalia, Germany*

<sup>b</sup>*Faculty of Physics, University of Duisburg-Essen, Duisburg, Lotharstr. 1, 47057, North Rhine-Westphalia, Germany*

<sup>c</sup>*School of Water Resources and Hydropower Engineering, Wuhan University, Bayi Road. 299, 430072, Hubei Province, China*

**Abstract:** In Sections 1-4 of this Supplemental Material (SM), we provide further information about the hydrological model introduced in Section 2 of the main document. Moreover, in Section 5 of this SM, the impacts of the four most influential reservoirs along Yellow River's mainstream, in the period from 1977 to 1988, are discussed, while the Noah-MP parameterization options used are described in Section 6. The sensitivity analysis of the annual cycles of averaged weekly streamflow on the hydrological parameters, including the parameters  $\beta$ ,  $B$ ,  $W$ ,  $n$ ,  $\alpha$  and  $C_s$  defined in both main document and SM, is then presented in Section 7. Furthermore, Section 8 provides the spatial distribution of the hydrological variables including (a) precipitation, (b) evapotranspiration, (c) runoff, (d) streamflow, (e) soil moisture, (f) groundwater depth, (g) surface runoff, (h) subsurface runoff, for the Yellow River basin averaged from 1979 to 1988. To conclude this SM, Section 9 presents the calibration and sensitivity analysis of the irrigation model parameters on the irrigation amount and streamflow.

#### B.1 Infiltration and Infiltration-Excess Runoff

Infiltration capacity or maximum infiltration rate ( $I_{\max}$ ) is a variable that determines the surface water input distribution between infiltration and runoff. The infiltration capacity indicates the infiltration rate under the condition of sufficient water supply, and depends on the characteristics of the soil, such as soil moisture and texture.

Previous studies (Beven, 1989; Chamizo et al., 2012; Gao et al., 2015; Yu et al., 1999) indicated that the soil infiltration capacity is, indeed, much smaller than the saturated hydraulic conductivity at surface ( $K_{\text{sat}}(0)$ ) in a coarse grid, owing to the spatial heterogeneity in hydraulic parameters of soil and precipitation. We thus assume the following model (Best et al., 2011),

$$I_{\text{max}} = \beta K_{\text{sat}}(0) \quad (\text{B.1})$$

$$R_{\text{ins}} = \max(0, Q_{\text{wat}} - I_{\text{max}}) \quad (\text{B.2})$$

$$I_{\text{sfc}} = Q_{\text{wat}} - R_{\text{ins}} \quad (\text{B.3})$$

where  $\beta$  is an empirical parameter ( $0 \leq \beta \leq 1$ ), which can be determined by calibration of the annual average runoff in the sub-basins of the Yellow River Basin,  $R_{\text{ins}}$  is the infiltration-excess runoff,  $Q_{\text{wat}}$  is the water input on the soil surface, and  $I_{\text{sfc}}$  is the infiltration rate at the surface.

## B.2 Interaction Fluxes of River-Groundwater and River-Vadose

Given the river channel considered in HMS, the river-groundwater ( $C_g$ ) and river-vadose ( $C_u$ ) interaction fluxes are also computed here using Darcy's law (Sophocleous, 2002; Yu et al., 2006). It is assumed that there is a layer of low-permeability material at the riverbed so that the water in the river can be separated from the groundwater system in each grid. If the water table is higher than the river bed, then  $C_g$  is proportional to  $h_r - h_g$ , and  $C_u = 0$ , where  $h_r$  is the river water level and  $h_g$  is the groundwater level. If the groundwater level is lower than the riverbed, then  $C_u$  is proportional to  $h_r - h_{\text{bot}}$ , and  $C_g = 0$ , where  $h_{\text{bot}}$  is the elevation of the stream bed. The exchange flow between river and groundwater is then calculated using,

$$C_g = \frac{K_b}{M} (h_r - h_g) = C_s (h_r - h_g) \quad (\text{B.4})$$

$$C_u = C_s (h_r - h_{\text{bed}}) \quad (\text{B.5})$$

where  $C_s$  is the hydraulic conductance of stream-aquifer interconnection ( $\text{s}^{-1}$ ),  $K_b$  is the hydraulic conductivity of streambed material ( $\text{m s}^{-1}$ ),  $M$  is the streambed

thickness (m),  $h_r$  is the stream water level (m),  $h_g$  is the groundwater head (m), and  $h_{\text{bed}}$  is the streambed elevation (m). The hydraulic conductance of the riverbed usually needs to be calibrated against the observed base flow of the river. The sensitivity of AHMS to  $C_s$  is discussed in Section B6.

### B.3 Terrestrial Water Budget and Changes

This section describes the terrestrial water budget equation used in this study. The discharge and balance of water play a key role in the water cycle. Therefore, the quantification and assessment of terrestrial water storage budget and changes constitute an essential prerequisite for the reliable simulation of hydrological processes. The total terrestrial water storage  $S_t$  and the terrestrial water balance are computed using

$$S_t = W_{\text{sn}} + W_{\text{un}} + W_{\text{sf}} + W_{\text{gw}} \quad (\text{B.6})$$

$$\frac{dS_t}{dt} = P_r - \text{ET} - R_{\text{sf}} - R_{\text{sub}} \quad (\text{B.7})$$

where  $S_t$  is the total terrestrial water storage (m),  $W_{\text{sn}}$  is the water storage in snowpack (liquid equivalent) (m),  $W_{\text{un}}$  is the soil moisture storage in the unsaturated soil layer (m),  $W_{\text{sf}}$  is the surface water storage (m), including water storage in the rivers, lakes and reservoirs,  $W_{\text{gw}}$  is the groundwater water storage (m),  $P_r$  is the precipitation ( $\text{m s}^{-1}$ ), ET is the evapotranspiration ( $\text{m s}^{-1}$ ),  $R_{\text{sf}}$  is the surface runoff ( $\text{m s}^{-1}$ ), including infiltration-excess runoff and saturation excess runoff, and  $R_{\text{sub}}$  is the subsurface runoff ( $\text{m s}^{-1}$ ), which includes the interaction fluxes of river-groundwater  $C_g$  and river-vadose  $C_u$ .

### B.4 Major Reservoirs Along the Yellow River

Human activities, such as irrigation and dam regulation, play an important role in the Yellow River Basin area. Table B.1 shows the information on the four most influential constructed reservoirs along the mainstream of the Yellow River, while Figure B.1 shows the annual cycle of the Longyangxia, Liujiaxia and Sanmenxia Reservoir inflow and outflow. This figure indicates that, during the period from 1979 to 1988, streamflow through Longyangxia and Sanmenxia reservoirs (left and right subfigures in Fig. B.2) was little affected by artificial regulation because of

unfinished construction work and reservoir sedimentation. However, streamflow through the Liujiaxia reservoir (subfigure in the centre of Fig. B.2) was greatly affected by artificial regulation. The Liujiaxia Reservoirs increased substantially the baseflow in spring for water supply to the downstream agricultural irrigation areas and decreased streamflow slightly in summer and autumn for flood interception during the period from 1979 to 1988.

**Table B.1:** Information of four major reservoirs along the mainstream of Yellow River.

Reservoirs	Location	Height (m)	Storage ( $10^9 \text{ m}^3$ )	Time of completion
Sanmenxia	Middle reaches	335	9.7	September 1960
Liujiaxia	Upper reaches	147	5.7	October 1968
Longyangxia	Upper reaches	178	27.6	October 1986
Xiaolangdi	Middle reaches	160	12.7	October 1999

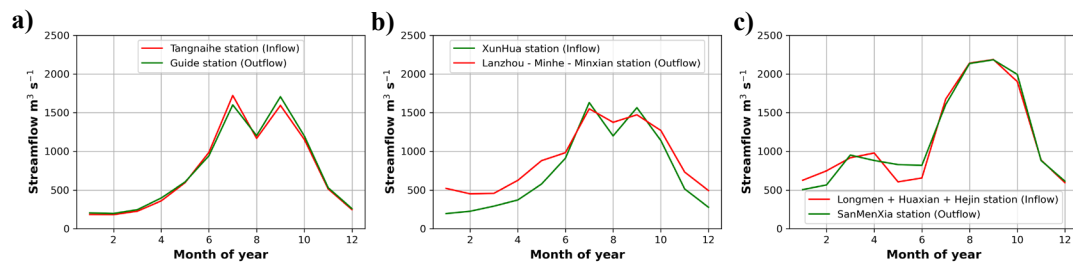


**Figure B.1:** Annual cycles of measured monthly inflow (Tangnaihe station) and outflow (Guide station) of the Longyangxia reservoir (a), monthly inflow (Xunhua station) and outflow (Lanzhou minus Minhe and Minxian station) of the Liujiaxia reservoir (b) and monthly inflow (Longmen plus Haxian and Hejin station) and outflow (Sanmenxia station) of the Sanmenxia reservoir (d), averaged over 1979-1988.

## B.5 Noah-MP Parameterization

**Table B.2:** Noah-MP parameterization options used in this study.

Parameterizations Description	Schemes Used
Dynamic vegetation	4: table LAI, shdfac = maximum
Stomatal resistance	1: Ball-berry, related to photosynthesis (Ball et al., 1987)
Soil moisture factor controlling stomatal resistance	1: Noah scheme, function of moisture (Chen & Dudhia, 2001)
Runoff and groundwater	9: Darcy's law (Xia, 2019)
Surface exchange coefficient for heat	1: M-O (Brutsaert, 2013)
Supercooled liquid water in frozen soil	NY06 (Niu & Yang, 2006)
Frozen soil permeability	1: NY06 (Niu & Yang, 2006)
Radiation transfer	3: gap = 1-FVEG
Snow surface albedo	2: CLASS (Verseghy, 1991)
Partitioning precipitation into rainfall and snowfall	1: Jordan91 (Jordan, 1991)
Lower boundary condition of soil temperature	1: zero flux
The first-layer snow or soil temperature time scheme	1: semi-implicit

## B.6 Sensitivity Analysis

Figures B.2-B.7 display observed annual cycles of averaged weekly streamflow at the main gauging stations along with the associated predictions from our simulations using the different values of  $\beta$ ,  $B$ ,  $W$ ,  $n$ ,  $\alpha$  and  $C_s$ , respectively. As can be seen from these figures, the model results are particularly sensitive to  $\alpha$ ,  $\beta$  and  $n$ . We thus calibrate AHMS to obtain the optimal combination of the two most sensitive river routing parameters ( $\alpha$  and  $n$ ) and soil parameters ( $\beta$  and  $C_s$ ) for the upper and middle reaches of the Yellow River.

As described in Table B.3, the calibrated values of soil saturated hydraulic conductivity amount to  $0.028K_{\text{sat}}$ ,  $0.035K_{\text{sat}}$ ,  $0.15K_{\text{sat}}$ , and  $0.12K_{\text{sat}}$  in the subbasins TNH, TNH-LZ, LZ-TDG, and TDG-HYK, respectively.

Furthermore, in large-scale hydrological simulations, empirical equations are used to estimate channel parameters due to the lack of a large-scale river hydraulic geometry dataset. Indeed, the quantitative assessment of these parameters experienced an improvement in recent years through the progress achieved in advanced satellite data applications. Neal et al. (2012) used high-resolution satellite imagery to estimate the width of rivers, and Yamazaki et al. (2011) developed the Global Width Database of Large Rivers (GWD-LR) based on observed water bodies. Notwithstanding this

significant progress, there is still considerably sparsity in the data available for obtaining channel depth and the Manning roughness coefficient in hydrological simulations. Therefore, based on previous research on large-scale river dynamics (De Paiva et al., 2013; Neal et al., 2012; Yamazaki et al., 2011; Yu et al., 2006), the Manning roughness coefficient ( $n$ ), the coefficients of the hydraulic geometry ( $B$  and  $W$ ), and the exponent of river bed fraction  $f_b$  are selected for the sensitivity analysis. The selected model parameters are summarized in Table B.3. In particular, the sensitivity analysis consists of perturbing the value of each parameter of the flow routing model in the Yellow River Basin by the factors 0.5, 0 and -0.5.

**Table B.3:** Experimental design for hydrological parameters sensitivity analysis.

Symbol	Name	Unit	Model default	Value
<i>Soil Parameters</i>				
$\beta$	Decay factor of soil saturated hydraulic conductivity	-	calibrated in subbasins as 0.028, 0.035, 0.15 and $0.12 \times K_{sat}$	$\times 0.5$ , 1.0, 1.5
$C_s$	hydraulic conductance of stream-aquifer interconnection	$s^{-1}$	calibrated in subbasins as $10^{-7}$ , $10^{-6}$ , $10^{-6}$ and $10^{-6}$	$\times 0.1$ , 1.0, 10
<i>River routing parameters</i>				
$w$	Channel width	m	$5.0 Q_{BF}^{0.5}$	$\times 0.5$ , 1.0, 1.5
$d$	Channel depth	m	$0.6 Q_{BF}^{0.3}$	$\times 0.5$ , 1.0, 1.5
$n$	Manning roughness coefficient	$s m^{-1/3}$	calibrated in subbasins as 0.025, 0.025, 0.01, 0.01	$\times 0.5$ , 1.0, 1.5
$\alpha$	an exponent used to calculate the fraction of the riverbed	-	0.5	0.4, 0.5, 0.8

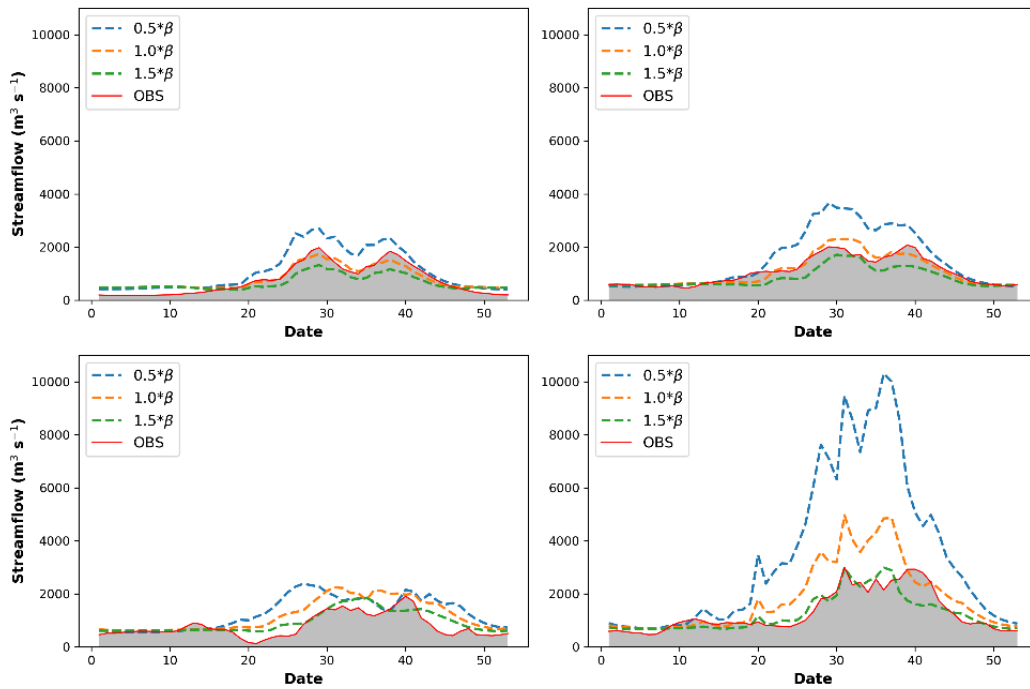


**Figure B.2:** Annual cycles of averaged weekly streamflow for the period of 1979-1988 at six main hydrological stations of the Yellow River, TangnaiHe (a), Lanzhou (b), Toudaoguai (c) and Huayuankou (e), with standard infiltration scheme  $0.5\beta$  (blue dashed line),  $1.0\beta$  (orange dashed line),  $1.5\beta$  (green dashed line) and observed discharge (red solid line with a grey fill), where  $\beta$  is the decay factor of soil saturated hydraulic conductivity.

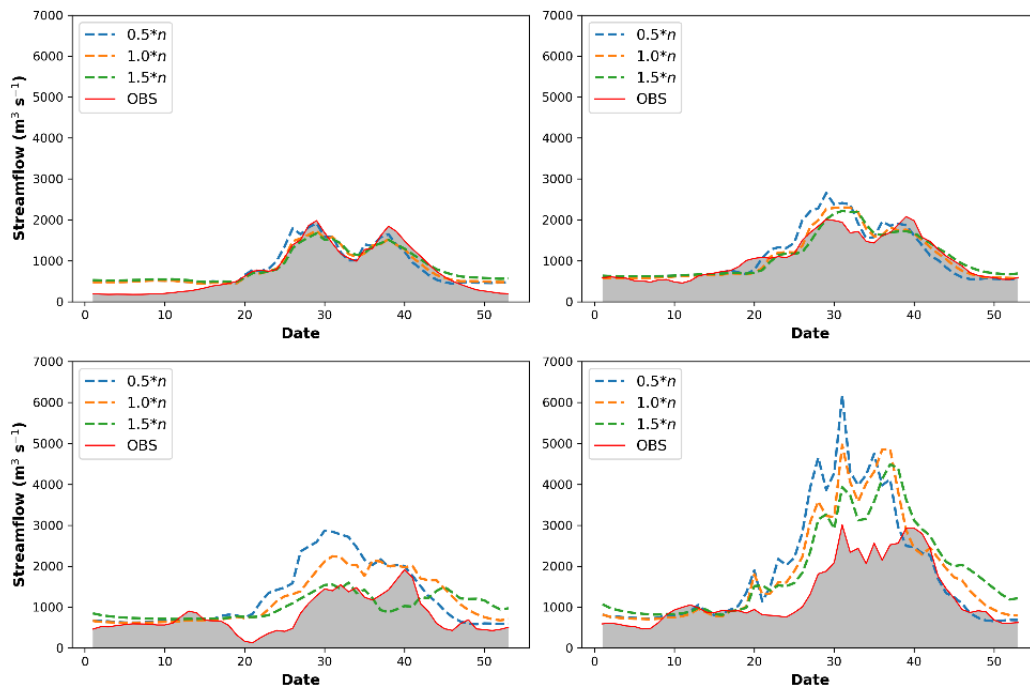


**Figure B.3:** Annual cycles of averaged weekly streamflow for the period of 1979-1988 at four main stations of Yellow River, Tangnaihe (a), Lanzhou (b), Toudaoguai (c) and Huayuankou (d), with Manning roughness coefficient of river  $n \times 0.5$  (blue),  $n$  (orange),  $n \times 1.5$  (green), observed discharge (red solid line with a grey fill).

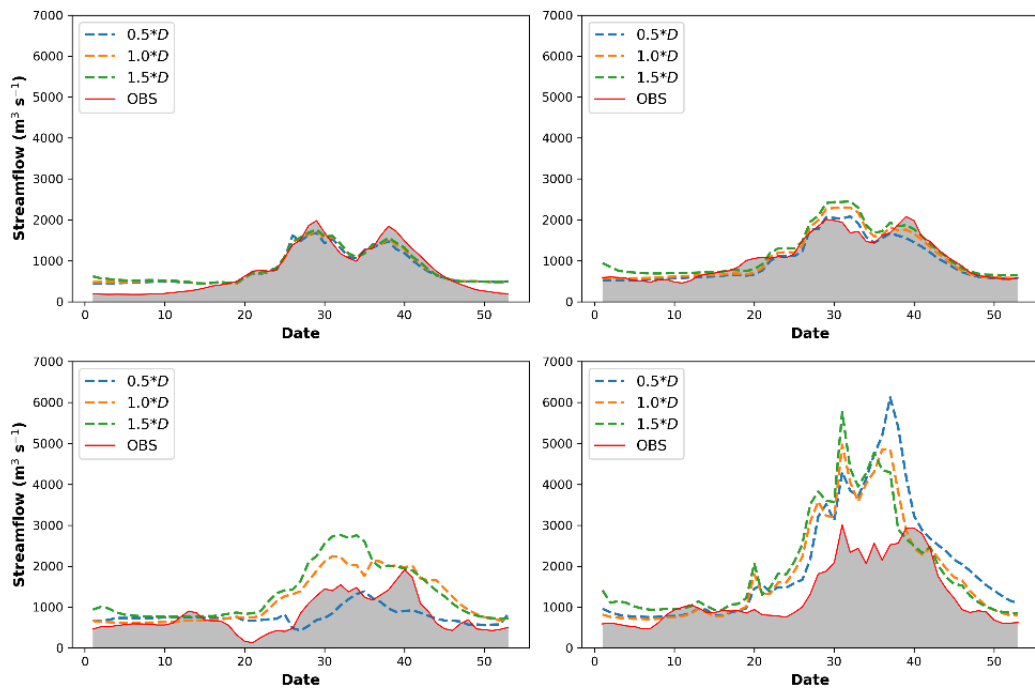


**Figure B.4:** Annual cycles of averaged weekly streamflow for the period of 1979-1988 at four main stations of the Yellow River, Tangnaihe (a), Lanzhou (b), Toudaoguai (c) and Huayankou (d), with the depth of river  $B \times 0.5$  (blue),  $B$  (orange),  $B \times 1.5$  (green), observed discharge (red solid line with a grey fill).

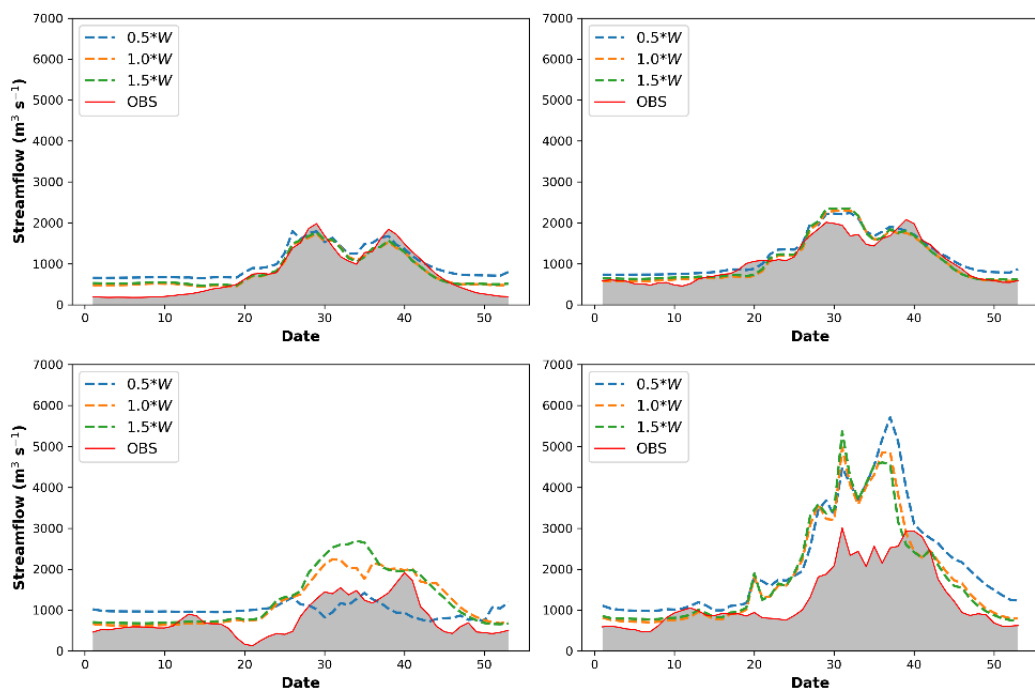


**Figure B.5:** Annual cycles of averaged weekly streamflow for the period of 1979-1988 at four main stations of Yellow River, Tangnaihe (a), Lanzhou (b), Toudaoguai (c) and Huayankou (d), with the width of the river  $W \times 0.5$  (blue),  $W$  (orange),  $W \times 1.5$  (green), observed discharge (red solid line with a grey fill).

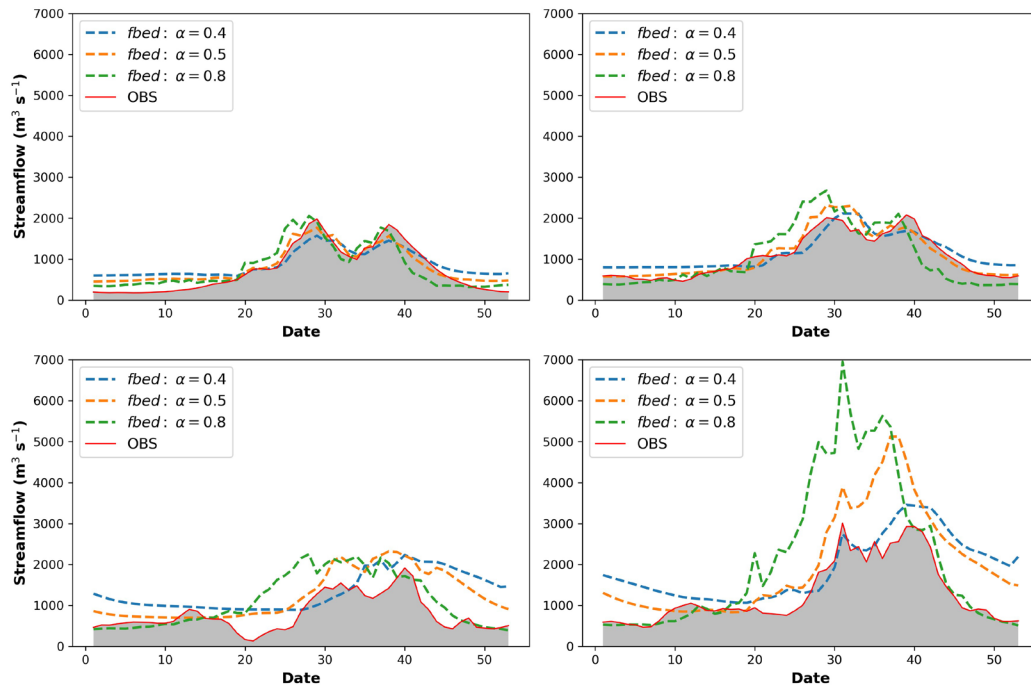


**Figure B.6:** Annual cycles of averaged weekly streamflow for the period of 1979-1988 at four main stations of the Yellow River, Tangnaihe (a), Lanzhou (b), Toudaoguai (c) and Huayuankou (d), with an exponent of the fraction of riverbed  $\alpha=0.4$  (blue), 0.5 (orange), 0.8 (green), observed discharge (red solid line with a grey fill).

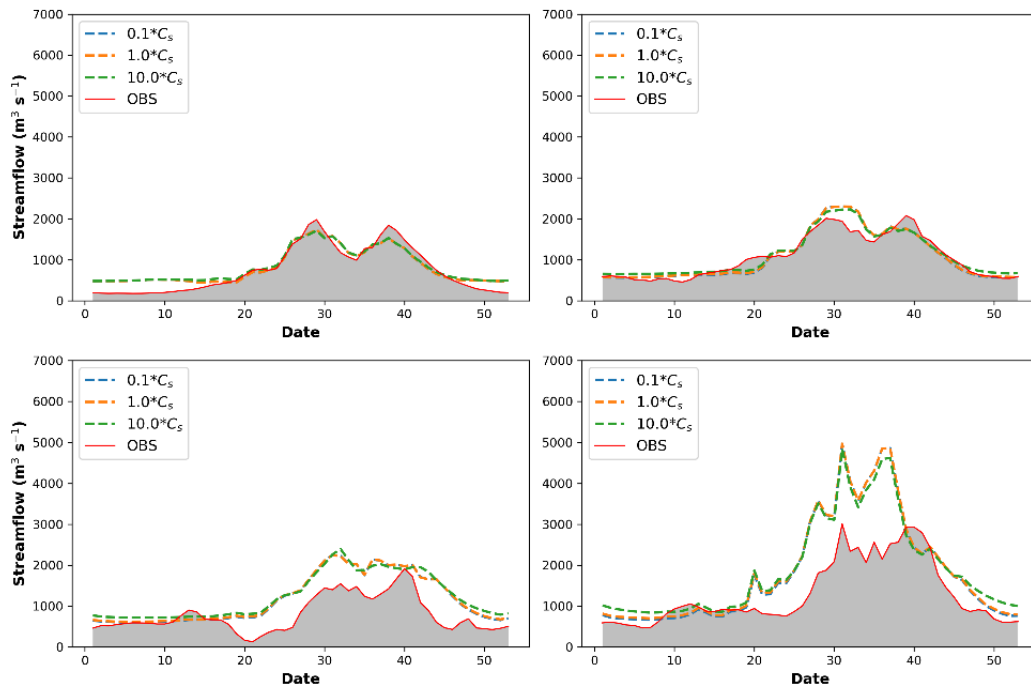


**Figure B.7:** Annual cycles of averaged weekly streamflow for the period of 1979-1988 at four main stations of the Yellow River, Tangnaihe (a), Lanzhou (b), Toudaoguai (c) and Huayuankou (d), with hydraulic conductance of stream-aquifer interconnection  $C_s=0.4$  (blue), 0.5 (orange), 0.8 (green), observed discharge (red solid line with a grey fill).

## B.7 Spatial Distribution of the Hydrological Variables

Figure B.8 shows the spatial distribution of hydrological variables including (a) precipitation, (b) evapotranspiration, (c) runoff, (d) streamflow, (e) soil moisture, (f) groundwater depth, (g) surface runoff and (h) subsurface runoff in the Yellow River Basin, averaged annually from 1979 to 1988. As shown in Fig. B.8a, the Yellow River Basin has a very uneven distribution of precipitation. In particular, this precipitation decreases considerably from south (700-1000 mm yr<sup>-1</sup>) to north (100-200 mm yr<sup>-1</sup>). Moreover, the precipitation distribution correlates strongly with the evapotranspiration map (Fig.B.8b), and appears consistent with the occurrence of two major runoff areas in the southern part of the Yellow River Basin, i.e., the upper reaches and the Wei He River Basin (Fig. B.8c). Furthermore, it can be seen in Fig. B.8d that the river network and flow magnitude predicted by the model match the corresponding observations. Figure B.8e shows that the maximum and minimum values of soil moisture are in the upper reaches and in the arid to semi-arid middle reaches of Yellow River Basin, respectively, and that the spatial distribution of soil moisture follows closely the river network. Moreover, groundwater depth exceeds 25 m over most of the Yellow River Basin (Fig. B.8f), except for the main river networks and the lower reaches – which have groundwater levels under 10 m. Figure B.8g shows that the distributions of runoff and surface runoff are consistent with each other, while it can be seen from Fig. B.8h that subsurface runoff is mainly generated in the upper reaches, with the Yellow River recharging groundwater from Lanzhou to Toudaoguai.

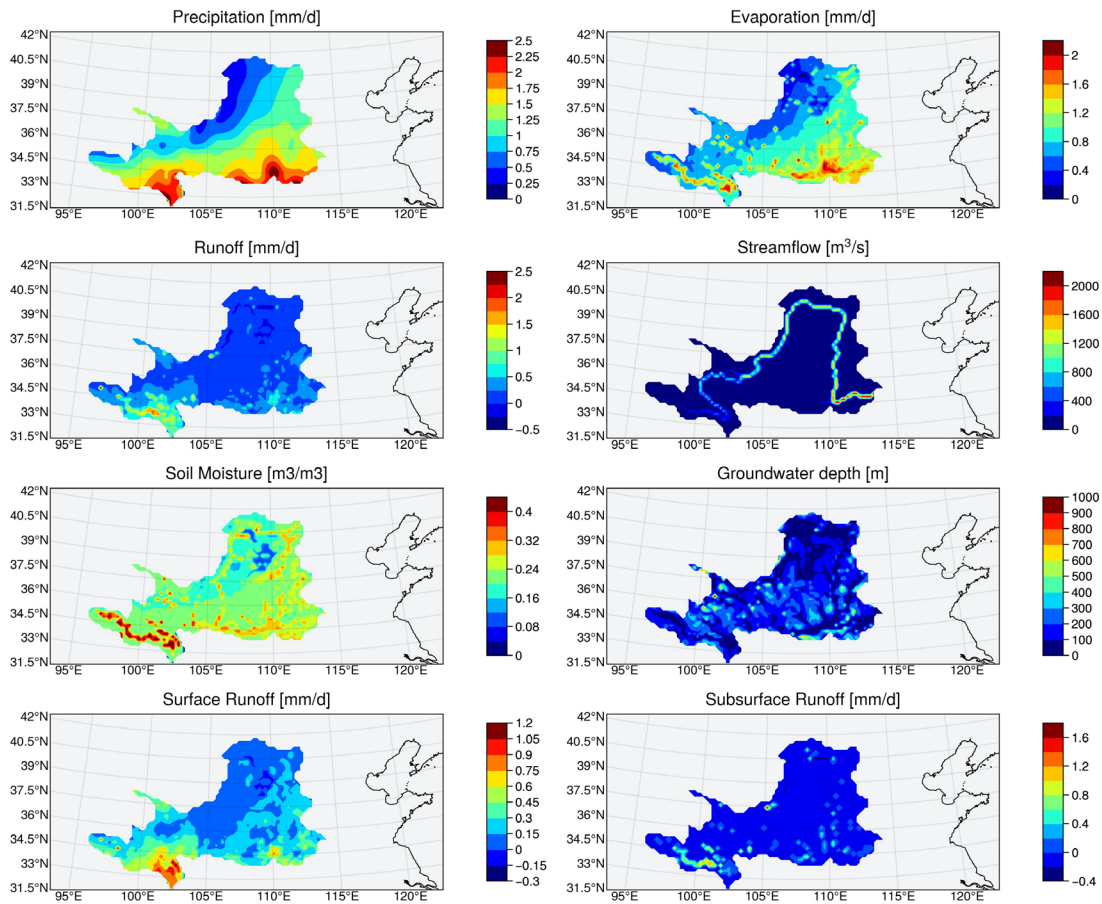


**Figure B.8:** Spatial distribution of mean annual (a) precipitation, (b) evapotranspiration, (c) runoff, (d) streamflow, (e) soil moisture, (f) groundwater depth, (g) surface runoff, (h) subsurface runoff, averaged over 1979-1988, at the Yellow River Basin.

## B.8 Calibration and Sensitivity Analysis of Irrigation Model Parameters

**Table B.4:** Experimental design for calibration and validation of irrigation model.

Experiment name	Irrigation scheme	Irrigation parameters	Objective
NO_IRR	No	No	As a reference with the calibrated hydrological parameters at the basin scale
CNTL_IRR	Yes	IRR_FRAC=0.25, IR_RAIN= 1.00, IRR_MAD=0.5, IRR_LAI=0.6, FILOSS=0.1	As a reference with the calibrated hydrological and irrigation parameters at the basin scale
MAD_0.4	Yes	Same as CNTL_IRR, but with IRR_MAD=0.4	To test the model sensitivity to IRR_MAD
MAD_0.6	Yes	Same as CNTL_IRR, but with IRR_MAD=0.6	
LAI_0.8	Yes	Same as CNTL_IRR, but with IRR_LAI=0.8	To test the model sensitivity to IRR_LAI
LAI_1.0	Yes	Same as CNTL_IRR, but with IRR_LAI=1.0	
ONLY STRAM	Yes, but sink term $Q_{irr\_sf}$ in flow routing model only irrigate the main streams flow across cells	Same as CNTL_IRR	As a reference with only irrigating the grid cells the streams flow across

**Table B.5:** Comparison of statistical and simulated areal average annual irrigation in the Yellow River Basin, as well as the NSE of monthly streamflow at outlet of YRB (HYK) from 1979 to 1987 ( $\text{mm yr}^{-1}$ ).

Experiment	River irrigation			Groundwater irrigation			Total irrigation			NSE
	Statistics	Sim	PE (%)	Statistics	Sim	PE (%)	Statistics	Sim	PE (%)	
CNTL_IRR	20.45	14.89	- 27.19	8.29	11.16	34.98	28.74	26.05	<b>-9.36</b>	<b>0.55</b>
MAD_0.4		9.89	- 51.64		6.66	-7.49		16.55	- 42.41	0.53
MAD_0.6		22.66	10.81		19.99	141.13		42.65	48.40	0.50
LAI_0.8		14.39	- 29.63		9.60	15.80		23.99	- 16.53	0.52
LAI_1.0		13.70	- 33.00		9.45	14.00		23.15	- 19.45	0.53
ONLY STRAM		<b>1.81</b>	- 91.15		10.55	27.26		12.36	- 57.00	<b>0.35</b>

## Appendix C

### Supplemental Material for *Evaluation of Precipitation-Reanalysis Products for Regional Hydrological Modelling*

Cong Jiang <sup>a</sup>, Eric J. R. Parteli <sup>b</sup>, Qian Xia <sup>c</sup> and Yaping Shao <sup>a</sup>

<sup>a</sup>*Institute for Geophysics and Meteorology, University of Cologne, Pohligstr. 3, Cologne, 50969, North Rhine-Westphalia, Germany*

<sup>b</sup>*Faculty of Physics, University of Duisburg-Essen, Duisburg, Lotharstr. 1, 47057, North Rhine-Westphalia, Germany*

<sup>c</sup>*School of Water Resources and Hydropower Engineering, Wuhan University, Bayi Road. 299, 430072, Hubei Province, China*

#### C.1 Required Meteorological Variables for Offline AHMS

**Table C.1:** List of meteorological variables required to run AHMS in an offline mode.

Number	Name	Meteorological variables	Unit
1	Wind	Near-surface wind speed	m s <sup>-1</sup>
2	Tair	Near-surface air temperature	K
3	PSurf	Surface air pressure	N m <sup>-2</sup>
4	Qair	Near-surface specific humidity	kg kg <sup>-1</sup>
5	LWdown	Surface downward longwave radiation	W m <sup>-2</sup>
6	SWdown	Surface downward shortwave radiation	W m <sup>-2</sup>
7	Rainf	Rainfall flux	kg m <sup>-2</sup> s <sup>-1</sup>
8	Snowf	Snowfall flux	kg m <sup>-2</sup> s <sup>-1</sup>

#### C.2 Irrigation Scheme in AHMS-IRR

The present work adopts the irrigation scheme AHMS-IRR developed by Jiang et al. (2022) for arid and semi-arid river basins, which is briefly described below.

The soil moisture deficit method calculates the irrigation water requirements, i.e., when, where and how much water is required to irrigate (Ozdogan et al., 2010; Xu et al., 2019). The equations for the integrated soil moisture availability (SMA) in root zones and irrigation water requirements (IWR) are,

$$SMA = \frac{SM - SM_{wlt}}{SM_{ref} - SM_{wlt}} \quad (C.1)$$

$$IWR = (SM_{ref} - SM) \cdot F_{veg} \cdot F_{crop} \cdot (1.0 + F_{iloss}) \quad (C.2)$$

where  $SM$  represents the integrated soil moisture [m];  $SM_{ref}$  and  $SM_{wlt}$  are the integrated field capacity and wilting point in the root zone [m], respectively;  $F_{veg}$  is the vegetation fraction, taken from the MODIS-based climatological dataset from 2001 to 2012 (Broxton et al., 2014);  $F_{crop}$  represents the associated 500-m MODIS-based irrigation fraction (Ozdogan & Gutman, 2008), and  $F_{iloss}$  is the fraction of flood irrigation loss, and is set as 0.1 in this study.

The actual total irrigation water flow  $Q_{irr}$  is related to both surface water and groundwater irrigation. However, this actual irrigation flow is limited by the availability of surface water in rivers and lakes. The following formulae applies,

$$Q_{irr} = Q_{irr,sf} + Q_{irr,gw} \quad (C.3)$$

$$Q_{irr,sf} = \min(I_{max} * A_g * F_{irr,sw}, W_{sf,avail}) \quad (C.4)$$

$$Q_{irr,gw} = I_{max} * A_g * F_{irr,gw} \quad (C.5)$$

$$IWRR(t) = \max\left(IWRR(t-1) - \frac{Q_{irr} * \Delta t}{A_g}, 0\right) \quad (C.6)$$

where  $Q_{irr,sf}$  and  $Q_{irr,gw}$  represent the actual irrigation water flow from surface water and groundwater [ $m^3 s^{-1}$ ], respectively;  $F_{irr,sw}$  and  $F_{irr,gw}$  are the corresponding area fractions of surface water (river) and groundwater irrigation according to the ‘‘Global Map of Irrigation Areas’’ (Siebert et al., 2005);  $I_{max}$  is the infiltration capacity [ $m s^{-1}$ ], and  $A_g$  denotes the grid area [ $m^2$ ]. Moreover,  $W_{sf,avail}$  denotes the available surface water in the river or lake according to the channel routing model [ $m^3 s$ ]. We assume that groundwater is sufficient to meet irrigation demand.  $IWRR(t)$  and  $IWRR(t-1)$  denote the remaining irrigation water demand [m] at times  $t$  and  $t-1$ , respectively, while  $\Delta t$  is the time step.

### C.3 Evaluation Metrics for Performance

**Table C.2:** Evaluation metrics, range, and perfect agreement value.

Evaluation metrics	Range	The value indicates perfect agreement
Nash–Sutcliffe model efficiency coefficient (NSE)	$(-\infty, 1]$	1
Root mean square error (RMSE)	$[0, +\infty)$	0
Pearson correlation coefficient (PCC)	$[-1, 1]$	1
Mean absolute error (MAE)	$[0, +\infty)$	0
Mean absolute percentage error (MAPE)	$[0, +\infty)$	0
Relative error in percent (BIAS)	$[-\infty, +\infty)$	0
Modified Kling-Gupta efficiency (mKGE)	$(-\infty, 1]$	1

#### C.4 Calibration of Rainfall-Runoff Model

In our study, the soil saturation hydraulic conductivity is derived from the default soil parameter table (SOILPARM.TBL) of the Noah-MP land surface model (Chen & Dudhia, 2001; Niu et al., 2011). They are further calibrated in four sub-basins, namely, Headwater-Tangnaihai (HW-TNH), Tangnaihai-Lanzhou (TNH-LZ), Lanzhou-Toudaouai (LZ-TDG) and Toudaoguai-Huanyuankou (TDG-HYK), as shown in Table C.3.

**Table C.3:** Calibrated soil parameters against observed runoff in the sub-basins.

Para	The soil saturated hydraulic conductivity ( $\times K_{sat}$ ) in sub-basins			
	1	2	3	4
1	0.039	0.060	0.400	0.300
2	0.020	0.035	0.250	0.140
3	0.008	0.020	0.100	0.080
4	0.010	0.025	0.250	0.130
5	0.025	0.035	0.200	0.150
6	1.000	1.000	0.300	0.090
7	0.065	0.100	0.400	0.280

As seen in Table C.4, during the calibration period, in the upper reaches of the Yellow River Basin, which is rarely affected by human activity, the BIAS of the gauge-corrected reanalysis products is calibrated to less than 10% (except for NCEP/NCAR at LZ station BIAS=25%). In the middle reaches of the basin, where irrigation has large influence on the water balance (Jiang et al., 2022), the BIAS of the gauge-corrected reanalysis products is calibrated to less than 15% (except for CMFD at TDG station BIAS=23%). The slightly larger errors in the sub-basin areal runoff for the NCEP/NCAR at LZ station and CMFD at TDG station may be due to the lack of further calibration of other parameters (e.g. hydraulic conductivity of the

riverbed). However, this error is within acceptable limits, while further increasing the number of considered parameters would make the parameter calibration process substantially more difficult.

**Table C.4:** Simulated and observed mean annual area runoff from 1979 to 1987 in the Yellow River Basin including four subbasins, Sub-basins 1 (HW-TNH), Sub-basins 2 (TNH-LZ), Sub-basins 3 (LZ-TDG) and Sub-basins 4 (TDG-HYK).

Para	Areal Runoff (mm)											
	Sub-basins 1			Sub-basins 2			Sub-basins 3			Sub-basins 4		
	Observed runoff	Simulated runoff minus Irrigation	BIAS	Observed runoff	Simulated runoff minus irrigation	BIAS	Observed runoff	Simulated runoff minus irrigation	BIAS	Observed runoff	Simulated runoff minus irrigation	BIAS
1 calibration	210.96	203.32	3.62	100.92	107.39 - 1.62=105.77	4.80	-53.34	9.57-54.82 =-45.25	15.17	48.57	51.08-3.17 = 47.91	1.36
1 validation	171.11	188.00	9.54	101.94	111.06-1.31=109.75	7.66	-53.92	10.26-47.58 =-37.31	30.80	46.09	40.62-3.53 =37.09	19.53
2 calibration	210.96	209.21	0.83	100.92	99.12-1.48 =97.64	3.25	-53.34	6.48-47.46 =-40.98	23.17	48.57	47.85-2.68 =45.17	7.00
2 validation	171.11	195.59	14.30	101.94	98.02-1.03 =96.99	4.86	-53.92	8.83-44.73 =-35.90	33.43	46.09	41.44-2.78 =38.66	16.12
3 calibration	210.96	201.66	4.40	100.92	107.69-2.66 =105.03	4.07	-53.34	22.94-74.63 =-51.69	3.09	48.57	55.47-4.52 =50.95	4.90
3 validation	171.11	190.05	11.07	101.94	114.70-2.13 =112.57	10.43	-53.92	24.31-77.22 =-52.91	1.87	46.09	44.74-6.55 =38.19	17.14
4 calibration	210.96	200.60	4.91	100.92	98.80-2.17 =96.63	4.25	-53.34	12.49-59.30 =-46.81	12.24	48.57	53.21-4.21 =49.00	0.89
4 validation	171.11	192.49	12.49	101.94	107.87-1.85 =106.02	4.00	-53.92	10.87-66.34 =-55.47	2.87	46.09	42.56-6.20 =36.36	21.11
5 calibration	210.96	205.92	2.39	100.92	104.04-1.53 =102.51	1.58	-53.34	14.44-60.10 =-45.66	14.40	48.57	48.41-3.10 =45.31	6.71
5 validation	171.11	190.89	11.56	101.94	109.96-1.29 =108.67	6.60	-53.92	16.75-53.17 =-36.42	32.46	46.09	41.96-3.71 =38.25	17.01
6 calibration	210.96	233.88	10.86	100.92	126.99-2.07 =126.43	25.28	-53.34	9.53-58.98 =-49.46	7.26	48.57	54.03-4.18 =49.85	0.58
6 validation	171.11	268.56	56.95	101.94	146.21-2.46=143.75	41.01	-53.92	11.87-46.91 =-35.04	35.01	46.09	59.00-2.45 =56.55	22.69

7 calibration	210.96	202.30	4.10	100.92	102.32-1.03 =101.29	0.37	-53.34	9.48-42.77 =-33.29	37.59	48.57	48.04-1.71 =46.33	4.61
7 validation	171.11	218.34	27.6	101.94	123.93-0.88 =123.05	20.71	-53.92	11.67-37.55 =-25.88	52.00	46.09	51.53-1.86 =49.47	7.33

### C.5 Performance Evaluation Using Offline Atmospheric and Hydrological Modelling System (AHMS)

**Table C.5:** Comparison of monthly streamflow simulated with gauge-calibrated parameters using seven different precipitation products and observed streamflow.

Precipitation products	Tangnaihe		Lanzhou		Toudaoguai		Huayuankou		Mean	
	NSE	mKGE	NSE	mKGE	NSE	mKGE	NSE	mKGE	NSE	mKGE
Calibration period										
OBS	0.77	0.86	0.46	0.61	0.03	0.54	0.47	0.73	0.43	0.69
CMFD	0.49	0.57	0.21	0.55	-0.16	0.27	-0.42	0.08	0.03	0.37
GLDAS 2.0	-0.49	-0.20	-1.02	-0.14	-1.07	-0.51	-1.20	-0.61	-0.95	-0.37
WFDE5/CRU	-0.32	0.03	-0.76	0.15	-0.79	-0.19	-0.95	-0.36	-0.71	-0.09
WFDE5/(CRU+GPCC)	0.54	0.59	0.32	0.60	-0.18	0.27	-0.52	-0.02	0.04	0.36
NCEP/NCAR	-2.13	-0.15	-6.44	-0.20	-7.46	-0.65	-0.53	0.32	-4.14	-0.17
ERA5	0.53	0.52	0.12	0.62	-0.59	0.37	0.40	0.63	0.12	0.54
Validation period										
OBS	<b>0.82</b>	<b>0.82</b>	0.51	0.59	-0.18	0.58	0.43	0.70	0.40	0.67
CMFD	<b>0.72</b>	<b>0.73</b>	<b>0.40</b>	<b>0.62</b>	0.03	0.42	-0.43	<b>0.14</b>	<b>0.18</b>	<b>0.48</b>
GLDAS 2.0	-0.29	0.07	-0.89	0.17	-1.09	-0.33	-1.31	-0.47	-0.90	-0.14
WFDE5/CRU	-0.08	0.26	-0.56	0.36	-0.94	-0.17	-1.18	-0.30	-0.69	0.04
WFDE5/(CRU+GPCC)	<b>0.75</b>	<b>0.72</b>	<b>0.54</b>	<b>0.69</b>	-0.06	0.32	-0.50	<b>0.05</b>	<b>0.18</b>	<b>0.45</b>
NCEP/NCAR	-6.50	-0.64	-15.51	-0.62	-19.23	-1.33	-3.53	-0.12	-11.19	-0.68
ERA5	0.01	0.17	-0.94	0.35	-3.67	-0.27	-0.44	0.32	-1.26	0.14

**Table C.6:** Same as Table C.5, but with recalibrated parameters for each of the six precipitation products (Scenario 2).

Precipitation products	Tangnaihe		Lanzhou		Toudaoguai		Huayuankou		Mean	
	NSE	mKGE	NSE	mKGE	NSE	mKGE	NSE	mKGE	NSE	mKGE
Calibration period										
OBS	0.77	0.86	0.46	0.61	0.03	0.54	0.47	0.73	0.43	0.69
CMFD	0.78	0.82	0.54	0.71	0.19	0.65	0.51	0.74	0.51	0.73
GLDAS 2.0	0.82	0.83	0.57	0.76	0.08	0.60	0.49	0.74	0.49	0.73
WFDE5/CRU	0.83	0.82	0.63	0.76	0.19	0.64	0.49	0.72	0.54	0.74
WFDE5/(CRU+GPCC)	0.77	0.76	0.60	0.76	0.23	0.65	0.52	0.70	0.53	0.72
NCEP/NCAR	0.68	0.65	0.70	0.85	0.33	0.66	0.50	0.65	0.55	0.70
ERA5	0.57	0.56	0.49	0.66	0.08	0.47	0.51	0.59	0.41	0.57
Validation period										
OBS	<b>0.82</b>	<b>0.82</b>	0.51	0.59	-0.18	0.58	0.43	0.70	0.40	0.67
CMFD	0.77	0.77	0.57	0.64	0.07	0.64	0.60	<b>0.81</b>	<b>0.50</b>	<b>0.72</b>
GLDAS 2.0	0.77	0.78	0.38	0.64	-0.14	0.58	0.61	0.80	0.41	0.70
WFDE5/CRU	0.72	0.77	0.32	0.60	0.17	0.67	0.59	0.77	0.45	0.70
WFDE5/(CRU+GPCC)	<b>0.81</b>	<b>0.78</b>	<b>0.62</b>	<b>0.74</b>	0.11	0.63	<b>0.61</b>	<b>0.81</b>	<b>0.54</b>	<b>0.74</b>
NCEP/NCAR	0.13	0.36	-0.51	0.53	-2.08	0.10	0.42	0.40	-0.51	0.35
ERA5	0.62	0.46	0.52	0.67	-0.33	0.30	0.47	0.58	0.32	0.50

**Table C.7:** Root-Mean-Square Error (RMSE) and Nash-Sutcliffe Efficiency (NSE) computed between the measured and simulated evapotranspiration produced by the numerical experiments for the period January 1980 to December 1987.

Scenario	Setup	Precipitation products	Basin			
			RMSE	MAE	NSE	$r^2$
I	1	OBS	6.56	4.79	0.90	0.979
	2	CMFD	6.77	5.00	0.89	0.983
	3	GLDAS 2.0	6.68	4.90	0.90	0.978
	4	WFDE5/CRU	6.78	5.02	0.89	0.981
	5	WFDE5/(CRU+GPCC)	7.42	5.44	0.87	0.982
	6	NCEP/NCAR	9.24	7.69	0.80	0.985
	7	ERA5	11.90	9.57	0.67	0.982
II	8	CMFD	5.90	4.39	0.92	0.982
	9	GLDAS 2.0	5.11	4.02	0.94	0.975
	10	WFDE5/CRU	5.13	3.90	0.94	0.979
	11	WFDE5/(CRU+GPCC)	6.41	4.67	0.91	0.980
	12	NCEP/NCAR	9.32	7.76	0.80	0.985
	13	ERA5	12.52	10.05	0.64	0.983

## Appendix D

### Supplemental Material for *A Model for Continental-Scale Water Erosion and Sediment Transport and Its Application to the Yellow River Basin*

Cong Jiang<sup>a</sup>, Eric J. R. Parteli<sup>b</sup> and Yaping Shao<sup>a</sup>

<sup>a</sup>*Institute for Geophysics and Meteorology, University of Cologne, Pohligstr. 3, Cologne, 50969, North Rhine-Westphalia, Germany*

<sup>b</sup>*Faculty of Physics, University of Duisburg-Essen, Duisburg, Lotharstr. 1, 47057, North Rhine-Westphalia, Germany*

#### D.1 Definition of Slope and Interpolation Method

In a raster dataset, the slope is defined as the steepness of the terrain or the steepest gradient at each cell or pixel. It represents how quickly the elevation changes from one cell to another. The calculation of slope is typically carried out using elevation data, such as a Digital Elevation Model (DEM), within a three-by-three cell neighbourhood, utilizing a moving window approach. The slope for the central cell is determined using the following formula:

$$S_{radians} = \arctan \left[ \left( \frac{dz}{dx} \right)^2 + \left( \frac{dz}{dy} \right)^2 \right] \quad (D.1)$$

where  $S_{radian}$  is the slope in radians,  $dz/dx$  represents the rate of change in elevation in the x-direction, and  $dz/dy$  represents the rate of change in elevation in the y-direction.

The method of interpolation using the four-point bilinear interpolation method from the WRF Preprocessing System (WPS). Four-point bi-linear interpolation requires four nearby source points to interpolate a value at a target point  $(x, y)$ . It involves linear interpolation between these neighbouring points in both the x and y directions.

## D.2 Observed and Predicted Sediment Discharge at Five Stations

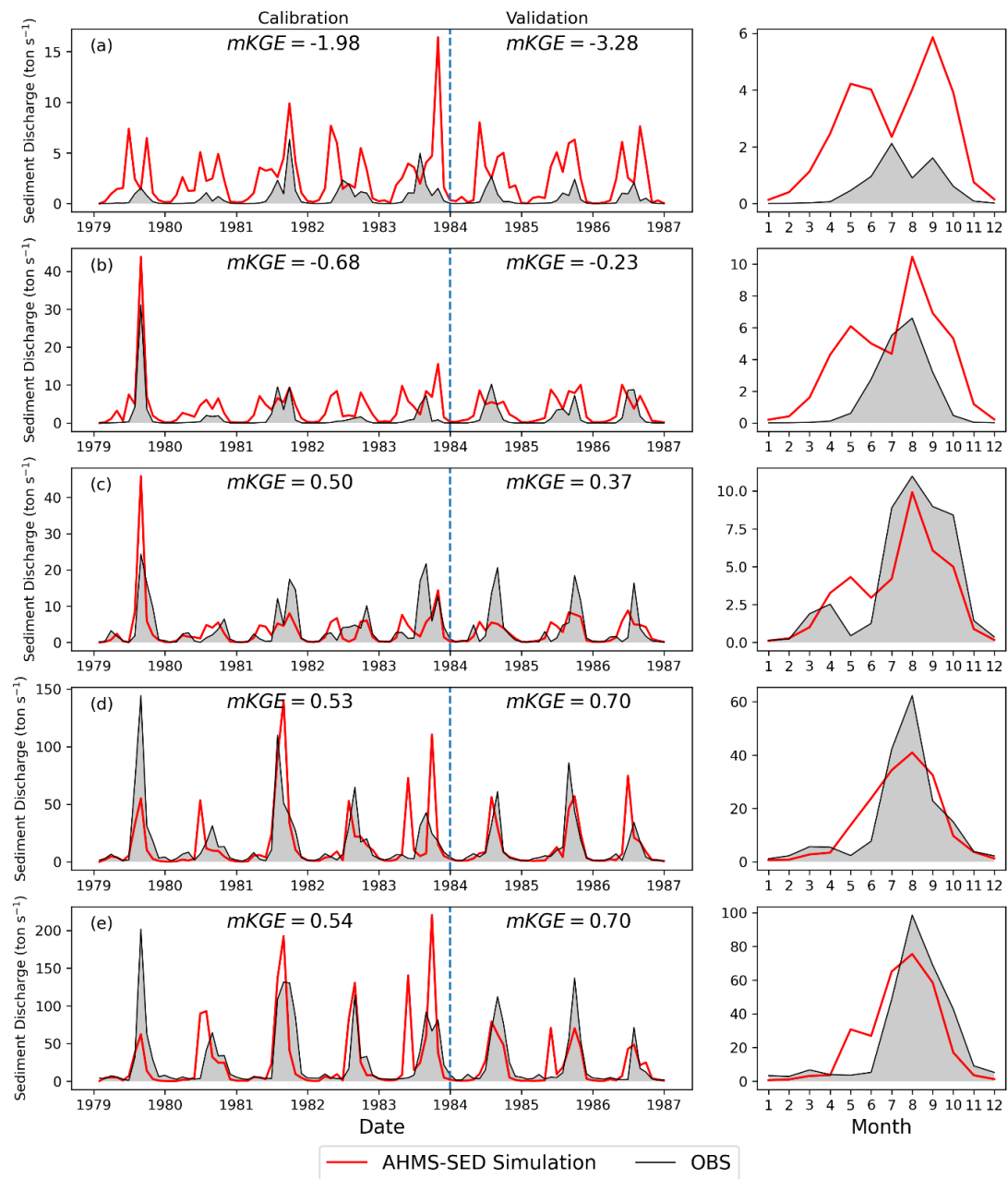


**Figure D.1:** Same as Fig. 6.2 but use the runoff in the KR equation (EXP 10).

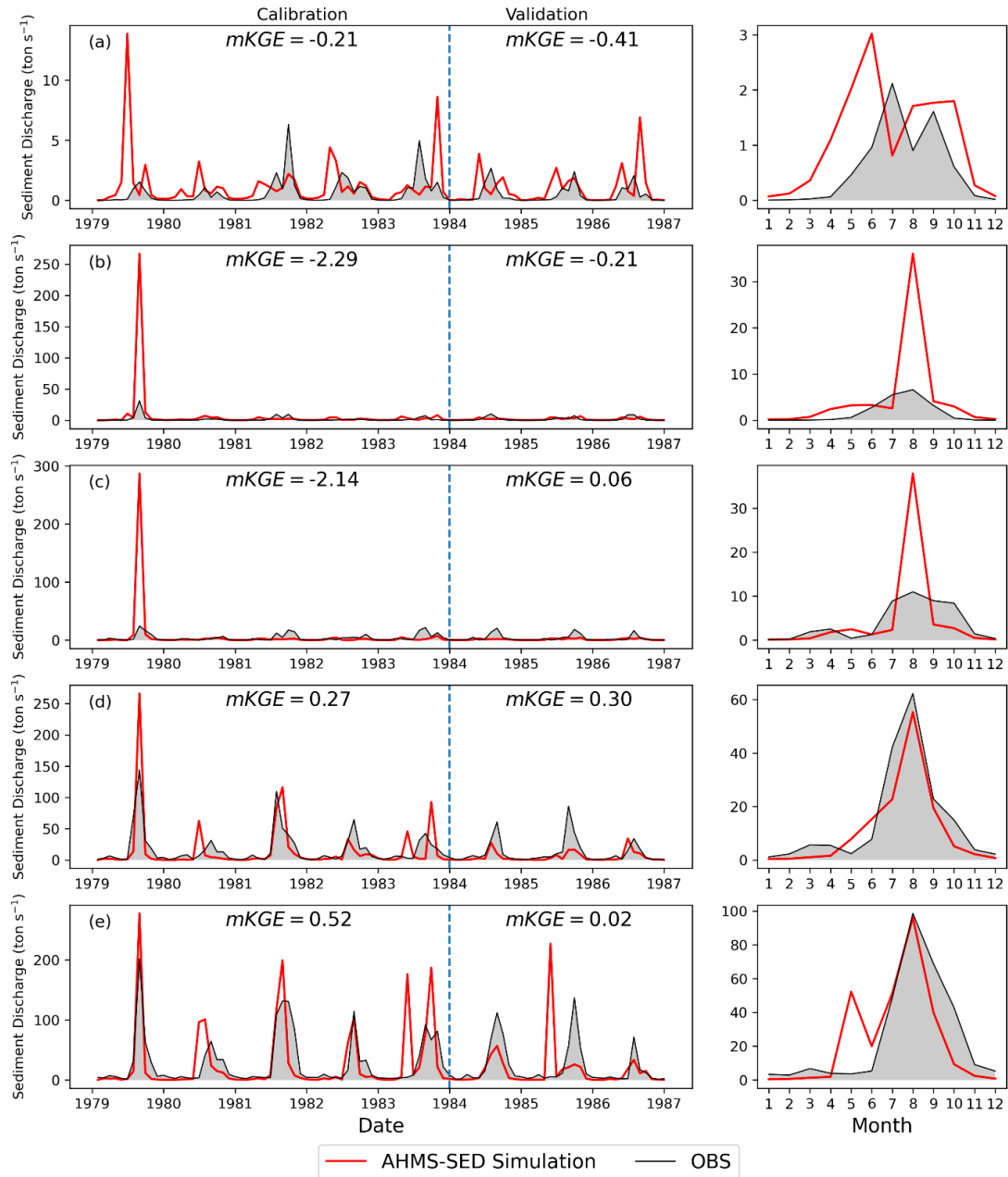


Figure D.2: Same as Fig. 6.2 but use the overland flow in the KR equation (EXP 17).

## Bibliography

- Akan, O. (2006). Open Channel Hydraulics. In *Open Channel Hydraulics*. <https://doi.org/10.1016/B978-0-7506-6857-6.X5000-0>
- Ali, M., Seeger, M., Sterk, G., & Moore, D. (2013). A unit stream power based sediment transport function for overland flow. *CATENA*, *101*, 197–204. <https://doi.org/https://doi.org/10.1016/j.catena.2012.09.006>
- Allen, M. R., & Ingram, W. J. (2002). Constraints on future changes in climate and the hydrologic cycle. In *Nature* (Vol. 419, Issue 6903). <https://doi.org/10.1038/nature01092>
- Amjad, M., Yilmaz, M. T., Yucel, I., & Yilmaz, K. K. (2020). Performance evaluation of satellite- and model-based precipitation products over varying climate and complex topography. *Journal of Hydrology*, *584*, 124707. <https://doi.org/10.1016/j.jhydrol.2020.124707>
- Arnold, J. G., Srinivasan, R., Muttiah, R. S., & Williams, J. R. (1998). LARGE AREA HYDROLOGIC MODELING AND ASSESSMENT PART I: MODEL DEVELOPMENT1. *JAWRA Journal of the American Water Resources Association*, *34*(1), 73–89. <https://doi.org/https://doi.org/10.1111/j.1752-1688.1998.tb05961.x>
- Bacon, D. P., Ahmad, N. N., Boybeyi, Z., Dunn, T. J., Hall, M. S., Lee, P. C. S., Sarma, R. A., Turner, M. D., Waight, K. T., Young, S. H., & Zack, J. W. (2000). A dynamically adapting weather and dispersion model: The operational multiscale environment model with grid adaptivity (OMEGA). *Monthly Weather Review*, *128*(7 I), 2044–2076. [https://doi.org/10.1175/1520-0493\(2000\)128<2044:ADAWAD>2.0.CO;2](https://doi.org/10.1175/1520-0493(2000)128<2044:ADAWAD>2.0.CO;2)
- Bagarello, V., Di Piazza, G. V, Ferro, V., & Giordano, G. (2008). Predicting unit plot soil loss in Sicily, south Italy. *Hydrological Processes*, *22*(5), 586–595. <https://doi.org/https://doi.org/10.1002/hyp.6621>
- Bagnold, R. A. (1966). An Approach to the Sediment Transport Problem from General Physics. *USGS Professional Paper*.
- Bagnold, R. A. (1980). Empirical Correlation of Bedload Transport Rates in Flumes and Natural Rivers. *Proceedings of The Royal Society of London, Series A: Mathematical and Physical Sciences*, *372*(1751), 453–473. <https://doi.org/10.1098/rspa.1980.0122>
- Bates, P. D., Horritt, M. S., & Fewtrell, T. J. (2010). A simple inertial formulation of the shallow water equations for efficient two-dimensional flood inundation modelling. *Journal of Hydrology*, *387*(1–2), 33–45. <https://doi.org/10.1016/j.jhydrol.2010.03.027>
- Bathurst, J. C., & Cooley, K. R. (1996). Use of the SHE hydrological modelling system to investigate basin response to snowmelt at Reynolds Creek, Idaho. *Journal of Hydrology*, *175*(1–4). [https://doi.org/10.1016/S0022-1694\(96\)80011-4](https://doi.org/10.1016/S0022-1694(96)80011-4)
- Beck, H. E., Pan, M., Roy, T., Weedon, G. P., Pappenberger, F., Van Dijk, A. I. J. M.,

- Huffman, G. J., Adler, R. F., & Wood, E. F. (2019). Daily evaluation of 26 precipitation datasets using Stage-IV gauge-radar data for the CONUS. *Hydrology and Earth System Sciences*, 23(1), 207–224. <https://doi.org/10.5194/hess-23-207-2019>
- Beck, H. E., Vergopolan, N., Pan, M., Levizzani, V., Van Dijk, A. I. J. M., Weedon, G. P., Brocca, L., Pappenberger, F., Huffman, G. J., & Wood, E. F. (2017). Global-scale evaluation of 22 precipitation datasets using gauge observations and hydrological modeling. *Hydrology and Earth System Sciences*, 21(12), 6201–6217. <https://doi.org/10.5194/hess-21-6201-2017>
- Beck, H. E., Vergopolan, N., Pan, M., Levizzani, V., van Dijk, A. I. J. M., Weedon, G. P., Brocca, L., Pappenberger, F., Huffman, G. J., & Wood, E. F. (2020). Global-scale evaluation of 22 precipitation datasets using gauge observations and hydrological modeling. *Advances in Global Change Research*, 69(12), 625–653. [https://doi.org/10.1007/978-3-030-35798-6\\_9](https://doi.org/10.1007/978-3-030-35798-6_9)
- Best, M. J., Pryor, M., Clark, D. B., Rooney, G. G., Essery, R. . L. H., Ménard, C. B., Edwards, J. M., Hendry, M. A., Porson, A., Gedney, N., Mercado, L. M., Sitch, S., Blyth, E., Boucher, O., Cox, P. M., Grimmond, C. S. B., & Harding, R. J. (2011). The Joint UK Land Environment Simulator (JULES), model description – Part 1: Energy and water fluxes. *Geoscientific Model Development*, 4(3), 677–699. <https://doi.org/10.5194/gmd-4-677-2011>
- Beven, K. (1989). Changing ideas in hydrology - The case of physically-based models. *Journal of Hydrology*, 105(1–2), 157–172. [https://doi.org/10.1016/0022-1694\(89\)90101-7](https://doi.org/10.1016/0022-1694(89)90101-7)
- Bitew, M. M., Gebremichael, M., Ghebremichael, L. T., & Bayissa, Y. A. (2012). Evaluation of high-resolution satellite rainfall products through streamflow simulation in a hydrological modeling of a small mountainous watershed in Ethiopia. *Journal of Hydrometeorology*, 13(1), 338–350. <https://doi.org/10.1175/2011JHM1292.1>
- Brandt, C. J. (1990). Simulation of the size distribution and erosivity of raindrops and throughfall drops. *Earth Surface Processes and Landforms*, 15(8). <https://doi.org/10.1002/esp.3290150803>
- Brown, L. C., & Foster, G. R. (1987). Storm erosivity using idealized intensity distributions. *Transactions of the ASAE*, 30(2), 379.
- Broxton, P. D., Zeng, X., Scheffic, W., & Troch, P. A. (2014). A MODIS-based global 1-km maximum green vegetation fraction dataset. *Journal of Applied Meteorology and Climatology*, 53(8), 1996–2004. <https://doi.org/10.1175/JAMC-D-13-0356.1>
- Chahine, M. T. (1992). The hydrological cycle and its influence on climate. In *Nature* (Vol. 359, Issue 6394). <https://doi.org/10.1038/359373a0>
- Chamizo, S., Cantón, Y., Lázaro, R., Solé-Benet, A., & Domingo, F. (2012). Crust Composition and Disturbance Drive Infiltration Through Biological Soil Crusts in Semiarid Ecosystems. *Ecosystems*, 15(1), 148–161. <https://doi.org/10.1007/s10021-011-9499-6>
- Chen, F., & Dudhia, J. (2001). Coupling and advanced land surface-hydrology model

- with the Penn State-NCAR MM5 modeling system. Part I: Model implementation and sensitivity. *Monthly Weather Review*, 129(4), 569–585. [https://doi.org/10.1175/1520-0493\(2001\)129<0569:CAALSH>2.0.CO;2](https://doi.org/10.1175/1520-0493(2001)129<0569:CAALSH>2.0.CO;2)
- Chen, J. L., Wilson, C. R., & Tapley, B. D. (2010). The 2009 exceptional Amazon flood and interannual terrestrial water storage change observed by GRACE. *Water Resources Research*, 46(12).
- Chow, V. Te. (1968). Applied hydrology. In *Journal of Hydrology* (Vol. 6, Issue 2). Tata McGraw-Hill Education. [https://doi.org/10.1016/0022-1694\(68\)90169-8](https://doi.org/10.1016/0022-1694(68)90169-8)
- Chow, V. Te, Maidment, D. R., & Mays, L. W. (1988). Applied hydrology. In *Applied Hydrology*.
- Cong, Z., Yang, D., Gao, B., Yang, H., & Hu, H. (2009). Hydrological trend analysis in the Yellow River basin using a distributed hydrological model. *Water Resources Research*, 45(7). <https://doi.org/10.1029/2008WR006852>
- Cucchi, M., P. Weedon, G., Amici, A., Bellouin, N., Lange, S., Müller Schmied, H., Hersbach, H., & Buontempo, C. (2020). WFDE5: Bias-adjusted ERA5 reanalysis data for impact studies. *Earth System Science Data*, 12(3), 2097–2120. <https://doi.org/10.5194/essd-12-2097-2020>
- Cunge, J. A., Holly, F. M., & Verwey, A. (1980). Practical aspects of computational river hydraulics. *Pitman Publishing Ltd. London, (17 CUN), 1980, 420.*
- Cuntz, M., Mai, J., Samaniego, L., Clark, M., Wulfmeyer, V., Branch, O., Attinger, S., & Thober, S. (2016). The impact of standard and hard-coded parameters on the hydrologic fluxes in the Noah-MP land surface model. *Journal of Geophysical Research*, 121(18), 10,676–10,700. <https://doi.org/10.1002/2016JD025097>
- Davis, R. O. E., & Bennett, H. H. (1927). *Grouping of soils on the basis of mechanical analysis*. 419, 1–15.
- de Graaf, I. E. M. de, Sutanudjaja, E. H., Van Beek, L. P. H., & Bierkens, M. F. P. (2015). A high-resolution global-scale groundwater model. *Hydrology and Earth System Sciences*, 19(2), 823–837.
- De Paiva, R. C. D., Buarque, D. C., Collischonn, W., Bonnet, M. P., Frappart, F., Calmant, S., & Bulhões Mendes, C. A. (2013). Large-scale hydrologic and hydrodynamic modeling of the Amazon River basin. *Water Resources Research*, 49(3), 1226–1243. <https://doi.org/10.1002/wrcr.20067>
- De Roo, A. P. J., Wesseling, C. G., & Ritsema, C. J. (1996). LISEM: a single-event physically based hydrological and soil erosion model for drainage basins. I: theory, input and output. *Hydrological Processes*, 10(8), 1107–1117. [https://doi.org/https://doi.org/10.1002/\(SICI\)1099-1085\(199608\)10:8<1107::AID-HYP415>3.0.CO;2-4](https://doi.org/https://doi.org/10.1002/(SICI)1099-1085(199608)10:8<1107::AID-HYP415>3.0.CO;2-4)
- de Vente, J., & Poesen, J. (2005). Predicting soil erosion and sediment yield at the basin scale: Scale issues and semi-quantitative models. *Earth-Science Reviews*, 71(1), 95–125. <https://doi.org/https://doi.org/10.1016/j.earscirev.2005.02.002>
- de Vente, J., Poesen, J., Verstraeten, G., Govers, G., Vanmaercke, M., Van Rompaey, A., Arabkhedri, M., & Boix-Fayos, C. (2013). Predicting soil erosion and

- sediment yield at regional scales: Where do we stand? *Earth-Science Reviews*, 127, 16–29. <https://doi.org/https://doi.org/10.1016/j.earscirev.2013.08.014>
- Dietachmayer, G. S. (1992). Application of continuous dynamic grid adaption techniques to meteorological modeling. Part II: efficiency. *Monthly Weather Review*, 120(8), 1707–1722. [https://doi.org/10.1175/1520-0493\(1992\)120<1707:AOCDDGA>2.0.CO;2](https://doi.org/10.1175/1520-0493(1992)120<1707:AOCDDGA>2.0.CO;2)
- Dietrich, W. E., Bellugi, D. G., Sklar, L. S., Stock, J. D., Heimsath, A. M., & Roering, J. J. (2003). Geomorphic Transport Laws for Predicting Landscape form and Dynamics. In *Prediction in Geomorphology* (pp. 103–132). American Geophysical Union (AGU). <https://doi.org/https://doi.org/10.1029/135GM09>
- Dinku, T., Chidzambwa, S., Ceccato, P., Connor, S. J., & Ropelewski, C. F. (2008). Validation of high-resolution satellite rainfall products over complex terrain. *International Journal of Remote Sensing*, 29(14), 4097–4110. <https://doi.org/10.1080/01431160701772526>
- DuBoys, M. P. (1879). Le Rhône et les rivières à lit affouillable. *Annals de Ponts et Chaussée*, 18(5), 141–195.
- Dutta, S. (2016). Soil erosion, sediment yield and sedimentation of reservoir: a review. In *Modeling Earth Systems and Environment* (Vol. 2, Issue 3). <https://doi.org/10.1007/s40808-016-0182-y>
- Einstein, H. A. (1964). River sedimentation. *Handbook of Applied Hydrology*, Section--17.
- Engelund, F., & Hansen, E. (1967). A monograph on sediment transport in alluvial streams. *Monografia*.
- Everaert, W. (1991). Empirical relations for the sediment transport capacity of interrill flow. *Earth Surface Processes and Landforms*, 16(6), 513–532. <https://doi.org/10.1002/esp.3290160604>
- Ewen, J., Parkin, G., & O'Connell, P. E. (2000). SHETRAN: Distributed River Basin Flow and Transport Modeling System. *Journal of Hydrologic Engineering*, 5(3), 250–258. [https://doi.org/10.1061/\(ASCE\)1084-0699\(2000\)5:3\(250\)](https://doi.org/10.1061/(ASCE)1084-0699(2000)5:3(250))
- Fagundes, H. O., Fan, F. M., Paiva, R. C. D., Siqueira, V. A., Buarque, D. C., Kornowski, L. W., Laipelt, L., & Collischonn, W. (2021). Sediment Flows in South America Supported by Daily Hydrologic-Hydrodynamic Modeling. *Water Resources Research*, 57(2), 1–26. <https://doi.org/10.1029/2020WR027884>
- FAO. (1991). The digitized soil map of the world (release 1.0). In *World Soil Resources Report 67/1*.
- Farr, T. G., Rosen, P. A., Caro, E., Crippen, R., Duren, R., Hensley, S., Kobrick, M., Paller, M., Rodriguez, E., Roth, L., Seal, D., Shaffer, S., Shimada, J., Umland, J., Werner, M., Oskin, M., Burbank, D., & Alsdorf, D. (2007). The Shuttle Radar Topography Mission. *Reviews of Geophysics*, 45(2). <https://doi.org/https://doi.org/10.1029/2005RG000183>
- Feng, W., Zhong, M., Lemoine, J.-M., Biancale, R., Hsu, H.-T., & Xia, J. (2013). Evaluation of groundwater depletion in North China using the Gravity Recovery

- and Climate Experiment (GRACE) data and ground-based measurements. *Water Resources Research*, 49(4), 2110–2118.
- Folland, C. K., Karl, T. R., & Jim Salinger, M. (2002). Observed climate variability and change. *Weather*, 57(8). <https://doi.org/10.1256/004316502320517353>
- Gao, P., Geissen, V., Ritsema, C. J., Mu, X.-M., & Wang, F. (2013). Impact of climate change and anthropogenic activities on stream flow and sediment discharge in the Wei River basin, China. *Hydrology and Earth System Sciences*, 17(3), 961–972. <https://doi.org/10.5194/hess-17-961-2013>
- Gao, Y. C., & Liu, M. F. (2013). Evaluation of high-resolution satellite precipitation products using rain gauge observations over the Tibetan Plateau. *Hydrology and Earth System Sciences*, 17(2), 837–849. <https://doi.org/10.5194/hess-17-837-2013>
- Gao, Y., Li, K., Chen, F., Jiang, Y., & Lu, C. (2015). Assessing and improving Noah-MP land model simulations for the central Tibetan plateau. *Journal of Geophysical Research*, 120(18), 9258–9278. <https://doi.org/10.1002/2015JD023404>
- Genfo, A. D. D., Lacis, A. A., & Ruedy, R. A. (1991). Simulations of the effect of a warmer climate on atmospheric humidity. *Nature*, 351(6325). <https://doi.org/10.1038/351382a0>
- Gochis, D. J., Yu, W., & Yates, D. (2015). The WRF-Hydro model technical description and user's guide, version 3.0. *NCAR Technical Document*, May, 120.
- Govers, G. (1990). Empirical relationships for the transport capacity of overland flow. *IAHS Publication*, 189, 45–63.
- Govers, G. (1992). Evaluation of transporting capacity formulae for overland flow. *Overland Flow Hydraulics and Erosion Mechanics*, 243–273.
- Groisman, P. Y., & Legates, D. R. (1994). The accuracy of United States precipitation data. *Bulletin of the American Meteorological Society*, 75(2), 215–228.
- Gupta, H. V., Kling, H., Yilmaz, K. K., & Martinez, G. F. (2009). Decomposition of the mean squared error and NSE performance criteria: Implications for improving hydrological modelling. *Journal of Hydrology*, 377(1–2). <https://doi.org/10.1016/j.jhydrol.2009.08.003>
- Hajigholizadeh, M., Melesse, A. M., & Fuentes, H. R. (2018). Erosion and sediment transport modelling in shallowwaters: A review on approaches, models and applications. *International Journal of Environmental Research and Public Health*, 15(3). <https://doi.org/10.3390/ijerph15030518>
- Harmon, R. S., Doe III, W. W., & Doe, W. W. (2001). *Landscape erosion and evolution modeling*. Springer Science & Business Media.
- He, J., Yang, K., Tang, W., Lu, H., Qin, J., Chen, Y., & Li, X. (2020). The first high-resolution meteorological forcing dataset for land process studies over China. *Scientific Data*, 7(1), 1–11. <https://doi.org/10.1038/s41597-020-0369-y>
- Hersbach, H., B, B., P, B., S, H., A, H., J, M., J, N., C, P., R, R., D, S., & A, S.

- (2020). The ERA5 global reanalysis. *Quarterly Journal of the Royal Meteorological Society*, 146(730), 1999–2049.
- Hessel, R., & Jetten, V. (2007). Suitability of transport equations in modelling soil erosion for a small Loess Plateau catchment. *Engineering Geology*, 91(1), 56–71. <https://doi.org/10.1016/j.enggeo.2006.12.013>
- Hessel, R., Jetten, V., Baoyuan, L., Yan, Z., & Stolte, J. (2003). Calibration of the LISEM model for a small Loess Plateau catchment. *Catena*, 54(1–2), 235–254. [https://doi.org/10.1016/S0341-8162\(03\)00067-5](https://doi.org/10.1016/S0341-8162(03)00067-5)
- Hirpa, F. A., Gebremichael, M., & Hopson, T. (2010). Evaluation of high-resolution satellite precipitation products over very complex terrain in Ethiopia. *Journal of Applied Meteorology and Climatology*, 49(5), 1044–1051. <https://doi.org/10.1175/2009JAMC2298.1>
- Huntington, T. G. (2006). Evidence for intensification of the global water cycle: Review and synthesis. *Journal of Hydrology*, 319(1–4), 83–95. <https://doi.org/10.1016/j.jhydrol.2005.07.003>
- Izadi, N., Karakani, E. G., Saadatabadi, A. R., Shamsipour, A., Fattahi, E., & Habibi, M. (2021). Evaluation of era5 precipitation accuracy based on various time scales over iran during 2000–2018. *Water (Switzerland)*, 13(18), 2538. <https://doi.org/10.3390/w13182538>
- Jia, Y., Wang, H., Zhou, Z., Qiu, Y., Luo, X., Wang, J., Yan, D., & Qin, D. (2006). Development of the WEP-L distributed hydrological model and dynamic assessment of water resources in the Yellow River basin. *Journal of Hydrology*, 331(3–4), 606–629. <https://doi.org/10.1016/j.jhydrol.2006.06.006>
- Jiang, C., Parteli, E. J. R., & Shao, Y. (2020). Application of a Coupled Atmospheric and Hydrological Modelling System (AHMS) to the Yellow River Basin, China. *EGU General Assembly Conference Abstracts*, 5197. <https://doi.org/10.5194/egusphere-egu2020-5197>
- Jiang, C., Parteli, E. J. R., Xia, Q., Yin, X., & Shao, Y. (2022). A regional hydrological model for arid and semi-arid river basins with consideration of irrigation. *Environmental Modelling and Software*, 157, 105531. <https://doi.org/10.1016/j.envsoft.2022.105531>
- Jiang, Q., Li, W., Fan, Z., He, X., Sun, W., Chen, S., Wen, J., Gao, J., & Wang, J. (2021). Evaluation of the ERA5 reanalysis precipitation dataset over Chinese Mainland. *Journal of Hydrology*, 595, 125660. <https://doi.org/10.1016/j.jhydrol.2020.125660>
- Jiao, D., Xu, N., Yang, F., & Xu, K. (2021). Evaluation of spatial-temporal variation performance of ERA5 precipitation data in China. *Scientific Reports*, 11(1), 1–13. <https://doi.org/10.1038/s41598-021-97432-y>
- Johnson, B. E. (1997). *Development of a storm-event-based two-dimensional upland erosion model (sediment yield)*. Colorado State University.
- Johnson, B. E., Julien, P. Y., Molnar, D. K., & Watson, C. C. (2000). The two-dimensional upland erosion model CASC2D-SED. *Journal of the American Water Resources Association*, 36(1), 31–42. <https://doi.org/10.1111/j.1752->

1688.2000.tb04246.x

- Julien, P. Y. (2010). *Erosion and sedimentation*. Cambridge university press.
- Julien, P. Y., Saghafian, B., & Ogden, F. L. (1995). RASTER-BASED HYDROLOGIC MODELING OF SPATIALLY-VARIED SURFACE RUNOFF. *JAWRA Journal of the American Water Resources Association*, 31(3). <https://doi.org/10.1111/j.1752-1688.1995.tb04039.x>
- Julien, P. Y., & Simons, D. B. (1984). *Analysis of sediment transport equations for rainfall erosion*. Civil Engineering Department, Engineering Research Center, Colorado State~....
- Julien, P. Y., & Simons, D. B. (1985). Sediment Transport Capacity of Overland Flow. *Transactions of the ASAE*, 28(3), 755–762. <https://elibrary.asabe.org/abstract.asp?aid=32333&t=3>
- Kalnay, E., Kanamitsu, M., Kistler, R., Collins, W., Deaven, D., Gandin, L., Iredell, M., Saha, S., White, G., Woollen, J., & others. (1996). The NCEP/NCAR 40-year reanalysis project. *Bulletin of the American Meteorological Society*, 77(3), 437–472.
- Kilinc, M. Y. (1972). *Mechanics of soil erosion from overland flow generated by simulated rainfall*. Colorado State University.
- Kilinc, M. Y., & Richardson, E. V. (1973). Mechanics of Soil Erosion From Overland Flow Generated By Simulated Rainfall. *Colo State Univ (Fort Collins), Hydrol Papers*, 63.
- Kinnell, P. I. A. (2005). *Raindrop-impact-induced erosion processes and prediction : a review*. 2844(December 2003), 2815–2844. <https://doi.org/10.1002/hyp.5788>
- Kinnell, P. I. A., & Risse, L. M. (1998). USLE-M: Empirical Modeling Rainfall Erosion through Runoff and Sediment Concentration. *Soil Science Society of America Journal*, 62(6), 1667–1672. <https://doi.org/https://doi.org/10.2136/sssaj1998.03615995006200060026x>
- Kirkby, M. J. (1971). Hillslope process-response models based on the continuity equation. *Inst. Br. Geogr. Spec. Publ*, 3(1), 5–30.
- Kling, H., Fuchs, M., & Paulin, M. (2012). Runoff conditions in the upper Danube basin under an ensemble of climate change scenarios. *Journal of Hydrology*, 424–425. <https://doi.org/10.1016/j.jhydrol.2012.01.011>
- Laflen, J. M., Lane, L. J., & Foster, G. R. (1991). WEPP: A new generation of erosion prediction technology. *Journal of Soil and Water Conservation*, 46(1), 34–38.
- Lal, R. (2003). Soil erosion and the global carbon budget. In *Environment International* (Vol. 29, Issue 4). [https://doi.org/10.1016/S0160-4120\(02\)00192-7](https://doi.org/10.1016/S0160-4120(02)00192-7)
- Lal, R. (2017). Soil erosion by wind and water: Problems and prospects. In *Soil Erosion Research Methods*. <https://doi.org/10.1201/9780203739358>
- Langbein, W. B., & Schumm, S. A. (1958). Yield of sediment in relation to mean annual precipitation. *Eos, Transactions American Geophysical Union*, 39(6).

<https://doi.org/10.1029/TR039i006p01076>

- Leopold, L. B., & Maddock, T. Jr. (1953). The Hydraulic Geometry of Stream Channels and Some Physiographic Implications. In *Geological Survey Professional Paper 252*.
- Liu, B. Y., Nearing, M. A., & Risse, L. M. (1994). Slope gradient effects on soil loss for steep slopes. *Transactions of the American Society of Agricultural Engineers*, 37(6), 1835–1840. <https://doi.org/10.13031/2013.28273>
- Loaiciga, H. A., Valdes, J. B., Vogel, R., Garvey, J., & Schwarz, H. (1996). Global warming and the hydrologic cycle. *Journal of Hydrology*, 174(1–2), 83–127. [https://doi.org/10.1016/0022-1694\(95\)02753-X](https://doi.org/10.1016/0022-1694(95)02753-X)
- Ludwig, W., & Probst, J. L. (1996). Predicting the oceanic input of organic carbon by continental erosion. *Global Biogeochemical Cycles*, 10(1). <https://doi.org/10.1029/95GB02925>
- Maggioni, V., Meyers, P. C., & Robinson, M. D. (2016). A review of merged high-resolution satellite precipitation product accuracy during the Tropical Rainfall Measuring Mission (TRMM) era. *Journal of Hydrometeorology*, 17(4), 1101–1117. <https://doi.org/10.1175/JHM-D-15-0190.1>
- Mantz, P. A. (1977). INCIPIENT TRANSPORT OF FINE GRAINS AND FLAKES BY FLUIDS - EXTENDED SHIELDS DIAGRAM. *ASCE J Hydraul Div*, 103(6). <https://doi.org/10.1061/jyceaj.0004766>
- Mao, D., Cherkauer, K. A., & Flanagan, D. C. (2010). Development of a coupled soil erosion and large-scale hydrology modeling system. *Water Resources Research*, 46(8), 1–15. <https://doi.org/10.1029/2009WR008268>
- Marshall, J. S., & Palmer, W. M. (1948). Relation of raindrop size to intensity. *Journal of Meteorology*, 5, 165–166.
- Martens, B., Miralles, D. G., Lievens, H., Van Der Schalie, R., De Jeu, R. A. M., Fernández-Prieto, D., Beck, H. E., Dorigo, W. A., & Verhoest, N. E. C. (2017). GLEAM v3: Satellite-based land evaporation and root-zone soil moisture. *Geoscientific Model Development*, 10(5), 1903–1925. <https://doi.org/10.5194/gmd-10-1903-2017>
- Martens, B., Miralles, D., Lievens, H., Fernández-Prieto, D., & Verhoest, N. E. C. (2016). Improving terrestrial evaporation estimates over continental Australia through assimilation of SMOS soil moisture. *International Journal of Applied Earth Observation and Geoinformation*, 48, 146–162.
- Maurer, E. P., O'Donnell, G. M., Lettenmaier, D. P., & Roads, J. O. (2001). Evaluation of the land surface water budget in NCEP/NCAR and NCEP/DOE reanalyses using an off-line hydrologic model. *Journal of Geophysical Research: Atmospheres*, 106(D16), 17841–17862.
- Maxwell, R. M., Chow, F. K., & Kollet, S. J. (2007). The groundwater-land-surface-atmosphere connection: Soil moisture effects on the atmospheric boundary layer in fully-coupled simulations. *Advances in Water Resources*, 30(12), 2447–2466. <https://doi.org/10.1016/j.advwatres.2007.05.018>
- Maxwell, R. M., Lundquist, J. K., Mirocha, J. D., Smith, S. G., Woodward, C. S., &

- Tompson, A. F. B. (2011). Development of a coupled groundwater-atmosphere model. *Monthly Weather Review*, 139(1), 96–116. <https://doi.org/10.1175/2010MWR3392.1>
- McCool, D. K., Brown, L. C., Foster, G. R., Mutchler, C. K., & Meyer, L. D. (1987). Revised slope steepness factor for the Universal Soil Loss Equation. *Transactions of the ASAE*, 30(5), 1387–1396. <https://doi.org/https://doi.org/10.13031/2013.30576>
- Merritt, W. S., Letcher, R. A., & Jakeman, A. J. (2003). A review of erosion and sediment transport models. *Environmental Modelling and Software*, 18(8–9), 761–799. [https://doi.org/10.1016/S1364-8152\(03\)00078-1](https://doi.org/10.1016/S1364-8152(03)00078-1)
- Michaelides, S., Levizzani, V., Anagnostou, E., Bauer, P., Kasparis, T., & Lane, J. E. (2009). Precipitation: Measurement, remote sensing, climatology and modeling. *Atmospheric Research*, 94(4). <https://doi.org/10.1016/j.atmosres.2009.08.017>
- Milly, P. C. D., & Dunne, K. A. (2002). Macroscale water fluxes: 1. Quantifying errors in the estimation of basin mean precipitation. *Water Resources Research*, 38(10), 23-1-23–14. <https://doi.org/10.1029/2001wr000759>
- Montgomery, D. R. (2007). Soil erosion and agricultural sustainability. *Proceedings of the National Academy of Sciences*, 104(33), 13268–13272. <https://doi.org/10.1073/pnas.0611508104>
- Morgan, R. P. C., Quinton, J. N., Smith, R. E., Govers, G., Poesen, J. W. A., Auerswald, K., Chisci, G., Torri, D., & Styczen, M. E. (1998). The European Soil Erosion Model (EUROSEM): a dynamic approach for predicting sediment transport from fields and small catchments. *Earth Surface Processes and Landforms*, 23(6), 527–544. [https://doi.org/https://doi.org/10.1002/\(SICI\)1096-9837\(199806\)23:6<527::AID-ESP868>3.0.CO;2-5](https://doi.org/https://doi.org/10.1002/(SICI)1096-9837(199806)23:6<527::AID-ESP868>3.0.CO;2-5)
- Moriasi, D. N., Arnold, J. G., Van Liew, M. W., Bingner, R. L., Harmel, R. D., & Veith, T. L. (2007). Model evaluation guidelines for systematic quantification of accuracy in watershed simulations. *Transactions of the ASABE*, 50(3), 885–900.
- Nash, E., & Sutcliffe, V. (1970). River flow forecasting through conceptual models part I. A discussion of principles. *Journal of Hydrology*, 10(3), 282–290.
- Neal, J., Schumann, G., & Bates, P. (2012). A subgrid channel model for simulating river hydraulics and floodplain inundation over large and data sparse areas. *Water Resources Research*, 48(11). <https://doi.org/10.1029/2012WR012514>
- Neitsch, S. L., Arnold, J. G., Kiniry, J. R., & Williams, J. R. (2011). *Soil and water assessment tool theoretical documentation version 2009*.
- Newbold, T., Hudson, L. N., Hill, S. L. L., Contu, S., Lysenko, I., Senior, R. A., Börger, L., Bennett, D. J., Choimes, A., Collen, B., & others. (2015). Global effects of land use on local terrestrial biodiversity. *Nature*, 520(7545), 45–50. <https://doi.org/https://doi.org/10.1038/nature14324>
- Niu, G. Y., Yang, Z. L., Mitchell, K. E., Chen, F., Ek, M. B., Barlage, M., Kumar, A., Manning, K., Niyogi, D., Rosero, E., Tewari, M., & Xia, Y. (2011). The community Noah land surface model with multiparameterization options (Noah-

- MP): 1. Model description and evaluation with local-scale measurements. *Journal of Geophysical Research Atmospheres*, 116(12). <https://doi.org/10.1029/2010JD015139>
- Oost, K. Van, Quine, T. A., Govers, G., Gryze, S. De, Six, J., Harden, J. W., Ritchie, J. C., McCarty, G. W., Heckrath, G., Kosmas, C., Giraldez, J. V, da Silva, J. R. M., & Merckx, R. (2007). The Impact of Agricultural Soil Erosion on the Global Carbon Cycle. *Science*, 318(5850), 626–629. <https://doi.org/10.1126/science.1145724>
- Orsolini, Y., Wegmann, M., Dutra, E., Liu, B., Balsamo, G., Yang, K., De Rosnay, P., Zhu, C., Wang, W., Senan, R., & Arduini, G. (2019). Evaluation of snow depth and snow cover over the Tibetan Plateau in global reanalyses using in situ and satellite remote sensing observations. *Cryosphere*, 13(8), 2221–2239. <https://doi.org/10.5194/tc-13-2221-2019>
- Oschwald, W. R. (1972). Sediment-Water Interactions. *Journal of Environmental Quality*, 1(4), 360–366. <https://doi.org/https://doi.org/10.2134/jeq1972.00472425000100040005x>
- Osterkamp, W. R., & Toy, T. J. (1997). Geomorphic considerations for erosion prediction. *Environmental Geology*, 29(3), 152–157. <https://doi.org/10.1007/s002540050113>
- Ozdogan, M., & Gutman, G. (2008). A new methodology to map irrigated areas using multi-temporal MODIS and ancillary data: An application example in the continental US. *Remote Sensing of Environment*, 112(9), 3520–3537. <https://doi.org/10.1016/j.rse.2008.04.010>
- Ozdogan, M., Rodell, M., Beaudoin, H. K., & Toll, D. L. (2010). Simulating the effects of irrigation over the united states in a land surface model based on satellite-derived agricultural data. *Journal of Hydrometeorology*, 11(1), 171–184. <https://doi.org/10.1175/2009JHM1116.1>
- Pachepsky, Y., Timlin, D., & Rawls, W. (2003). Generalized Richards' equation to simulate water transport in unsaturated soils. *Journal of Hydrology*, 272(1–4), 3–13. [https://doi.org/10.1016/S0022-1694\(02\)00251-2](https://doi.org/10.1016/S0022-1694(02)00251-2)
- Parker, G. (1979). Hydraulic geometry of active gravel rivers. *Journal of the Hydraulics Division, ASCE*, 105(HY9, Proc.Paper, 14841), 1185–1201. <https://doi.org/10.1061/jycej.0005275>
- Pelletier, J. D. (2012). A spatially distributed model for the long-term suspended sediment discharge and delivery ratio of drainage basins. *Journal of Geophysical Research: Earth Surface*, 117(F2). <https://doi.org/https://doi.org/10.1029/2011JF002129>
- Pilgrim, D. H., CHAPMAN, T. G., & DORAN, D. G. (1988). Problems of rainfall-runoff modelling in arid and semiarid regions. *Hydrological Sciences Journal*, 33(4). <https://doi.org/10.1080/02626668809491261>
- Poesen, J., Nachtergaele, J., Verstraeten, G., & Valentin, C. (2003). Gully erosion and environmental change: importance and research needs. *CATENA*, 50(2), 91–133. [https://doi.org/https://doi.org/10.1016/S0341-8162\(02\)00143-1](https://doi.org/https://doi.org/10.1016/S0341-8162(02)00143-1)

- Poesen, J. W., Vandaele, K., & Van Wesemael, B. (1996). Contribution of gully erosion to sediment production on cultivated lands and rangelands. *IAHS Publications-Series of Proceedings and Reports-Intern Assoc Hydrological Sciences*, 236, 251–266.
- Pörtner, H. O., Roberts, D. C., M. Tignor, E.S. Poloczanska, K. Mintenbeck, A. Alegria, M. Craig, S. Langsdorf, S. Löschke, V. Möller, A. Okem, & B. Rama. (2022). IPCC, 2022: Climate Change 2022: Impacts, Adaptation, and Vulnerability. Contribution of Working Group II to the Sixth Assessment Report of the Intergovernmental Panel on Climate Change. In *Climate Change 2022: The Physical Science Basis*. <https://doi.org/10.1017/9781009325844.Front>
- Qi, W., Zhang, C., Fu, G., Sweetapple, C., & Zhou, H. (2016). Evaluation of global fine-resolution precipitation products and their uncertainty quantification in ensemble discharge simulations. *Hydrology and Earth System Sciences*, 20(2), 903–920. <https://doi.org/10.5194/hess-20-903-2016>
- Qian, N., & Dai, D. Z. (1980). The problems of river sedimentation and the present status of its research in China. *Proceedings of the International Symposium on River Sedimentation*, 24(29), 19–39.
- Rafiei-Sardooi, E., Azareh, A., Joorabian Shooshtari, S., & Parteli, E. J. R. (2022). Long-term assessment of land-use and climate change on water scarcity in an arid basin in Iran. *Ecological Modelling*, 467, 109934. <https://doi.org/10.1016/j.ecolmodel.2022.109934>
- Renard, K. G., Laflen, J. M., Foster, G. R., & McCool, D. K. (2017). The revised universal soil loss equation. In *Soil erosion research methods* (pp. 105–126). Routledge.
- Richards, L. A. (1931). Capillary conduction of liquids through porous mediums. *Journal of Applied Physics*, 1(5), 318–333. <https://doi.org/10.1063/1.1745010>
- Rijn, L. C. van. (1986). Mathematical modeling of suspended sediment in nonuniform flows. *Journal of Hydraulic Engineering*, 112(6), 433–455.
- Rodell, M., Houser, P. R., Jambor, U., Gottschalck, J., Mitchell, K., Meng, C. J., Arsenault, K., Cosgrove, B., Radakovich, J., Bosilovich, M., Entin, J. K., Walker, J. P., Lohmann, D., & Toll, D. (2004). The Global Land Data Assimilation System. *Bulletin of the American Meteorological Society*, 85(3), 381–394. <https://doi.org/10.1175/BAMS-85-3-381>
- Roering, J. J., Kirchner, J. W., & Dietrich, W. E. (1999). Evidence for nonlinear, diffusive sediment transport on hillslopes and implications for landscape morphology. *Water Resources Research*, 35(3). <https://doi.org/10.1029/1998WR900090>
- Rojas, R., Julien, P., & Johnson, B. (2003). A 2-dimensional rainfall-runoff and sediment model. *CASC2D-SED Reference Manual v1. 0*.
- Rojas, S. R. (2002). *GIS-based upland erosion modeling, geovisualization and grid size effects on erosion simulations with CASC2D-SED*. Colorado State University.

- Schlesinger, W. H., & Bernhardt, E. (2020). Biogeochemistry: An Analysis of Global Change. In *Biogeochemistry: An Analysis of Global Change*. <https://doi.org/10.1016/B978-0-12-814608-8.09991-6>
- Shangguan, W., Dai, Y., Liu, B., Ye, A., & Yuan, H. (2012). A soil particle-size distribution dataset for regional land and climate modelling in China. *Geoderma*, 171–172, 85–91. <https://doi.org/https://doi.org/10.1016/j.geoderma.2011.01.013>
- Shao, Y. (2008). Physics and Modelling of Wind Erosion. In *Springer*. <https://doi.org/10.1007/978-1-4020-8895-7>
- Sheffield, J., Goteti, G., & Wood, E. F. (2006). Development of a 50-year high-resolution global dataset of meteorological forcings for land surface modeling. *Journal of Climate*, 19(13), 3088–3111. <https://doi.org/10.1175/JCLI3790.1>
- Shi, H., Li, T., & Wei, J. (2017). Evaluation of the gridded CRU TS precipitation dataset with the point raingauge records over the Three-River Headwaters Region. *Journal of Hydrology*, 548, 322–332. <https://doi.org/10.1016/j.jhydrol.2017.03.017>
- Shi, H., & Shao, M. (2000). Soil and water loss from the Loess Plateau in China. *Journal of Arid Environments*, 45(1). <https://doi.org/10.1006/jare.1999.0618>
- Shields, I. A. (1936). Anwendung der Aehnlichkeitsmechanik und der Turbulenzforschung auf die Geschiebebewegung. [English title: Application of similarity principles and turbulence research to bed-load movement]. *Preussische Versuchsanstalt Für Wasserbau Und Schiffbau*, 26.
- Shrestha, P., Sulis, M., Masbou, M., Kollet, S., & Simmer, C. (2014). A scale-consistent terrestrial systems modeling platform based on COSMO, CLM, and ParFlow. *Monthly Weather Review*, 142(9), 3466–3483. <https://doi.org/10.1175/MWR-D-14-00029.1>
- Siebert, S., Döll, P., Hoogeveen, J., Faures, J. M., Frenken, K., & Feick, S. (2005). Development and validation of the global map of irrigation areas. *Hydrology and Earth System Sciences*, 9(5), 535–547. <https://doi.org/10.5194/hess-9-535-2005>
- Skamarock, W. C., & Klemp, J. B. (2008). A time-split nonhydrostatic atmospheric model for weather research and forecasting applications. *Journal of Computational Physics*, 227(7), 3465–3485. <https://doi.org/10.1016/j.jcp.2007.01.037>
- Smith, R. E., Goodrich, D. C., & Quinton, J. N. (1995). Dynamic, distributed simulation of watershed erosion: the KINEROS2 and EUROSEM models. *Journal of Soil & Water Conservation*, 50(5).
- Soil Survey Division Staff. (1993). *Soil survey manual* (Issue 18). US Department of Agriculture.
- Sophocleous, M. (2002). Interactions between groundwater and surface water: The state of the science. *Hydrogeology Journal*, 10(1), 52–67. <https://doi.org/10.1007/s10040-001-0170-8>
- Stewart, J. R., Livneh, B., Kasprzyk, J. R., Rajagopalan, B., Minear, J. T., & Raseman, W. J. (2017). A Multialgorithm Approach to Land Surface Modeling

- of Suspended Sediment in the Colorado Front Range. *Journal of Advances in Modeling Earth Systems*, 9(7), 2526–2544. <https://doi.org/10.1002/2017MS001120>
- Stisen, S., & Sandholt, I. (2010). Evaluation of remote-sensing-based rainfall products through predictive capability in hydrological runoff modelling. *Hydrological Processes*, 24(7), 879–891. <https://doi.org/10.1002/hyp.7529>
- Stokes, G. G. (1851). On the effect of the Internal friction of fluids on the motion of pendulums - Section III. *Transactions of the Cambridge Philosophical Society*, IX.
- Syvitski, J. P. M., Vorosmarty, C. J., Kettner, A. J., & Green, P. (2005). Impact of humans on the flux of terrestrial sediment to the global coastal ocean. *Science*, 308(5720), 376–380. <https://doi.org/10.1126/science.1109454>
- Tan, Z., Leung, L. R., Li, H. Y., & Tesfa, T. (2017). Modeling Sediment Yield in Land Surface and Earth System Models: Model Comparison, Development, and Evaluation. *Journal of Advances in Modeling Earth Systems*, 10(9), 2192–2213. <https://doi.org/10.1029/2017MS001270>
- Tang, G., Zeng, Z., Long, D., Guo, X., Yong, B., Zhang, W., & Hong, Y. (2016). Statistical and hydrological comparisons between TRMM and GPM Level-3 products over a midlatitude Basin: Is day-1 IMERG a good successor for TMPA 3B42V7? *Journal of Hydrometeorology*, 17(1), 121–137. <https://doi.org/10.1175/JHM-D-15-0059.1>
- Trenberth, K. E. (1999). Conceptual framework for changes of extremes of the hydrological cycle with climate change. *Climatic Change*, 42(1). <https://doi.org/10.1023/A:1005488920935>
- Tucker, G. E., & Hancock, G. R. (2010). Modelling landscape evolution. *Earth Surface Processes and Landforms*, 35(1), 28–50. <https://doi.org/https://doi.org/10.1002/esp.1952>
- Vanoni, V. A. (2006). *Sedimentation Engineering* (Classic Ed). American Society of Civil Engineers. <https://doi.org/10.1061/9780784408230>
- Vorosmarty, C. J., & Sahagian, D. (2000). Anthropogenic disturbance of the terrestrial water cycle. In *BioScience* (Vol. 50, Issue 9). [https://doi.org/10.1641/0006-3568\(2000\)050\[0753:ADOTTW\]2.0.CO;2](https://doi.org/10.1641/0006-3568(2000)050[0753:ADOTTW]2.0.CO;2)
- Wagner, S., Fersch, B., Yuan, F., Yu, Z., & Kunstmann, H. (2016). Fully coupled atmospheric-hydrological modeling at regional and long-term scales: Development, application, and analysis of WRF-HMS. *Water Resources Research*, 52(4), 3187–3211. <https://doi.org/10.1002/2015WR018185>
- Waichler, S. R., & Wigmosta, M. S. (2003). Development of hourly meteorological values from daily data and significance to hydrological modeling at H. J. Andrews experimental forest. *Journal of Hydrometeorology*, 4(2). [https://doi.org/10.1175/1525-7541\(2003\)4<251:DOHMFV>2.0.CO;2](https://doi.org/10.1175/1525-7541(2003)4<251:DOHMFV>2.0.CO;2)
- Walling, D. E. (1999). Linking land use, erosion and sediment yields in river basins. *Hydrobiologia*, 410, 223–240. <https://doi.org/10.1023/A:1003825813091>
- Wang, F., Hessel, R., Mu, X., Maroulis, J., Zhao, G., Geissen, V., & Ritsema, C.

- (2015). Distinguishing the impacts of human activities and climate variability on runoff and sediment load change based on paired periods with similar weather conditions: A case in the Yan River, China. *Journal of Hydrology*, 527. <https://doi.org/10.1016/j.jhydrol.2015.05.037>
- Wang, J., Zhuo, L., Han, D., Liu, Y., & Rico-Ramirez, M. A. (2023). Hydrological Model Adaptability to Rainfall Inputs of Varied Quality. *Water Resources Research*, 59(2). <https://doi.org/10.1029/2022WR032484>
- Wang, S., Fu, B., Piao, S., Lü, Y., Ciais, P., Feng, X., & Wang, Y. (2016). Reduced sediment transport in the Yellow River due to anthropogenic changes. *Nature Geoscience*, 9(1). <https://doi.org/10.1038/ngeo2602>
- Ward, R. C., & Robinson, M. (1975). *Principles of hydrology* (Vol. 367). McGraw-Hill London.
- Watts, J. (2021). Climate scientists shocked by scale of floods in Germany. *The Guardian*.
- Wicks, J. M. (1988). *Physically-based mathematical modelling of catchment sediment yield*. Newcastle University.
- Wicks, J. M., & Bathurst, J. C. (1996). SHESED: A physically based, distributed erosion and sediment yield component for the SHE hydrological modelling system. *Journal of Hydrology*, 175(1–4), 213–238. [https://doi.org/10.1016/S0022-1694\(96\)80012-6](https://doi.org/10.1016/S0022-1694(96)80012-6)
- Wiese, D. N., Yuan, D. N., Boening, C., Landerer, F. W., & Watkins, M. M. (2018). JPL GRACE mascon ocean, ice, and hydrology equivalent water height release 06 coastal resolution improvement (CRI) filtered version 1.0. *DAAC: Pasadena, CA, USA*.
- Wilby, R., Greenfield, B., & Glenny, C. (1994). A coupled synoptic-hydrological model for climate change impact assessment. *Journal of Hydrology*, 153(1–4), 265–290. [https://doi.org/10.1016/0022-1694\(94\)90195-3](https://doi.org/10.1016/0022-1694(94)90195-3)
- Wilkinson, B. H., & McElroy, B. J. (2007). The impact of humans on continental erosion and sedimentation. *Bulletin of the Geological Society of America*, 119(1–2). <https://doi.org/10.1130/B25899.1>
- Williams, J. R. (1975). Sediment-yield prediction with universal equation using runoff energy factor. *Present and Prospective Technology for Predicting Sediment Yield and Sources*, 244–252.
- Wischmeier, W. H., & Smith, D. D. (1978). *Predicting rainfall erosion losses: a guide to conservation planning* (Issue 537). Department of Agriculture, Science and Education Administration.
- Wood, E. F., Sivapalan, M., Beven, K., & Band, L. (1988). Effects of spatial variability and scale with implications to hydrologic modeling. *Journal of Hydrology*, 102(1–4). [https://doi.org/10.1016/0022-1694\(88\)90090-X](https://doi.org/10.1016/0022-1694(88)90090-X)
- Xia, Q. (2019). *Development and Application of a Coupled Atmospheric and Hydrological Modelling System*. 1–125. <https://kups.ub.uni-koeln.de/9450/>
- Xia, Q., Liu, P., Fan, Y., Cheng, L., An, R., Xie, K., & Zhou, L. (2022).

- Representing Irrigation Processes in the Land Surface-Hydrological Model and a Case Study in the Yangtze River Basin, China. *Journal of Advances in Modeling Earth Systems*, 14(7). <https://doi.org/10.1029/2021MS002653>
- Xia, Y. (2008). Adjustment of global precipitation data for orographic effects using observed annual streamflow and the LaD model. *Journal of Geophysical Research Atmospheres*, 113(4). <https://doi.org/10.1029/2007JD008545>
- Xu, X., Chen, F., Barlage, M., Gochis, D., Miao, S., & Shen, S. (2019). Lessons Learned From Modeling Irrigation From Field to Regional Scales. *Journal of Advances in Modeling Earth Systems*, 11(8), 2428–2448. <https://doi.org/10.1029/2018MS001595>
- Yalin, M. S. (1963). An Expression for Bed-Load Transportation. *Journal of the Hydraulics Division*, 89(3), 221–250. <https://doi.org/10.1061/JYCEAJ.0000874>
- Yamazaki, D., Ikeshima, D., Sosa, J., Bates, P. D., Allen, G. H., & Pavelsky, T. M. (2019). MERIT Hydro: A High-Resolution Global Hydrography Map Based on Latest Topography Dataset. *Water Resources Research*, 55(6), 5053–5073. <https://doi.org/10.1029/2019WR024873>
- Yamazaki, D., Kanae, S., Kim, H., & Oki, T. (2011). A physically based description of floodplain inundation dynamics in a global river routing model. *Water Resources Research*, 47(4). <https://doi.org/10.1029/2010WR009726>
- Yang, C., Lin, Z., Yu, Z., Hao, Z., & Liu, S. (2010). Analysis and simulation of human activity impact on streamflow in the huaihe river basin with a large-scale hydrologic model. *Journal of Hydrometeorology*, 11(3), 810–821. <https://doi.org/10.1175/2009JHM1145.1>
- Yang, C. T. (1972). Unit Stream Power and Sediment Transport. *Journal of the Hydraulics Division*, 98(10), 1805–1826. <https://doi.org/10.1061/JYCEAJ.0003439>
- Yang, C. T. (1973). INCIPIENT MOTION AND SEDIMENT TRANSPORT. *ASCE J Hydraul Div*, 99(HY10). <https://doi.org/10.1061/jyceaj.0003766>
- Yeh, P. J.-F., & Famiglietti, J. S. (2008). Regional terrestrial water storage change and evapotranspiration from terrestrial and atmospheric water balance computations. *Journal of Geophysical Research: Atmospheres*, 113(D9).
- Yin, S., Xie, Y., Nearing, M. A., & Wang, C. (2007). Estimation of rainfall erosivity using 5- to 60-minute fixed-interval rainfall data from China. *Catena*, 70(3), 306–312. <https://doi.org/10.1016/j.catena.2006.10.011>
- Yin, Z., Ottlé, C., Ciais, P., Zhou, F., Wang, X., Jan, P., Dumas, P., Peng, S., Li, L., Zhou, X., Bo, Y., Xi, Y., & Piao, S. (2021). Irrigation, damming, and streamflow fluctuations of the Yellow River. *Hydrology and Earth System Sciences*, 25(3), 1133–1150. <https://doi.org/10.5194/hess-25-1133-2021>
- Yu, Y., Schneider, U., Yang, S., Becker, A., & Ren, Z. (2020). Evaluating the GPCP Full Data Daily Analysis Version 2018 through ETCCDI indices and comparison with station observations over mainland of China. *Theoretical and Applied Climatology*, 142(3–4), 835–845. <https://doi.org/10.1007/s00704-020-03352-8>

- Yu, Y., Wang, H., Shi, X., Ran, X., Cui, T., Qiao, S., & Liu, Y. (2013). New discharge regime of the Huanghe (Yellow River): Causes and implications. *Continental Shelf Research*, 69, 62–72. <https://doi.org/10.1016/j.csr.2013.09.013>
- Yu, Z., Lakhtakia, M. N., & Barron, E. J. (1999). Modeling the river-basin response to single-storm events simulated by a mesoscale meteorological model at various resolutions. *Journal of Geophysical Research Atmospheres*, 104(D16), 19675–19689. <https://doi.org/10.1029/1999JD900339>
- Yu, Z., Pollard, D., & Cheng, L. (2006). On continental-scale hydrologic simulations with a coupled hydrologic model. *Journal of Hydrology*, 331(1–2), 110–124. <https://doi.org/10.1016/j.jhydrol.2006.05.021>
- Yuan, X., Ma, F., Wang, L., Zheng, Z., Ma, Z., Ye, A., & Peng, S. (2016). An experimental seasonal hydrological forecasting system over the Yellow River basin &ndash; Part 1: Understanding the role of initial hydrological conditions. *Hydrology and Earth System Sciences*, 20(6), 2437–2451. <https://doi.org/10.5194/hess-20-2437-2016>
- Zhang, K., Li, S., Peng, W., & Yu, B. (2004). Erodibility of agricultural soils on the Loess Plateau of China. *Soil and Tillage Research*, 76(2), 157–165. <https://doi.org/10.1016/j.still.2003.09.007>
- Zheng, F., & Wang, B. (2014). Soil Erosion in the Loess Plateau Region of China. In A. Tsunekawa, G. Liu, N. Yamanaka, & S. Du (Eds.), *Restoration and Development of the Degraded Loess Plateau, China* (pp. 77–92). Springer Japan. [https://doi.org/10.1007/978-4-431-54481-4\\_6](https://doi.org/10.1007/978-4-431-54481-4_6)

## Acknowledgments

I thank the German Research Foundation (DFG) for funding this work under the Heisenberg Programme “Multiscale Simulation of Earth Surface Processes” (project number: 434377576) and through the Collaborative Research Center SFB1211 “Earth – Evolution at the Dry Limit” (project number: 268236062). I thank the Regional Computing Center of the University of Cologne (RRZK) for providing computing time on the DFG-funded (Funding number: INST 216/512/1FUGG) High Performance Computing (HPC) system CHEOPS as well as support.

I thank the Graduate School of Geosciences (GSGS) at the University of Cologne for all its support and assistance. I would like to thank Dr. Karin Boessenkool for organising all the workshops and conferences and for providing enormous help and support to me. I thank Ms. Dagmar Janzen for the supporting paperwork and Ms. Nikopoulou Christina from Kölner Studierendenwerk for her help with accommodation during my PhD studies.

I thank my supervisors, Prof. Dr. Yaping Shao and Dr. Eric Parteli. A big thank you to Dr. Eric Parteli for his extensive guidance and support during my PhD study. I thank him for accepting to be my daily supervisor and allowing me to join his research group. I am always impressed by his passion for academia and his profound knowledge. I am very grateful to Prof. Dr. Yaping Shao for accepting me as a PhD candidate and providing invaluable guidance and assistance throughout my PhD study. His profound knowledge and rigorous academic attitude have had a profound impact on me and will always guide me in my academic journey. I thank Prof. Dr. Roel Neggers for participating in the Doctoral Committee and for helping me during the transition period. I thank Dr. Qian Xia for patiently leading me to learn the AHMS and many tools such as ArcGIS.

I thank Prof. Dr. Karl Schneider for being the second reviewer of this thesis and for providing valuable expert insights. I thank Prof. Dr. Bülent Tezkan for being the chairman of my defence committee. I thank Dr. Christian Wegener for taking the minutes in my PhD defence. I thank Dr. Markus Karrer, Dr. Jan Chylík, Dr. Franz Kanngießer, Dr. Qian Xia and Jonathan Kostelecky for reading my thesis and providing valuable feedback and grammatical corrections.

I thank everyone in the Research Group of Prof. Dr. Yaping Shao and the Research Group of Dr. Eric Parteli. I thank everyone who enjoys lunch at the Mensa and Bistro together. I thank all my colleagues at the Institute of Geophysics and Meteorology for their kindness and support.

I thank my family and friends. I thank my parents and brother for their support and understanding all the time. I thank my wife Xin Yin for her tremendous support and understanding throughout my PhD study. I am so lucky to have been through this journey with you, and I could not have done it without your support.

### **Eidesstattliche Versicherung**

Hiermit versichere ich an Eides statt, dass ich die vorliegende Dissertation selbstständig und ohne die Benutzung anderer als der angegebenen Hilfsmittel und Literatur angefertigt habe. Alle Stellen, die wörtlich oder sinngemäß aus veröffentlichten und nicht veröffentlichten Werken dem Wortlaut oder dem Sinn nach entnommen wurden, sind als solche kenntlich gemacht. Ich versichere an Eides statt, dass diese Dissertation noch keiner anderen Fakultät oder Universität zur Prüfung vorgelegen hat; dass sie - abgesehen von unten angegebenen Teilpublikationen und eingebundenen Artikeln und Manuskripten - noch nicht veröffentlicht worden ist sowie, dass ich eine Veröffentlichung der Dissertation vor Abschluss der Promotion nicht ohne Genehmigung des Promotionsausschusses vornehmen werde. Die Bestimmungen dieser Ordnung sind mir bekannt. Darüber hinaus erkläre ich hiermit, dass ich die Ordnung zur Sicherung guter wissenschaftlicher Praxis und zum Umgang mit wissenschaftlichem Fehlverhalten der Universität zu Köln gelesen und sie bei der Durchführung der Dissertation zugrundeliegenden Arbeiten und der schriftlich verfassten Dissertation beachtet habe und verpflichte mich hiermit, die dort genannten Vorgaben bei allen wissenschaftlichen Tätigkeiten zu beachten und umzusetzen. Ich versichere, dass die eingereichte elektronische Fassung der eingereichten Druckfassung vollständig entspricht.

Köln, 11. March 2023

Cong Jiang

*Cong Jiang*

### **Publications**

1. **Jiang, C.**, Parteli, E. J., Xia, Q., Yin, X., & Shao, Y. (2022). A regional hydrological model for arid and semi-arid river basins with consideration of irrigation. *Environmental Modelling & Software*, 105531. doi: [10.1016/j.envsoft.2022.105531](https://doi.org/10.1016/j.envsoft.2022.105531) (Impact factor: 5.471/Q1)

### **Manuscripts**

1. **Jiang, C.**, Parteli, E. J., Xia, Q. & Shao, Y. Evaluation of Precipitation-Reanalysis Products for Regional Hydrological Modelling
2. **Jiang, C.**, Parteli, E. J. & Shao, Y. A model for continental-scale water erosion and sediment transport and its application to the Yellow River Basin